Aus dem

Institut für Immunologie

Institut der Ludwig-Maximilians-Universität München

Investigating the role of RORgt- and BCL6-expressing dendritic cells in immunity

Dissertation

zum Erwerb des Doctor of Philosophy (Ph.D.)

an der Medizinischen Fakultät

der Ludwig-Maximilians-Universität München

vorgelegt von

Hamsa Narasimhan

aus

Chennai / India

Jahr

2025

Mit Genehmigung der Medizinischen Fakultät der
Ludwig-Maximilians-Universität München

Erstes Gutachten:	Prof. Dr. Barbara Schraml-Schotta
Zweites Gutachten:	Prof. Dr. Marc Schmidt-Supprian
Drittes Gutachten:	Dr. Jörg Renkawitz
Viertes Gutachten:	Prof. Dr. David Anz

Dekan: Prof. Dr. med. Thomas Gudermann

Tag der mündlichen Prüfung: 08.12.2025

Affidavit

Narasimhan, Hamsa

Surname, first name

I hereby declare, that the submitted thesis entitled

Investigating the role of RORgt- and BCL6-expressing dendritic cells in immunity

is my own work. I have only used the sources indicated and have not made unauthorised use of services of a third party. Where the work of others has been quoted or reproduced, the source is always given.

I further declare that the dissertation presented here has not been submitted in the same or similar form to any other institution for the purpose of obtaining an academic degree.

Munich, 10.12.2025

Place, Date

Hamsa Narasimhan

Signature doctoral candidate

LMU LUDWIG-MAXIMILIANS-UNIVERSITÄT MÜNCHEN

Dean's Office Medical Faculty
Doctoral Office

Confirmation of congruency between printed and electronic version of the doctoral thesis

Narasimhan, Hamsa

Surname, first name

I hereby declare that the electronic version of the submitted thesis, entitled

Investigating the role of RORgt- and BCL6-expressing dendritic cells in immunity

is congruent with the printed version both in content and format.

Munich, 10.12.2025

Place, Date

Hamsa Narasimhan

Signature doctoral candidate

Table of contents

List of abbreviations

AIRE	Autoimmune regulator
APC	Antigen presenting cell
ATAC	Assay for transposase-accessible chromatin
AUC	Area under the curve
BCL6	B cell lymphoma 6
CD	Cluster of differentiation
cDC	Conventional dendritic cell
cDC1	Type 1 conventional dendritic cells
cDC2	Type 2 conventional dendritic cells
CDP	Common dendritic cell progenitor
CFU	Colony forming units
Citro	*Citrobacter rodentium*
coLP	Colon lamina propria
CSF	Cerebrospinal fluid
CTV	Cell Trace Violet
d	day(s)
DC	Dendritic cell
DEG	Differentially expressed genes
DTR	Diptheria toxin receptor
EAE	Experimental autoimmune encephalomyelitis
eRegulon	Enhancer-driven gene regulatory network
eTAC	Extra thymic AIRE-expressing cell
FLT3L	Fms tyrosine kinase 3 ligand
FMO	Fluorescence minus one
GC	Germinal center
GFP	Green fluorescence protein
GO	Gene ontology
GSEA	Gene set enrichment analysis
HLA-DR	Human leukocyte antigen-DR isotype
i.p.	Intraperitoneal
IFN	Interferon
IL	Interleukin
ILC	Innate lymphoid cell
IRF	Interferon regulatory factors
JC	Janus cell
KEGG	Kyoto encyclopaedia of genes and genomes
KO	Knock out
LNs	Lymph nodes
LP	Lamina propria
LTi	Lymphoid tissue inducer cells
MDP	Monocyte dendritic cell progenitor
MFI	Mean fluorescence intensity
MHC	Major histocompatibility complex
mLNs	Mesenteric lymph nodes
MOG	Myelin oligodendrocyte glycoprotein
mTEC	Medullary thymic epithelial cells
NES	Negative enrichment score
OTI	Ovalbumin-specific $CD8^+$ T cell receptor transgenic T cells

OTII	Ovalbumin-specific $CD4^+$ T cell receptor transgenic T cells
OVA	Ovalbumin
OVA-MEF	Ovalbumin-expressing mouse embryonic fibroblasts
$OVA_{323-339}$	Olvabumin peptide 323-339
p.i.	Post infection
PC	Principal component
PCA	Principal component analysis
pDC	Plasmacytoid dendritic cell
Ped.	Paediatric
pLNs	Peripheral lymph nodes
R848	Resiquimod
RORE	Retinoic-related receptor enhancer sequences
RORγt	Retinoic acid-related orphan receptor gamma t
RSS	Regulon specificity score
scRNAseq	Single cell RNA-sequencing
siLP	Small intestinal lamina propria
SRBC	Sheep red blood cells
TC	Thetis cells
TCR	T cell receptor
tDC	Transitional dendritic cells
TF	Transcription factor
Tfh	T follicular helper cells
Tfr	T follicular regulatory cells
TGF	Transforming growth factor
Th17	T helper 17
Th2	T helper 2
TLR	Toll like receptor
TNF	Tumour necrosis factor
TOM	Tomato
Treg	Regulatory T cells
UMAP	Uniform Manifold Approximation and Projection
Untx	Untreated
w	Week(s)
WT	Wild type
YFP	Yellow fluorescent protein

List of publications

Publications used in this cumulative thesis:

1) **Narasimhan H**, et al. RORγt-expressing dendritic cells are functionally versatile and evolutionarily conserved antigen presenting cells. Proc. Natl. Acad. Sci. USA. 2025 Mar 4;122(9):e2417308122. doi: 10.1073/pnas.2417308122.

2) Xiao H, Ulmert I, Bach L, Huber J, **Narasimhan H**, et al. Genomic deletion of Bcl6 differentially affects conventional dendritic cell subsets and compromises Tfh/Tfr/Th17 cell responses. Nat Commun. 2024 Apr 30;15(1):3554. doi: 10.1038/s41467-024-46966-6.

Complete list of publications:

1) **Narasimhan H**, et al. RORγt-expressing dendritic cells are functionally versatile and evolutionarily conserved antigen presenting cells. Proc. Natl. Acad. Sci. USA. 2025 Mar 4;122(9):e2417308122. doi: 10.1073/pnas.2417308122.

2) Woelk J, **Narasimhan H, et al.** NR2F6 regulates stem cell hematopoiesis and myelopoiesis in mice. Front Immunol. 2025 Jan 7;15:1404805. doi: 10.3389/fimmu.2024.1404805. eCollection 2024.

3) Xiao H, Ulmert I, Bach L, Huber J, **Narasimhan H, et al.** Genomic deletion of Bcl6 differentially affects conventional dendritic cell subsets and compromises Tfh/Tfr/Th17 cell responses**.** Nat Commun. 2024 Apr 30;15(1):3554. doi: 10.1038/s41467-024-46966-6.

4) Wyczanska M, Thalmeier F, Keller U, Klaus R, **Narasimhan H**, et al. Interleukin-10 enhances recruitment of immune cells in the neonatal mouse model of obstructive nephropathy. Sci Rep. 2024 Mar 6;14(1):5495. doi: 10.1038/s41598-024-55469-9.

1. Introductory Summary

1.1 Conventional dendritic cells are critical activators of T cell responses

Antigen presenting cells (APCs) are critical regulators of immunity through processing and presenting antigens on MHC molecules to T cells. T cells with cognate T cell receptor (TCR) are then activated to initiate antigen-specific adaptive immune responses[1, 2]. While many immune cell types can serve as APCs, conventional dendritic cells (cDCs) are the most potent APCs capable of activating naïve T cells[3]. Importantly, cDCs integrate signals from their environment and direct context-specific T cell effector responses by secreting various cytokines and providing additional signals through co-stimulatory or co-inhibitory molecules[1, 2].

cDCs are an evolutionarily conserved immune cell type which have been phenotypically and functionally characterized in various species[4]. Across mammalian lymphoid and non-lymphoid tissues cDCs serve as immune sentinel cells that actively surveil their environment for signs of infection or damage. Armed with an array of pattern recognition receptors (PRRs), they can recognize various pathogen-associated molecular patterns (PAMPs) or damage-associated molecular patterns (DAMPs)[2]. Such endogenously or exogenously derived signals are internalized and processed by cDCs, and antigen-derived peptides are then loaded onto MHC molecules – a process termed 'antigen presentation'[5, 6]. cDCs patrolling tissues typically exist in an immature state and upon pathogen encounter undergo a maturation process which enhances their immunostimulatory capacity[5]. Termed 'migratory cDCs' (migDCs) these cDCs are characterized by an upregulation of surface MHC and costimulatory molecules and increased secretion of cytokines and chemokines. MigDCs are also marked by high expression of chemokine receptor CCR7, which enables them to migrate from tissues to draining lymph nodes, or within lymphoid tissues to T cell zones where they activate T cells. Collectively these features of antigen processing and presentation, maturation, and migration represent hallmark characteristics of cDCs which allow them to excel at priming T cell responses.

cDCs are capable of orchestrating diverse T cell responses ranging from inducing tolerance to differentiation of distinct effector subsets in a context-dependent manner. This makes them attractive targets for vaccination for instance in cancer immunotherapy which is a burgeoning area of research in the cDC field[7, 8]. However, it is not a singular cDC population that directs diverse T cell responses. cDCs themselves are diverse and exist as functionally distinct subsets. Understanding this diversity and its determinants is key to uncovering the full functional spectrum of cDCs which would allow for targeting specific functional subsets for therapy.

1.2 Revisiting dendritic cell nomenclature

cDCs belong to the mononuclear phagocyte system and are historically described to arise in bone marrow from myeloid hematopoietic progenitors. Macrophage and DC progenitors (MDPs) differentiate into common or conventional dendritic cell progenitors (CDPs) which were initially described to give rise to cDCs as well as plasmacytoid dendritic cells (pDC)[9]. pDCs play a critical role in antiviral immunity as they are potent producers of type I interferons. pDCs are transcriptionally distinct from cDCs and are shown to largely arise from lymphoid progenitors[10, 11]. Importantly, unlike cDCs, pDCs are poor at antigen processing and presentation and do not migrate via lymphatics to T cell zones. Therefore, due to their lack of such cDC hallmarks it has been proposed that pDCs should not be classified as “dendritic cells” and instead be aligned with innate lymphocytes and be called “plasmacytoid cells” or “interferon-producing cells”[12, 13].

cDC-restricted CDPs express the gene *Clec9a* encoding c-type lectin receptor DNGR-1 which continues to be expressed as they differentiate into pre-cDCs[14]. *Clec9a*$^{+}$ pre-cDCs exit the bone marrow and travel via blood to seed various tissues where they retain proliferative capacity before they terminally differentiate into cDCs which can be broadly divided into two subtypes – cDC1 which actively express DNGR-1 and cDC2, which do not[15]. A mouse model with expression of Cre-recombinase under the *Clec9a* promoter (*Clec9a*^{Cre}), crossed to a Rosa26-stop-floxed fluorescent reporter mouse tracks cDCs arising from *Clec9a*-expressing myeloid progenitors, allowing to distinguish them from other mononuclear phagocytes and establishing them as a developmentally distinct lineage[14]. Furthermore, *Clec9a*^{Cre} can also be used for cDC-specific depletion when crossed to Rosa26-stop-floxed-diptheria toxin mice (*Rosa26*^{DTA}), as this results in a deletion of all *Clec9a*-expressing myeloid progenitors and their progeny[16]. Studies using such models played a pivotal role in advancing knowledge of cDC development and biology. As cDCs were shown to be a distinct immune lineage descending from specific myeloid progenitors, this led to defining cDCs based on ontogeny[17, 18].

However, numerous recent studies challenge such an ontogeny-based definition of this cell type. In the absence of myeloid cDC progenitors, a lymphoid contribution to the adult cDC2 pool has been shown in adult *Clec9a*^{Cre}*Rosa26*^{DTA} mice[16]. Furthermore, *Clec9a*^{Cre} based fate-mapping has revealed dual ontogeny for cDC2 in early life[19]. cDC2 in early life develop in waves, first arising from fetal liver lymphoid progenitors which are then replaced by cells arising from *Clec9a*-expressing myeloid progenitors[19]. These cDC2 in early life while of distinct origin are otherwise identical in terms of phenotype, transcriptional profile and function to those arising from canonical myeloid cDC progenitors[16, 19]. Notably, in these studies, dendritic cells arising from non-*Clec9a*-expressing progenitors are called “DC2” not “cDC2” to reflect their different origin from ‘conventional’ dendritic

cells. Other populations phenotypically and functionally resembling cDCs but having distinct origin are emerging. Sulczewski et al.[20] describe a cell type resembling both cDC2 and pDC, termed 'transitional DCs' (tDCs)[21]. tDCs in mice arise from bone marrow lymphoid progenitors shared with pDC, however in steady state tDCs functionally align with cDCs as they can internalize, process and present antigens to activate naïve T cells[20]. Another recent study describes a population of cells in mice termed 'DC3' which resemble a homonymous population described in humans[22, 23]. Murine DC3 overlap in phenotype with monocytes and cDC2 and are reported to be a distinct lineage arising via a pro-DC3 progenitor from a Ly6C-expressing fraction of MDP. Like cDCs, murine DC3s are capable of activating naïve T cells and are shown to be superior to cDC2 in polarizing Th17 responses in vitro[24]. Collectively, these studies demonstrate that APCs which transcriptionally, phenotypically, and importantly functionally resemble cDCs can arise from diverse progenitors in steady state. Therefore, defining a dendritic cell solely based on origin would exclude numerous APC populations which are phenotypically and functionally indistinguishable from cDCs. This would also lead to an expansion in new "cell types", which unless thoroughly characterised would lack proper contextualization and lead to confusion regarding identity and lineage relationships. Therefore, current knowledge strongly recommends employing the nomenclature of "DC" for cells in steady state exhibiting hallmarks of cDCs, serving as immune sentinels excelling at activating and polarizing T cell responses.

1.3 Dendritic cells exist as functionally and developmentally distinct subsets.

cDCs residing across murine tissues are defined by high expression of the integrin CD11c and MHCII. Broadly, cDCs can be divided into two developmentally distinct subtypes – cDC1 and cDC2 in mice and humans[25]. cDC1 across tissues are characterised by expression of chemokine receptor XCR1 and c-type lectin receptor DNGR-1 (CLEC9A)[12]. They also express tissue-specific markers, for example cDC1 in peripheral tissues express CD24 and CD103[26]. cDC1 are developmentally dependent on transcription factors such as BATF3 and IRF8. Early commitment to pre-cDC1 at the CDP stage is dependent for instance on *Irf8*[27]. cDC1 are absent in *Batf3*$^{-/-}$ mice, however pre-cDC1 do develop and are diverted to a cDC2-like transcriptional state due to the lack of *Batf3*-dependent IRF8 expression indicating that these transcription factors act differentially in cDC1 development[28, 29]. cDC1 are specialized to present exogenous antigens via MHCI to activate CD8^{+} T cells in a process termed 'cross presentation'. This makes them critical players in anti-tumor immunity. cDC1 are also important in protection against intracellular pathogens through their production of IL-12 to initiate Th1 responses[30].

cDC2 are typically marked by high expression of integrin ITGAM (CD11b) and Sirpα (CD172a), and do not express XCR1 or DNGR-1. In peripheral tissues such as lung or small intestine, fractions of cDC2 also express CD24 and CD103[26]. cDC2 are specialized in activating $CD4^+$ T cells and polarizing their differentiation into effector subtypes in particular Th2 and Th17, making them important in immunity against parasites, allergens and extracellular pathogens[31].

cDC2 themselves are diverse and were historically divided based on dependency on transcription factors *Notch2* or *Klf4*. Deletion of *Klf4* in cDC2 was shown to result in impaired Th2 priming[32]. *Notch2*-dependent cDC2, marked by high expression of cell adhesion molecule ESAM ($ESAM^{high}$ cDC2) in spleen and LNs and CD103 in the intestines, were shown to regulate Th17 and Tfh responses in these tissues[33, 34]. Development of high dimensional technologies in the last decade has enabled further study of cDC2 heterogeneity. For instance, using transcriptional profiling and chromatin analyses Brown et al.[35], proposed that cDC2 in mice and humans may be divided into two transcriptionally and functionally distinct lineages based on transcription factors T-bet and RORγt, which were historically associated with subsets of lymphocytes. Phenotypic, transcriptional and chromatin accessibility profiling aligned $T\text{-}bet^+$ cells with *Notch2*-dependent $ESAM^{high}$ cDC2 which were named “cDC2A”. The second population lacking T-bet termed “cDC2B” was heterogenous containing cells expressing surface markers CLEC10A and CLEC12A. Chromatin accessibility analyses revealed that cDC2B had an enrichment of peaks associated with the RORE motif leading to the proposal that the transcriptional identity of cDC2B is regulated by RORγt. However, neither *Rorc* transcripts nor active expression of RORγt was found in cDC2B and only a small fraction of cDC2 were shown to have expression history of *Rorc*, the gene encoding RORγt. This division of cDC2 into two lineages, and although tenuous - the notion that cDC2B express and are regulated by RORγt, was widely adopted by the scientific community[36-38]. It is important to note that active expression of RORγt was not shown in cDC2B, in light of an increasing number of studies demonstrating that APCs marked by active expression of RORγt are critical for regulating peripheral T cell mediated tolerance[39].

Advancement in high dimensional technologies have also led to the description of several new DC populations in mice and humans, providing a powerful way to map these populations across species using transcriptional signatures. For example, the emerging populations mentioned in the previous section - DC3 derived from monocytic progenitors, and tDC arising from lymphoid progenitors were first identified through single cell RNA sequencing (scRNAseq) of human PBMCs or various mouse tissues[21, 22]. However, studies using such technologies must be interpreted with caution to determine if they describe

a cell state acquired due to external cues or a new cell subset as this is critical for putting emerging populations into context.

1.4 Transcription factors shape dendritic cell identity

Transcription factors are critical in shaping various aspects of cDC identity such as development, differentiation and consequently heterogeneity. Dependence on growth factor Fms tyrosine kinase 3 ligand (FLT3L) is a key feature of murine cDCs[12]. Receptor for FLT3L, FLT3 (CD135) is expressed on all cDC-committed progenitors and mice lacking FLT3 or FLT3L exhibit a significant reduction in cDCs[40]. FLT3L cultures are the gold standard for generating both murine and human cDC subsets in vitro[41, 42]. Transcription factors such as PU.1, RUNX1 and CBFβ play an important role in shaping early cDC differentiation from hematopoietic stem cells (HSCs) through their role in regulating FLT3 expression on cDC progenitors and thereby their access to cell-extrinsic signals.

ZBTB46 (zDC) is transcription factor typically used to define cDCs in mice and humans as it was initially shown to be specifically expressed by cDCs and their progenitors[43, 44]. ZBTB46 is not essential for cDC development, but regulates the activation of cDCs in steady state and therefore their initiation of immune responses[45]. Mice expressing Diptheria toxin receptor under the zDC promoter (zDC-DTR) have been commonly used in studies investigating the role of cDCs in immunity[46]. However, it should be noted that recent studies show that ZBTB46 expression is not restricted to cDCs. ZBTB46 is also expressed in a subset of intestinal CCR6-expressing type-3 innate lymphocytes (ILC3s), and is critical for restricting their pro-inflammatory capacity allowing them to be important regulators of intestinal inflammation[47]. In tumors, ZBTB46 is expressed by endothelial cells and fibroblasts and critically regulates their anti-tumor function[48]. Therefore, while ZBTB46 expression remains a key feature of cDCs, studies manipulating this transcription factor need to consider other cell types which could be affected.

B cell lymphoma 6 (BCL6) is a transcription factor well-studied for its role in regulating germinal center T follicular helper cells (Tfh) and B cells[49, 50]. BCL6 was also found to be expressed in cDC subsets and cDC progenitors in mice and humans[51]. Experiments with *Bcl6*$^{-/-}$ mice suggested that BCL6 has a role in the development of cDC subsets in vitro and in vivo, specifically in the development of cDC1 identified with the markers CD8α in the spleen, and CD103 in the small intestinal lamina propria[51, 52]. However, a study using *Csf1r*^{Cre}*Bcl6*^{flox} *Zbtb46*^{GFP} mice in which only myeloid cell-specific Cre-expression results in lack of *Bcl6*, showed lower CD11c expression in *Bcl6*-deficient cDCs[53]. This study used *Zbtb46*^{GFP} expression as an alternative approach to quantify cDC subsets, which revealed that there was actually a comparable number of cDC1 in WT and *Csf1r*^{Cre}*Bcl6*^{flox} mice suggesting that *Bcl6* affects cDC phenotype, but not development[53]. Therefore, the

exact role of *Bcl6* in regulating the identity and function of cDC subsets remained unclear. This question is investigated in Publication II included in this thesis.

Functionally distinct cDC subtypes exhibit distinct transcriptional profiles and transcription factor dependence as introduced in Section 1.3. Transcription factors such as *Irf8*, *Batf3*, *Id2* and *Nfil3* are critical for development of cDC1 but not cDC2. Other transcription factors such as DC-SCRIPT (*Zfp336*) not only affect cDC1 development, but also shape the functional identity of mature cDC1 by regulating their key effector functions such as secretion of cytokine IL-12 and cross presentation[54]. More recently in the cDC field, Ascic et al.[55], harnessed key cDC1-associated transcription factors to reprogram tumor cells into cDC1-like cells. Using an adenoviral vector to deliver transcription factors PU.1, IRF8 and BATF3 to tumor cells in vivo, they demonstrate that these three factors are sufficient to reprogram tumor cells to adopt cDC1 phenotype as well as effector functions such as cross presentation and priming of $CD8^+$ T cell responses. This study not only represents a powerful advance for immunotherapy, but also highlights the importance of understanding how and which transcription factors critically shape the functional identity of cDC subsets.

Understanding transcription factors governing cDC2 development and identity has proven to be more complex as cDC2 themselves are heterogenous. High dimensional studies as well as use of various mouse models to delete transcription factors globally or conditionally have provided us with some pieces of information regarding the transcriptional basis for development and functional diversification of cDC2. cDC2 express high levels of *Irf4*, and *Irf4*$^{-/-}$ mice were observed to have a severely reduced cDC2 population[56]. However, it was later shown that cDC2 in these mice do exist but with an altered phenotype and function demonstrating that *Irf4* regulates cDC2-associated genes impacting specific aspects of cDC2 identity[57, 58]. T-bet$^+$ cDC2A corresponding to *Notch2*-dependent ESAM^{high} cDC2 are more potent activators of $CD4^+$ T cell responses compared to T-bet$^-$ cDC2B (largely corresponding to *Klf4*-dependent ESAM^{low} cDC2) which are more potent producers of cytokines[34, 35]. It was initially thought that these subtypes are induced in the periphery in response to environmental signals, however recent work demonstrates that specification to these subtypes takes place at the progenitor level in the bone marrow[59], providing insight into how these functionally distinct subtypes may be affected in disease or be targeted for therapeutic modulation.

Identification of distinct enhancer elements regulating differentiation of cDC subsets has added nuance to our understanding of the role of TFs in shaping cDC identity and diversity. An example can be found in transcription factor *Zeb2* which has a role in regulating development of cDC subsets as well as pDCs. A specific enhancer -165kb upstream of *Zeb2* transcription start site is required for development of pDCs[60]. Binding of different

transcription factors - *Nfil3* versus C/EBPs at three sites within this enhancer region determines development of cDC1 or cDC2 from CDPs, respectively[61]. A mouse model lacking all three of these sites in the *Zeb2* enhancer exhibited a complete loss of cDC2 due to the lack of C/EBP-mediated *Zeb2* expression required for cDC2 development. This is the first mouse model of total cDC2-decificiency allowing for the study of cDC2 specific functions in vivo. Such studies highlight the significance of multiomic profiling such as paired transcriptional and chromatin accessibility analyses in improving our understanding of transcriptional and regulatory networks governing differentiation of cDC subsets. Use of such methods is essential in advancing our understanding of the role of transcription factors in unprecedented ways, providing avenues for future studies to answer longstanding questions in the cDC field such as the lymphoid contribution to the cDC pool, or to understand the relationship between newly emerging DC populations such as tDC and DC3 and cDC subsets.

1.5 Emerging family of RORγt-expressing antigen presenting cells are also potent regulators of T cell responses

Apart from cDCs, APCs marked by expression of the transcription factor RORγt have emerged in the last decade to also be potent regulators of T cell responses[39]. Encoded by the gene *Rorc*, the longer isoform RORγ is found across various tissues, while the shorter isoform RORγt was first described in the thymus, specifically in immune cells[62]. Historically, RORγt is mainly known to be a lineage specifying transcription factor expressed by Th17 cells and ILC3, leading to the notion that RORγt is a master regulator of type 3 immune responses. In fetal life, RORγt is only expressed by lymphoid tissue inducer cells (LTi) which are critical orchestrators of lymphoid tissue organogenesis. LTi are developmentally dependent on RORγt, and consequently mice deficient in RORγt are characterised by absent or aberrant secondary lymphoid tissues[63]. While LTi were the first MHCII-expressing cell type described to express and depend on RORγt, it was later shown that a subset of ILC3 also express MHCII and can serve as APCs. These “LTi-like ILC3” were first described in adult murine intestinal tissues and were shown to limit microbiota specific $CD4^+$ T cell responses[64]. Subsequently it was shown that intestinal $MHCII^+$ ILC3s directly delete commensal-specific $CD4^+$ T cells by inducing their apoptosis[65]. This ability of ILC3s to regulate adaptive immunity was also shown in another study to be context specific, as peripheral ILC3s upregulate expression of co-stimulatory molecules and MHCII upon stimulation with IL-1β[66].

The discovery of Autoimmune Regulator (AIRE) expression in some populations of $ROR\gamma t^+$ APCs added further complexity to this field. AIRE is a transcription factor typically expressed in medullary thymic epithelial cells (mTECs)[67]. In mTECs, AIRE regulates the

expression of tissue-restricted antigens (TRAs), critical for establishing central T cell tolerance. mTECs, while not of hematopoietic origin, express co-stimulatory molecule CD80 as well as MHCII molecules in steady state and serve as APCs in the thymus to regulate central tolerance with and without the support of thymic DCs[68]. In both mice and humans, AIRE is also expressed outside of the thymus by cells which are termed extrathymic AIRE-expressing cells (eTACs). eTACs which were initially described in murine lymph nodes as $CD11c^{low}ZBTB46^{+}CCR7^{+}$ cDC-like cells, are of hematopoietic origin and regulate self-tolerance in the periphery through interactions with both $CD8^{+}$ and $CD4^{+}$ T cells[67, 69]. eTACs were subsequently shown to be heterogenous including other cell types such as a population termed $Aire^{+}$ILC3-like cells in murine peripheral lymph nodes capable of presenting endogenous antigens to $CD4^{+}$ T cells[70]. These ILC3-like cells displayed lymphoid morphology, were intrinsically dependent on RORγt for their development and shared expression of several TFs with ILC3s. Although they resembled $CCR6^{+}$LTi-like ILC3, it is important to note that they lacked expression of IL7Rα, CD4 and CD90 which are expressed by LTi. $Aire^{+}$ILC3-like cells were found primarily in peripheral lymph nodes and not those draining mucosal sites[70]. A subsequent study using a single cell multiomics approach to characterize eTACs in murine LNs divided them into two populations of migratory-DC like cells – the first characterised by *Aire* and *Ccr7* expression which they called “AmDCs” (*Aire*-expressing migratory DC) and the second by co-expression of *Aire* and *RORγt* which they termed “Janus cells” (JCs)[71]. Expression of self-antigen by both populations, presumably via *Aire* promoter led to deletion of autoreactive $CD8^{+}$ T cells in the periphery. JCs, while expressing *Ccr6* reminiscent of the previously described ILC3-like cells*,* aligned more with myeloid cells and displayed a cDC-like phenotype in their analyses. JCs also shared transcriptional similarity and chromatin accessibility landscape with mTECs, possibly due to an *Aire*-driven program. While $Aire^{+}$ILC3-like cells were lacking in mucosal draining LNs, JCs were described from mixed LNs including those draining peripheral sites as well as the intestines.

$ROR\gamma t^{+}$ APCs rose to prominence in 2022 with the simultaneous release of three publications[72-74] describing their indispensable role in generating microbiota-specific pTregs in the intestines. These studies made waves in the scientific community as they proposed that $ROR\gamma t^{+}$ APCs were the sole cell type required for tolerance to intestinal microbiota, negating the role of cDCs in this process. While most of their major findings aligned, these studies varied in their conclusion regarding which specific $ROR\gamma t^{+}$ APC subset mediated this process. Lyu et al.[72], proposed that LTi-like ILC3s induce microbiota-specific $ROR\gamma t^{+}$ Tregs in the mLNs via an ITGAV-ITGB3 mediated mechanism of processing TGFβ. While they found JCs in their profiling of $ROR\gamma t^{+}$ APCs in the mLNs, they use various mouse models to deplete Aire-expressing cells to show that JCs are not the cell

type inducing pTregs. The second publication by Kedmi et al.[74], remained inconclusive on the identity of this population, attributing this function to either MHCII$^+$ILC3 or JCs having antigen presentation machinery, requiring CCR7 for homing to mLNs and integrin αV for activating TGFβ. While the two studies mentioned above looked in adult murine mLNs, the third publication by Akagbosu et al.[73], looked at neonatal murine mLNs and propose that an entirely different RORγt$^+$ APC population – a new cell type they term "Thetis cells" (TCs) is responsible for the induction of pTregs. TC numbers peaked in the mLNs in early life coinciding with the peak in pTreg differentiation. TCs share features with mTECs and DCs, and consist of four subsets some of which express *Aire*. The *Aire*^{neg} TC subset IV also called 'RORγt cDC2' due to expression of CD11c and CD11b, was shown to express integrin β8 and was proposed to be the cell type inducing pTregs primarily in early life. Collectively, these three publications highlight the importance of RORγt$^+$ APCs in regulating tolerance to microorganisms in the intestines and associated tissues. A fourth publication that year revealed a new role for *Aire*-expressing RORγt$^+$ APCs in anti-fungal Th17 immunity. Dobeš et al.[75], reported that cells they term "Aire$^+$ILC3s" resembling JCs, can sense, internalize, process and present *C. albicans* to polarize effector Th17 responses. This function was dependent on cell-intrinsic expression of *Aire*, indicating that extrathymic *Aire* may have context-specific roles that extend beyond regulating peripheral tolerance.

It is evident from the above publications that there is marked overlap in phenotype, function and molecular identity between some subsets of RORγt$^+$ APCs (**Figure 1**) but the relationship between all these RORγt$^+$ APC subtypes remains unclear. Therefore, it was proposed in a review from Sonnenberg and colleagues that this growing family of RORγt$^+$ APCs can be broadly divided into RORγt$^+$ ILC3s, RORγt$^+$ eTACs and *Rorc*$^+$ DC-like cells[39]. What remained controversial as evidenced from the proposed nomenclature, was active expression of RORγt in cDCs or non-ILC3 cells resembling cDCs. While cDC2B were proposed to express and be dependent on RORγt, active expression of this isoform in these cells was not shown. The novel *Rorc*-reporter mouse model used to describe Thetis cells reports both isoforms of *Rorc* gene leading to further doubt regarding active expression of isoform RORγt in cDC-like cells. The first evidence of active RORγt expression in DCs was reported by our lab in 2021 in a study by Papaioannou et al[19]. This

	ILC3			cDC-like		
	LTi-like ILC3[64, 65, 72, 74]	***Aire*⁺ ILC3**[75]	***Aire*⁺ ILC3-like cells**[70]	**Janus cells**[71, 74] **/RORγt⁺ eTACs**[72]	**Thetis cells**[73]	**RORγt⁺ DC2**[19]
						
TF expression	RORγt ZBTB46 RORA	RORγt AIRE	RORγt *Aire* *Id2*	RORγt AIRE *Zbtb46*	RORγt AIRE* *Zbtb46*	RORγt *Zbtb46*
Surface markers	MHCII IL7R CCR6 CXCR6 IL-23R CCR7 CD25 *Kit*	MHCII *Ccr6* *Kit*	MHCII CD11c* EpCAM* CCR6 KIT	MHCII CD11c* EpCAM* CCR6 CCR7 *Kit*	MHCII CD11c* EpCAM* CCR6* CD11b* CCR7 CD26	MHCII CD11c CD11b CCR6* CD172a CLEC4A4 KIT CD26
Co-stimulatory markers	-	CD80 CD86 *Cd40* *Icosl*	CD80 CD86 CD40 ICOSL	CD80 CD86	CD80 *Cd86* CD40	CD80 CD86
Tissues	mLNs and coLP	pLNs	More abundant in pLN, low in mLN	Mixed pLNs and mLNs	mLN	mLN
Age	Young and adult mice	Adult mice	Peak in 2-week old mice	Young and adult mice	Peak in 2-week old mice	Enriched in neonatal mice
Functional attributes	Induction of microbiota-specific Tregs	*Aire*-dependent induction of *Candida*-specific Th17 cells	Peripheral deletion of self-reactive CD4⁺ T cells	Induction of microbiota-specific Tregs	Induction of microbiota-specific Tregs	-

Figure 1. *Summary of key features associated with the indicated RORγt⁺ APC subtypes. (*) mark heterogeneously expressed molecules.*

study described a fraction of cells expressing RORγt within the population of DC2 not arising from *Clec9a*-expressing progenitors in the neonatal murine spleen. Using a transgenic mouse model specifically reporting RORγt, these cells were shown to actively express this isoform of *Rorc*. Phenotypic and transcriptional analyses revealed them to be distinct from MHCII⁺ILC3, and aligned them with cDC2s. Therefore, they were initially called 'RORγt⁺ DC2' and were observed to reduce with age within the cDC2 compartment. Interestingly these RORγt⁺ cells phenotypically and transcriptionally resembled cDC2A and not cDC2B further supporting their unique identity. Whether these cells displayed other hallmark features of cDCs such as the ability to activate naïve T cells, remained unanswered. This would be critical for resolving the debate of whether RORγt is expressed by cDC-like cells. It remained to be seen if RORγt⁺ DC2 persist with age within the total cDC compartment and if they are present across other lymphoid and non-lymphoid tissues. Importantly, the relationship between RORγt⁺ DC2 and cDC subsets, ILC3 as well as other emerging RORγt⁺ APC populations remained a key question to answer. The results of my PhD project investigating these questions are reported in Publication I included in this thesis.

2. Contribution to papers

2.1 Contribution to publication I:

"RORγt-expressing dendritic cells are functionally versatile and evolutionarily conserved antigen presenting cells"

DOI: 10.1073/pnas.2417308122

In this project, I set out to characterize the population of RORγt-expressing cells within the dendritic cell compartment previously discovered in our lab[19] and to understand thir function and relation to other emerging populations of RORγt-expressing APCs. As first author of this resulting publication I designed, performed and analyzed experiments, organized international collaborative experiments, generated bioinformatics datasets and drove the bioinformatics analyses under the supervision of Prof. Barbara Schraml-Schotta. I prepared all figures and also contributed to writing and editing the manuscript with Prof. Barbara Schraml-Schotta. A detailed account of my contributions to this publication is provided below.

I profiled RORγt$^+$ DCs in murine spleen, intestines, lung, and lymph nodes across mice of different ages - data are shown in Fig. 1 A-F, Fig. 4 A,B and D, Fig. S1 A-D, Fig. S7, and Fig. S8A-C. I designed experiments and analyzed data generated by collaborators and colleagues who profiled RORγt$^+$ DCs in murine colon lamina propria and skin draining LNs (Fig 4C, E. Fig. S8D-F).

Experiments profiling RORγt$^+$ DCs in various mouse models used to investigate developmental requirements or ontogeny, I performed myself at collaborators facilities, or designed experiments and analyzed data generated by collaborators (data are shown in Fig 1G-I, Fig. S1E).

To better understand how splenic RORγt$^+$ DC relate to other cDC subsets and MHCII$^+$ ILC3 we used a multiomic approach profiling RNA and chromatin accessibility from the same nucleus. I established for our lab a protocol for multiomic profiling using the 10X Genomics platform and generated the libraries with nuclei isolated from spleen of 2-week-old and adult mice. This allowed for the analyses of both the transcriptional and accessible chromatin profiles from the same cell allowing us to infer gene regulatory networks which could impact cell identity. I drove the analyses of this dataset all of which were performed by Dr. Maria L. Richter (data are shown in Fig. 2A-E, G, Fig. 5A, B, E-G, Fig. S2A-F, Fig. S9A-C, F, and Fig. S10A-C). I performed the flow cytometric profiling experiments accompanying these bioinformatics data – shown in Fig. 2F, H, Fig. 4C,D,

Fig. S2H, and Fig. S10D. Flow cytometry data in Fig. 5C-D and Fig. S9D,E were generated with Dr. Christina Stehle. The neonatal small intestine scRNAseq dataset was generated by me and analyzed by Kaushikk Ravi Rengarajan (Fig. 2I,J, Fig. S2J, Fig S3A, B). To understand how RORγt$^+$ DCs relate to other subsets of RORγt$^+$ APCs we integrated datasets generated in our lab with publicly available datasets describing other populations of RORγt$^+$ APCs. Integration and analyses of these eight transcriptional profiling datasets was performed by Dr. Maria L. Richter with direction provided by me and Prof. Barbara Schraml-Schotta (Fig. 2I-J, Fig. S2J).

To determine if RORγt$^+$ DCs are also present in human spleen, I analyzed a publicly available scRNAseq dataset of human splenic DCs from Brown et al. Cell, 2019. Here I identified a cluster of cells excluded from the original analyses as ILC3 contaminant, which I could show were RORγt$^+$ DCs (data shown in Fig. 3A, B, Fig. S4A-C). Ramin Shakiba analyzed other human tissue scRNAseq datasets containing DCs with direction from me, and performed the integration analyses of the two scRNAseq datasets from human spleen shown in Figure 3C-F and Fig. S4D-F. Identification and analyses of RORγt$^+$ DCs in other human and murine tissue scRNAseq datasets was also performed by Ramin Shakiba (Fig.3H, I, Fig. S2J, Supplementary Fig. 3C,D, Fig. S5A-I, Fig. S6F). Identification of RORγt$^+$ DCs in human CSF datasets was done by both Ramin Shakiba and me (data are in Fig. 3 H,I, Fig. 7A, and Fig. S6A-E). Prof. Barbara Schraml-Schotta and I deduced the set of genes which identify RORγt$^+$ DCs across mouse and human tissues which are shown in Fig. 3G-I and Fig. S6E,F.

To assess the functional repertoire of RORγt$^+$ DCs, Prof. Barbara Schraml-Schotta and I designed various experiments. I performed flow cytometric profiling to show that RORγt$^+$ DCs express costimulatory molecules in steady state (Fig. S10D). To demonstrate that RORγt$^+$ DCs indeed bear the hallmark T cell activation and proliferation ability of cDCs, I optimized a protocol for performing DC-T cell co-culture assays with limited cell numbers to demonstrate that RORγt$^+$ DCs can activate and polarize naïve T cells upon loading of peptide ex vivo or after targeted in vivo antigen delivery. These data are shown in Fig. 6A-L, and Fig. S11. Kaushikk Ravi Rengarajan generated the flow cytometric profiling data shown in Fig. 6M. Migration to LNs upon antigen encounter is another hallmark feature of cDCs. Dr. Isabel Ulmert and I performed the experiments assessing the migration ability of RORγt$^+$ DCs in neonatal intestine after oral gavage with R848 shown in Fig. 6N. Following the identification of RORγt$^+$ DCs in human CSF scRNAseq datasets, we found that they expressed markers well studied in murine cDCs in the mouse model of EAE. Therefore, we quantified RORγt$^+$ DCs in brain and spinal cord of mice subject to MOG-induced EAE. These experiments were done in collaboration with Dr. Arek Kendirli and Clara de la Rosa and data are shown in Fig. 7B,C and Fig. S12A.

Our work shows that RORγt$^+$ DCs bear hallmark features of cDCs, which warrants their affiliation with dendritic cells. RORγt$^+$ DCs encompass several previously described populations of RORγt$^+$ APCs, and are a unique population of dendritic cells present across tissues in mice and humans. RORγt$^+$ DCs can activate naïve T cells and display a pro-inflammatory transcriptional profile in neuroinflammation and after viral stimulus. This indicates that they could have a function beyond pTreg induction reported in intestinal tissues, and suggests that their functional state could be regulated by tissue-specific or inflammatory signals. Future studies investigating their origin and factors regulating their functional identity will be critical as our work suggests that RORγt$^+$ DCs harbor the potential for being targeted for therapeutic intervention.

2.2 Contribution to publication II:

"Genomic deletion of Bcl6 differentially affects conventional dendritic cell subsets and compromises Tfh/Tfr/Th17 cell responses"

DOI: 10.1038/s41467-024-46966-6

In 2020 I set out to characterize the cDC compartment across tissues in *Clec9a*^{Cre} *Bcl6*^{flox}-*Rosa*^{YFP} mice. In this mouse model, *Bcl6* is conditionally deleted in all cDCs derived from *Clec9a*-expressing myeloid progenitors and YFP reports Cre activity. In these initial experiments, a striking change in the cDC compartment was observed. cDCs expressing XCR1 a marker specifically expressed on cDC1, co-expressed CD11b a marker for cDC2 which is typically absent on cDC1. Shortly after these observations, we began a collaboration with the lab of Dr. Katharina Lahl, who had observed a similar phenotype in the cDC compartment of *CD11c*^{Cre}*Bcl6*^{flox} mice and was putting together this publication.
In this study various mouse models for conditionally depleting *Bcl6* are used to investigate the cell-intrinsic role of *Bcl6* in cDCs and subsets. Using *XCR1*^{Cre} and *CD11c*^{Cre} to conditionally delete *Bcl6* in all XCR1 or CD11c-expressing cells respectively, revealed a population of XCR1$^+$CD11b$^+$ cDCs across tissues, which is typically absent in WT mice. Bulk RNA-sequencing of splenic cDC subsets from these conditional depletion models showed that *Bcl6* deficiency did not affect the core transcriptional identity of cDC subsets, but did alter the gene expression profile of cDC1 and cDC2 in a differential manner. However, *Bcl6*-deficient cDC1 remained functionally comparable to WT cDC1. Phenotype, numbers and transcriptomic profile of cDC2 were also affected in *CD11c*^{Cre}*Bcl6*^{flox} mice. A specific reduction in the ESAM^{high} *Notch2*-dependent subset of cDC2 was observed. This reduction in ESAM^{high} cDC2 in the spleen resulted in an impaired induction

of Tfh and Tfr cells. Lack of the corresponding *Notch2*-dependent CD103^{+} cDC2 population in the colon LP resulted in an impaired Th17 response against *C. rodentium* in the intestines.

However, CD11c expression is not exclusive to cDCs. It is also expressed on other immune cells such as monocytes, macrophages, and subsets of B cells and activated T cells. Therefore, to further support the point that *Bcl6* has a cell-intrinsic role in cDC subsets, especially cDC2, profiling the cDC compartment across tissues in mice with *Clec9a*^{Cre}-based deletion of *Bcl6* mice was important. I designed, performed and analyzed the flow cytometry experiments profiling the cDC compartment in *Clec9a*^{Cre}*Bcl6*^{flox} mice. Data I generated are presented in Figure. 6 panels c-f, Supplementary Figure 6 panels a,b, and the plots in the lower row depicting staining of cDC compartment in Clec9a.Bcl6^{KO} mice in Supplementary Figure 7. Additionally, I designed panels and performed flow cytometric profiling of myeloid progenitors in the bone marrow of *Clec9a*^{Cre}*Bcl6*^{flox} compared to controls, which was important in the review process and shaping the direction of the study, but ultimately did not make it into the final publication. In conclusion, this publication provides novel insights into the cell-intrinsic role of the transcription factor BCL6 in regulating the subset-specific development, phenotype, and function of cDCs across murine tissues.

3. Paper I

PNAS RESEARCH ARTICLE | IMMUNOLOGY AND INFLAMMATION OPEN ACCESS

RORγt-expressing dendritic cells are functionally versatile and evolutionarily conserved antigen-presenting cells

Hamsa Narasimhan[a,b], Maria L. Richter[c], Ramin Shakiba[a,b], Nikos E. Papaioannou[b,1], Christina Stehle[d], Kaushikk Ravi Rengarajan[a,b], Isabel Ulmert[e], Arek Kendirli[f,g,h], Clara de la Rosa[f,g,i], Pin-Yu Kuo[a,b], Abigail Altman[j,k], Philipp Münch[l], Saba Mahboubi[l], Vanessa Küntzel[b], Amina Sayed[a], Eva-Lena Stange[m], Jonas Pes[m], Alina Ulezko Antonova[n], Carlos-Filipe Pereira[j,k], Ludger Klein[a], Diana Dudziak[o], Marco Colonna[n], Natalia Torow[m,2], Mathias W. Hornef[m], Björn E. Clausen[l], Martin Kerschensteiner[f,g,h], Katharina Lahl[e,p,q,r], Chiara Romagnani[d], Maria Colomé-Tatché[c], and Barbara U. Schraml[a,b,3]

Affiliations are included on p. 11.

Edited by Hongbo Chi, St Jude Children's Research Hospital, Memphis, TN; received August 28, 2024; accepted January 13, 2025 by Editorial Board Member Warren J. Leonard

Conventional dendritic cells (cDCs) are potent antigen-presenting cells (APCs) that integrate signals from their environment allowing them to direct situation-adapted immunity. Thereby they harbor great potential for being targeted in vaccination, autoimmunity, and cancer. Here, we use fate mapping, functional analyses, and comparative cross-species transcriptomics to show that RORγt$^+$ DCs are a conserved, functionally versatile, and transcriptionally distinct type of DCs. RORγt$^+$ DCs entail various populations described in different contexts including Janus cells/RORγt-expressing extrathymic Aire-expressing cells (eTACs), subtypes of Thetis cells, RORγt$^+$-DC (R-DC) like cells, cDC2C and ACY3$^+$ DCs. We show that in response to inflammatory triggers, RORγt$^+$ DCs can migrate to lymph nodes and in the spleen can activate naïve CD4$^+$ T cells. These findings expand the functional repertoire of RORγt$^+$ DCs beyond the known role of eTACs and Thetis cells in inducing T cell tolerance to self-antigens and intestinal microbes in mice. We further show that RORγt$^+$ DCs with proinflammatory features accumulate in autoimmune neuroinflammation in mice and men. Thus, our work establishes RORγt$^+$ DCs as immune sentinel cells that exhibit a broad functional spectrum ranging from inducing peripheral T cell tolerance to T cell activation depending on signals they integrate from their environment.

dendritic cells | RORγt; AIRE | innate lymphocytes | antigen presenting cells

Significance

Antigen-presenting cells (APCs) orchestrate T cell immunity. Retinoic acid receptor-related orphan receptor-γt (RORγt)-expressing APCs are heterogenous regulators of T cell tolerance but their subtypes and lineage relationships are ill-defined. We report that RORγt$^+$ dendritic cells (DCs) are evolutionarily conserved, exhibit wide tissue distribution and reconcile various RORγt$^+$ APC populations known to promote peripheral T cell tolerance. We show that RORγt$^+$ DCs can sense pathogens, migrate to lymph nodes, activate naïve CD4$^+$ T cells, and accumulate in demyelinating neuroinflammation with a proinflammatory phenotype. Thus, RORγt$^+$ DCs have a broad functional spectrum ranging from inducing T cell tolerance to T cell activation depending on signals they integrate from their environment. This highlights their therapeutic potential and their affiliation with DCs.

cDCs are immune sentinels located in lymphoid and nonlymphoid tissues (1–3). They effectively sense pathogens and subsequently migrate to and initiate T cell responses in secondary lymphoid organs (1–3). Their functional versatility makes them attractive for being targeted in autoimmunity and vaccination against pathogens or cancer (2–5). Accordingly, considerable work has been invested in understanding the functional and ontogenetic diversity of cDCs, yet these cells remain ambiguous to define as fate mapping has recently uncovered novel populations with overlapping phenotype but distinct origin (2, 6–11).

Type 2 cDCs (cDC2) are potent regulators of CD4$^+$ T cell responses (1–3) that entail Notch2-dependent ESAM^{high} or T-bet-expressing cDC2A and Notch2-independent ESAM^{low} or T-bet-negative cDC2B that derive from myeloid progenitors (12–14). Both subtypes can induce Th17 responses but cDC2A regulate T follicular helper cell (Tfh) responses (15), while cDC2B may better promote Th2 responses (16). Recently, fetal liver lymphoid progenitors and lymphoid-derived transitional DCs (tDCs) have been shown to differentiate into cells resembling cDC2A and cDC2B (8–10, 17), the functional consequences of which are still unclear. tDCs can also contribute to antiviral responses and inflammation induced-immunopathology (8, 9, 17). Additionally, DC3 arise from monocytic progenitors, resemble cDC2B but in vitro appear superior to cDC2B in polarizing producing Th17 cells (11, 18, 19). The above heterogeneity suggests a careful division of labor between DC subtypes which needs to be better defined to uncover the full functional spectrum of cDCs.

Next to cDCs, RORγt-expressing APCs have emerged as potent regulators of T cell–mediated tolerance (20–30). RORγt is a ligand-activated transcription factor encoded by the *Rorc* gene that differs from its isoform RORγ by three amino acids at the amino terminus (31–33). RORγt-expressing APCs include subsets of ILC3s, RORγt$^+$ extrathymic AIRE-expressing cells (eTACs—including Janus and AIRE$^+$ ILC3-like cells), as well as other surfacing populations like Thetis cells (28–31, 34, 35). Their lineage relationships and functional specializations are ill-defined because RORγt-expressing APCs phenotypically resemble each other and share expression of CD11c and ZBTB46 with cDCs (25,

[1]Present address: Immune Regulation Laboratory, Center of Basic Research, Biomedical Research Foundation Academy of Athens, 11527 Athens, Greece.

[2]Present address: Helmholtz Centre for Infection Research, Braunschweig 38124, Germany.

[3]To whom correspondence may be addressed. Email: Barbara.schraml@bmc.med.lmu.de.

This article contains supporting information online at https://www.pnas.org/lookup/suppl/doi:10.1073/pnas.2417308122/-/DCSupplemental.

Published XXXX.

29, 30, 35, 36). Janus cells express *Aire*, RORγt and the integrin b8 (*Itgb8*) but lack ILC3 markers CXCR6 and IL7R. They phenotypically and transcriptionally resemble CCR7$^+$ migratory cDCs (29, 35) and have primarily been profiled from pooled cervical, brachial, axillary, inguinal, and mesenteric lymph nodes (mLN) (35). Thus, it is unclear if they exhibit site-specific heterogeneity. Thetis cells have first been described in neonatal mLN and resemble Janus cells although they are apparently absent from skin draining LN (30). Only a fraction of Thetis cells (TCI and TCIII) expresses *Aire*, while TCIV expresses *Itgb8* but lacks *Aire* (30). While Janus and Thetis cells in mice drive T cell tolerance, human R-DC-like cells that resemble Thetis cells can activate allogeneic T cells (37). Thus, the above cell types may function beyond T cell tolerance, highlighting the need for a more accurate alignment of Janus cells, Thetis cells, and RORγt$^+$ eTAC subsets, and the tissue-specific signals that regulate them.

cDC2B from adult mouse spleen show accessible chromatin at ROR response elements (RORE) in bulk ATAC sequencing, leading to the notion that cDC2B expresses RORγt (12, 31). However, active RORγt protein expression in cDC2B from adult mice has not been reported and only a minor fraction of cDC2B show RORγt expression history (10, 12). In contrast, we have demonstrated active RORγt protein expression in a fraction of cDC2-like cells in neonatal mouse spleen and Peyer's patches, that phenotypically and transcriptionally more closely resemble cDC2A than cDC2B (10, 38). These RORγt$^+$ cDC2-like cells in the neonatal spleen do not arise from *Clec9a*-expressing myeloid cDC progenitors (10), suggesting they could be a unique type of APC, possibly related to Thetis cell subsets, which resemble cDC2 in terms of CD11b expression (30).

Here, we show that RORγt$^+$ DCs are a transcriptionally distinct and evolutionarily conserved DC subtype that reconciles various previously described RORγt$^+$ APC populations, including RORγt$^+$ eTACs, Janus and Thetis cells, RORγt$^+$ cDC2-like cells, R-DC like cells, ACY3$^+$ DCs (39) and PRDM16$^+$ cDC2C (40). We demonstrate that RORγt$^+$ DCs are ontogenetically and transcriptionally distinct from other cDC subtypes, as well as from ILC3. Yet, RORγt$^+$ DCs bear hallmark features of cDCs, including migration to lymph nodes and ability to activate naïve CD4$^+$ T cells in response to inflammatory stimuli that warrant their affiliation with DCs.

Results

RORγt$^+$ DCs Exist in the Murine Spleen Across Age. We first profiled spleens from *RORγt^{GFP}Clec9a^{Cre}Rosa^{Tom}* and *Clec9a^{Cre}Rosa^{Tom}* mice systematically across age by flow cytometry. In these mice, Tomato expression tracks cells arising from committed *Clec9*a-expressing myeloid cDC progenitors (41), while GFP expression reports the RORγt-specific isoform encoded by *Rorc* (42). We first identified MHCII$^+$ILC3s as CD90$^+$CD127$^+$MHCII$^+$GFP$^+$ cells and then gated cDCs as CD11c$^+$MHCII$^+$ cells lacking the canonical ILC3 markers CD90 and CD127—also known as interleukin-7 receptor (IL-7R) (Fig. 1*A* and *SI Appendix*, Fig. S1*A*). Within CD11c$^+$MHCII$^+$ splenocytes, we detected GFP-expressing cells at all ages examined (Fig. 1*A*). Importantly, GFP$^+$CD11c$^+$MHCII$^+$ cells also stained with an anti-RORC antibody (Fig. 1*E*), confirming that GFP signal in *RORγt^{GFP}* mice accurately reports RORγt protein expression and that anti-RORC antibody staining in CD11c$^+$MHCII$^+$ cells predominantly identifies cells expressing the γt isoform of RORC. Unbiased gating of GFP$^+$ cells showed that RORγt$^+$CD11c$^+$MHCII$^+$ cells lacked ILC3 markers CD127, CD90, and CXCR6 (Fig. 1 *B* and *C* and *SI Appendix*, Fig. S1 *B* and *C*). The frequency of RORγt$^+$ cells within CD11c$^+$MHCII$^+$ cells declined with age; however, their absolute numbers correlated with organ size and increased until weaning age and remained constant until adulthood (8 to 15 wk of age, Fig. 1*F* and *SI Appendix*, Fig. S1*D*).

We had previously found that CD11b$^+$ RORγt$^+$ cDC2-like cells were nearly undetectable by two weeks of age (10). Indeed, at one week of age, CD11c$^+$MHCII$^+$RORγt$^+$ cells uniformly expressed CD11b but lacked CD24. Starting at two weeks of age RORγt$^+$ cells showed a CD11b^{low} to negative phenotype, while retaining the cDC2 marker CD172a (10) (Fig. 1*D*), and stained positive for CD24 (Fig. 1 *A* and *B*). At all ages examined RORγt$^+$CD11c$^+$MHCII$^+$ cells stained negative for the cDC1-specific marker XCR1 (Fig. 1*B*). Thus, the apparent lack of CD11b by two weeks of age explains why we had previously missed these cells in adult mice and suggests that these cells are either heterogenous or change their phenotype with age. In line with our previous work (10), RORγt$^+$CD11c$^+$MHCII$^+$ cells lacked Tomato expression in *Clec9a^{Cre}Rosa^{TOM}* mice at all ages examined, supporting that they do not arise from *Clec9a*-expressing DC progenitors (10, 41). RORγt$^+$CD11c$^+$MHCII$^+$ cells were present in *Rag2$^{-/-}$γc$^{-/-}$* mice, which lack lymphocytes, including ILC3s and their precursors (Fig. 1 *G* and *H*) (43), but fate mapped prominently in lymphoid-specific hCD2^{iCre}Rosa^{YFP} lineage-tracer mice (*SI Appendix*, Fig. S1*E*). RORγt$^+$CD11c$^+$MHCII$^+$ cells were strongly reduced in mice deficient for fms-like tyrosine kinase 3 ligand (FLT3L) (Fig. 1*I*), a growth factor critical for the development of all DCs and ILCs (44, 45). Thus, RORγt$^+$CD11c$^+$MHCII$^+$ cells exist in the murine spleen across age and can either be detected using an anti-RORC antibody or by GFP signal in *RORγt^{GFP}* mice (Fig. 1 *A* and *E*). As these cells do not develop in FLT3L$^{-/-}$ mice and phenotypically resemble DCs (10), we refer to these cells as RORγt$^+$ DCs from hereon in accordance with suggestions for DC and ILC nomenclature (1, 31, 46).

Single-Cell Multiomic Profiling Aligns Murine RORγt$^+$ DCs with Janus Cells, RORγt$^+$ eTACs and Thetis Cells. To gain insight into the transcriptional and regulatory relatedness of RORγt$^+$ DCs to cDCs and ILC3s across age, we performed paired single-cell RNA sequencing (scRNA-seq) and single-cell assay for transposase-accessible chromatin (scATAC) from the same cell using 10X multiomic profiling. RORγt$^+$ DCs and MHCII$^+$ILC3s were sorted from spleens of two-week-old or adult *RORγt^{GFP}* mice and mixed at a 1:1 ratio to enrich for RORγt$^+$ DCs. CD11c$^+$MHCII$^+$ cDCs were added in 10-fold excess to capture their heterogeneity. After quality filtering, we retained chromatin accessibility and gene expression profiles from 9,899 and 11,980 nuclei respectively. Unsupervised clustering based on gene expression (RNA) and open chromatin (ATAC) profiles revealed 18 and 16 clusters, respectively, that were largely congruent and could be classified as cDC1, cDC2, migratory cDCs (migDCs), ILC3s, pDCs, and tDCs (Fig. 2*A* and *SI Appendix*, Fig. S2 *A–F* and Table S1). cDC2 split into 5 clusters based on gene expression, of which clusters 1, 2, and 3 corresponded to cDC2A (12, 47) (*SI Appendix*, Fig. S2*C*). Of note, cDC2 clusters 1 and 2 showed uniform chromatin accessibility (*SI Appendix*, Fig. S2 *B* and *D*), as discussed below. cDC2 clusters 4 and 5 transcriptionally resembled both cDC2B and DC3 and were denoted as cDC2B/DC3 as they could not confidently be delineated as either cell type (Fig. 2*A* and *SI Appendix*, Fig. S2 *C* and *E*) (11, 12). pDCs showed uniform chromatin accessibility but split into two clusters based on gene expression (*SI Appendix*, Fig. S2 *A, B,* and *D*). *Rorc*$^+$ cells distributed across 5 clusters, of which ILC3_1 and ILC3_2 scored high for ILC3 signature genes and expressed *Rora, Il7r, Cxcr6*, and one cluster transcriptionally resembled ex-ILC3 (48) (Fig. 2 *A* and *B* and *SI Appendix*, Fig. S2*C* and Table S2). Additionally, one cluster expressed *Rorc*, *Prdm16,* and *Lingo4* (10) while lacking *Il7r, Rora*, and *Cxcr6* and transcriptionally resembled RORγt$^+$ cDC2-like cells from neonatal

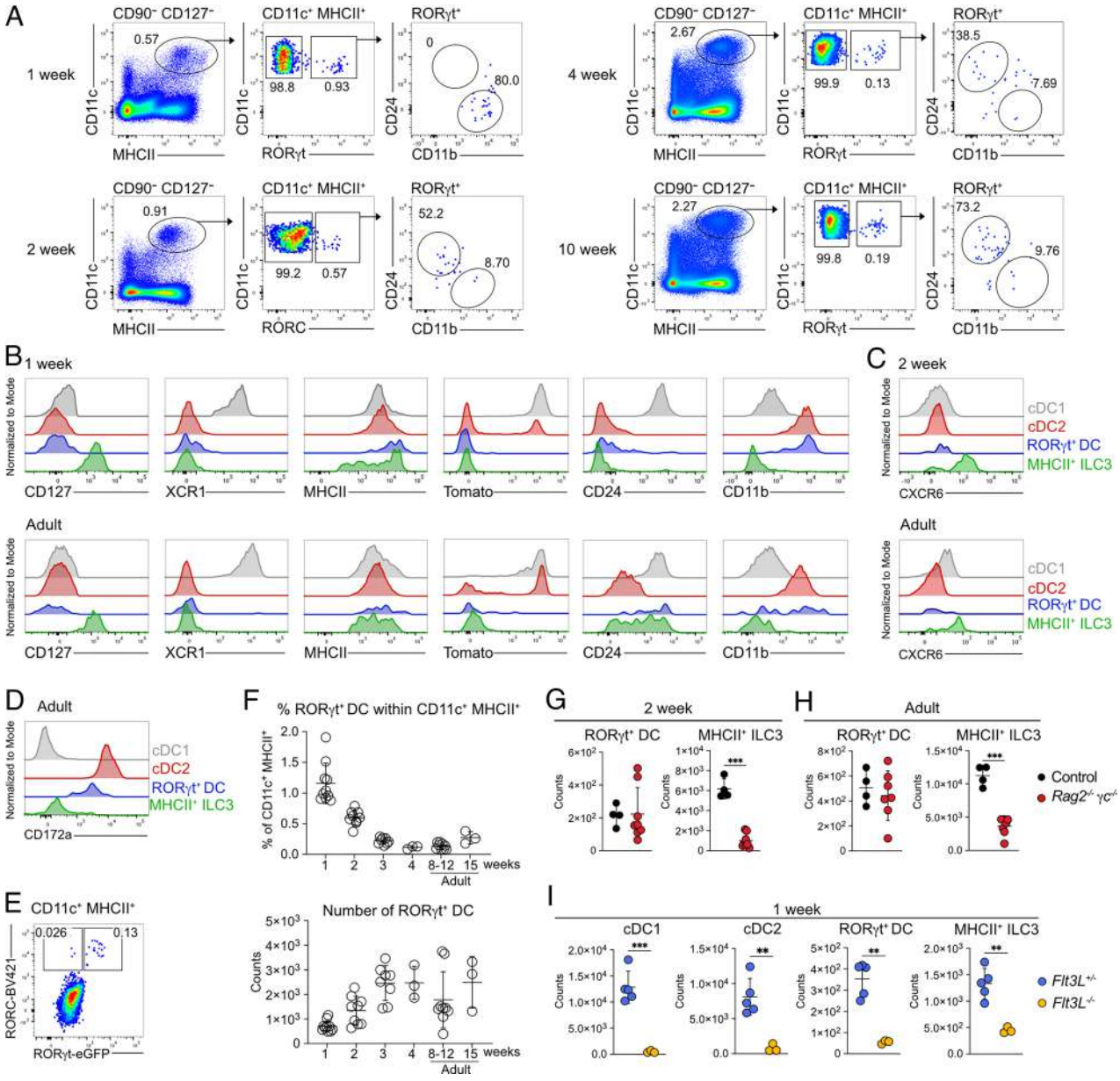

Fig. 1. RORγt$^+$ DCs exist in the murine spleen across age. (*A* and *B*) Splenocytes from *Clec9a*^{Cre}*Rosa*^{Tom} or *Clec9a*^{Cre}*Rosa*^{Tom}*RORγt*^{GFP} mice at the indicated ages were analyzed by flow cytometry. (*A*) Live CD90$^-$CD127$^-$CD11c$^+$MHCII$^+$ cells were gated and RORγt$^+$ cells revealed by GFP or anti-RORC intranuclear staining (2-wk time point). GFP$^+$ or RORC$^+$ cells were further analyzed for CD11b and CD24 expression. (*B–D*) Expression of the indicated surface markers in cDC1 (gray), cDC2 (red), MHCII$^+$ ILC3 (green), and CD11c$^+$MHCII$^+$RORγt$^+$ cells (blue) from spleens of mice at the indicated ages. Gating strategy *SI Appendix*, Fig. S1*A*. (*E*) CD11c$^+$MHCII$^+$ cells from *RORγt*^{GFP} mice were stained using an anti-RORC antibody to demonstrate that anti-RORC staining and RORγt driven GFP are largely congruent. (*F*) Frequency of RORγt$^+$ cells within CD11c$^+$MHCII$^+$ cells and number of RORγt$^+$ DCs in spleens of the indicated ages (1-wk-old n = 10; 2-wk-old, n = 9; 3-wk-old n = 8, 4-wk-old n = 3; 8 to 12-wk-old n = 6; 15-wk-old n = 3). Data are pooled from 1 to 2 independent experiments; each data point represents a biological replicate. (*G* and *H*) MHCII$^+$ ILC3 and RORγt$^+$ DCs were quantified in spleens from 2-wk-old (*G*) and adult *Rag2*$^{-/-}$*γc*$^{-/-}$ mice (*H*) and littermate controls. Each data point represents an individual mouse from two independent experiments. (*I*) Quantification of cDC1, cDC2, RORγt$^+$ DC, and MHCII$^+$ ILC3 in spleens from 1-wk-old *Flt3l*$^{-/-}$ and *Flt3l*$^{+/-}$ littermate controls. RORγt$^+$ DC quantified by intranuclear staining against RORC. Each dot represents one mouse, horizontal bars represent mean, error bars represent SD. ***P* (0.0021) ****P* (0.0002). Statistical analyses in (*G–I*) were performed using two-tailed Welch's *t* test.

mouse spleen (10), establishing it as RORγt$^+$ DCs (Fig. 2 *B–D* and *SI Appendix*, Table S1). This cluster expressed higher levels of *Ccr6*, *Cd200,* and *Epcam* compared to other DC subtypes and we could confirm higher expression of these markers on RORγt$^+$ DCs compared to cDC1 and cDC2 by flow cytometry (Fig. 2*F*).

Some migratory DCs expressed *Aire* (Fig. 2 *B* and *D*), as expected (35, 49) but we could also identify a distinct cluster of cells expressing *Aire, Rorc,* and *Prdm16*, which we termed RORγt$^+$ eTACs. RORγt$^+$ DCs and RORγt$^+$ eTACs most closely resembled each other and migratory cDCs transcriptionally and based on chromatin accessibility (Fig. 2*E*). While RORγt$^+$ eTACs and RORγt$^+$ DCs showed similar chromatin accessibility, they somewhat diverged based on gene expression profile (Fig. 2*A*). The *Aire* locus, including the conserved noncoding sequence 1 (CNS1) region (35) showed accessible chromatin peaks in migDCs, RORγt$^+$ DCs and RORγt$^+$ eTACs. Highest accessibility of the CNS1 region was observed in RORγt$^+$ eTACs and RORγt$^+$ DCs; however, some cell type–specific peaks were observed close to the transcriptional start site of *Aire* only in RORγt$^+$ eTACs (Fig. 2*G*). The RORγt$^+$ DC cluster was distinguished from other clusters by expression of genes including *Prdm16, Col17a1, Pigr, Ltb,* and *Lingo4*, of which *Prdm16* and *Col17a1* expression were shared with RORγt$^+$ eTACs (Fig. 2*D* and *SI Appendix*, Table S2). RORγt$^+$ eTACs showed specific expression of *Aire, Tnfrsf11a* (RANK), and *Itgb8* (Fig. 2*D*). Flow cytometry in

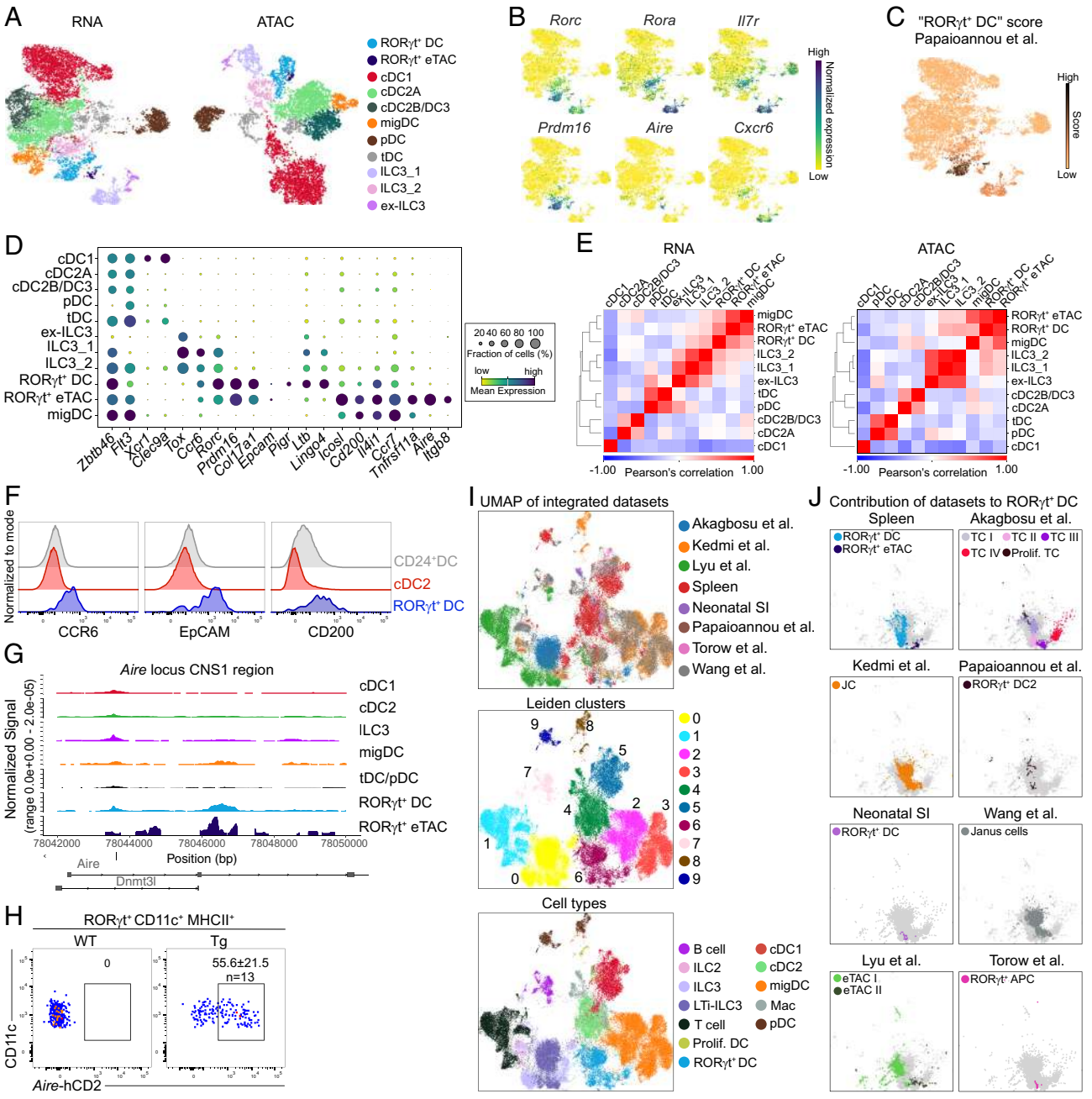

Fig. 2. Integrative transcriptional analyses align RORγt$^+$ DCs with Janus cells, RORγt$^+$ eTACs and Thetis cells. (*A–E*) Single-cell multiomic profiling (paired scATAC and scRNA-seq) of RORγt$^+$ DCs, RORγt^{neg}CD11c$^+$MHCII$^+$ cells, and MHCII$^+$ ILC3 from spleens of two-week-old (n = 2) or adult (n = 3) *RORγt^{GFP}* mice was performed. (*A*) RNA-based and ATAC-based UMAP of 11,980 nuclei annotated by cell type (see also *SI Appendix*, Fig. S2). (*B*) Expression of indicated genes on the RNA-based UMAP. (*C*) RNA-based UMAP depicting enrichment score for genes that distinguished RORγt$^+$ cDC2-like cells in the neonatal spleen (10). (*D*) Bubble plot of select cell type defining genes. (*E*) Pearson's correlation to show the similarity between clusters identified based on RNA and ATAC profiles. (*F*) Staining of the indicated surface markers on RORγt$^+$ DCs (blue), cDC2 (red), and CD24$^+$ DCs (gray). (*G*) Chromatin accessibility at the CNS1 region of *Aire* locus in the indicated cell types. (*H*) AIRE expression in RORγt$^+$CD11c$^+$MHCII$^+$ cells revealed by anti-hCD2 staining in the spleen of adult *Aire^{hCD2}* mice. (*I*) The indicated murine datasets were integrated. UMAP of the integrated datasets colored by dataset and by Leiden clusters. (*J*) Zoomed-in display of the RORγt$^+$ DC cluster from the UMAP in (*I*) with all cells contributing to the cluster in gray. The contribution of the specified populations from the indicated publications is shown.

Aire^{hCD2} reporter mice (50) confirmed that a fraction of RORγt$^+$ DCs indeed express AIRE (Fig. 2*H*) but *Aire* deficiency did not influence the development of RORγt$^+$ DCs in mixed bone marrow chimeras (*SI Appendix*, Fig. S2*G*). AIRE$^+$ RORγt$^+$ DCs stained slightly higher for CCR7, CD24, MCHII, and CD200 but resembled AIRE^{neg} RORγt$^+$ DCs in terms of EpCAM, ICOSL, and CCR6 expression (*SI Appendix*, Fig. S2*H*). Altogether, these data suggest that RORγt$^+$ eTACs are a transcriptional state of RORγt$^+$ DCs.

Some of the aforementioned genes (*Prdm16, Col17a1, Pigr, Ltb, Aire, Tnfrsf11a)* have been reported in Thetis cells and Janus cells/eTACs (29, 30, 34, 35). Therefore, we performed data integration of the above dataset, together with published scRNA-seq datasets of DCs from neonatal murine spleen (10), RORγt$^+$ APCs from neonatal Peyer's patch (38), Thetis cells from neonatal mLN (30), Janus cells from mLN (*SI Appendix*, Fig. S3 *C* and *D*) and sdLN (29, 35), and RORγt$^+$ eTACs from mLN (23). We additionally integrated scRNA-seq data from neonatal small intestine in which we identified a cluster of RORγt-expressing DCs (*SI Appendix*, Fig. S3 *A* and *B*). After unsupervised dataset integration using scVI (51) cells from individual datasets were distributed evenly across

Leiden clusters (Fig. 2*I*). Cells originally annotated as the same broad cell types in the individual datasets (cDC1, cDC2, migDCs, pDCs, ILC3) clustered together in the integrated analysis irrespective of study and tissue of origin, and Leiden clusters corresponded well to the different cell types included (Fig. 2*I* and *SI Appendix*, Fig. S2*I*). We found that cells originally annotated as eTACs, Janus cells, Thetis cells, or RORγt$^+$ APCs clustered together with RORγt$^+$ DCs identified in our study, into a transcriptionally distinct cluster (Leiden 6), termed RORγt$^+$ DCs (Fig. 2*J* and *SI Appendix*, Fig. S2*I*). Of note, Thetis cells from neonatal mLN also show heterogeneity in terms of *Aire* expression (*SI Appendix*, Fig. S2*J*) (30), supporting that RORγt$^+$ DCs entail distinct transcriptional states. Together, this comprehensive multiomic profiling and meta-analysis establishes RORγt$^+$ DCs as a transcriptionally distinct cell type with strong resemblance to RORγt$^+$ eTACs, Janus and Thetis cells.

Comparative Transcriptomics Reveals RORγt$^+$ DCs are Evolutionarily Conserved. To investigate whether RORγt$^+$ DCs exist in the human spleen, we analyzed a scRNA-seq dataset of human spleen cDCs from a 61-year-old patient (12). 11 of 12 identified clusters corresponded to the previously identified clusters, including cDC1, CLEC10A$^-$ cDC2A, and CLEC10A$^+$ cDC2B, DC progenitor-like cells (pre-DC/ASDCs), CCR7$^+$ migratory DCs (CCR7$^+$ DCs), and one cluster of dividing cells (Fig. 3*A* and *SI Appendix*, Fig. S4 *A–C*). Cluster 11 expressed *RORC* and *PRDM16,* but not the ILC3 genes *RORA* and *IL7R* (*SI Appendix*, Fig. S4*C*), and had been excluded from the original analyses as putative ILC3 contamination. Indeed, this *RORC*$^+$ cluster scored high for expression of ILC3 signature genes (Fig. 3*B*) but also for genes that distinguished RORγt$^+$ DCs in multiome and scRNA-seq analyses from murine spleen (10) (Fig. 3*B* and *SI Appendix*, Table S1). From the Tabula Sapiens human reference atlas, we selected spleen cells annotated as CD1c$^+$ and CD141$^+$ myeloid DCs, pDCs, and ILCs (52), which formed 8 clusters corresponding to cDC1 (cluster 2), cDC2 (cluster 4), ILC3 (cluster 1, 0, 5), and pDCs (clusters 6 and 3) (Fig. 3 *C* and *D* and *SI Appendix*, Fig. S4 *D–F*). Cells in cluster 7 expressed *RORC* and *PRDM16,* but not *RORA* and *IL7R* and scored highest for genes distinguishing RORγt$^+$ DCs in mouse spleen, whereas ILC3s scored highest for ILC3 signature genes (Fig. 3*D* and *SI Appendix*, Table S1). This *RORC*$^+$ cluster contained cells from multiple donors aged 59, 61, and 69 y and did not segregate by the sequencing method or cell cycle phase, validating it as a bona fide population (*SI Appendix*, Fig. S4*F*). After integration, *RORC*$^+$ cells from both datasets clustered together and away from DCs and ILCs (Fig. 3 *E* and *F*). Comparative gene expression analyses identified conserved markers, including *PRDM16, UBE2E2, IL4I1, PIGR,* and *LTB,* that distinguished RORγt$^+$ DCs in murine spleen and the *RORC*$^+$ clusters in the human spleen (Fig. 3*G*). Thus, RORγt$^+$ DCs also exist in the human spleen.

We also identified *RORC*- and *PRDM16*-expressing cells that lacked *RORA* and resembled the *RORC*$^+$ cluster in the human spleen in single-cell RNA-seq data from small and large intestines from healthy adults (25 to 75 y old) (53) (*SI Appendix*, Fig. S5 *A–D* and Table S5), as well as in small intestine of healthy pediatric donors and pediatric Crohn's disease patients (*SI Appendix*, Fig. S5*E*). These data indicate that RORγt$^+$ DCs are conserved in the human intestine across age. In the Tabula Sapiens lymph node dataset (52), we also detected *RORC-*, *PRDM16-*, and *LTB*-expressing cells, some of which expressed *AIRE* (*SI Appendix*, Fig. S5 *F–I*), and that derived from multiple donors and anatomically distinct LNs (*SI Appendix*, Fig. S5 *F* and *H*) and have recently been dubbed cDC2C (40).

By performing comparative gene expression analyses of RORγt$^+$ DCs in each dataset described above and identifying commonalities, we revealed a set of genes, including *RORC*, *PRDM16*, *LTB*, *PIGR*, and *IL4I1,* that reliably distinguished RORγt$^+$ DCs across tissues and species in all of the above mouse and human datasets (Fig. 3 *H* and *I* and *SI Appendix*, Tables S1 and S5 and Fig. S6 *E* and *F*). R-DC-like cells from tonsil, which correspond to Thetis cells (37) showed higher expression of these genes compared to other populations in the same dataset (Fig. 3*H*), indicating that these cells are homologous to RORγt$^+$ DCs. Additionally, we could align RORγt$^+$ DCs with PRDM16$^+$ cDC2C from glioblastoma (GBM) (40, 54) and ACY3$^+$ DCs from cerebral spinal fluid (CSF) of patients with multiple sclerosis (39) (Fig. 3*H* and *SI Appendix*, Fig. S6 *A* and *B*) and identified RORγt$^+$ DCs in two additional datasets from CSF of patients with demyelinating disease (55, 56) (*SI Appendix*, Fig. S6 *C–E*). This comprehensive meta-analysis establishes RORγt$^+$ DCs as a transcriptionally distinct and evolutionarily conserved cell type that encompasses previously described populations including RORγt$^+$ eTACs, Janus cells, Thetis cells, R-DC-like cells, cDC2C and ACY3$^+$ DCs.

Distribution and Phenotype of RORγt$^+$ DCs Across Lymphoid and Nonlymphoid Tissues in Mice. We next assessed the tissue distribution of RORγt$^+$ DCs across age in *RORγt*^{GFP} mice. Migratory cDCs in nonlymphoid tissues express CD127 (25, 57) (*SI Appendix*, Fig. S7*A*). Thus, we gated cDCs irrespective of CD127 as CD90$^-$ CD11c$^+$MHCII$^+$ cells negative for the monocyte marker CD64. In mLN, we detected RORγt$^+$ DCs at all ages examined and found their frequency was highest in neonatal mLN and declined with age (Fig. 4*A*). As reported (30), we consistently detected the highest numbers of RORγt$^+$ DCs at two weeks of age (Fig. 4*A* and *SI Appendix*, Fig. S7*B*). In small intestinal lamina propria (siLP) the frequency of RORγt$^+$ DCs within CD11c$^+$MHCII$^+$ cDCs was highest in neonates and absolute numbers peaked at two weeks of age (Fig. 4*B*). Of note, for technical reasons, Peyer's patches (PP) were removed from SI only for mice older than two weeks (Fig. 4*B*). RORγt$^+$ DCs were present in the colon, which lacks PP, of neonatal and adult mice (Fig. 4*C*). RORγt$^+$ DCs differed phenotypically from MHCII$^+$ILC3s (CD90$^+$CD127$^+$MHCII$^+$GFP$^+$ cells, *SI Appendix*, Fig. S7 *A*, *C*, *E*, and *F*) and in mLN lacked the ILC3 marker CXCR6 (*SI Appendix*, Fig. S7*D*). In mLN and siLP from one-week-old, but not adult mice, RORγt$^+$ DCs expressed CD11b (*SI Appendix*, Fig. S7 *C* and *F*). In both tissues RORγt$^+$ DCs expressed high levels of MHCII, consistent with a migratory DC phenotype and lacked the cDC1 marker XCR1, although some RORγt$^+$ DCs expressed XCR1 in adult mLN (*SI Appendix*, Fig. S7 *C* and *F*). In the lung, RORγt$^+$ DCs were least frequent and their numbers peaked at two weeks of age (Fig. 4*D* and *SI Appendix*, Fig. S8 *A–C*). Pulmonary RORγt$^+$ DCs lacked XCR1 but expressed CD11b and were distinguished from ILC3s by expression of CD11c, MHCII and lack of CD90 (*SI Appendix*, Fig. S8 *A* and *B*). Importantly, we also detected RORγt$^+$ DCs with high MHCII expression in skin draining lymph nodes (Fig. 4*E* and *SI Appendix*, Fig. S8 *D–F*).

Transcriptional Regulation of RORγt$^+$ DCs. We next investigated the transcriptional regulation of RORγt$^+$ DCs in the spleen (Fig. 2). While cells from different ages distributed evenly across ATAC and RNA clusters, RNA cluster cDC2_2 was dominated by cells from the adult time point (*SI Appendix*, Fig. S9*A*). Because cDC2 clusters 1 and 2 showed uniform chromatin accessibility but split into two clusters based on gene expression (*SI Appendix*, Fig. S2 *A*, *B*, and *D*), these data indicate that while cDC2 chromatin identity is conserved environmental signals may shape gene expression in cDC2 across age, as reported (10, 38, 58). Accordingly, we identified 687 differentially expressed genes between the cDC2 metacluster across age (*SI Appendix*, Table S3). cDC2 from adult mice were enriched for genes downstream of IFNγ, tumor

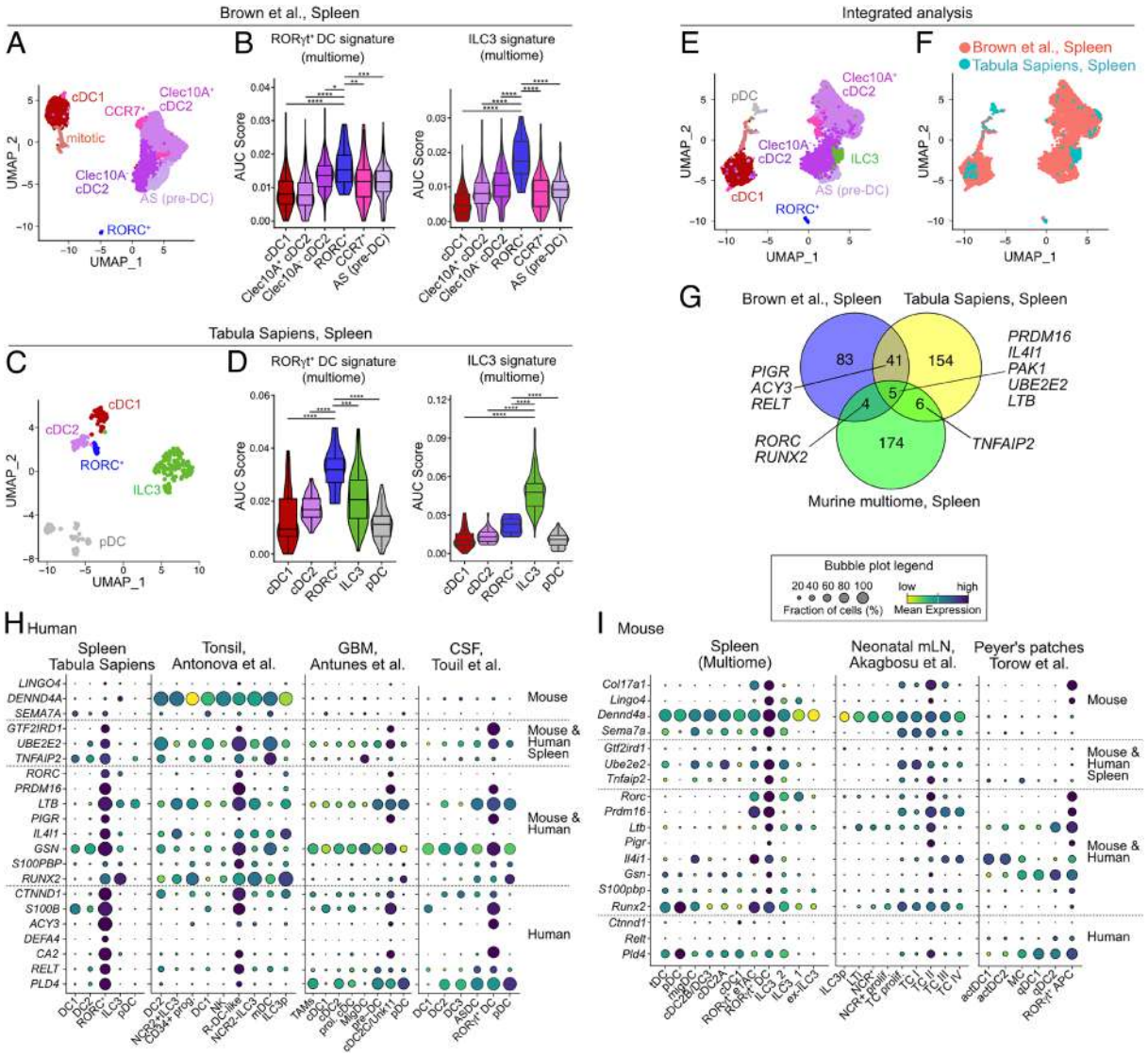

Fig. 3. Comparative transcriptomics reveals RORγt$^+$ DCs are evolutionarily conserved. (*A*) Annotated UMAP of 4,717 cells from scRNA-seq dataset of human splenic DCs. (*B*) Enrichment scores for the RORγt$^+$ DC and ILC3 signatures from the murine multiome dataset were calculated for each cluster. (*C*) Annotated UMAP of 262 cells from scRNA-seq dataset of human spleen. (*D*) Enrichment scores for the RORγt$^+$ DC signature or ILC3 signature from the murine multiome dataset were calculated for each cluster. (*E* and *F*) Annotated UMAP (*E*) of integrated scRNA-seq datasets generated using Seurat Integration of scRNA-seq datasets pipeline, and colored by dataset (*F*). (*G*) Venn diagram showing the overlap of genes distinguishing RORγt$^+$ DCs in the indicated mouse and human scRNA-seq datasets. (*H* and *I*) Bubble plots of selected genes deduced from comparative gene expression analyses that distinguish RORγt$^+$ DCs in various human (*H*) and murine (*I*) scRNA-seq datasets. Genes are ordered according to the species and organs they were found in to differentiate RORγt$^+$ DCs from other cell types. *P < 0.05, **P < 0.01, ***P < 0.001, ****P < 0.0001. Statistical analysis was performed using the Wilcoxon nonparametric ranked sum test.

necrosis factor-α (TNF-α), IL-2, and IFNα signaling (*SI Appendix*, Fig. S9*B*), corroborating our previous findings (10), and validating the suitability of our dataset to compare populations across age. Contrary to cDC2, RORγt$^+$ DC clusters had equal contribution of cells from both ages and only 29 genes were differentially expressed between RORγt$^+$ DCs across age (*SI Appendix*, Fig. S9*A* and Table S3). Thus, RORγt$^+$ DCs are transcriptionally stable between 2 wk of age and adulthood.

Focused multiomic analysis of the RORγt$^+$ DC and RORγt$^+$ eTAC clusters confirmed that RORγt$^+$ eTACs form a separate cluster from RORγt$^+$ DCs in ATAC and mRNA profiles (Fig. 5 *A* and *B* and *SI Appendix*, Fig. S9*C*). *Aire*^{neg}RORγt$^+$ DCs could further be divided into 3 clusters (Fig. 5 *A* and *B* and *SI Appendix*, Fig. S9*C*). Of note, *Itgb8* expression, which promotes Treg differentiation (29, 30) was restricted to the RORγt$^+$ eTAC cluster (Fig. 5*B*). RORγt$^+$ DC cluster b showed lower expression of *Rorc* than the other two clusters (Fig. 5*B*), suggesting that RORγt$^+$ DCs can lose RORγt expression. Indeed, in spleens from two-week-old and adult *RORγt*^{Cre}*Rosa*^{YFP}*RORγt*$^{GFP\text{-}knockin}$ reporter mice cells with RORγt expression history (YFP) outnumbered those with active RORγt expression (GFP; Fig. 5*C*) although these cells were otherwise phenotypically similar (*SI Appendix*, Fig. S9*D*). Similar observations were made in the lung, mLN and siLP (Fig. 5*D* and *SI Appendix*, Fig. S9*E*). Especially in lung and mLN from two-week-old mice, cells with *RORγt*^{Cre} expression history largely outnumbered those actively expressing RORγt (Fig. 5*D* and *SI Appendix*, Fig. S9*E*).

Finally, combining chromatin accessibility and gene expression profiles from individual cells we used SCENIC+ (59) to identify cell type–specific enhancer-driven gene regulatory networks (eRegulons). Dimensionality reduction based on target gene and target region enrichment scores of eRegulons separated the same main cell states as identified above (Fig. 5*E*). Of note, RORγt$^+$ DCs and RORγt$^+$ eTACs were similar in this analysis suggesting that they are closely related cell states. SCENIC+ identified well-known master regulators of cDC1 (*Irf8*), cDC2 (*Runx3*), pDCs (*Tcf4/E2-2, Spib*), and ILC3 (*Rora, Ikzf1, Rorc*), confirming the

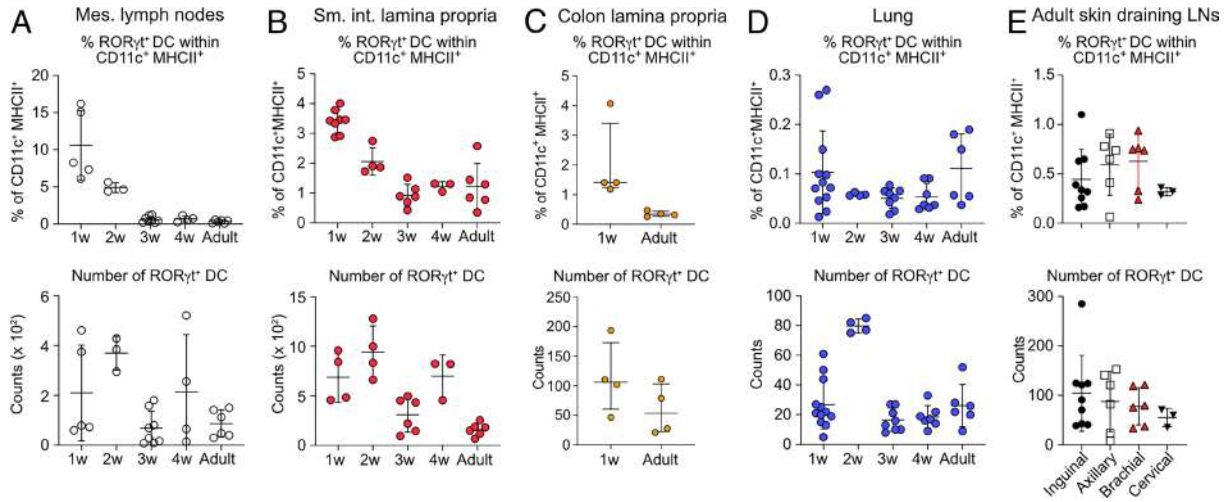

Fig. 4. RORγt$^+$ DCs exist across lymphoid and nonlymphoid tissues in mice and humans. (*A–C*) RORγt$^+$ DCs were quantified in mLN (*A*), siLP (*B*) colon LP (*C*), lung (*D*), and skin draining lymph nodes (*E*) of *RORγt^{GFP}* reporter mice (representative gating in *SI Appendix*, Fig. S7 and S8). (*A*) Frequency of RORγt$^+$ cells within CD11c$^+$MHCII$^+$ cells (*Upper* plot) and number of RORγt$^+$ cells (*Lower* plot) in mLN of mice of indicated ages (1 wk n = 5; 2 wk n = 3; 3 wk n = 8, 4 wk n = 4; Adult n = 6). (*B–D*) Frequency of RORγt$^+$ cells within CD11c$^+$MHCII$^+$CD64$^-$ cells (*Top*) and number (*Bottom*) in siLP (1-wk-old n = 4 to 8; 2-wk-old n = 4; 3-wk-old n = 6, 4-wk-old n = 3; Adult n = 6), colon (1-wk-old n = 4; adult n = 4), and lung (1-wk-old n = 11; 2-wk-old n = 4; 3-wk-old n = 7, 4-wk-old n = 6; Adult n = 6) from mice of indicated ages. (*E*) RORγt$^+$ DCs from axial, brachial, cervical, and inguinal skin draining LN were gated as in *SI Appendix*, Fig. S8*D* and quantified. The frequency of RORγt$^+$ cells within CD11c$^+$MHCII$^+$ cells (*Top*) and number of RORγt$^+$ DCs (*Bottom*) is shown.

validity of our approach (*SI Appendix*, Fig. S9*F*). RORγt$^+$ DCs and RORγt$^+$ eTACS shared regulatory networks *Nfat5* and *Relb* with migDCs and *Rel* with cDC2 and migDCs, aligning them with DCs (Fig. 5*F* and *SI Appendix*, Fig. S9*F*). SCENIC+ predicted RORγt$^+$ DCs and RORγt$^+$ eTACs to be specifically regulated by *Prdm16*, which is also specifically expressed in these cells (Figs. 2 *B* and *D* and 5*F* and *SI Appendix*, Fig. S9*F*). eRegulons of the nuclear receptors *Thrb/Nr1a2, Rorc,* and *Ppara* were equally predicted by SCENIC+ to regulate RORγt$^+$ DCs (Fig. 5*G* and *SI Appendix*, Fig. S9*F*). PRDM16 is a master regulator of brown adipogenesis that in adipocytes directly controls expression of *Ppara*, a nuclear receptor that, like RORγt, integrates signals from free fatty acids and is involved in lipid metabolism (60, 61). Visualization of the eRegulons formed by *Rorc* and *Prdm16* in RORγt$^+$ DCs suggests cooperativity between these factors in RORγt$^+$ DCs (Fig. 5*G*). Downstream target genes of PRDM16 showed higher expression in RORγt$^+$ DCs and RORγt$^+$ eTACs than in other cell types and some of these genes, including *Ltb,* appear coregulated by *Prdm16* and *Rorc* (*SI Appendix*, Fig. S10*B*). SCENIC+ predicted *Rorc* to regulate expression of *Pigr*, *Gtf2ird1,* and *Col17a1* (Fig. 5*G* and *SI Appendix*, Fig. S10*B*), suggesting that RORγt shapes the identity of RORγt$^+$ DCs (Fig. 5*G*). *Prdm16* was predicted to regulate expression of *Tlr12* and *Il23a*, which showed highest expression in RORγt$^+$ DCs over other clusters (Fig. 5*G* and *SI Appendix*, Fig. S10*B*). RORγt$^+$ DCs did not show enrichment of genes reported to promote Tregs in Thetis cells (*SI Appendix*, Fig. S10*A*) (30), except for expression of *Itgb8* in a subset of RORγt$^+$ DCs expressing *Aire*. Importantly, RORγt$^+$ DCs showed comparable expression of genes involved in antigen processing and presentation to cDCs and migratory DCs (*SI Appendix*, Fig. S10*C*) and flow cytometry confirmed that RORγt$^+$ DCs express costimulatory molecules, including CD80, CD86, PD-L1, and CD83. Notably, RORγt$^+$ DCs expressed highest levels of CD40 and CCR7 when compared to cDC1 and cDC2 (*SI Appendix*, Fig. S10*D*), altogether suggesting that RORγt$^+$ DCs have the necessary machinery to serve as APCs.

RORγt$^+$ DCs are Bona Fide DCs. The capacity to activate naïve T cells is a hallmark feature of cDCs (2). We, thus, sort-purified RORγt$^+$ DCs from spleens of two-week-old and adult *RORγt^{GFP}* mice, pulsed them with Ovalbumin peptide 323 to 339 ($OVA_{323-339}$) and cultured them with cell trace violet (CTV)-labeled naïve OTII transgenic T cells from adult mice with or without T cell polarizing cytokines. cDC2 and MHCII$^+$ILC3 from the same mice were used as controls (*SI Appendix*, Fig. S11*A*). As expected, cDC2 from two-week-old and adult mice induced T cell proliferation under all conditions tested, while MHCII$^+$ILC3s were poor inducers of OTII proliferation (Fig. 6 *A* and *E* and *SI Appendix*, Fig. S11 *C*, *D*, *F*, and *G*). Under all conditions tested RORγt$^+$ DCs from two-week-old and adult mice stimulated the proliferation of naïve T cells, although to a lower extent than cDC2, and supported the differentiation of OTII cells into effector T cells, as measured by intracellular cytokine and FOXP3 staining (Fig. 6 *A–H*). While RORγt$^+$ DCs supported the differentiation of FOXP3$^+$ Tregs equally or better than cDC2, the induction of Th17 cells by RORγt$^+$ DCs was reduced compared to cDC2 (Fig. 6 *C*, *D*, *G*, and *H*). Thus, RORγt$^+$ DCs can activate naïve CD4$^+$ T cells and induce their effector differentiation with qualitative and quantitative differences compared to cDC2. In contrast, MHCII$^+$ ILC3 induced little if any T cell proliferation and may require cytokine stimulation to achieve their full APC potential (62).

We next asked whether RORγt$^+$ DCs have the capacity to process and present antigen. Specific expression of CLEC4A4 on cDC2 and RORγt$^+$ DCs from neonatal and adult mice (10), but not on cDC1 or MHCII$^+$ ILC3 (Fig. 6*I*) (63), suggested that anti-CLEC4A4-OVA (63) may allow to deliver antigen to RORγt$^+$ DCs in vivo. We thus injected adult *RORγt^{GFP}* mice with anti-CLEC4A4-OVA or isotype-matched control antibody in the presence of the adjuvant CpG-B (Fig. 6 *J–L*), which did not alter the activation status of RORγt$^+$ DCs relative to cDC1 or cDC2 (Fig. 6*M* and *SI Appendix*, Fig. S11*H*). 12 h later, we sorted 300 cDC1, cDC2, RORγt$^+$ DCs and MHCII$^+$ILC3s and cocultured them with 3000 naïve CTV-labeled OTII T cells (Fig. 6 *K* and *L*). cDC2 and RORγt$^+$ DCs induced OTII proliferation after targeting with anti-CLEC4A4-OVA but not isotype-matched control antibody (Fig. 2 *K* and *L*), demonstrating successful targeting. In contrast, cDC1 and MHCII$^+$ ILC3s did not induce T cell proliferation demonstrating cell type–specific antigen targeting (Fig. 2 *K* and *L*). OTII proliferation induced by RORγt$^+$ DCs appeared marginally lower than that achieved by cDC2, which could be due to differences in CLEC4A4 targeting efficiency, responsiveness to CpG-B,

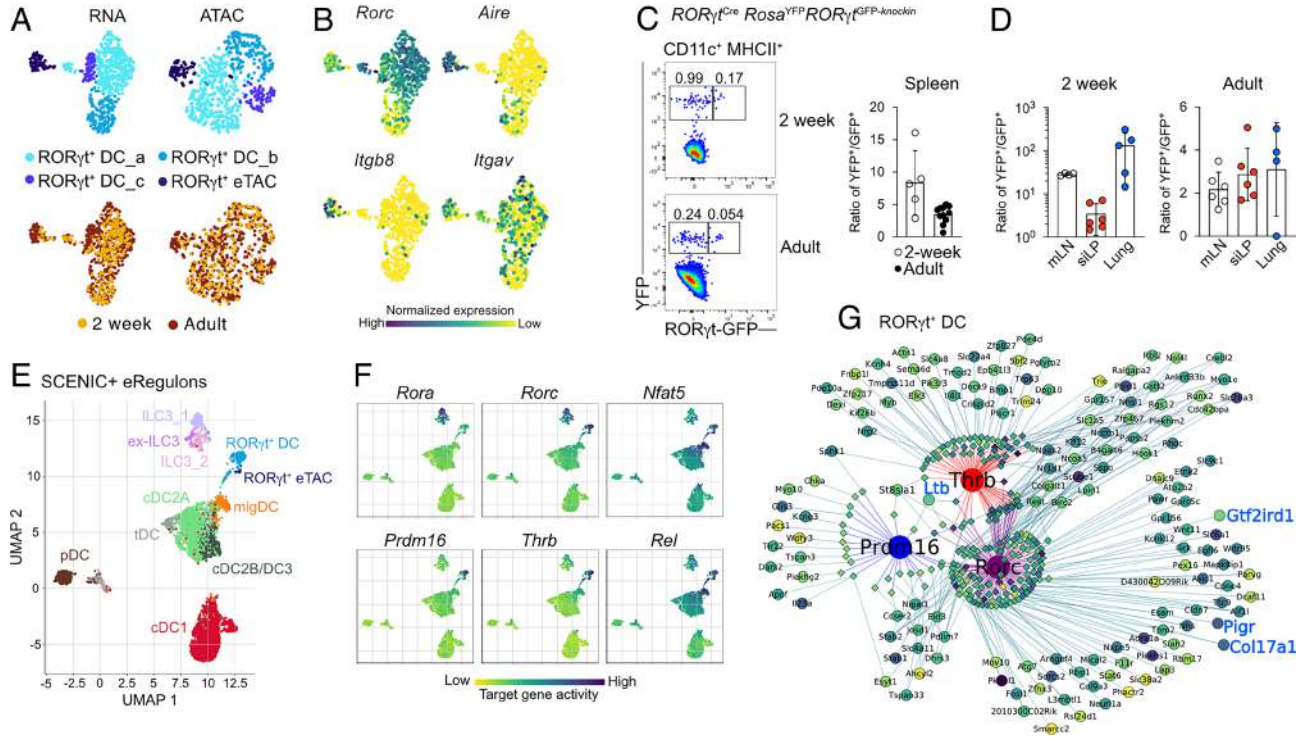

Fig. 5. Single-cell multiomic profiling reveals the unique identity of RORγt$^+$ DCs. (*A*) RORγt$^+$ DCs and RORγt$^+$ eTACs from the multiome analysis in Fig. 2 *A*–*E* were reclustered. The resulting UMAPs based on RNA and ATAC profiles are shown and annotated by timepoint. (*B*) Expression of *Rorc, Aire, Itgav,* and *Itgb8* on the RNA-based UMAP from (*A*). (*C* and *D*) Spleen (*C*), mLN, siLP and lung (*D*) from 2-week-old and adult *RORγt^{Cre}Rosa^{YFP}RORγt$^{GFP/wt}$* mice were analyzed by flow cytometry. YFP (RORγt-expression history) versus GFP (active RORγt) expression in CD11c$^+$MHCII$^+$ cells were plotted and the ratio of YFP$^+$ to GFP$^+$ cells was calculated. Each dot represents one mouse. (*E*) UMAP display of dimensionality reduction based on target genes and region enrichment scores generated using SCENIC+. (*F*) UMAP colored by target gene activity of the indicated eRegulons predicted to regulate specific cell types (*SI Appendix*, Fig. S9*F*). (*G*) Visualization of the gene regulatory network formed by *Prdm16*, *Thrb,* and *Rorc* in RORγt$^+$ DCs. Genes that determine the identity of RORγt$^+$ DCs are colored in blue.

or expression of costimulatory molecules between RORγt$^+$ DCs and cDC2. Taken together, these data demonstrate that RORγt$^+$ DCs can process and present antigen, and activate naïve CD4$^+$ T cells in response to an inflammatory trigger.

Finally, we tested whether RORγt$^+$ DCs have the capacity to migrate to lymph nodes in response to inflammation. Gavage of neonatal mice with R848 induces cDC migration to mLN (64). Indeed, 24 h after R848 gavage we observed an increase in the frequency and number of cDC1, but not ILC3s in mLN, which served as positive and negative controls for migration, respectively (Fig. 6*N*). RORγt$^+$ DCs also increased in frequency and number in mLN (Fig. 6*N*), suggesting that oral R848 stimulates RORγt$^+$ DCs to migrate to mLN. Thus, RORγt$^+$ DCs bear classical migratory features of cDCs upon inflammatory triggers, validating their affiliation with DCs.

RORγt$^+$ DCs Exhibit a Proinflammatory Profile in Autoimmune Neuroinflammation. We next performed comparative gene expression analyses of RORγt$^+$ DCs in three independent scRNA-seq datasets from CSF of patients with autoimmune demyelinating disease and found common genes that distinguished RORγt$^+$ DCs from other cells in each dataset (Fig. 7*A*). These genes included *S100B* and *LTB*, which propagate neuroinflammation (65, 66), *TNFSF15* (TL1A), which promotes Th17 differentiation (67) and *CCR6*, which enables trafficking of DCs to LNs for the priming of autoimmune T cells in EAE (68). Of note, RORγt$^+$ DCs also expressed the aryl hydrocarbon receptor (*AHR*) and *FFAR4* (also known as GPR120), which are reported to integrate environmental signals to modulate DC function in EAE (69, 70). We thus immunized mice with MOG to induce EAE and observed an increase in frequency and number of cDC1, RORγt$^+$ DCs and MHCII$^+$ ILC3s in the brain and spinal cord of mice at peak disease compared to healthy control mice (Fig. 7 *B* and *C* and *SI Appendix*, Fig. S12*A*). Of note, in inflamed CNS, RORγt$^+$ DCs became a sizable population and reached comparable numbers to cDC1 and MHCII$^+$ ILC3s (Fig. 7 *B* and *C*), which influence EAE pathogenesis (27, 71).

Discussion

Here, we demonstrate the existence of RORγt-expressing DCs that are transcriptionally and developmentally distinct from other DC subtypes and entail murine Janus cells/ RORγt$^+$ eTACs (29, 35), Thetis cells (30), RORγt$^+$ APCs in Peyer's patches (38), as well as human R-DC-like cells (37), cDC2C (40), and ACY3$^+$ DCs (39). Previous work has demonstrated that RORγt$^+$ DCs—also known as Thetis and Janus cells induce peripheral T cell tolerance and Tregs, particularly at mucosal sites (29, 35, 72–74). We show that RORγt$^+$ DCs, like cDCs, respond to inflammation by inducing the activation of naïve T cells and that they can migrate to lymph nodes. They further accumulate in the inflamed CNS of mice and exhibit proinflammatory features in CSF of patients with inflammatory demyelinating disease, including multiple sclerosis. Thus, RORγt$^+$ DCs are bona fide immune sentinels with a versatile functional spectrum ranging from inducing T cell activation to mediating peripheral T cell tolerance (*SI Appendix*, Fig. S12*B*). This versatility makes them an attractive target for therapeutic manipulation in inflammatory diseases, cancer, and neuroinflammation.

In the spleen, RORγt$^+$ DCs lack a particular tolerogenic profile and, like cDCs, respond to inflammation with the activation of naïve CD4$^+$ T cells. Similarly, R-DC-like cells from human lymph nodes can stimulate allogeneic CD4$^+$ T cells, although their APC potential has not been compared to that of cDCs (37). Although

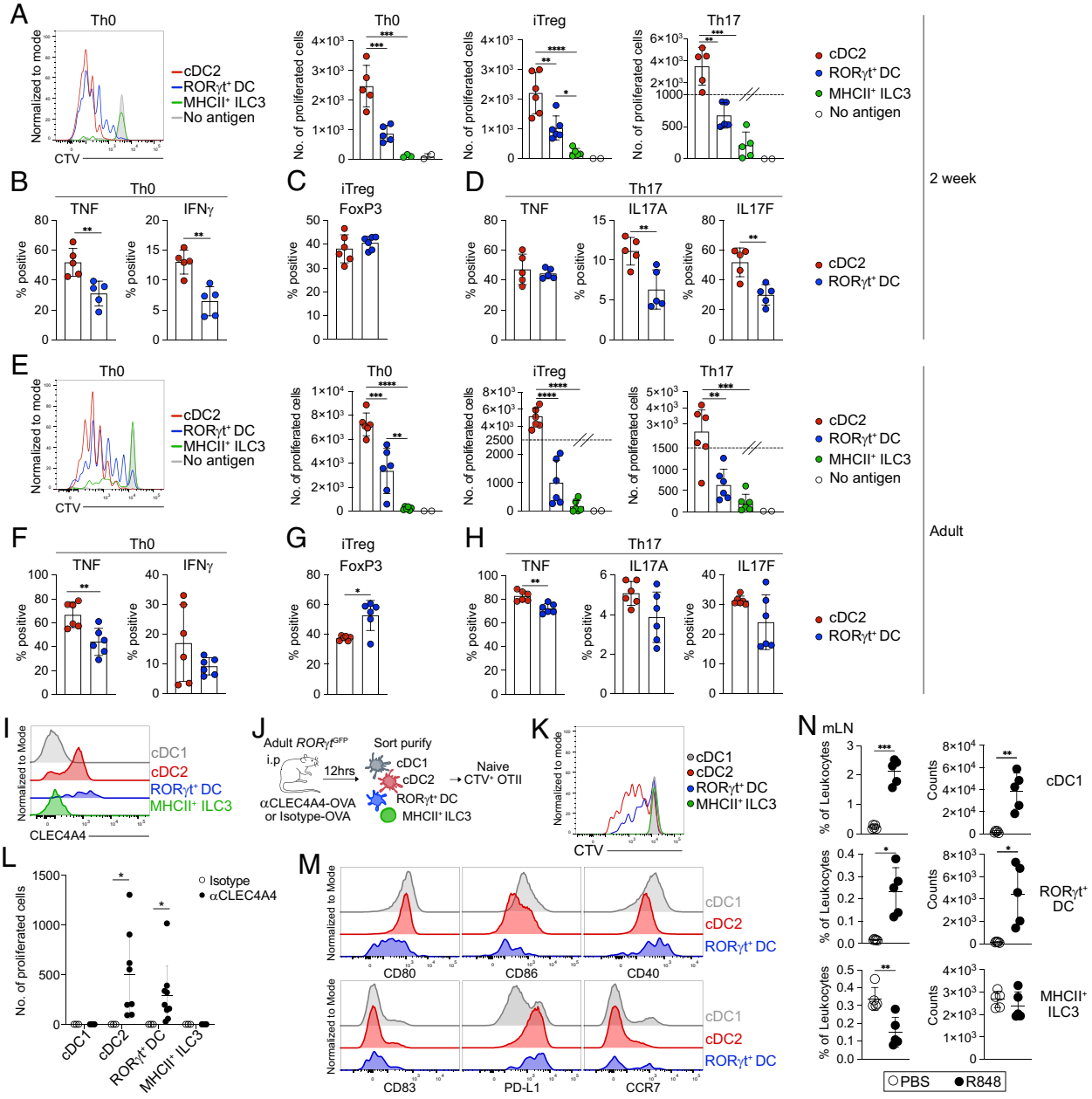

Fig. 6. RORγt$^+$ DCs are bona fide dendritic cells (DCs). (*A–H*) 250 cDC2, MHCII$^+$ ILC3, and RORγt$^+$ DCs from spleens of 2-wk-old (*A–D*) or adult (*E–H*) *RORγt^{GFP}* mice were pulsed with $OVA_{323-339}$ and cocultured with 2500 CTV-labeled naïve OTII cells as indicated. 3.5 d later, proliferation (CTV dilution), cytokine production, and FOXP3 expression in proliferated T cells were quantified. (*A*) CTV-trace of OTII cells cocultured with cDC2, RORγt$^+$ DCs, MHCII$^+$ ILC3, or cDC2 without $OVA_{323-339}$ (gray) under nonpolarizing conditions (Th0). *Right*: Quantification of proliferated cells after culture with cDC2, RORγt$^+$ DCs, MHCII$^+$ ILC3, or cDC2 without $OVA_{323-339}$ (open circle) under the indicated conditions. (*B–D*) Proliferated OTII cells were analyzed for TNF and IFNγ production (*B*), FOXP3 expression (*C*), or TNF, IL-17A, and IL-17F production (*D*). (*E–H*) OTII T cells cocultured with cDC2, MHCII$^+$ ILC3, and RORγt$^+$ DCs from adult mice were analyzed as in *A–D* above. (*I*) CLEC4A4 expression on the indicated populations. (*J–L*) Adult *RORγt^{GFP}* mice were injected i.p. with anti-CLEC4A4-OVA or isotype-OVA control antibody plus CpG-B. After 12 h 300 cDC2, cDC1, MHCII$^+$ILC3, and RORγt$^+$ DCs were sorted and cocultured with 3000 naïve CTV-labeled OTII cells. (*J*) Experimental setup. (*K*) CTV dilution and (*L*) number of proliferated OTII cells after coculture with the indicated populations (n ≥ 5). (*M*) Expression of the indicated markers on cDC1 (gray), cDC2 (red), and RORγt$^+$ DCs (blue) 12 h after i.p injection of CpG-B. (*N*) Frequency and absolute number of cDC1, MHCII$^+$ILC3, and RORγt$^+$ DCs in mLN of 11-d-old *RORγt^{GFP}* reporter mice 24 h after oral administration of R848. Each dot represents one biological replicate pooled from two independent experiments. Horizontal bars represent mean, error bars represent SD. **P* (0.0332), ***P* (0.0021) ****P* (0.0002), *****P* < 0.0001. Statistical analysis: two-tailed Welch's *t* test (*B–D*, *F–H*, and *L*) or one-way ANOVA with Tukey's multiple comparisons (*A* and *E*). Only statistically significant comparisons are indicated.

RORγt$^+$ DCs are infrequent in steady-state tissues, we found them to increase in the inflamed mLN and in the CNS of mice with active EAE. They also accumulate in the inflamed esophagus, where they express the eosinophilic esophagitis risk gene *ATP10A* (40), and in the CSF from patients with demyelinating disease (39). In patient CSF, RORγt$^+$ DCs display a proinflammatory profile and have been predicted to interact with memory CD4$^+$ T cells (39). Since RORγt$^+$ APCs contribute to CNS pathology in EAE (27), the functions of RORγt$^+$ DCs in neuroinflammation require further investigation. AhR cooperates with RORγt to drive IL-22 expression in Th17 cells (70). In patient CSF, RORγt$^+$ DCs express *AHR,* raising the possibility that these two transcription factors drive gene expression in RORγt$^+$ DCs. Since *AHR*, *FFAR4,* and *RORC* are druggable molecules, the possibility to manipulate RORγt$^+$ DCs therapeutically in EAE can be explored in future studies. The prominent expression of *LTβ* in RORγt$^+$ DCs suggest

that they can contribute to the spatial organization of immune cells (75). RORγt$^+$ DCs also express the tryptophan-metabolizing enzyme IL4i1 that generates bioactive immunomodulatory metabolites (76). IL4i1-derived metabolites can for instance activate AhR or protect cells from ferroptosis (76), suggesting that RORγt$^+$ DCs may function beyond T cell priming, for instance, by modulating metabolic communication between cells.

Taken together, the above data suggest that RORγt$^+$ DCs exhibit tissue-specific functional diversity. Tolerogenic immune functions in RORγt$^+$ APCs have been linked to AIRE (29, 35), the expression of which is restricted to subtypes of RORγt$^+$ DCs (29, 30). *AIRE* shapes gene expression in tumor-associated macrophages, DCs and ILC3s (28, 49). Our data suggest that *Aire* marks a distinct functional state since AIRE$^+$RORγt$^+$ DCs express higher levels of CCR7 and MHCII than AIRE^{neg} cells and show a distinct transcriptional profile. RANK signaling induces AIRE in eTACs and ILC3s (34, 35) and RANKL or other tissue/age-specific signals may shape the transcriptional and functional attributes of RORγt$^+$ DCs. RORγt$^+$ DCs may receive such signals in specific tissue niches.

RORγt-Cre lineage tracing experiments show that some cells that have previously expressed RORγt downregulate it. Although they phenotypically still resemble those cells actively expressing RORγt, these data indicate that RORγt itself may not be a good lineage defining marker. CCR6, EpCAM, CLEC4A4, and CD200 are good candidates to design a combinatorial sort strategy to identify RORγt$^+$ DCs in mice. However, RORγt is currently the most reliable marker to identify these cells by flow cytometry in mouse tissues either by using *RORγt^{GFP}* reporter mice or intracellular staining using an anti-RORC antibody. Other genes, including *PRDM16*, may be better candidates to reliably define RORγt$^+$ DCs across tissues and species. A gating strategy independent of RORγt would be critical for example in neonatal lung, where cells with *RORγt^{Cre}* expression history vastly outnumber cells with active RORγt expression. The neonatal lung is considered an environment that promotes type 2 immunity (77), while RORγt is generally associated with type 3/Th17 mediated immunity. Factors specifically expressed in neonatal lung may suppress RORγt expression, which could alter the phenotype and functions of RORγt$^+$ DCs by rendering them unresponsive to natural ligands of RORγt.

Indeed, SCENIC+ predicted RORγt itself to shape the transcriptional identity of RORγt$^+$ DCs, consistent with a recent report describing a role for RORγt in the development of Thetis cells (72). PRDM16 is a master regulator of brown fat adipogenesis that can act as transcriptional activator and repressor. Loss of PRDM16 increases γδ T17 differentiation, suggesting PRDM16 antagonizes RORγt in γδ T cells (78). GTF2IRD1, a predicted target of RORγt, can mediate the repressive action of PRDM16 (79). PRDM16 also regulates stem cell quiescence (80), raising the possibility that RORγt$^+$ DCs serve as progenitors. Indeed, RNA velocity analyses in humans suggest that RORγt$^+$ DCs may serve as alternative progenitors for cDC or ILC3-like cells (37). Although we found no evidence for that in steady-state neonatal spleen (10), the fact that cells with RORγt-expression history outnumber those with active RORγt expression would be consistent with the possibility of RORγt$^+$ DCs serving as progenitors. However, RORγt$^+$ DCs express costimulatory molecules and can activate naive T cells, indicating that they themselves constitute mature APCs. Consistent with previous reports (30), our observation that RORγt$^+$ DCs arise from lymphoid bone marrow progenitors in a Rag2-common-γ–chain-independent manner suggests that these cells are a lineage distinct from myeloid cDCs and ILC3s.

Owing to their expression of CD11c, ZBTB46, and RORγt, RORγt$^+$ DCs need to be considered in the interpretation of studies using promoters for the above genes to drive Cre or other transgenes, such as diphtheria toxin receptor. Models to specifically manipulate this cell type are urgently needed to understand its functions in immunity. However, inducible depletion models are necessary, given the necessity of RORγt$^+$ DCs for differentiating RORγt$^+$FoxP3$^+$ T regs, which regulate intestinal homeostasis and dampen type II immune responses (29, 35, 72, 73). In the absence of such models, the anti-CLEC4A4 based antigen-targeting

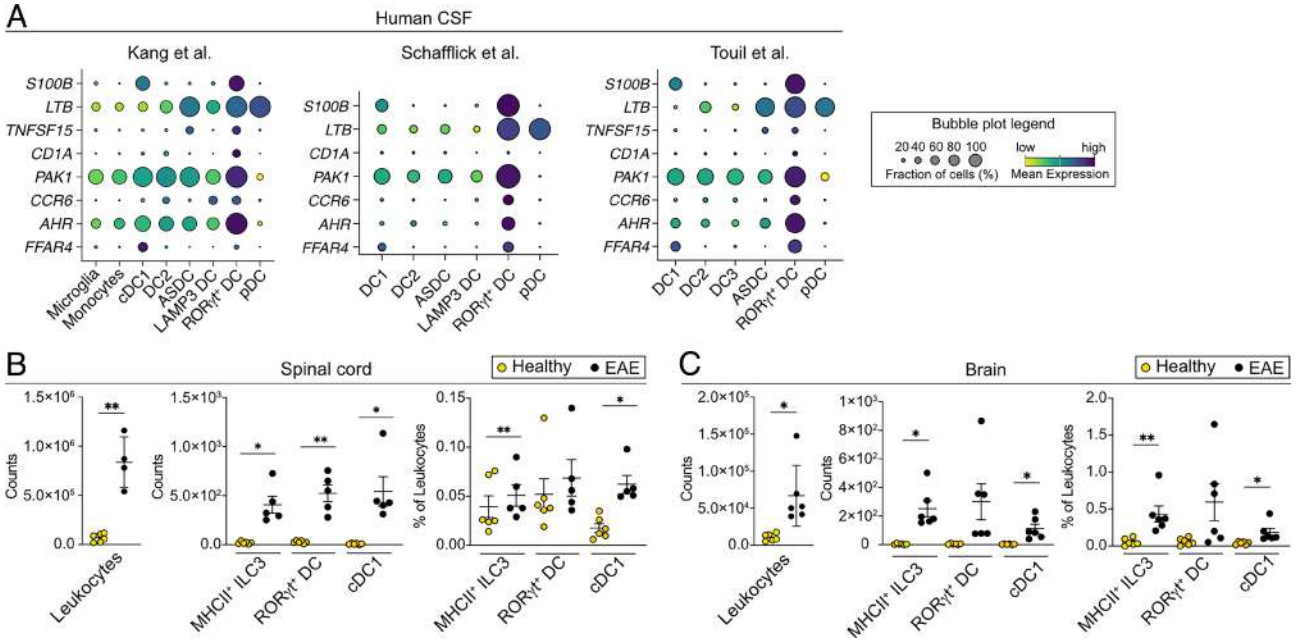

Fig. 7. RORγt$^+$ DCs in autoimmune neuroinflammation. (*A*) Bubble plots depicting expression of select genes that distinguished RORγt$^+$ DCs from other APCs in at least two of the indicated human CSF datasets. (*B* and *C*). Quantification of total leukocytes, frequency and number of MHCII$^+$ ILC3, cDC1, and RORγt$^+$ DCs in the spinal cord (*B*) and brain (*C*) of mice during peak EAE (day 16, n = 5/6) compared to healthy controls (n = 6). Each dot represents one mouse, horizontal bars represent mean, error bars represent SD. **P* (0.0332), ***P* (0.0021) ****P* (0.0002), *****P* < 0.0001. Statistical analysis was performed using two-tailed Welch's *t* test comparing cells from healthy mice vs EAE mice for each cell type. Only statistically significant comparisons are indicated.

approach used here will prove valuable to determine the specific functions of RORγt$^+$ DCs, especially compared to cDC2. RORγt$^+$ DCs also express *Ly75,* the gene encoding DEC205, suggesting they are targetable by anti-DEC205, enabling functional comparison to cDC1.

RORγt$^+$ DCs have been termed Janus cells and Thetis cells in other studies for their two-faced and shape-shifting transcriptional features and resemblance to cDCs and thymic epithelial cells. Our work shows that RORγt$^+$ DCs are indeed multifaceted in nature and bear hallmark features of DCs including the ability to integrate signals from the environment to direct appropriate immunity. Their functional versatility ranging from inducing T cell tolerance to T cell activation highlights the potential of these cells to be targeted for therapeutic applications.

Materials and Methods

Mice. Female and male age and sex-matched mice and littermate controls were housed under specific pathogen-free conditions and used in this study. All animal procedures were performed in accordance with national and institutional guidelines for animal welfare and approved by the respective authorities. See also *SI Appendix, Material and Methods*.

Cell Isolation for Flow Cytometry. Tissues were enzymatically digested; see *SI Appendix, Material and Methods*. For SI, Peyer's patches were removed only for mice 3 wk or older. mLN from 2 to 3 one-week-old mice were pooled prior to processing; mice older than 3wks were perfused with ice-cold PBS before lung isolation.

Flow Cytometry and Cell Sorting. Cells were incubated with CD16/32/FcBlock for 10 min at 4 °C and then for 30 min at 4 °C with antibodies against surface epitopes and Fixable Viability Dye eFluor 780. To preserve GFP signal after intranuclear staining, cells were prefixed with 2% paraformaldehyde at RT for 15 min. Intracellular cytokine and transcription factor staining was performed using Intracellular Fixation and Permeabilization Buffer Set and FOXP3 Transcription Factor Staining Set, respectively (both Thermo Fisher Scientific). Anti-RORC staining was performed for 1 h at RT.

Sorting: splenocytes were depleted of T cells (CD3e), B cells (CD19), Neutrophils (Ly6G), and Erythroid cells (Ter119) using magnetic beads. Cells were sorted on a BD FACSAria Fusion. Data were acquired on an LSR Fortessa (BD Biosciences) and analyzed using FlowJo V10.8.1 (Tree Star). For antibodies and further details see *SI Appendix, Material and Methods*.

In Vitro T Cell Proliferation. 250 APCs were pulsed with 10 μg/mL $OVA_{323-339}$ (Invivogen) for 3 h, washed, and cocultured with 2500 naïve CTV-labeled OTII T cells. 5 ng/mL TGF-β, 10 μg/mL anti-IL-4, and 10 μg/mL anti-IFNγ were added for Treg polarization, and 5 ng/mL TGF-β, 20 ng/mL IL-6, 10 μg/mL anti-IL-4, and 10 μg/mL anti-IFNγ for Th17 polarizing condition. 3.5 d later cells were restimulated with 10 ng/mL phorbol 12-myristate 13-acetate (PMA) (Calbiochem) and 1 μg/mL Ionomycin (Sigma-Aldrich) for a total of 5 h. Brefeldin A (BioLegend) was added during the last 3 h. See also *SI Appendix, Material and Methods*.

In Vivo Targeting. Adult RORγt^{GFP} mice were injected intraperitoneally (i.p.) with 10 μg anti-CLEC4A4-OVA or 10 μg OVA-coupled-isotype matched control antibody plus 0.2 μg/g body weight CpG-B ODN 1826 (InvivoGen). 12 h later 300 APCs were cocultured with 3000 naïve CTV-labeled OTII cells as above.

R848 Treatment. Ten-day-old *RORγt^{GFP}* mice were orally gavaged with 2 μg R848 (Invivogen) in 50μL PBS or 50μL PBS as control and analyzed 24 h later.

Single-Cell Multiomics and Transcriptomics. MHCII$^+$ ILC3, CD11c$^+$MHCII$^+$ DC, and RORγt$^+$ DCs were sorted from of 2-wk-old (P13, n = 2) and adult (8-wk-old, n = 3) *RORγt^{GFP}Clec9a$^{cre/wt}$Rosa26$^{Tom/wt}$* mice. EDTA-free buffer was used for cell isolation. For each timepoint, cells were pooled at a ratio of 1:1:10 (RORγt$^+$ DCs: MHCII$^+$ ILC3: CD11c$^+$ MHCII$^+$ DC) and nuclei isolated following the 10X Genomics Low Cell Input Nuclei Isolation protocol. 20,000 cells were lysed for 3 min on ice, resuspended in diluted Nuclei Buffer and lysis efficiency and nucleus quality assessed by trypan blue staining. 8,400 nuclei for the adult timepoint and 10,400 nuclei for the 2-wk timepoint were loaded for transposition. RNA and ATACseq libraries were prepared with the 10X Genomics Chromium Next GEM Single Cell Multiome ATAC + Gene Expression Kit and sequenced as recommended. Details of the analyses and all other transcriptomics are provided in *SI Appendix, Material and Methods*.

EAE. 12-wk-old male C57BL/6 mice were immunized subcutaneously with 250 μl of a 1:1 volume emulsion of recombinant MOG_{1-125} (400 μg) and Complete Freund's Adjuvant (Sigma). Pertussis toxin was injected i.p. on Day 0 and Day 2. Animals were scored as described in *SI Appendix, Material and Methods* and analyzed at peak disease three to five days after disease onset with mice scoring 2.5 to 3. Cell isolation from brain and spinal cord as described in *SI Appendix, Material and Methods*.

Statistics. Statistical significance was calculated in Prism 10 software (GraphPad). For pairwise comparisons two-tailed *t* test with Welch's correction was used. For multiple comparisons, one-way ANOVA with Tukey's test was performed. The Wilcoxon nonparametric ranked sum test was used to calculate differences in AUC scores in R. A P-value < 0.05 was considered significant.

Data, Materials, and Software Availability. Single-cell RNA sequencing and Multiome sequencing data have been deposited in BioStudies (S-BSST1322) (81). All study data are included in the article and/or supporting information.

ACKNOWLEDGMENTS. We thank Anne Krug and members of the Schraml lab for helpful discussions and critical reading of the manuscript. We thank members of the Krug and Dudziak laboratories, Malte Benjamin Braun, and Doğuş Altunöz for technical help, and Vasileios Bekiaris for providing *RORγt^{GFP}* mice for migration experiments. We acknowledge the Core Facilities for Flow Cytometry, Bioimaging and Animal Models at the Biomedical Center, LMU Munich for providing equipment and expertise. High-throughput sequencing was performed by the Laboratory for Functional Genome Analysis (LAFUGA) of LMU Munich. The Schraml lab is funded by an ERC Starting Grant (ERC-2016-STG-715182) and by the Deutsche Forschungsgemeinschaft (DFG, German Research Foundation) - TRR 359–Project number 491676693 (projects A01 and B05), SFB 1335/P08–Project number 360372040 and FOR2599 (Project P03, SCHR 1444/2-1). D.D. was supported by the DFG TRR 374/1 2024 TP B07 (Project number 509149993) and DU548/6-1 (Project number 431402787) and BEC by CRC1292/2-TP20 (Project Nr. 318346496) and TRR355/1-A09 (Project Nr. 490846870).

Author affiliations: [a]Institute for Immunology, Biomedical Center Munich, Faculty of Medicine, Ludwig-Maximilians-Universität in Munich, Planegg-Martinsried 82152, Germany; [b]Biomedical Center, Institute of Cardiovascular Physiology and Pathophysiology, Faculty of Medicine, Ludwig-Maximilians-Universität in Munich, Planegg-Martinsried 82152, Germany; [c]Biomedical Center, Physiological Chemistry, Faculty of Medicine, Ludwig-Maximilians-Universität in Munich, Planegg-Martinsried 82152, Germany; [d]Institute for Medical Immunology, Charité Universitätsmedizin Berlin, Corporate Member of Freie Universität Berlin and Humboldt Universität zu Berlin, Berlin 10117, Germany; [e]Section for Experimental and Translational Immunology, Institute for Health Technology, Technical University of Denmark, Kongens Lyngby 2800, Denmark; [f]Institute of Clinical Neuroimmunology, University Hospital, Ludwig-Maximilians-Universität in Munich, Planegg-Martinsried 82152, Germany; [g]Biomedical Center, Medical Faculty, Ludwig-Maximilians-Universität in Munich, Planegg-Martinsried 82152, Germany; [h]Munich Cluster of Systems Neurology (SyNergy), Munich 81377, Germany; [i]Graduate School of Systemic Neurosciences, LMU, Planegg-Martinsried 82152, Germany; [j]Molecular Medicine and Gene Therapy, Lund Stem Cell Centre, Lund University, Lund 221 84, Sweden; [k]Wallenberg Centre for Molecular Medicine at Lund University, Lund 221 84, Sweden; [l]Institute for Molecular Medicine and Research Center for Immunotherapy (Forschungszentrum für Immuntherapie), University Medical Center Johannes Gutenberg-University Mainz, Mainz 55131, Germany; [m]Institute of Medical Microbiology, Rheinisch-Westfälische Technische Hochschule Aachen University Hospital, Aachen 52074, Germany; [n]Department of Pathology and Immunology, Washington University School of Medicine, Saint Louis, MO 63110; [o]Institute of Immunology, Jena University Hospital of the Friedrich-Schiller-University, Jena 07747, Germany; [p]Immunology Section, Lund University, Lund 221 84, Sweden; [q]Calvin, Phoebe and Joan Snyder Institute for Chronic Diseases, University of Calgary, Calgary, AB T2N 1N4, Canada; and [r]Department of Microbiology, Immunology, and Infectious Diseases, Cumming School of Medicine, University of Calgary, Calgary, AB T2N 1N4, Canada

Author contributions: H.N., M.C.-T., and B.U.S. designed research; H.N., N.E.P., C.S., K.R.R., I.U., A.K., C.d.I.R., P.-Y.K., A.A., P.M., S.M., V.K., A.S., E.-L.S., J.P., and N.T. performed research; C.-F.P., L.K. and D.D., M.C., M.W.H., B.E.C., M.K., K.L., C.R. contributed new reagents/analytic tools/scientific input; H.N., M.L.R., R.S., K.R.R., and A.U.A. analyzed data; N.E.P. first observed RORγt+DCs in adult tissues; H.N. and B.U.S. wrote the paper.

The authors declare no competing interest.

This article is a PNAS Direct Submission. H.C. is a guest editor invited by the Editorial Board.

1. M. Guilliams *et al.*, Dendritic cells, monocytes and macrophages: A unified nomenclature based on ontogeny. *Nat. Rev. Immunol.* **14**, 571–578 (2014).
2. M. Cabeza-Cabrerizo, A. Cardoso, C. M. Minutti, M. P. da Costa, C. R. Sousa, Dendritic cells revisited. *Annu. Rev. Immunol.* **39**, annurev-immunol-061020-053707-36 (2021).
3. M. Dalod, S. Scheu, Dendritic cell functions in vivo: A user's guide to current and next- generation mutant mouse models. *Eur. J. Immunol.* **52**, 1712–1749 (2022), 10.1002/eji.202149513.
4. S. K. Wculek *et al.*, Dendritic cells in cancer immunology and immunotherapy. *Nat. Rev. Immunol.* **20**, 7–24 (2020).
5. C. Lehmann *et al.*, Direct delivery of antigens to dendritic cells via antibodies specific for endocytic receptors as a promising strategy for future therapies. *Vaccines* **4**, 8–32 (2016).
6. R. Leylek *et al.*, Integrated cross-species analysis identifies a conserved transitional dendritic cell population. *Cell Rep.* **29**, 3736–3750.e8 (2019).
7. M. Alcántara-Hernández *et al.*, High-dimensional phenotypic mapping of human dendritic cells reveals interindividual variation and tissue specialization. *Immunity* **47**, 1037–1050.e6 (2017).
8. F. B. Sulczewski *et al.*, Transitional dendritic cells are distinct from conventional DC2 precursors and mediate proinflammatory antiviral responses. *Nat. Immunol.* **24**, 1265–1280 (2023), 10.1038/s41590-023-01545-7.
9. P. F. Rodrigues *et al.*, pDC-like cells are pre-DC2 and require KLF4 to control homeostatic CD4 T cells. *Sci. Immunol.* **8**, eadd4132 (2023).
10. N. E. Papaioannou *et al.*, Environmental signals rather than layered ontogeny imprint the function of type 2 conventional dendritic cells in young and adult mice. *Nat. Commun.* **12**, 464 (2021), 10.1038/s41467-020-20659-2.
11. Z. Liu *et al.*, Dendritic cell type 3 arises from Ly6C+ monocyte-dendritic cell progenitors. *Immunity* **56**, 1761–1777.e6 (2023), 10.1016/j.immuni.2023.07.001.
12. C. C. Brown *et al.*, Transcriptional basis of mouse and human dendritic cell heterogeneity. *Cell*, **179**, 846–863.e24 (2019), 10.1016/j.cell.2019.09.035.
13. M. L. Caton, M. R. Smith-Raska, B. Reizis, Notch–RBP-J signaling controls the homeostasis of CD8- dendritic cells in the spleen. *J. Exp. Med.* **204**, 1653–1664 (2007).
14. A. T. Satpathy *et al.*, Notch2-dependent classical dendritic cells orchestrate intestinal immunity to attaching-and-effacing bacterial pathogens. *Nat. Immunol.* **14**, 937–948 (2013).
15. H. Xiao *et al.*, Genomic deletion of Bcl6 differentially affects conventional dendritic cell subsets and compromises Tfh/Tfr/Th17 cell responses. *Nat. Commun.* **15**, 3554 (2024).
16. R. Tussiwand *et al.*, Klf4 expression in conventional dendritic cells is required for T helper 2 cell responses. *Immunity* **42**, 916–928 (2015).
17. K. Lutz *et al.*, Ly6D+Siglec-H+ precursors contribute to conventional dendritic cells via a Zbtb46+Ly6D+ intermediary stage. *Nat. Commun.* **13**, 3456 (2022).
18. C.-A. Dutertre *et al.*, Single-cell analysis of human mononuclear phagocytes reveals subset-defining markers and identifies circulating inflammatory dendritic cells. *Immunity* **51**, 1–26 (2019).
19. U. Cytlak *et al.*, Differential IRF8 transcription factor requirement defines two pathways of dendritic cell development in humans. *Immunity* **53**, 353–370.e8 (2020).
20. M. R. Hepworth *et al.*, Group 3 innate lymphoid cells mediate intestinal selection of commensal bacteria-specific CD4+ T cells. *Science (New York, NY)* **348**, 1031–1035 (2015).
21. F. Teng *et al.*, ILC3s control airway inflammation by limiting T cell responses to allergens and microbes. *Cell Rep.* **37**, 110051 (2021).
22. M. R. Hepworth *et al.*, Innate lymphoid cells regulate CD4+ T-cell responses to intestinal commensal bacteria. *Nature*, **498**, 113–117 (2013), 10.1038/nature12240.
23. M. Lyu *et al.*, ILC3s select microbiota-specific regulatory T cells to establish tolerance in the gut. *Nature* **610**, 744–751 (2022), 10.1038/s41586-022-05141-x.
24. L. Zhou *et al.*, Innate lymphoid cells support regulatory T cells in the intestine through interleukin-2. *Nat. Publish. Group* **12**, 1–23 (2019).
25. W. Zhou *et al.*, ZBTB46 defines and regulates ILC3s that protect the intestine. *Nature* **609**, 159–165 (2022), 10.1038/s41586-022-04934-4.
26. J. G. Castellanos *et al.*, Microbiota-induced TNF-like ligand 1A drives group 3 innate lymphoid cell-mediated barrier protection and intestinal T cell activation during colitis. *Immunity* **49**, 1077–1089.e5 (2018).
27. J. B. Grigg *et al.*, Antigen-presenting innate lymphoid cells orchestrate neuroinflammation. *Nature* **600**, 707–712 (2021).
28. J. Dobeš *et al.*, Extrathymic expression of Aire controls the induction of effective TH17 cell–mediated immune response to Candida albicans. *Nat. Immunol.* **23**, 1098–1108 (2022).
29. R. Kedmi *et al.*, A RORγt+ cell instructs gut microbiota-specific Treg cell differentiation. *Nature* **610**, 737–743 (2022).
30. B. Akagbosu *et al.*, Novel antigen-presenting cell imparts Treg-dependent tolerance to gut microbiota. *Nature* **610**, 752–760 (2022).
31. J. Abramson, J. Dobeš, M. Lyu, G. F. Sonnenberg, The emerging family of RORγt+ antigen-presenting cells *Nat. Rev. Immunol.* **24**, 64–77 (2023), 10.1038/s41577-023-00906-5.
32. G. Eberl, D. R. Littman, The role of the nuclear hormone receptor RORγt in the development of lymph nodes and Peyer's patches. *Immunol. Rev.* **195**, 81–90 (2003).
33. G. Eberl, RORγt, a multitask nuclear receptor at mucosal surfaces. *Mucosal Immunol.* **10**, 27–34 (2017).
34. T. Yamano *et al.*, Aire-expressing ILC3-like cells in the lymph node display potent APC features. *J. Exp. Med.* **216**, 1027–1037 (2019), 10.1084/jem.20181430.
35. J. Wang *et al.*, Single-cell multiomics defines tolerogenic extrathymic Aire-expressing populations with unique homology to thymic epithelium. *Sci. Immunol.* **6**, eabl5053 (2021).
36. J. M. Gardner *et al.*, Extrathymic aire-expressing cells are a distinct bone marrow-derived population that induce functional inactivation of CD4+ T Cells. *Immunity* **39**, 560–572 (2013), 10.1016/j.immuni.2013.08.005.
37. A. U. Antonova *et al.*, A distinct human cell type expressing MHCII and RORγt with dual characteristics of dendritic cells and type 3 innate lymphoid cells. *Proc. Natl. Acad. Sci. U.S.A.* **120**, e2318710120 (2023).
38. N. Torow *et al.*, M cell maturation and cDC activation determine the onset of adaptive immune priming in the neonatal Peyer's patch. *Immunity* **56**, 1220–1238.e7 (2023).
39. J. Kang *et al.*, AXL+SIGLEC6+ dendritic cells in cerebrospinal fluid and brain tissues of patients with autoimmune inflammatory demyelinating disease of CNS. *Clin. Immunol.* **253**, 109686 (2023).
40. J. Ding *et al.*, An esophagus cell atlas reveals dynamic rewiring during active eosinophilic esophagitis and remission. *Nat. Commun.* **15**, 3344 (2024).
41. B. U. Schraml *et al.*, Genetic tracing via DNGR-1 expression history defines dendritic cells as a hematopoietic lineage. *Cell* **154**, 843–858 (2013).
42. G. Eberl, D. R. Littman, Thymic origin of intestinal αβ T cells revealed by fate mapping of RORγt+ cells *Science* **305**, 248–251 (2004).
43. S. Cording *et al.*, Mouse models for the study of fate and function of innate lymphoid cells. *Eur. J. Immunol.* **48**, 1271–1280 (2018).
44. H. J. McKenna *et al.*, Mice lacking flt3 ligand have deficient hematopoiesis affecting hematopoietic progenitor cells, dendritic cells, and natural killer cells. *Blood* **95**, 3489–3497 (2000).
45. A. Baerenwaldt *et al.*, Flt3 ligand regulates the development of innate lymphoid cells in fetal and adult mice. *J. Immunol.* **196**, 2561–2571 (2016).
46. H. Spits *et al.*, Innate lymphoid cells–a proposal for uniform nomenclature. *Nat. Rev. Immunol.* **13**, 145–149 (2013).
47. C. M. Lau *et al.*, Leukemia-associated activating mutation of Flt3 expands dendritic cells and alters T cell responses. *J. Exp. Med.* **63**, jem.20150642-19 (2016).
48. R. Fiancette *et al.*, Reciprocal transcription factor networks govern tissue-resident ILC3 subset function and identity. *Nat Immunol* **22**, 1245–1255 (2021).
49. E. Lindmark *et al.*, AIRE expressing marginal zone dendritic cells balances adaptive immunity and T-follicular helper cell recruitment. *J. Autoimmun.* **42**, 62–70 (2013).
50. K. Aschenbrenner *et al.*, Selection of Foxp3+ regulatory T cells specific for self antigen expressed and presented by Aire+ medullary thymic epithelial cells. *Nat. Immunol.* **8**, 351–358 (2007).
51. A. Gayoso *et al.*, A Python library for probabilistic analysis of single-cell omics data. *Nat. Biotechnol.* **40**, 163–166 (2022).
52. T. S. Consortium *et al.*, The Tabula Sapiens: A multiple-organ, single-cell transcriptomic atlas of humans. *Science* **376**, eabl4896 (2022).
53. R. Elmentaite *et al.*, Cells of the human intestinal tract mapped across space and time. *Nature* **597**, 250–255 (2021).
54. A. R. P. Antunes *et al.*, Single-cell profiling of myeloid cells in glioblastoma across species and disease stage reveals macrophage competition and specialization. *Nat. Neurosci.* **24**, 595–610 (2021).
55. D. Schafflick *et al.*, Integrated single cell analysis of blood and cerebrospinal fluid leukocytes in multiple sclerosis. *Nat. Commun.* **11**, 247 (2020).
56. H. Touil *et al.*, A structured evaluation of cryopreservation in generating single-cell transcriptomes from cerebrospinal fluid. *Cell Rep. Methods* **3**, 100533 (2023).
57. T. K. Vogt, A. Link, J. Perrin, D. Finke, S. A. Luther, Novel function for interleukin-7 in dendritic cell development. *Blood* **113**, 3961–3968 (2009).
58. A. Weckel *et al.*, Long-term tolerance to skin commensals is established neonatally through a specialized dendritic cell subgroup. *Immunity* **56**, 1239–1254.e7 (2023).
59. C. B. González-Blas *et al.*, SCENIC+: Single-cell multiomic inference of enhancers and gene regulatory networks. *Nat. Methods* **20**, 1355–1367 (2023).
60. M. J. Harms *et al.*, PRDM16 binds MED1 and controls chromatin architecture to determine a brown fat transcriptional program. *Genes Dev.* **29**, 298–307 (2015).
61. P. Seale *et al.*, PRDM16 controls a brown fat/skeletal muscle switch. *Nature* **454**, 961–967 (2008).
62. N. von Burg *et al.*, Activated group 3 innate lymphoid cells promote T-cell–mediated immune responses. *Proc. Natl. Acad. Sci. U.S.A.* **111**, 12835–12840 (2014).
63. D. Dudziak *et al.*, Differential antigen processing by dendritic cell subsets in vivo. *Science (New York, NY)* **315**, 107–111 (2007).
64. A. G. López *et al.*, Migration of murine intestinal dendritic cell subsets upon intrinsic and extrinsic TLR3 stimulation. *Eur. J. Immunol.* **50**, 1525–1536 (2020).
65. F. Michetti *et al.*, The S100B protein: A multifaceted pathogenic factor more than a biomarker. *Int. J. Mol. Sci.* **24**, 9605 (2023).
66. S. Columba-Cabezas *et al.*, Suppression of established experimental autoimmune encephalomyelitis and formation of meningeal lymphoid follicles by lymphotoxin β receptor-Ig fusion protein. *J. Neuroimmunol.* **179**, 76–86 (2006).
67. B. P. Pappu *et al.*, TL1A–DR3 interaction regulates Th17 cell function and Th17-mediated autoimmune disease. *J. Exp. Med.* **205**, 1049–1062 (2008).
68. A. Liston *et al.*, Inhibition of CCR6 function reduces the severity of experimental autoimmune encephalomyelitis via effects on the priming phase of the immune response. *J. Immunol.* **182**, 3121–3130 (2009).
69. C. Feng *et al.*, Docosahexaenoic acid ameliorates autoimmune inflammation by activating GPR120 signaling pathway in dendritic cells. *Int. Immunopharmacol.* **97**, 107698 (2021).
70. C. Gutiérrez-Vázquez, F. J. Quintana, Regulation of the immune response by the aryl hydrocarbon receptor. *Immunity* **48**, 19–33 (2018).
71. M. Gargaro *et al.*, Indoleamine 2,3-dioxygenase 1 activation in mature cDC1 promotes tolerogenic education of inflammatory cDC2 via metabolic communication. *Immunity* **55**, 1032–1050.e14 (2022).
72. L. Fu *et al.*, RORγt-dependent antigen-presenting cells direct regulatory T cell–mediated tolerance to food antigen. bioRxiv [Preprint] (2024), 10.1101/2024.07.23.604803 (Accessed 20 August 2024).
73. A. Rudnitsky, H. Oh, J. Talmor, R. Kedmi, Coordinated network of T cells and antigen presenting cells regulate tolerance to food. bioRxiv [Preprint] (2024), 10.1101/2024.07.11.603064 (Accessed 20 August 2024).
74. Y. F. Parisotto *et al.*, Thetis cells induce food-specific Treg cell differentiation and oral tolerance. bioRxiv [Preprint] (2024), 10.1101/2024.05.08.592952 (Accessed 20 August 2024).
75. J. L. Gommerman, J. L. Browning, C. F. Ware, The lymphotoxin network: Orchestrating a type I interferon response to optimize adaptive immunity. *Cytokine Growth Factor Rev.* **25**, 139–145 (2014).
76. L. Zeitler, P. J. Murray, IL4i1 and IDO1: Oxidases that control a tryptophan metabolic nexus in cancer. *J. Biol. Chem.* **299**, 104827 (2023).
77. I. M. de Kleer *et al.*, Perinatal activation of the interleukin-33 pathway promotes type 2 immunity in the developing lung. *Immunity* **45**, 1285–1298 (2016).
78. J. Nah, Y. Lee, R. H. Seong, PRDM16 regulates γδT17 cell differentiation via controlling type 17 program and lipid-dependent cell fitness. *Front. Immunol.* **14**, 1332386 (2024).
79. Y. Hasegawa *et al.*, Repression of adipose tissue fibrosis through a PRDM16-GTF2IRD1 complex improves systemic glucose homeostasis. *Cell Metab.* **27**, 180–194.e6 (2018).
80. K. O. Gudmundsson *et al.*, Prdm16 is a critical regulator of adult long-term hematopoietic stem cell quiescence. *Proc. Natl. Acad. Sci. U.S.A.* **117**, 31945–31953 (2020).
81. H. Narasimhan, M. Richter, B. Schraml, Data from "RORγt-expressing dendritic cells are functionally versatile and evolutionarily conserved antigen presenting cells". Biostudies. http://www.ebi.ac.uk/biostudies/studies/S-BSST1322. Deposited 31 January 2025.

PNAS

Supporting Information for

RORγt-expressing dendritic cells are functionally versatile and evolutionarily conserved antigen presenting cells

Authors: Hamsa Narasimhan, Maria L. Richter, Ramin Shakiba, Nikos E. Papaioannou, Christina Stehle, Kaushikk Ravi Rengarajan, Isabel Ulmert, Arek Kendirli, Clara de la Rosa, Pin-Yu Kuo, Abigail Altman, Philipp Münch, Saba Mahboubi, Vanessa Küntzel, Amina Sayed, Eva-Lena Stange, Jonas Pes, Alina Ulezko Antonova, Carlos-Filipe Pereira, Ludger Klein, Diana Dudziak, Marco Colonna, Natalia Torow, Mathias W. Hornef, Björn E. Clausen, Martin Kerschensteiner, Katharina Lahl, Chiara Romagnani, Maria Colomé-Tatché, Barbara U. Schraml*

* Correspondence: Barbara.schraml@bmc.med.lmu.de

This PDF file includes:

Supporting Information Text

SI Materials and Methods

Mice

Tg(*Rorc*-EGFP)1Ebe (1), C57BL/6-*Flt3l*$^{tm1Imx/TacMmjax}$ (MMRRC Stock No:37395-JAX), OTII mice (Tg(TcraTcrb)425Cbn; Jackson Laboratory Stock No: 004194) crossed to a Thy1.1 (CD90.1) background, *Clec9a*$^{tm2.1(icre)Crs}$ (Jackson Laboratory Stock No: 025523), Gt(ROSA)26Sor$^{tm9(CAG-tdTomato)Hze}$ (*Rosa26*$^{lox-STOP-lox-tdtomato}$) (Jackson Laboratory Stock No: 007909), C57BL/6JRccHsd, CD45.2 *Aire*$^{-/-}$, and CD45.1 BALB/c mice were bred and maintained at the Biomedical Center, LMU, Munich. *Rag2*$^{-/-}$*Il2rg*$^{-/-}$*, Rorc(γt)*$^{GFP/wt}$ (2) crossed to *Rorc(γt)*cre (3) and *Rosa26*^{YFP} mice were bred and maintained at the Federal Institute for Risk Assessment (Berlin, Germany) and the Research Institute for Experimental Medicine (FEM) of the Charité (Berlin, Germany). *RORγt*^{GFP}*RORγt*^{Cre}*Rosa26*^{RFP} were a gift from Vasileios Bekiaris and bred and maintained at the Technical University of Denmark BioFacility. hCD2^{iCre} (4) mice crossed to Rosa^{YFP} reporter mice were bred and maintained in Lund University. All mice were housed under specific pathogen free conditions, with a 12 h dark/light cycle, in individually vented cages. Food and water were provided *ad libitum*. Both female and male mice were used in this study. Age and sex-matched mice were used for experiments. In most experiments littermates were used. All animal procedures were performed in accordance with national and institutional guidelines for animal welfare and approved by the Regierung of Oberbayern, Landesamt für Gesundheit und Soziales, the Landesuntersuchungsamt Rheinlandpfalz or the Danish Animal Experiments Inspectorate.

Cell isolation for flow cytometry

Spleens were cut into small pieces and enzymatically digested in 1mL RPMI containing 200 U/mL Collagenase IV (Worthington) and 0.2 mg/mL DNaseI (Roche, 11284932001) for 30 minutes at 37°C while shaking at 180 rpm. Digested suspensions were passed through a 70 μm strainer and washed with FACS buffer (PBS, 1% fetal calf serum (FCS), 2.5 mM EDTA, 0.02% sodium azide). Erythrocytes were then lysed with Ammonium-chloride-potassium (ACK) lysis buffer (1 mM EDTA, 1.55 M NH_4Cl, 100 mM $KHCO_3$, filtered) for two minutes at room temperature (RT) followed by a wash with FACS buffer. Cell pellets were resuspended in FACS buffer for further analysis.

Mesenteric lymph nodes (mLN) from 2-3 one-week old mice were pooled prior to processing. For all other timepoints mLN from individual mice were processed. Tissue was processed as above but

without erythrocyte lysis. Axillary, brachial, inguinal, and cervical skin draining lymph nodes from adult mice were enzymatically digested in 1 mL of RPMI with 200 U/mL Collagenase IV (Worthington) and 0.2 mg/mL DNaseI (Roche) for 30 minutes at 37 °C while shaking at 180 rpm. Digested samples were passed through 70 μm strainer, washed and resuspended in FACS buffer for further analysis.

Small intestines (SI) were isolated and flushed with ice-cold wash medium (Hank's Balanced Salt solution (HBSS), 5 mM EDTA, 5% FCS, 10 mM HEPES, without calcium or magnesium). For mice 3 weeks or older, Peyer's patches were then removed. Intestines from mice younger than 3 weeks were cut open with a scalpel and washed in ice cold PBS. SI from one-day old mice were pooled by 2-3. Tissues were cut into pieces and incubated in wash medium and 1 mM dithiothreitol (DTT) for 30 minutes at 37°C with shaking (180 rpm). Supernatant containing epithelial cells and intraepithelial lymphocytes was discarded. Samples were then washed with digestion medium (HBSS with Calcium and Magnesium, 5% FCS and 10 mM HEPES) and then cut to smaller pieces for enzymatic digestion. Samples were then digested in 3 mL digestion medium containing 400 U/mL Collagenase IV (Worthington) and 0.4 mg/mL DNaseI (Roche, 11284932001), for 30 minutes at 37 °C with shaking (180 rpm). Digested samples were passed through 100 μm strainer and washed with gut medium (RPMI with 1% Glutamine, 1% Penicillin/Streptomycin, 10% FCS, 10 mM HEPES, and 50 μM β-Mercaptoethanol). Supernatant was removed by suction with vacuum pump. Leukocytes were enriched by 70%-37%-30% Percoll (Sigma Aldrich) gradient centrifugation (2000 rpm, RT, 30 minutes, Accel=3, Decel=0).). Cells were collected from the 70%-37% interphase and washed once in gut medium and resuspended in FACS buffer (without sodium azide) for further analyses.

For lung isolation mice were perfused with ice cold PBS. Lungs from mice younger than 3 weeks were isolated without perfusion. Tissue was minced and enzymatically digested in 1 mL RPMI containing 200 U/mL Collagenase IV (Worthington) and 0.2 mg/mL DNaseI (Roche) for 1 hour at 37 °C with shaking (180 rpm). Digested tissue was passed through a 70 μm strainer and washed with FACS buffer. Leukocytes were enriched by gradient centrifugation as above.

OTII enrichment

Spleens from OTII mice were collected in 1 mL RPMI, mechanically disrupted and passed through a 70 μm strainer and washed with FACS buffer without sodium azide ((PBS, 1% fetal calf serum (FCS), 2.5 mM EDTA). Naïve $CD4^+$ OTII cells were isolated using MojoSort™ mouse CD4 Naïve T Cell Isolation Kit (BioLegend) according to the manufacturer's instructions. OTII cells were

labelled with CellTrace™ Violet (CellTrace™ Violet Cell Proliferation Kit, Invitrogen) according to the manufacturer's recommendations.

Flow cytometry

Cells were first incubated with 50 µL purified anti-mouse CD16/32/FcBlock (BD Pharmingen, Cat No. 553142) for 10 minutes at 4°C in 96-well v-bottom plates. Next, cell surface epitopes were stained for 30 minutes at 4°C by addition of 50 µL antibodies in a 2X mastermix (total staining volume of 100 µL). Fixable Viability Dye eFluor 780 (Thermo Fisher Scientific) was added at this step. To preserve GFP signal after intranuclear staining, cells were pre-fixed with 2% paraformaldehyde at RT for 15 min. Intracellular staining for cytokines was performed using Intracellular Fixation & Permeabilization Buffer Set and for transcription factors with the FOXP3 Transcription Factor Staining Set (both Thermo Fisher Scientific) according to the manufacturer's instructions after staining for surface epitopes. Anti-RORC staining was performed for 1 hour at RT. Cells were quantified using CountBright™ Absolute Counting Beads (Thermo Fisher Scientific). Flow cytometry data was collected using LSR Fortessa (BD Biosciences) and analyzed using FlowJo software V10.8.1 (Tree Star). Antibodies used for flow cytometry are provided in Materials and methods Table1 below.

Cell sorting

For sorting of APC populations splenocytes were depleted of T cells (CD3e), B cells (CD19), Neutrophils (Ly6G) and Erythroid cells (Ter119) by staining with FITC-conjugated antibodies followed by anti-FITC magnetic bead negative selection with LS columns (both Miltenyi) according to the manufacturer's instructions. Cells were stained in total volume of 600 µL in 50 mL conical tubes. For in vitro coculture assays PBS + 10% FCS was used as collection medium. Cells for single cell multiome analyses were collected in complete RPMI (1% L-Glutamine, 1% Penicillin/Streptomycin, 10% FCS, 1% Sodium Pyruvate, 0.1% β-Mercaptoethanol and 1% non-essential amino acids). Cell sorting was performed using BD FACSAria Fusion (BD Biosciences). Antibodies used for sorting are provided in Materials and Methods Table1 below.

Sorting from neonatal small intestine for scRNA-seq: Single cell suspensions from small intestines from one-day old (n=5, pooled as 2 and 3 for processing) and nine-day old (n=3) *Clec9a*^{Cre} *Rosa*^{TOM} mice were generated. Cells from each timepoint were stained with TotalSeq^{TM} anti-mouse Hashtag antibodies (BioLegend) when staining for cell surface epitopes. Live CD45^{+}

singlets, CD19$^-$ CD90.2$^-$ CD11c$^+$ MHCII$^+$ cells were sorted from each timepoint and pooled in a 1:1 ratio for sequencing using the 10X Genomics Chromium Next GEM Single Cell 3' v3.1 (Dual Index) with Feature Barcode Technology for Cell Surface Protein protocol.

In vitro T cell proliferation

MHCII$^+$ ILC3, cDC2, and RORγt$^+$ DCs were sorted as described above (gating strategy Fig S11a). 250 cells from each population were pulsed with 10 μg/mL Ovalbumin peptide ($OVA_{323-339}$, Invivogen) in a 96-well v-bottom plate for 3 hours, then washed and resuspended in complete RPMI (cRPMI; 1% L-Glutamine, 1% Penicillin/Streptomycin, 10% FCS, 1% Sodium Pyruvate, 0.1% β-Mercaptoethanol and 1% non-essential amino acids) and co-cultured with 2500 naïve CTV-labelled OTII cells at a 1:10 ratio. Cultures were supplemented with 5 ng/mL TGF-β, 10 μg/mL anti-IL-4, and 10 μg/mL anti-IFNγ for Treg polarization, and 5 ng/mL TGF-β, 20 ng/mL IL-6, 10 μg/mL anti-IL-4, and 10 μg/mL anti-IFNγ (all Biolegend) for Th17 polarizing condition. Cells were cultured in a total volume of 200 μL. After 3.5 days of culture at 37°C, supernatant was collected from all samples, following which cells were restimulated with 10 ng/mL phorbol 12-myristate 13-acetate (PMA) (Calbiochem) and 1 μg/mL Ionomycin (Sigma-Aldrich) for a total of 5 hours. 2 hours after start of restimulation 5 μg/mL of Brefeldin A (BioLegend) was added to each well for the remaining 3 hours. Cytokines and FOXP3 were detected by intranuclear staining as described above.

In vivo targeting

Adult *RORγt^{GFP}* mice were injected intraperitoneally (i.p.) with 10 μg anti-CLEC4A4-OVA or 10 μg OVA-coupled-isotype matched control antibody as described (5) plus 0.2 μg/g body weight of CpG-B ODN 1826 (InvivoGen). 12 hours later 300 cDC1, cDC2, and RORγt$^+$ DCs were sort-purified from spleens and co-cultured with 3000 naïve CTV-labelled OTII cells in cRPMI. 3.5 days later OTII proliferation was assessed by flow cytometry.

R848 treatment

10-day old *RORγt^{GFP}* mice were orally gavaged with 2 μg R848 (Invivogen) in 50 μL PBS or received 50 μL PBS as control. 24 hours later organs were isolated and processed as above.

Single cell multiome sequencing of RORγt$^+$ DCs, cDCs and ILC3s

MHCII$^+$ ILC3, CD11c$^+$MHCII$^+$ DC and RORγt$^+$ DCs were sorted from of 2-week-old (P13, n=2) or adult (8-week-old, n=3) *RORγt^{GFP}Clec9a$^{cre/wt}$Rosa26$^{Tom/wt}$* mice into cRPMI as described above. EDTA-free buffer was used in all steps for processing of spleen tissue. For each timepoint, cells were pooled in a ratio of approx. 1:1:10 (RORγt$^+$ DCs: MHCII$^+$ ILC3: CD11c$^+$ MHCII$^+$ DC) and nuclei were isolated following the 10X Genomics Low Cell Input Nuclei Isolation protocol. Briefly, 20,000 cells of mixture were lysed for 3 minutes on ice and resuspended in diluted Nuclei Buffer. Lysis efficiency and nucleus quality were assessed after trypan blue staining by microscopy. 8400 nuclei for the adult timepoint and 10,400 nuclei for the 2-week timepoint were loaded for transposition. Gene expression and ATACseq libraries were prepared with the 10X Genomics Chromium Next GEM Single Cell Multiome ATAC + Gene Expression Kit according to the manufacturer's instructions. Concentration and purity of the libraries were analyzed at the required steps with a Agilent TapeStation. Libraries from each timepoint were pooled and sequenced together in accordance with 10X Genomics recommended sequencing depth, using NextSeq1000/2000.

Multiome computational analysis

Alignment: *Cell Ranger ARC v2.0.2* was used to map the multiome reads against the mm10 reference genome customized to include sequences for *eGFP*, and *tomato*.

Gene expression analyses: The raw reads of the 2-week and the adult samples were combined and genes that were present in fewer than 5 cells were removed. Cells were included if they had between 500 and 5,000 genes detected, fewer than 30,000 counts and less than 1% mitochondrial reads. Library size normalization was done using *scran* before log-transforming the counts. Cell cycle analysis was done in *Scanpy.* Initial Leiden clustering was performed at resolution of 0.5 and expression of marker genes and scoring based on published signatures for cell types (*SI* Table S1) was used to annotate the clusters. Based on marker gene expression, cluster 7 was re-clustered at resolution of 0.05 to separate migDCs from eTACs and cluster 3 was re-clustered at resolution of 0.1 to separate tDCs from cDC2s. Clusters were compared between RNA and ATAC to focus on the cellular subtypes that were identifiable from both omics. Differential expression analysis was performed between groups of interest using *Scanpy's sc.tl.rank_genes_groups* on all genes. Significantly differentially expressed genes were defined by having an adjusted p-value below 0.05 and an absolute $\log_2$-fold change greater than 0.5. Gene set enrichment analysis was done using *gseapy* (6).

ATAC analyses: The bam files output by Cell Ranger ARC were merged for the 2-week and adult sample and peaks were called using *macs3.* Count matrices were built for the 2-week and adult sample using *epiScanpy's epi.ct.peak_mtx* function with the fragment files and the combined peak set as input. After combining 2-week and adult, the counts were binarized and nuclei having between 4,000 and 25,000 peaks were kept. Furthermore, cells with nucleome signal above 2 and TSS-enrichment score below 0.5 were removed. Peaks were removed if they were present in fewer than 2 cells. Highly variable peaks were selected using *epi.pp.highly_variable* with *min_score=0.53.* Initial Leiden clustering was performed at resolution of 0.5. RNA labels were transferred to the ATAC cells and clustering was refined to yield similar clusters between both omics. Some clusters showed sample-wise separation based on gene expression, which could not be observed in the ATAC. Apart from these RNA-specific subclusters, only those clusters present in both RNA and ATAC were further considered. Differential chromatin openness was also performed using *Scanpy's sc.tl.rank_genes_groups* on all peaks. Significantly differentially open peaks were defined by having an adjusted p-value below 0.05 and an absolute $\log_2$-fold change greater than 0.5. In addition to the count matrix on peaks, a count matrix was built similarly on known transcription factor binding sites (TFBS), obtained from https://remap2022.univ-amu.fr/. In this matrix, cells were kept if they had between 4,000 and 50,000 TFBS and TFBS were removed if they were present in fewer than 10 cells. Highly variable TFBS were selected using *epi.pp.highly_variable* with *min_score=0.51.* Cell labels from the gene expression and the peak matrix were transferred to the TFBS matrix and Leiden clustering was performed to annotate the same cell types as for the peak matrix. Finally, the counts were summed up per cell for all binding sites of each unique transcription factor. For the visualization of chromatin openness between cell types at specific regions of interest, we followed the blog post of Andrew John Hill (http://andrewjohnhill.com/blog/2019/04/12/streamlining-scatac-seq-visualization-and-analysis/).

SCENIC+ analyses

To combine the information of gene expression and chromatin openness, SCENIC+ was used(7). For this analysis, we followed the SCENIC+ tutorial on analyzing PBMC multiome data from 10X Genomics (https://scenicplus.readthedocs.io/en/latest/pbmc_multiome_tutorial.html#Tutorial:-10x-multiome-pbmc). For the cistopic part of SCENIC+, 48 topics were chosen. In SCENIC+, only eRegulons with a positive correlation between transcription factor expression and target region openness were considered. Visualization was performed as described in the tutorial and network graphs were modified in Cytoscape 3.10.1.

Mouse scRNA-seq analyses

Annotated sequencing data from scRNAseq in Lyu et al. (8) was downloaded from GEO: GSE184175; annotated gene expression data from single cell multiome sequencing in Akagbosu et al. (9) was downloaded from GEO: GSE174405. Without any further processing, expression of signature genes for RORγt$^+$ DCs for the different annotated cell types in each dataset was plotted.

Raw gene expression matrices of scRNAseq in Wang et al. (10) were downloaded from GEO: GSE176282 and analyzed using the Seurat package in R. Doublets were identified using the scDblFinder package and subsequently removed. Cells expressing less than 750 unique genes, or with a mitochondrial gene content higher than 5% were also removed. The SCTransform function was used to scale and normalize the data. After dimensional reduction, unsupervised clustering resulted in 23 clusters. Cell types were identified using the genes provided in Fig. S2 of the original publication (10) and equivalent populations could be identified. Expression of signature genes for RORγt$^+$ DCs was plotted for the different cell types.

Raw gene expression matrices of the CITE-seq dataset in Kedmi et al. (11) were downloaded from GEO: GSE200148 and analyzed in R using the Seurat package. Cells from both tdTomato-ON^{CD11c} and tdTomato-ON^{RORγt} x *Zbtb46*-EGFP mice were combined into one workspace. Doublets were removed using the scDblFinder package. Cells with more than 750 unique genes or with a mitochondrial gene content lower than 5% were included for further processing. The SCTransform function was used to scale and normalize the data. After dimensional reduction, unsupervised clustering resulted in 23 clusters which were filtered to only retain cell types included in original publication (11).The filtered dataset was re-scaled and dimensional reduction and unsupervised clustering then resulted in 18 clusters, which were identified by the expression of marker genes used for annotation in Fig. S3d of the original publication. Expression of signature genes for RORγt$^+$ DCs was plotted for the different cell types.

Human scRNA-seq analyses

Raw sequencing data GEO: GSE137710 (12) was downloaded. Cells with more than 6000 total RNA fraction and a mitochondrial gene content of less than 7% were isolated. Normalization, scaling, and dimensional reduction of filtered raw counts was performed using the Seurat v4 package. Unsupervised clustering was performed with a resolution of 0.9 resulting in 11 clusters which were identified by the expression of marker genes. Cells annotated as CD1c$^+$ myeloid dendritic cells, CD141$^+$ myeloid dendritic cells, innate lymphoid cell and plasmacytoid dendritic cells from the spleen scRNA-seq data from the Tabula Sapiens Consortium (13) were reclustered.

Normalization, scaling, and dimensional reduction was performed using Seurat v4. Unsupervised clustering at resolution 1.4 resulted in 7 clusters, which were classified by the expression of marker genes.

The published normalized and log-transformed scRNA-seq data from the Gut Cell Atlas (14) was analyzed using *Scanpy*. Cells annotated as derived from healthy adult donors and annotated as lymphoid DC, cDC1, cDC2 and pDC were selected for further analysis. After dimensionality reduction, unsupervised clustering was performed at a resolution of 1.5. The resulting cluster 0, which contained $XCR1^+$ cDC1 and $ZFP36L2^+$ cDC2 was subclustered at a resolution of 0.4 to better reflect the DC subset heterogeneity. The resulting 13 clusters were identified by expression of marker genes. Cells derived from paediatric healthy donors or donors with Crohn's diagnosis annotated as lymphoid DC, cDC1, cDC2 and pDC were selected for further analyses. Post dimensionality reduction, unsupervised clustering was performed at a resolution of 1.6. The resulting 13 clusters were identified by expression of marker genes.

The Tabula Sapiens Lymph Node dataset was analysed using *Scanpy*. After normalization and log-transformation of the data, cells annotated as $CD1c^+$ myeloid DC, $CD141^+$ myeloid DC, conventional DC, hematopoietic stem cell, innate lymphoid cell and plasmacytoid DCs were selected for further analysis. After performing dimensionality reduction, unsupervised clustering at a resolution of 1.0 resulted in 15 clusters which were identified by expression of marker genes.

After pre-processing in *Scanpy,* the above datasets were converted to Seurat objects and further processed using Seurat v4 package. Genes expressed in more than 20% of cells and with an adjusted p-value <0.05 and log2_FC > 0.4 were considered for differential gene expression analyses. To score cells for enrichment of specific gene signatures, the AUCell package was used. Signatures from the mouse single cell multiome analyses were converted to human orthologs using the Orthogene package prior to scoring. Integration of the two human spleen datasets was performed according to the standard Seurat Integration workflow. Both datasets were normalized by SCTransform before finding integration features and integration anchors. Subsequently, dimensional reduction was performed to display cells from both datasets in the same low-dimensional space.

Raw sequencing data from GSE194078 (15) were downloaded and analysed using the Seurat Package. The CSF sample from one patient (ID: YYS; Disease: Ab-mediated IDD) was excluded because of low cell numbers. From the remaining 10 CSF samples cells expressing less than 750 unique genes and cells with a mitochondrial gene content above 20% were excluded. The normalized count data was integrated using Harmony. Unsupervised clustering of the integrated

dataset resulted in 22 clusters, which were annotated by expression of marker genes. Myeloid cells present in the dataset were reclustered and all DC subtypes as well as monocytes and microglia were identified. The raw gene expression matrices and cell type annotations from GSE163120 (16) and GSE234069 (17) were downloaded. Cells originally annotated as DC were analysed using the Seurat Package in R re-annotated based on expression of marker genes. RORγt$^+$ DCs were identified based on high enrichment score for RORγt$^+$ DCs. The annotated dataset from https://figshare.com/ndownloader/files/27405182 (18) was downloaded and cells annotated as "mDC1", "mDC2", "pDC", and "Mono" from CSF samples only were reclustered and annotated based on expression of marker genes. ACY3$^+$ DCs, which were re-annotated as RORγt$^+$ DCs were identified based on high enrichment score for RORγt$^+$ DCs.

Neonatal murine small intestinal scRNA-seq analyses

Sequencing data were processed using 10X Genomics Cell Ranger v6.0.0 pipeline using default parameters. The resulting count matrix was loaded into R (v4.3.2) and downstream analyses were performed using Seurat v4 and v5. We removed genes detected in less than 3 cells from further analysis and only included cells with less than 5% mitochondrial gene content, or between 1500 and 6000 different genes detected per cell. Hash Tag Oligo (HTO) information was integrated and HTO demultiplexing was performed per Seurat workflow, excluding cells marked as doublets. A second round of doublet exclusion was performed using the DoubletFinder package (https://github.com/chris-mcginnis-ucsf/DoubletFinder). The resulting Seurat object contained 1391 cells consisting of 662 cells belonging to P1 timepoint and 729 cells belonging to the P9 timepoint. Cell cycle state was scored based on published cell cycle gene lists (https://satijalab.org/seurat/articles/cell_cycle_vignette). SCTransform package was used for scaling, normalization, and cell cycle regression. The first 60 Principal Components were used for dimensional reduction using UMAP. Unsupervised clustering was performed with a resolution of 1.5. *FindAllMarkers* function of Seurat was used to calculate differentially expressed genes between the clusters.

Integration of datasets

The indicated published datasets were downloaded from GEO: GSE184175, GSE174405, GSE176282, and GSE200148 and the original cell type annotation used except for GSE200148 (11) and GSE176282 (10), which were annotated analogous to the original publications as described above. For easier integration and higher comparability between datasets we grouped cell

types into broad categories, e.g. subgroups of T cells only described in one dataset (8) were combined into one T cell cluster, B cell subgroups into a B cell cluster and so forth. Furthermore, cell types that were present in only one of the datasets were removed to facilitate the integration task. The raw datasets were combined into an AnnData object. On the combined data, cells were included if they had between 1000 to 50,000 counts and if they had between 500 genes and 6000 genes. Any cells outside these ranges were excluded. Genes were removed if they were detected in under 5 cells. Scanpy's *sc.pp.highly_variable_genes* was used with the datasets as batch variable to select the top 2000 variable genes for integration. Finally, scVI was used for unsupervised integration, following the tutorial https://docs.scvi-tools.org/en/stable/tutorials/notebooks/scrna/harmonization.html. For visualization, UMAPs were calculated on the scVI embedding. Additionally, Leiden clustering was performed on the scVI embedded cells at resolution 0.2, resulting in 10 clusters closely corresponding to the originally annotated broad cell types across datasets (exceptions: ILC2 clustered with T-cells, LTi-ILC3 and ILC3 were together in one cluster, proliferating DC clustered with pDC, and Mac clustered with cDC2). As shown in Fig. 2j, the "RORγt$^+$ DC" cluster contained *Rorc*$^+$ or *Aire*$^+$ APC populations annotated distinctly in various publication as well as the RORγt$^+$ DCs and RORγt$^+$ eTACs reported in this publication. To further validate how well the Leiden clusters represented the reported cell types, the percentage of cells from a given cell type in each Leiden cluster was calculated and visualized in a heatmap. Additionally, the ARI score between the broad cell type annotation based on the original publications and the Leiden clusters on the integrated datasets was calculated. This resulted in a score of 0.64.

Bone Marrow Chimeras

CD45.1/2 congenic BALB/C mice were irradiated (2 × 350 rad, 4 hours apart) and then reconstituted with 1:1 mixture of CD45.1 WT and CD45.2 *Aire*$^{-/-}$ bone marrow. Bone marrow cells were depleted with antibodies against CD4, CD8, CD19 and NK1.1 using magnetic beads before transfer. Each mouse was reconstituted with 4 x 10^6 total bone marrow cells and analyzed 7 weeks later.

EAE induction

Active EAE was induced in 12-week-old male C57BL/6 mice by immunizing them with 250 µl of a 1:1 volume emulsion of in-house-purified recombinant MOG1-125 (400 µg) and Complete Freund's Adjuvant (Sigma) containing 10mg/ml Mycobacterium tuberculosis (BD Difco), injected

subcutaneously at the flanks and the base of the tail. Pertussis toxin (Sigma) dissolved in 100 µl of PBS (350 ng) was administered intraperitoneally (i.p.) on Day 0 and Day 2 post-immunization. Animals were scored daily for weight loss and as follows for clinical symptoms: 0, no clinical signs; 0.5, partial tail weakness; 1, tail paralysis; 1.5, gait instability or impaired righting ability; 2, hind limb paresis; 2.5, hind limb paresis with dragging of at least one foot; 3, total hind limb paralysis; 3.5, hind limb paralysis and forelimb paresis; 4, hind limb and forelimb paralysis; 5, death. The first day of a clinical score above zero was considered as onset, with analysis three to five days post onset at peak of disease with mice scoring as 2.5 – 3 for clinical symptoms.

Tissue isolation from EAE animals

Animals with EAE clinical signs were sacrificed and perfused with PBS-heparin. Spinal cord and brain cortex were isolated through microdissection. Spinal cord and brain tissues were homogenized with a glass dounce homogenizer (Wheaton) with loose pestle, transferred into a PBS solution containing Collagenase D (0.8 mg/ml, Roche) and DNase I (10 ng/ml, Roche) and incubated for 30 minutes at 37°C with shaking (1000 rpm) for dissociation of cells. Cell suspensions were passed through a 100 µm pore diameter cell strainer (Corning). Cells from spinal cord and brain were isolated with Percoll (Sigma) gradient to remove the myelin. Cells were resuspended with 1 ml of 100% FBS and 9 ml of 33% Percoll (in PBS), and 1ml of 10% FBS (in PBS) was added on the top slowly to form a layer. Samples were centrifuged without brake at 800 g for 30 minutes at 4°C. The myelin layer was carefully sucked with vacuum and pelleted cells were washed with PBS to remove the Percoll solution.

Statistical analyses

Statistical significance was calculated in Prism 10 software (GraphPad). For pairwise comparisons two-tailed t-test with Welch's correction was used. For multiple comparisons, one-way analysis of variance with Tukey's test was performed. Wilcoxon non-parametric ranked sum test was used to calculate differences in AUCscores in R. A p-value <0.05 was considered significant.

Materials and Methods Table1

Antibodies used for flow cytometry	Clone	Vendor	Catalog number
anti-CD3ε FITC	145-2C11	BioLegend	100306
anti-CD3ε PE	145-2C11	eBioscience	12-0031-83
anti-CD4 APC	GK1.5	BioLegend	100412
anti-CD8a BV605	53-6.7	BioLegend	100744
anti-CD11b BV421	M1/70	BioLegend	101236
anti-CD11b BUV737	M1/70	BD Biosciences	612800
anti-CD11b AF700	M1/70	Invitrogen	56-112-82
anti-CD11c BV421	N418	BioLegend	117330
anti-CD11c BV650	N418	BioLegend	121113
anti-CD11c BV785	N418	BioLegend	117336
CD16/CD32 (2.4G2) FcBlock	2.4G2	BD Biosciences	553142
anti-CD19 FITC	6D5	BioLegend	115506
anti-CD24 BUV395	M1/69	BD Biosciences	744471
anti-CD25 BV785	PC61	BioLegend	102051
anti-CD40 PE	3/23	BioLegend	124610
anti-CD45.1 PB	A20	BioLegend	110722
anti-CD45.1 AF647	A20	BioLegend	110720
anti-CD45.2 BUV395	104	BD Biosciences	564616
anti-CD45.2 PB	104	BioLegend	109820
anti-CD45.2 FITC	104	BioLegend	109806
anti-CD45.2 PE Cy7	104	BioLegend	109830
anti-CD45R/B220 PB	RA3-6B2	BioLegend	103227
anti-CD45R/B220 FITC	RA3-6B2	BioLegend	103206
anti-CD45R/B220 PE	RA3-6B2	BioLegend	103208
anti-CD45R/B220 AF647	RA3-6B2	BioLegend	103226
anti-CD62L PE Cy7	MEL-14	Tonbo Biosciences	60-0621-U100
anti-CD64 (FcɤRI) PE	X54-5/7.1	BioLegend	139304
anti-CD64 (FcɤRI) PE Cy7	X54-5/7.1	BioLegend	139314
anti-CD64 (FcɤRI) APC	X54-5/7.1	BioLegend	139306
anti-CD80 PE	16-10A1	BioLegend	104707
anti-CD83 APC	Michel-19	BioLegend	121508
anti-CD86 BV605	GL-1	BioLegend	105037
anti-CD90/CD90.1 AF700	OX-7	BioLegend	202528
anti-CD90.2 PE Cy7	30-H12	BioLegend	105320
anti-CD90.2 AF700	30-H12	BioLegend	105326

anti-CD103 BUV395	M290 (RUO)	BD Biosciences	740238
anti-CD103 PE	2E7	BioLegend	121406
anti-CD127 (IL-7Rα) PE Cy5	A7R34	eBioscience	15-1271-81
anti-CD127 (IL-7Rα) BUV737	SB/199	BDBiosciences	564399
anti-CD135 PE	A2F10	BioLegend	135306
anti-CD172a (SIRPα) PE Cy7	P84	BioLegend	144008
anti-CD172a (SIRPα) PerCP ef710	P84	eBioscience	46-1721-82
anti-CD186 (CXCR6) APC	DANID2	eBioscience	17-9186-82
anti-CD196 (CCR6) BV421	29-2L17	BioLegend	129817
anti-CD197 PE	4B12	BioLegend	120105
anti-CD197 BV650	4B12	BioLegend	120137
anti-CD200 (OX2) PE Cy7	OX-90	BioLegend	123817
anti-CD205 (DEC205) PE Cy7	NLDC-145	BioLegend	138209
anti-CD205 (DEC205) APC	NLDC-145	BioLegend	138206
anti-CD274 (PD-L1) BV421	10F.9G2	BioLegend	124315
anti-CD275 (ICOSL) PE	HK5.3	BioLegend	107405
anti-CD326 (EpCAM) BV650	G8.8	BioLegend	118241
anti-F4/80-BV605	BM8	BioLegend	123133
anti-F4/80-BV785	BM8	BioLegend	123141
anti-F4/80-AF647	BM8	BioLegend	123122
anti-F4/80-APC Cy7	BM8	BioLegend	123117
anti-I-A/I-E (MHCII) PE	M5/114.15.2	eBioscience	12-5321-82
anti-I-A/I-E (MHCII) AF700	M5/114.15.2	BioLegend	107622
anti-Ly-6G FITC	1A8	BioLegend	127606
anti-V-alpha2 TCR BUV395	B20.1	BD Biosciences	743834
anti-Clec4a4 (33D1) APC	33D1	BioLegend	124914
anti-XCR1 BV421	ZET	BioLegend	148216
anti-XCR1 BV650	ZET	BioLegend	148220
anti-XCR1 BV785	ZET	BioLegend	148225
anti-TER-119 FITC	TER-119	BioLegend	116206
anti-SiglecH APC	551	BioLegend	129611
anti-FOXP3 AF647	150D	BioLegend	320014
anti-FOXP3 PE	FJK-16s	eBioscience	12-5773-80
anti-IFN-γ BV650	XMG1.2	BioLegend	505831
anti-IL-17F AF647	9D3.1C8	BioLegend	517003
anti-IL-17A FITC	TC11-18H10.1	BioLegend	506907
anti-Ki-67 BV786	B56	BD Biosciences	563756

anti-ROR gamma (t) BV421	Q31-378	BD Biosciences	562894
anti-TNF-alpha PE Cy7	MP6-XT22	BioLegend	506324
CD16/CD32 FcBlock	2.4G2	BD Biosciences	553142
TotalSeq™-B0305 anti-mouse Hashtag 5 Antibody	M1/42; 30-F11	BioLegend	155839
TotalSeq™-B0302 anti-mouse Hashtag 2 Antibody	M1/42; 30-F11	BioLegend	155833

Antibodies used for *in vitro* co-culture	**Clone**	**Source**	**Catalog number**
Recombinant Mouse IL-6 (carrier-free)		BioLegend	575706
Recombinant Mouse TGF-β1 (carrier-free)		BioLegend	763014
anti-IL-4	11B11	BioLegend	504135
anti-IFNγ	XMG1.2	BioLegend	505847

Antibody used for *in vivo* targeting	**Clone**	**Source**	**Catalog number**
αDCIR2-OVA	33D1	Diana Dudziak	N/A

Antibody used for hCD2 staining	**Clone**	**Source**	**Catalog number**
αhCD2-AF647	M-T910	Ludger Klein	N/A

SI Appendix Table Legends

- Table S1 Gene lists for scoring
- Table S2 Significant genes for clusters in murine spleen multiome
- Table S3 Differentially expressed genes across age cDC2 and RORγt^{+} DCs
- Table S4 Top 20 genes for RORγt^{+} DC subclusters
- Table S5 Human RORγt^{+} DC signature

SI References

1. Lochner, M. *et al.* In vivo equilibrium of proinflammatory IL-17+ and regulatory IL-10+ Foxp3+ RORγt+ T cells. *J. Exp. Med.* **205**, 1381–1393 (2008).

2. Eberl, G. *et al.* An essential function for the nuclear receptor RORγt in the generation of fetal lymphoid tissue inducer cells. *Nat. Immunol.* **5**, 64–73 (2004).

3. Eberl, G. & Littman, D. R. Thymic Origin of Intestinal αß T Cells Revealed by Fate Mapping of RORγt+ Cells. *Science* **305**, 248–251 (2004).

4. Xiao, C. & Sauer, K. hCD2-iCre and Vav-iCre mediated gene recombination patterns in murine hematopoietic cells. *PLoS One* **10**, e0124661 (2015).

5. Dudziak, D. *et al.* Differential antigen processing by dendritic cell subsets in vivo. *Science (New York, NY)* **315**, 107–111 (2007).

6. Fang, Z., Liu, X. & Peltz, G. GSEApy: a comprehensive package for performing gene set enrichment analysis in Python. *Bioinformatics* **39**, btac757 (2022).

7. González-Blas, C. B. *et al.* SCENIC+: single-cell multiomic inference of enhancers and gene regulatory networks. *Nat. Methods* **20**, 1355–1367 (2023).

8. Lyu, M. *et al.* ILC3s select microbiota-specific regulatory T cells to establish tolerance in the gut. *Nature* 1–8 (2022) doi:10.1038/s41586-022-05141-x.

9. Akagbosu, B. *et al.* Novel antigen-presenting cell imparts Treg-dependent tolerance to gut microbiota. *Nature* **610**, 752–760 (2022).

10. Wang, J. *et al.* Single-cell multiomics defines tolerogenic extrathymic Aire-expressing populations with unique homology to thymic epithelium. *Sci Immunol* **6**, eabl5053 (2021).

11. Kedmi, R. *et al.* A RORγt+ cell instructs gut microbiota-specific Treg cell differentiation. *Nature* **610**, 737–743 (2022).

12. Brown, C. C. *et al.* Transcriptional Basis of Mouse and Human Dendritic Cell Heterogeneity. *Cell* 1–43 (2019) doi:10.1016/j.cell.2019.09.035.

13. Consortium*, T. S. *et al.* The Tabula Sapiens: A multiple-organ, single-cell transcriptomic atlas of humans. *Science* **376**, eabl4896 (2022).

14. Elmentaite, R. *et al.* Cells of the human intestinal tract mapped across space and time. *Nature* **597**, 250–255 (2021).

15. Kang, J. *et al.* AXL+SIGLEC6+ dendritic cells in cerebrospinal fluid and brain tissues of patients with autoimmune inflammatory demyelinating disease of CNS. *Clin. Immunol.* **253**, 109686 (2023).

16. Antunes, A. R. P. *et al.* Single-cell profiling of myeloid cells in glioblastoma across species and disease stage reveals macrophage competition and specialization. *Nat. Neurosci.* **24**, 595–610 (2021).

17. Touil, H. *et al.* A structured evaluation of cryopreservation in generating single-cell transcriptomes from cerebrospinal fluid. *Cell Rep. Methods* **3**, 100533 (2023).

18. Schafflick, D. *et al.* Integrated single cell analysis of blood and cerebrospinal fluid leukocytes in multiple sclerosis. *Nat. Commun.* **11**, 247 (2020).

Supplementary Figure 1

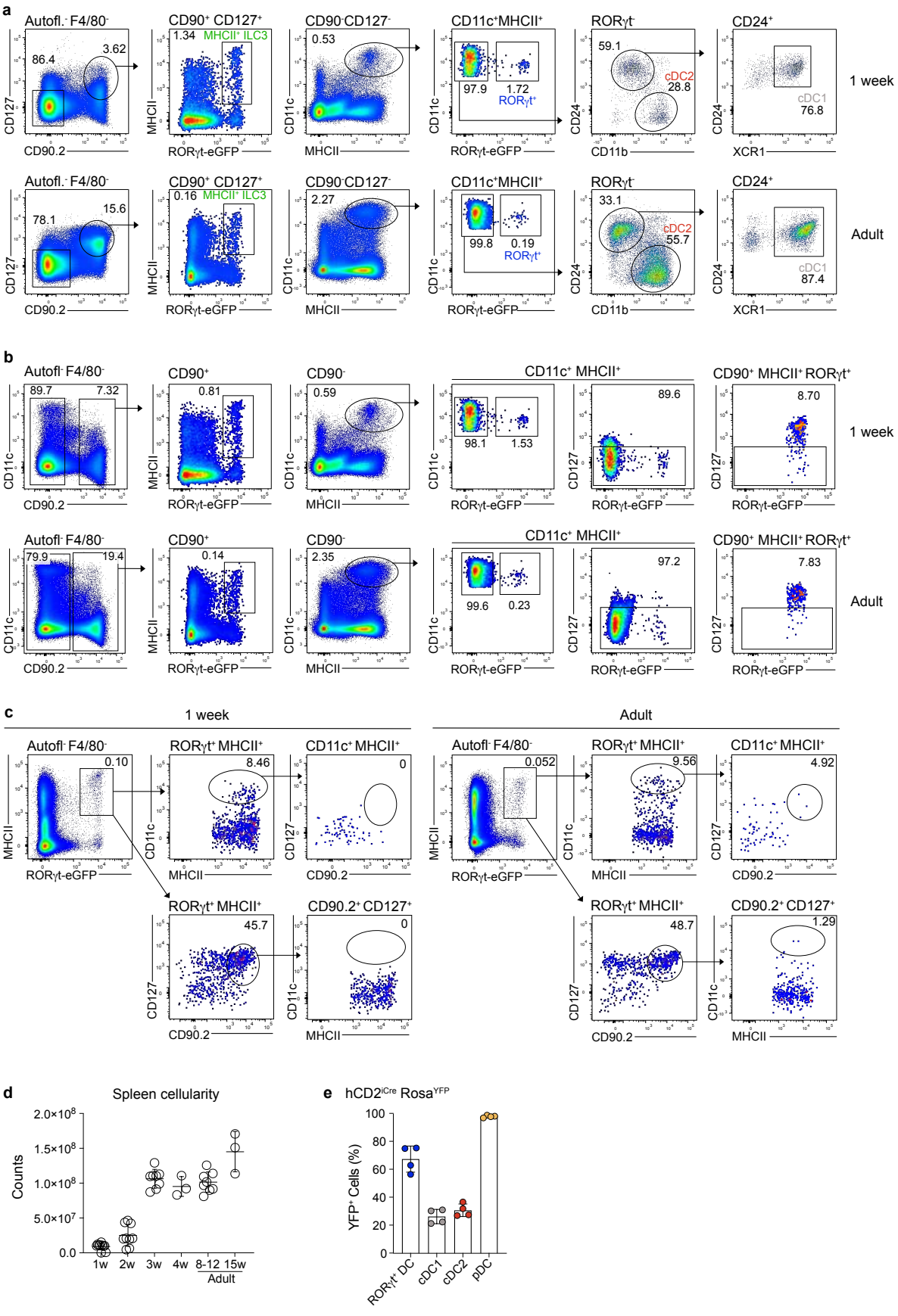

Supplementary Figure 1. CD11c^{+}MHCII^{+}RORγt^{+} cells are phenotypically more similar to cDCs than MHCII^{+}ILC3s, and are conserved across age.

a-d. Spleens from *RORγt^{GFP}Clec9a^{Cre}Rosa^{Tom}* or *Clec9a^{Cre}Rosa^{Tom}* mice at the indicated ages were analyzed by flow cytometry **a.** Representative gating strategy for cDC1, cDC2, MHCII^{+}ILC3 and RORγt^{+} DC. Live autofluorescence negative cells were gated. Within CD127^{+}CD90^{+} cells MHCII^{+}GFP^{+} cells were gated as MHCII^{+} ILC3. In the CD127^{-}CD90^{-} fraction CD11c^{+}MHCII^{+} cells were gated and RORγt^{+} DC identified as GFP^{+} or RORC positive cells as indicated. **b.** CD11c^{+}MHCII^{+}RORγt^{+} cells do not express CD127. CD90^{-}CD11c^{+}MHCII^{+} cells were gated without prior exclusion of CD127^{+} cells and then analyzed for GFP and CD127 expression. CD90^{+}MHCII^{+}GFP^{+} ILC3 stained positive for CD127. **c.** RORγt^{+}MHCII^{+} cells in 1-week-old and adult spleen were gated and further analyzed for expression of CD11c, CD90 and CD127. **d.** Spleen leukocyte cellularity at the indicated ages. Each dot represents one mouse Data are representative of at least two independent experiments with at least 2 mice per group. **e.** Frequency of YFP^{+} cells in RORγt^{+} DC, cDC1, cDC2 and pDCs from spleen of adult *hCD2^{iCre}Rosa^{YFP}* mice.

Supplementary Figure 2

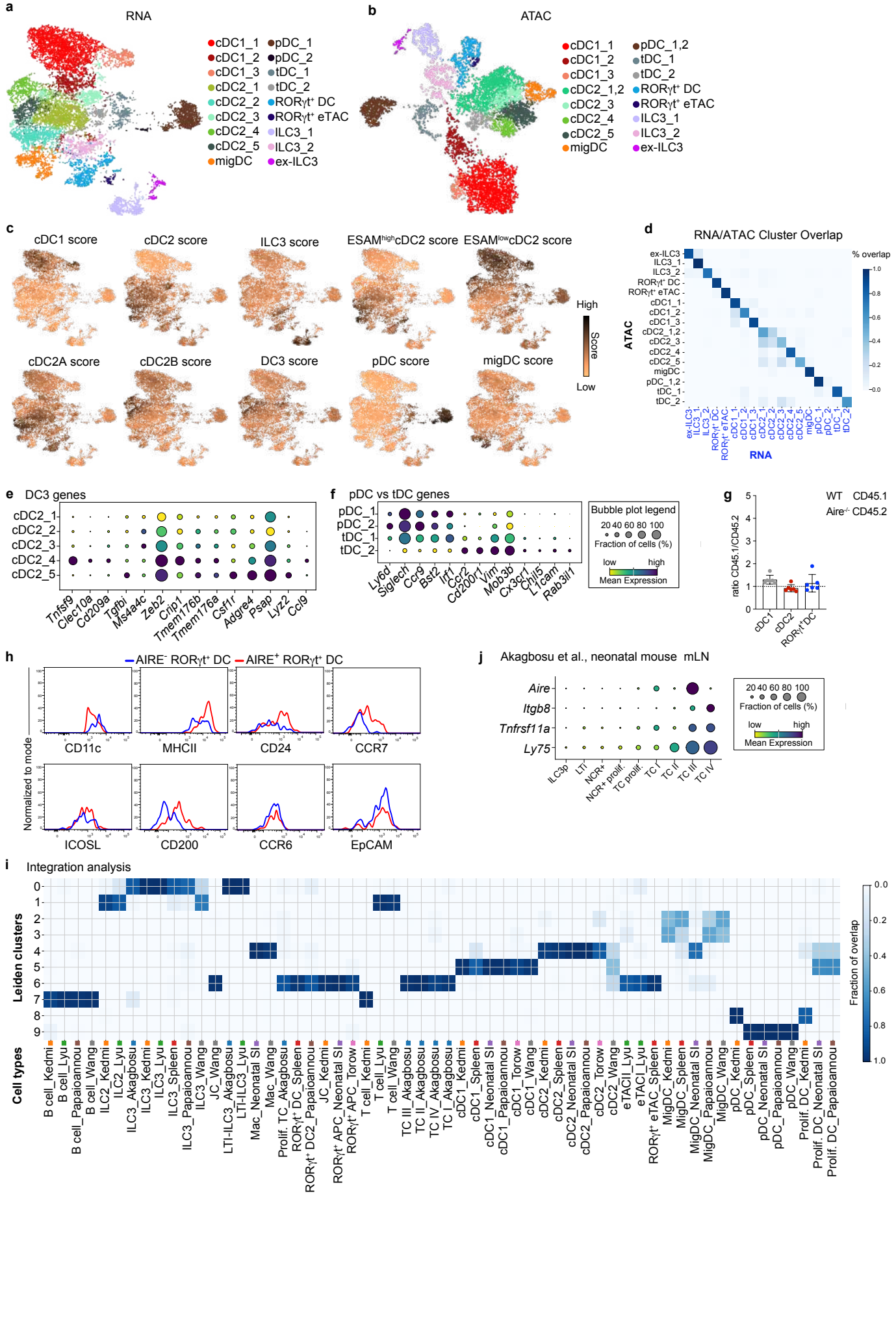

Supplementary Figure 2. Cluster annotation and downstream analyses of single cell multiomic profiling.

RORγt^{+} DC, CD11c^{+}MHCII^{+} cDC and MHCII^{+} ILC3 from spleens of 2-week-old (n=2) or adult (n=3) *RORγt^{GFP}Clec9a^{Cre}Rosa^{Tom}* mice were sorted, pooled at a 1:10:1 ratio and subjected to 10X multiome analyses. **a.** Annotated UMAP representing RNA-based analysis of 11,980 nuclei. **b.** Annotated UMAP representing open chromatin-based analysis of 9899 nuclei. **c.** RNA-based UMAPs depicting expression scores for the indicated gene signatures provided in *SI Appendix,* Table S1. **d.** Correspondence of clusters between scATAC- and scRNA-based analyses. **e, f**. Bubble plots showing mean expression of select DC3 genes **(e)**, pDC and tDC genes **(f)**. **g.** Lethally irradiated CD45.1/2 mice were reconstituted with a 1:1 mix of CD45.1 WT and CD45.2 *Aire$^{-/-}$* bone marrow. Contribution of donor cells to cDC1, cDC2 and RORγt^{+} DCs in spleen 7 weeks post transfer is shown. **h.** Expression of indicated markers on AIRE^{+} (red) and AIRE^{neg} (blue) RORγt^{+} DCs. **i.** Heatmap depicting fraction of overlap of cell types from the indicated datasets with each Leiden cluster (see also Fig. 2i). **j.** Bubble blot showing expression of the indicated genes in Thetis cell clusters from Akagbosu et al (9).

Supplementary Figure 3

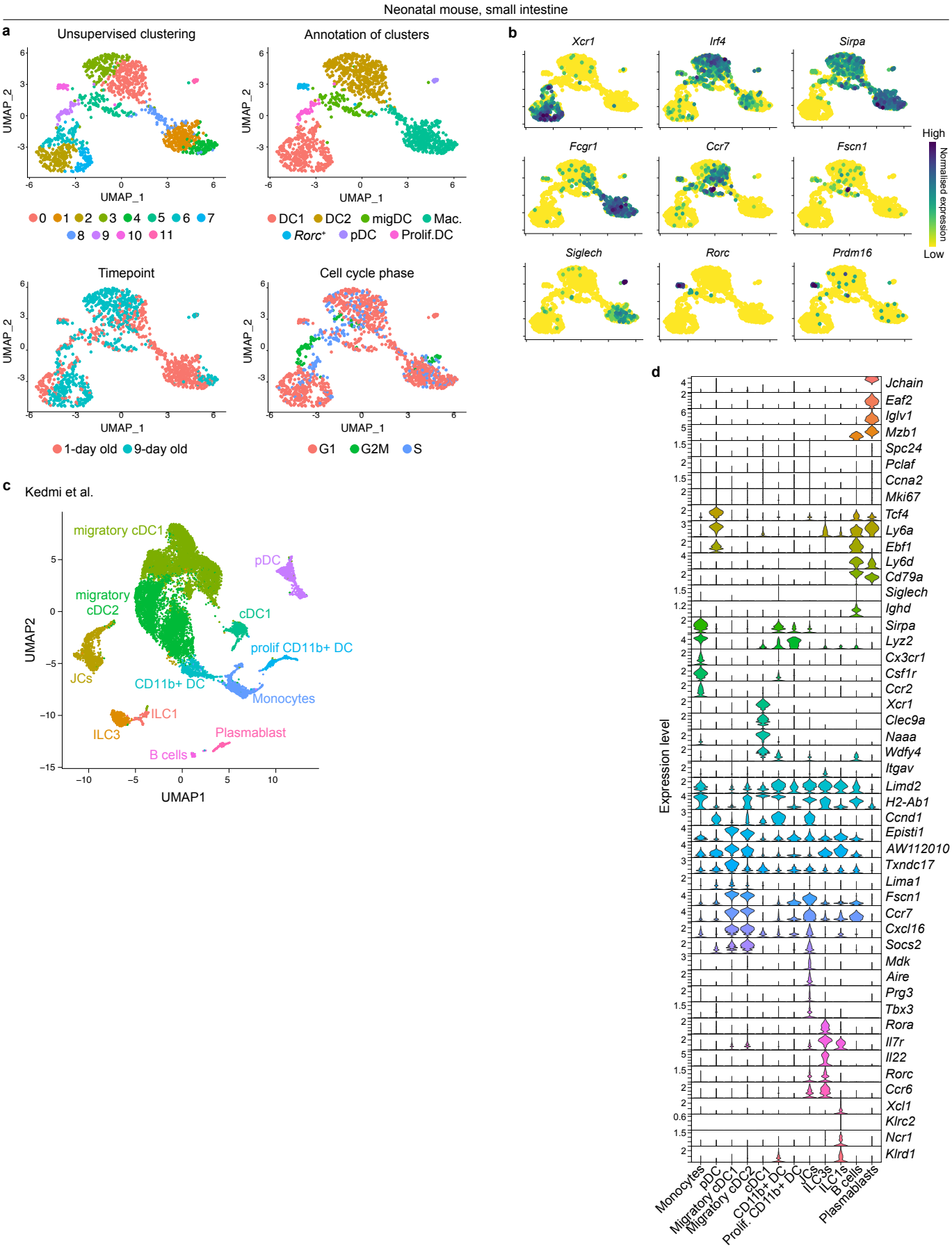

Supplementary Figure 3. RORγt^{+} DCs in scRNAseq datasets of murine tissues.

a, b. scRNA-seq of neonatal siLP. Live CD45^{+}CD19^{-}CD90^{-}CD11c^{+}MHCII^{+} cells from siLP of one-day old and nine-day old *Clec9a*^{Cre}*Rosa*^{Tom} mice were sorted, pooled, and subjected to 10X scRNA-seq analyses. **a.** UMAP display of 2053 cells colored by cluster, cell type annotation, timepoint and cell cycle phase. **b.** UMAP showing expression of the indicated genes used for cluster annotation. **c.** UMAP display of 16,302 cells in dataset from Kedmi et al. (11) colored by clusters and cell types. **d.** Stacked violin plots of selected genes from Extended Data Figure 2 in Kedmi et al. (11).

Supplementary Figure 4

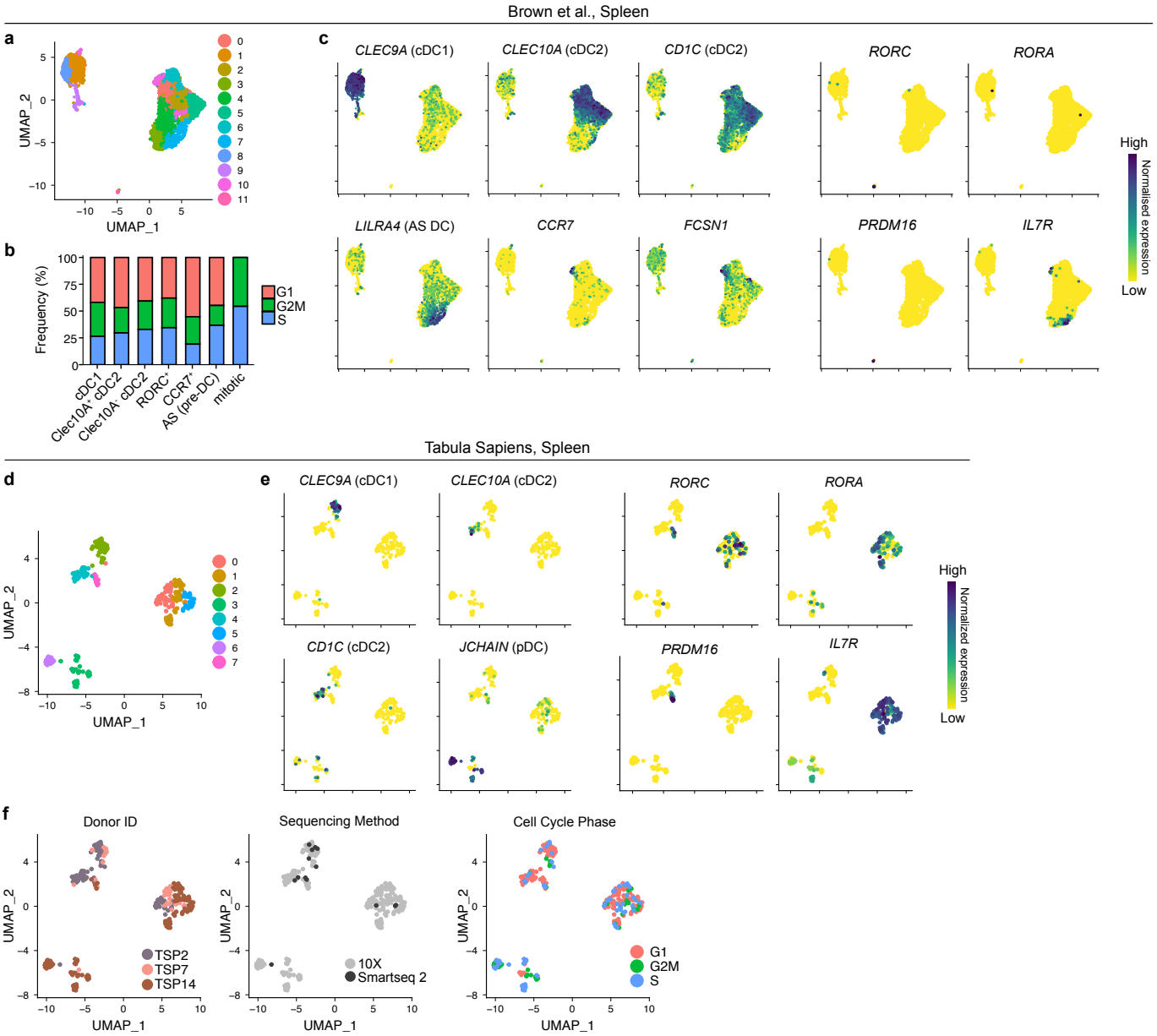

Supplementary Figure 4. RORγt^{+} DCs exist in human spleen.

a-c. Human splenic DCs profiled by scRNA-seq in Brown et al. (12) were analyzed using Seurat. **a.** UMAP display of 4717 cells colored by cluster. **b**. Proportion of cells per annotated cluster in indicated cell cycle phases. **c.** Expression of genes used for cluster annotation. **d-f.** 262 cells annotated as DCs, pDCs and ILCs in the scRNA-seq spleen reference dataset from the Tabula Sapiens Consortium (13) were reclustered. UMAP displaying Leiden clustering **(d)** and expression of the indicated genes used for cluster annotation **(e)**. **f.** UMAP annotated by donor ID (left), sequencing method (middle) and cell cycle phase (right).

Supplementary Figure 5

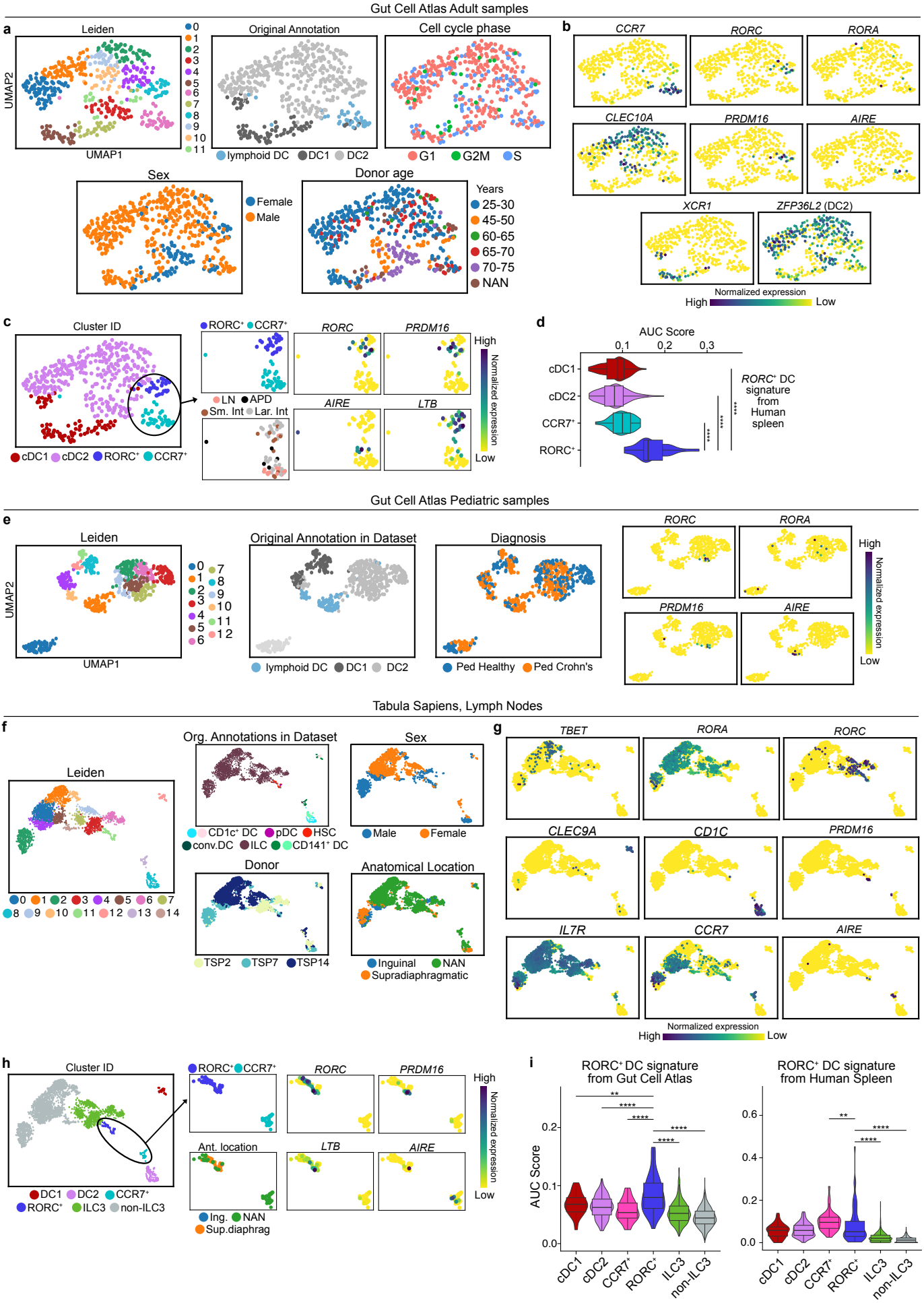

Supplementary Figure 5. RORγt$^+$ DCs in scRNAseq datasets of human intestine and lymph nodes.

a-d. Human gut cell atlas scRNA-seq analyses. **a.** 480 cells annotated as lymphoid DCs, DC1 and DC2 from healthy adult donors from the human gut cell atlas were reclustered using *Scanpy*. UMAP display depicting Leiden clustering, original annotation, sex, donor age, cell cycle phase **(a)** and the indicated genes used for cluster identification **(b). c.** UMAP from **(a)** annotated using signature genes and zoomed in display of *RORC*$^+$ and *CCR7*$^+$ clusters to illustrate anatomical location and expression of *RORC*, *PRDM16*, *AIRE* and *LTB* in individual cells. **d.** Enrichment score for genes delineating *RORC*$^+$ cells in human spleen computed for each cluster with AUCell package. **e.** 644 cells annotated as lymphoid DC, DC1 and DC2 from pediatric donors from the human gut cell atlas were reclustered using *Scanpy*, Leiden clusters are indicated on the left UMAP. Middle UMAPs depict the original cluster annotation and stratification of cells per donor diagnosis (healthy vs. pediatric Crohn's disease). UMAPs on the right show expression of the *PRDM16, RORC, AIRE*, and *RORA* to visualize presence of *PRDM16*$^+$*RORC*$^+$ cells resembling RORγt$^+$ DC, distinct from *AIRE*-expressing cells. **f.** 2668 cells from the Tabula Sapiens Lymph node reference data set originally annotated as CD1c$^+$DC, CD141$^+$DC, cDC (conv.DC), ILC, pDC, and HSC were reclustered using *Scanpy*. The resulting UMAP is colored by Leiden clusters, original cell annotation, sex, donor, anatomical location **(f),** and the indicated marker genes used for cluster identification **(g)**. **h.** UMAP from **(f)** annotated using signature genes and zoomed in display of *RORC*$^+$ and *CCR7*$^+$ clusters to illustrate anatomical location and expression of *RORC*, *PRDM16*, *AIRE* and *LTB* in individual cells. **i.** Enrichment score for expression of genes distinguishing RORγt$^+$ DC in the healthy adult gut (left) and healthy adult spleen (right) across annotated clusters in Tabula Sapiens Lymph Nodes dataset. *p (<0.05), **p (<0.01) ***p (<0.001), ****p < 0.0001. Statistical analysis was performed using Wilcoxon non-parametric ranked sum test to calculate differences in AUCscores between indicated clusters.

Supplementary Figure 6

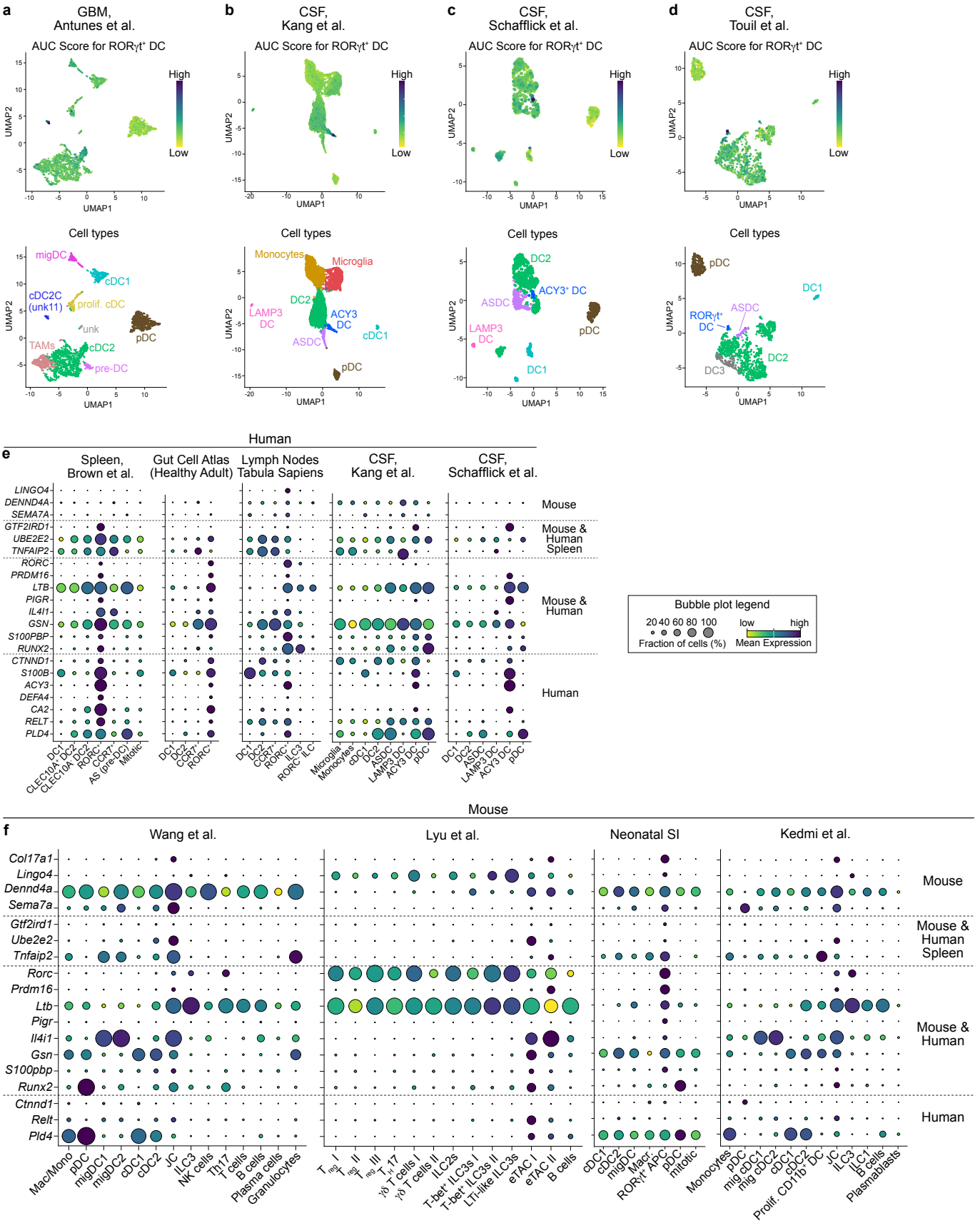

Supplementary Figure 6. RORγt^{+} DCs in human and murine scRNAseq datasets.

a-d. Cells annotated as myeloid cells from the indicated datasets were reclustered and annotated by original annotation **(a,b)** or based on signature genes **(c,d).** Annoated UMAP (bottom) and enrichment score for genes delineating *RORC*$^{+}$ cells (*SI Appendix,* Table S5) computed for each cluster with AUCell package (top) are shown. **e,f.** Bubble plots showing expression of selected genes deduced from comparative genes expression analyses that distinguish RORγt^{+} DCs in the indicated human **(e)** and mouse datasets **(f)**.

Supplementary Figure 7

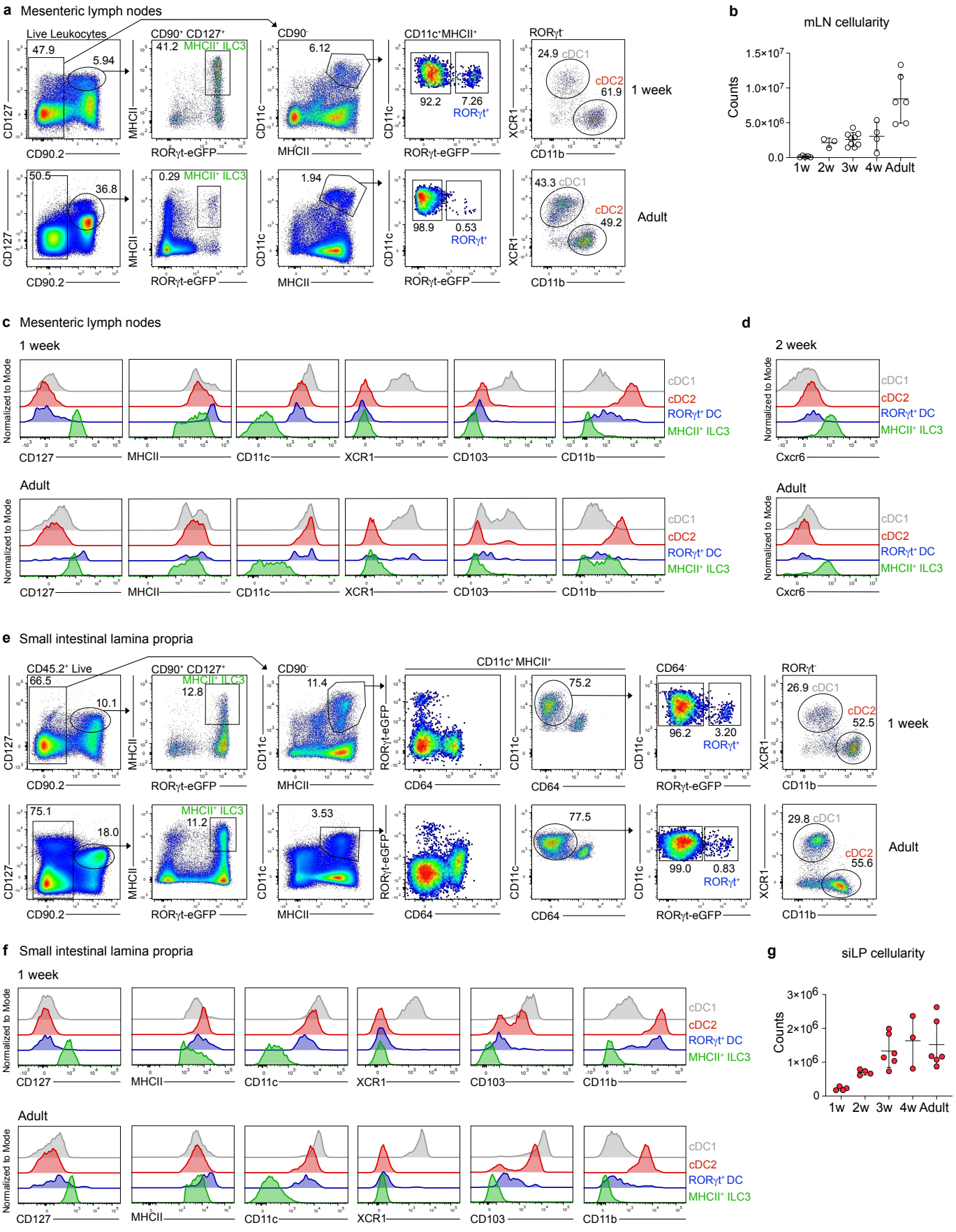

Supplementary Figure 7. Characterization of RORγt$^+$ DCs in mesenteric lymph node and small intestinal lamina propria of neonatal and adult mice.

Mesenteric lymph node (mLN) **(a-d)** and small intestinal lamina propria (siLP) **(e-g)** from *RORγt^{GFP}* mice at the indicated ages were analyzed by flow cytometry. **a.** Representative gating strategy for the identification of MHCII$^+$ ILC3, RORγt$^+$ DC, cDC1 and cDC2 in mLN of 1-week-old and adult mice. **b.** mLN cellularity across age (1-week-old n=5; 2-week-old n=3; 3-week-old n=8, 4-week-old n=4; Adult n=6). **c, d.** Histogram overlays of the indicated surface markers on cDC1 (grey), cDC2 (red), RORγt$^+$ DC (blue) and MHCII$^+$ILC3 (green). **e.** Representative gating strategy for identification of MHCII$^+$ILC3, RORγt$^+$ DC, cDC1 and cDC2 in siLP of 1-week-old and adult mice. **f**. Histogram overlays of the indicated markers on cDC1 (grey), cDC2 (red), RORγt$^+$ DC (blue) and MHCII$^+$ILC3 (green). **g.** Total leukocyte count per siLP at the indicated ages (1-week-old n=4-8; 2-week-old n=4; 3-week-old n=6, 4-week-old n=3; Adult n=6). mLN from 1-week-old mice were pooled by 2 or 3, otherwise each dot represents one mouse. Error bars represent mean ± SD.

Supplementary Figure 8

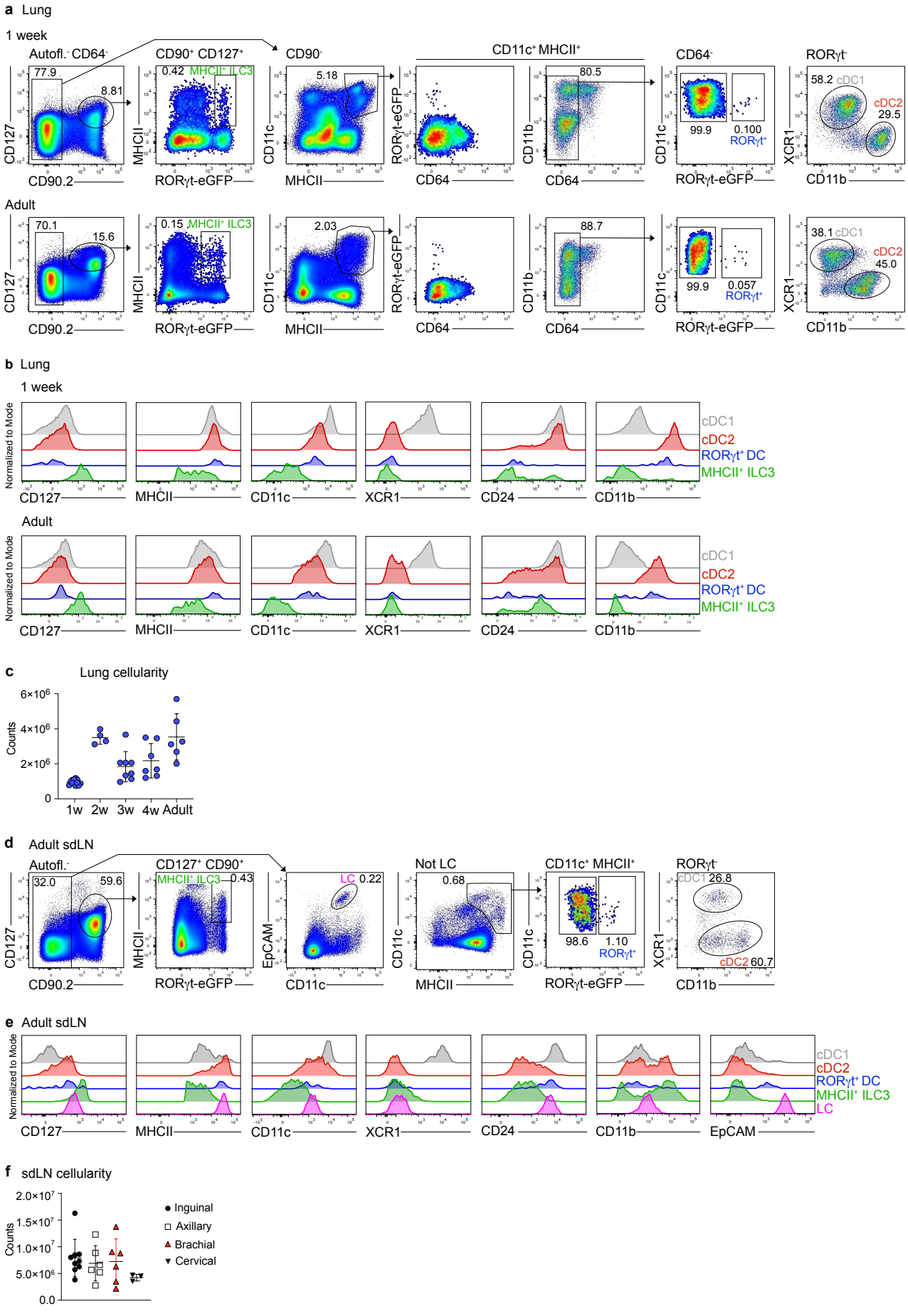

Supplementary Figure 8. Identification and phenotypic characterization of RORγt$^+$ DCs in murine lung and skin draining lymph nodes.

a. Representative gating strategy for the identification of MHCII$^+$ILC3, RORγt$^+$ DC, cDC1 and cDC2 in murine lung at indicated ages. **b.** Histogram overlays of the indicated surface markers on cDC1 (grey), cDC2 (red), RORγt$^+$ DC (blue) and MHCII$^+$ ILC3 (green). **c.** Lung cellularity across age (1-week-old n=11; 2-week-old n=4; 3-week-old n=7, 4-week-old n=6; Adult n=6) from mice of indicated ages. Data are pooled from at least 2 independent experiments. Each dot represents one mouse. **d-f.** Axial, brachial, inguinal and cervical sdLN were isolated from adult *RORγt^{GFP}* or WT mice. **d.** Representative gating strategy for identification of MHCII$^+$ ILC3, Langerhans cells (LC), RORγt$^+$ DC, cDC1 and cDC2 in adult murine adult skin-draining lymph nodes. **e.** Histogram overlays of the indicated surface markers on cDC1 (grey), cDC2 (red), RORγt$^+$ DC (blue), MHCII$^+$ ILC3 (green) and LC (pink). **f.** Axial, brachial, inguinal and cervical sdLN cellularity for each site. Data pooled from 2 independent experiments performed with 3 mice each, each dot represents a biological replicate. Error bars represent mean ± SD.

Supplementary Figure 9

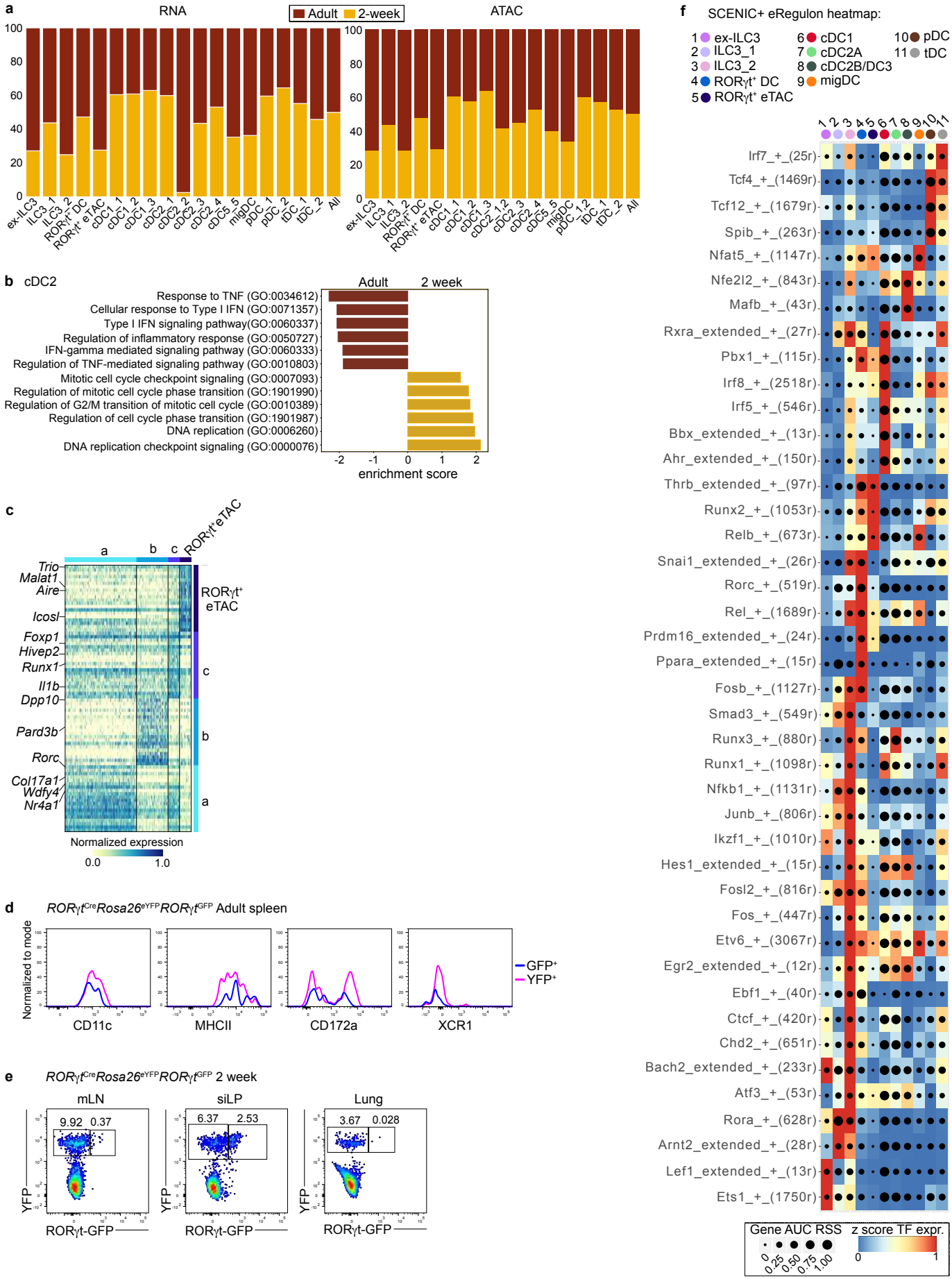

Supplementary Figure 9: Multiomic analyses of ATAC and gene expression profiles reveals gene regulatory networks unique to RORγt$^+$ DCs.

a. Contribution of cells from the 2-week (yellow) or adult (red) timepoints to RNA and ATAC based clusters. **b.** Normalized enrichment scores of selected gene sets enriched in all cDC2 clusters from 2-week-old and adult mice. **c.** Heatmap showing top 20 differentially expressed genes between RORγt$^+$ DC sub-clusters and RORγt$^+$ eTACs with selected genes highlighted. For full list of genes see *SI Appendix,* Table S4. **d.** Expression of indicated markers on CD11c$^+$MHCII$^+$ cells with active RORγt expression (GFP$^+$) or RORγt expression history (YFP$^+$) in spleen of adult *RORγt^{Cre}Rosa^{YFP}RORγt$^{GFP/wt}$* mice. **e.** mLN, siLP and lung from 2-week-old *RORγt^{Cre}Rosa^{YFP}RORγt$^{GFP/wt}$* mice were analyzed by flow cytometry. CD11c$^+$MHCII$^+$ cells were gated as indicated above and analyzed for GFP (active RORγt) versus YFP (RORγt expression history). **f.** Heat map/dot-plot showing eRegulons computed with SCENIC+. Transcription factor expression is given on a color scale and cell-type specificity of the genes regulated by the transcription factors (eRegulon) on a size scale.

Supplementary Figure 10

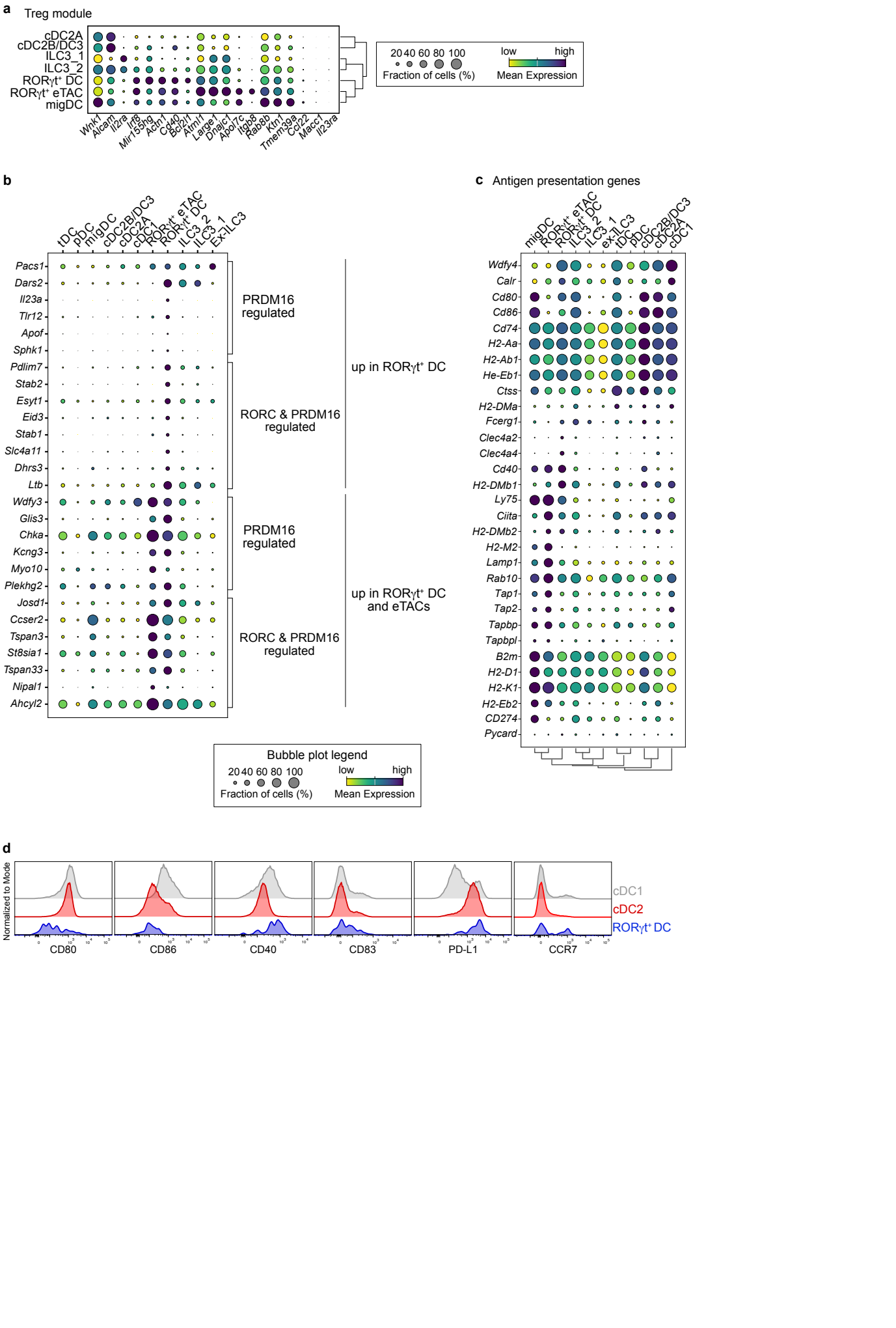

Supplementary Figure 10. Unique transcriptional profile and expression of antigen presentation genes in RORγt$^+$ DCs.

a. Bubble plot of genes implicated in promoting Treg differentiation in Akagbosu et al. (8) **b.** Expression of genes regulated by PRDM16 or PRDM16 and RORγt in RORγt$^+$ DCs or RORγt$^+$ eTACs. **c.** Expression of genes involved in antigen presentation. **d.** Expression of indicated markers on cDC1 (grey), cDC2 (red) and RORγt$^+$ DCs (blue) from spleen of adult mice.

Supplementary Figure 11

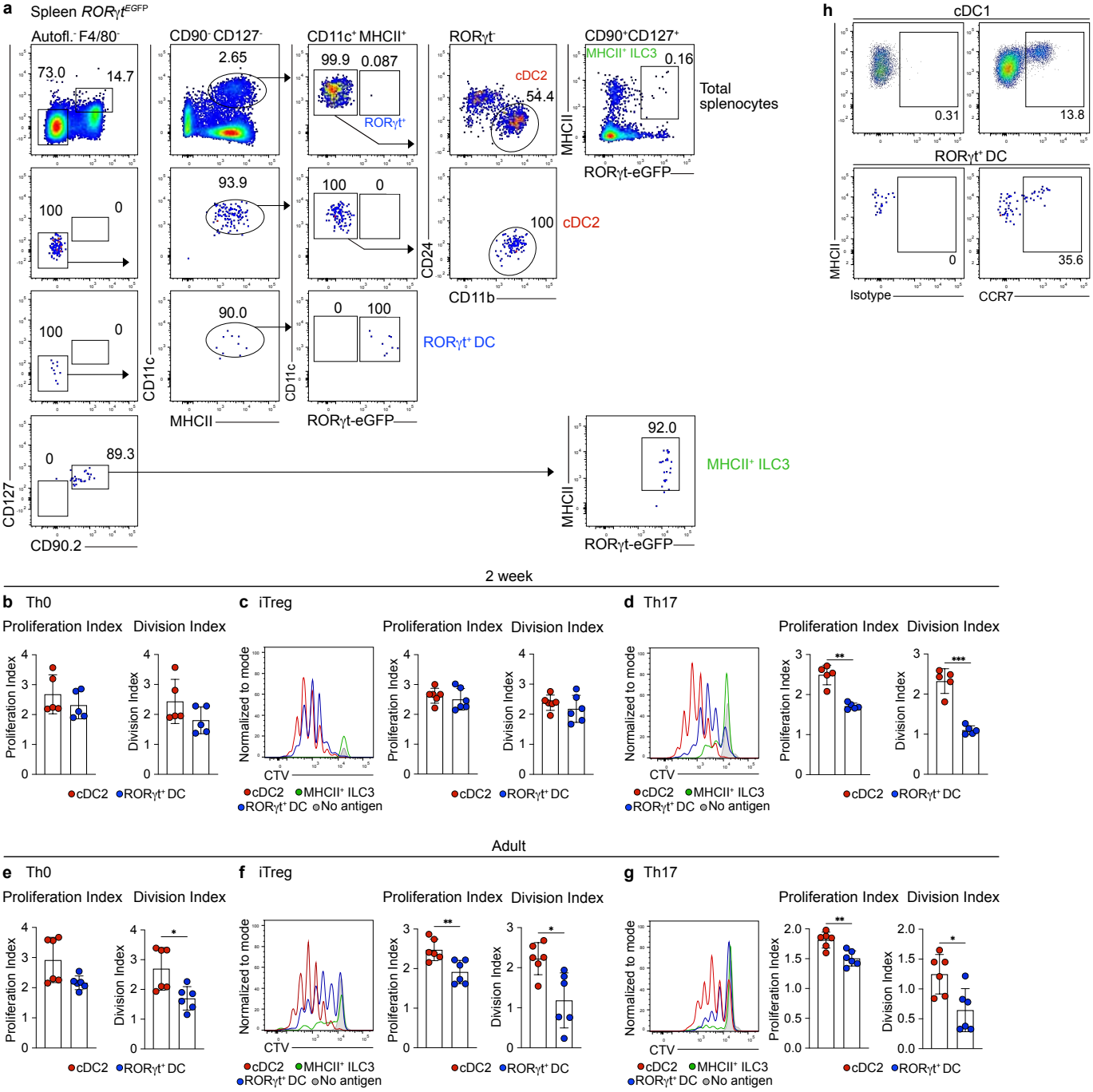

Supplementary Figure 11. Sort purity of APC populations and proliferation of OTII cells.
a-g. cDC2, MHCII^{+} ILC3 and GFP^{+} RORγt^{+} DC were sorted from spleens of 2-week-old or adult *RORγt^{GFP}* mice and pulsed with $OVA_{323-339}$. 250 APCs were then co-cultured with 2500 CTV-labelled naïve OTII cells under the indicated conditions for 3.5 days. **a.** Gating strategy (top row) and sort purity analyses of cDC2, MHCII^{+} ILC3 and RORγt^{+} DC from adult mice. **b-g.** Division and proliferation indexes of OTII cells after co-culture with the specified populations from 2-week-old **(b-d)** or adult **(e-g)** mice under indicated conditions. **h.** Expression of CCR7 on cDC1 and RORγt^{+} DC in spleen of adult *RORγt^{GFP}* mice 12 hours post i.p. injection of CpG-B. Dots represent biological replicates from at least 2 independent experiments. *p (0.0332), **p (0.0021) ***p (0.0002), ****p < 0.0001. Statistical analysis was performed using two-tailed Welch's t-test. Only statistically significant comparisons are indicated.

Supplementary Figure 12

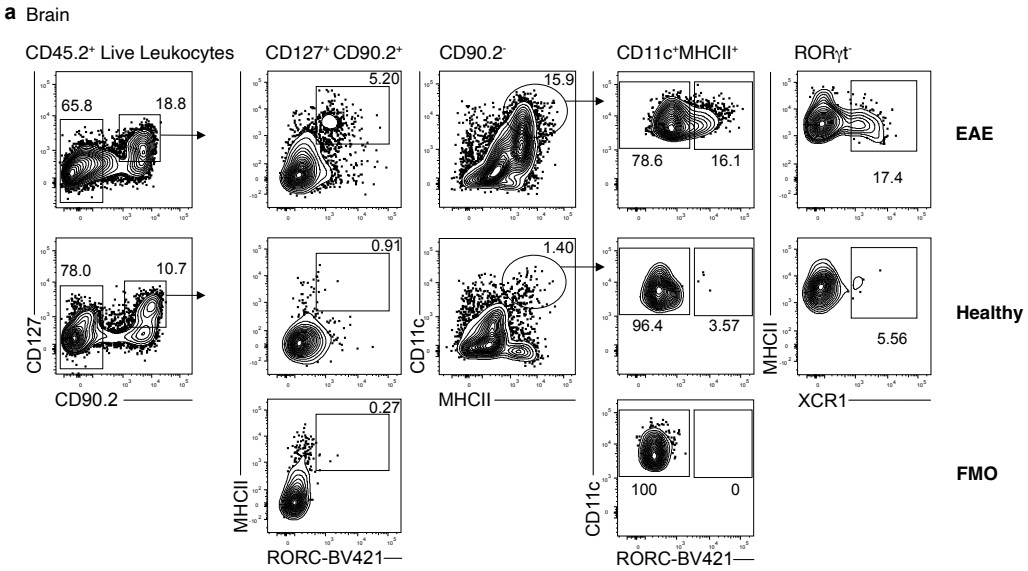

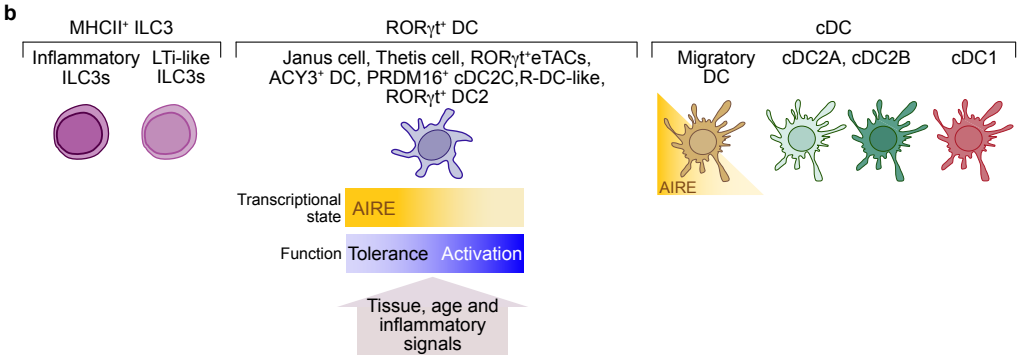

Supplementary Figure 12. Characterization of RORγt$^+$ DCs in CNS of mice with active EAE. **a.** Representative gating strategy for identification of MHCII$^+$ ILC3s, RORγt$^+$ DCs and cDC1 in CNS (brain) of mice during peak EAE (d16) compared to healthy controls. MHCII$^+$ ILC3s were gated as CD127$^+$CD90.2$^+$MHCII$^+$RORγt$^+$ cells. Within CD127$^-$CD90.2$^-$ cells CD11c$^+$MHCII$^+$ were gated and RORγt$^+$ DCs identified as anti-RORC$^+$ cells, and cDC1 as anti-RORC$^-$XCR1$^+$ cells. Fluorescence minus one (FMO) control for anti-RORC staining (no anti-RORC antibody was added). Plots are representative of n=6. **b.** RORγt$^+$ DCs are a distinct immune lineage that entails Janus cells, Thetis cells, RORγt$^+$ eTACs, R-DC-like cells, cDC2C, ACY3$^+$ DCs and RORγt$^+$ DC2. RORγt$^+$ DCs exhibit a transcriptional and functional spectrum ranging from inducing T cell activation to T cell tolerance that is shaped by tissue and age-specific signals, as well as inflammation.

4. Paper II

nature communications

Article

https://doi.org/10.1038/s41467-024-46966-6

Genomic deletion of Bcl6 differentially affects conventional dendritic cell subsets and compromises Tfh/Tfr/Th17 cell responses

Received: 8 December 2022

Accepted: 13 March 2024

Published online: 30 April 2024

Check for updates

Hongkui Xiao[1,13], Isabel Ulmert[1,13], Luisa Bach[2], Johanna Huber[3], Hamsa Narasimhan[4,5], Ilia Kurochkin[6,7], Yinshui Chang[2,3], Signe Holst[1,8,9], Urs Mörbe[1], Lili Zhang[10], Andreas Schlitzer[10], Carlos-Filipe Pereira[6,7,11], Barbara U. Schraml[4,5], Dirk Baumjohann[2,3] ✉ & Katharina Lahl[1,8,9,12] ✉

Conventional dendritic cells (cDC) play key roles in immune induction, but what drives their heterogeneity and functional specialization is still ill-defined. Here we show that cDC-specific deletion of the transcriptional repressor Bcl6 in mice alters the phenotype and transcriptome of cDC1 and cDC2, while their lineage identity is preserved. Bcl6-deficient cDC1 are diminished in the periphery but maintain their ability to cross-present antigen to $CD8^+$ T cells, confirming general maintenance of this subset. Surprisingly, the absence of Bcl6 in cDC causes a complete loss of Notch2-dependent cDC2 in the spleen and intestinal lamina propria. DC-targeted Bcl6-deficient mice induced fewer T follicular helper cells despite a profound impact on T follicular regulatory cells in response to immunization and mounted diminished Th17 immunity to *Citrobacter rodentium* in the colon. Our findings establish Bcl6 as an essential transcription factor for subsets of cDC and add to our understanding of the transcriptional landscape underlying cDC heterogeneity.

Conventional dendritic cells (cDC) have the unique ability to present antigens to naïve T cells within lymphoid organs[1–3]. Upon encounter of antigen, migratory cDC scanning the peripheral environment mature and relocate to the draining lymph nodes (LN), where they collaborate with LN-resident cDC to initiate immunity[4]. The spleen is the secondary lymphoid organ responsible for the induction of immune responses to blood-derived antigen[5], and maturation of splenic cDC leads to similar relocation from the marginal zone and red pulp into the white pulp,

[1]Section for Experimental and Translational Immunology, Institute for Health Technology, Technical University of Denmark (DTU), 2800 Kongens, Lyngby, Denmark. [2]Medical Clinic III for Oncology, Hematology, Immuno-Oncology and Rheumatology, University Hospital Bonn, University of Bonn, Bonn, Germany. [3]Institute for Immunology, Biomedical Center, Faculty of Medicine, LMU Munich, Planegg-Martinsried, Munich, Germany. [4]Biomedical Center, Institute of Cardiovascular Physiology and Pathophysiology, Faculty of Medicine, Ludwig-Maximillians-Universität München, Planegg-Martinsried, Munich, Germany. [5]Walter-Brendel-Centre of Experimental Medicine, University Hospital, LMU Munich, Planegg-Martinsried, Munich, Germany. [6]Cell Reprogramming in Hematopoiesis and Immunity Laboratory, Lund Stem Cell Center, Molecular Medicine and Gene Therapy, Lund University, Lund, Sweden. [7]Wallenberg Center for Molecular Medicine, Lund University, Lund, Sweden. [8]Department of Microbiology, Immunology, and Infectious Diseases, Cumming School of Medicine, University of Calgary, Calgary, Alberta, Canada. [9]Calvin, Phoebe and Joan Snyder Institute for Chronic Diseases, University of Calgary, Calgary, Alberta, Canada. [10]Quantitative Systems Biology, Life and Medical Sciences (LIMES) Institute, University of Bonn, Bonn, Germany. [11]Center for Neuroscience and Cell Biology, University of Coimbra, Coimbra, Portugal. [12]Immunology Section, Lund University, Lund 221 84, Sweden. [13]These authors contributed equally: Hongkui Xiao, Isabel Ulmert. ✉e-mail: dirk.baumjohann@uni-bonn.de; katharina.lahl@ucalgary.ca

where naïve B and T cells reside[6,7]. "Resident" resting DC are also found in the spleen, where they are located in the T cell zones in the absence of stimulation[8].

cDC are broadly divided into two main subsets, cDC1 and cDC2[1]. cDC1 are characterized by their expression of the cDC1-exclusive chemokine receptor XCR1 and the absence of CD11b and Sirpα. Their development and functions are dependent on the transcription factors (TF) IRF8[9,10], BATF3[11], Nfil3[12,13], and Id2[14], and they excel at cross-presenting antigen to $CD8^+$ T cells, which is at least in part attributable to their ability to engulf apoptotic material[15–19]. cDC2 express high levels of CD11b and Sirpα, but not XCR1 and the transcriptional network governing their development is less well defined. cDC2 show a higher level of heterogeneity than cDC1[20], and recent attempts to subset cDC2 further have suggested separation based on Notch2 versus Klf4-dependency[21]. IRF4-deficiency leads to a partial loss of cDC2 and is thought to impact primarily on their survival and ability to migrate[22–24]. Other TFs reported to influence cDC2 development or function include ZEB2[25], IRF2[26], and Rel-B[27]. In the spleen, the majority of cDC2 express endothelial cell-specific adhesion molecule (ESAM), a marker defining cDC2 located in the bridging channels of the marginal zone, where they fulfill critical functions in activating $CD4^+$ T cells and germinal center (GC) formation[28,29]. The development of $ESAM^{hi}$ cDC2 depends on Notch2-signaling induced by delta-like ligand 1 (DLL1) expressed by stromal cells[22,28,30,31] and on the chemokine receptor Ebi2 (GPR183)[32].

The TF Bcl6 plays an essential role in GC reactions, being required for the differentiation of both germinal center (GC) B cells and T follicular helper (Tfh) cells in a cell-intrinsic manner[33]. Bcl6 is expressed in cDC1 and to a lower extent in cDC2[20], and we have shown previously that complete Bcl6-deficiency causes a loss of $CD11b^-$ cDC, presumed to be cDC1[20]. Other work has confirmed that Bcl6-deficient mice lack splenic CD8-expressing cDC1 but also reported a reduction in splenic $CD4^+$ cDC2[34]. However, a more recent study has disputed these findings by showing normal cDC1 numbers in mice with conditional *Bcl6* deletion driven by cre recombinase under the control of the *Csf1* promoter. Importantly, these authors suggested that the down-regulation of CD11c in the absence of Bcl6 may have compromised the detection of cDC1 in the earlier studies[35].

Here we reconcile these conflicting data by performing in-depth analysis of the cDC compartment in mice lacking Bcl6 in all cDC or specifically in cDC1, using CD11c- and Clec9a- or XCR1-driven cre drivers, respectively. Our results show that while cDC1 showed substantial alterations in gene expression including deregulation of genes involved in cytokine signaling and cell adhesion, their ability to cross-present antigen is largely conserved in the absence of Bcl6. Bcl6-deficiency in DC leads to a complete loss of the Notch2-dependent $ESAM^{hi}$ cDC2 subset in the spleen and consequently to alterations in splenic Tfh and T follicular regulatory (Tfr) cells as well as antibody responses following immunization. Likewise, Notch2-dependent cDC2 in the intestinal lamina propria (LP) are reduced in the absence of Bcl6 in DC, leading to a decrease in T helper 17 cell (Th17)-responses and delayed healing upon infection with the enteric pathogen *Citrobacter rodentium*. Our findings suggest that the core subset identities of cDC1 and cDC2 are maintained in the absence of Bcl6 but that its deficiency in DC causes cell-intrinsic, subset-specific alterations in DC abundance and function, which translates into corresponding defects in adaptive immune responses.

Results

Bcl6-deficiency alters DC subset phenotypes and numbers across tissues

We have previously shown that mice completely lacking Bcl6 are largely devoid of $CD11b^-$ cDC, presumed to be cDC1[20]. To better define the impact of Bcl6-deficiency on cDC1, we generated mice lacking Bcl6, specifically in cDC1, by crossing XCR1.cre mice to mice carrying a floxed Bcl6 gene (*XCR1.Bcl6^{KO}*). Additionally, we deleted Bcl6 in all CD11c-expressing cells by crossing CD11c.cre mice to $Bcl6^{flox}$ mice (*CD11c.Bcl6^{KO}*). As controls, we used the respective cre negative $Bcl6^{flox}$ littermates (designated as control throughout). As expected, flow cytometry revealed mutually exclusive populations of $CD11c^+MHCII^+$ cDC in control spleens based on the expression of XCR1 or CD11b to identify cDC1 and cDC2, respectively. However, there was a clear population of $XCR1^+CD11b^+$ cDC in the absence of Bcl6 in the spleens of both Bcl6-deficient mouse lines (Fig. 1A, for complete gating strategies see Suppl. Fig. 1). $XCR1^+CD11b^+$ cDC were also abundant within the resident populations of peripheral and mesenteric lymph node (pLN and mLN) cDC in the absence of Bcl6 (Fig. 1B). The absolute numbers of total $XCR1^+$ cDC (independent of CD11b expression) were only mildly reduced in *XCR1.Bcl6^{KO}* and normal in *CD11c.Bcl6^{KO}* mice, while $XCR1^-CD11b^+$ cDC were significantly diminished in *CD11c.Bcl6^{KO}* mice, but normal in *XCR1.Bcl6^{KO}* mice (Fig. 1A). Resident cDC numbers were not substantially altered in either pLNs or mLNs (Fig. 1B).

We next analyzed migratory DC populations in different organs. Mice lacking Bcl6 in cDC1 or in all DC had significantly fewer migratory $XCR1^+$ cDC in pLNs and mLNs, and these also expressed CD11b (Fig. 2A, for complete gating strategies, see Suppl. Fig. 1). Interestingly, we also detected a loss of $XCR1^-CD11b^+CD103^+$ cDC in the migratory compartment of the mLNs of *CD11c.Bcl6^{KO}* mice, whereas the numbers of $XCR1^-CD11b^+CD103^-$ cDC were normal (Fig. 2A). As the majority of migratory cDC in the mLNs derive from the small intestinal lamina propria (SILP), we next analyzed this compartment. There were fewer $XCR1^+$ cDC in the SILP of both *XCR1.Bcl6^{KO}* and *CD11c.Bcl6^{KO}* mice, all of which again expressed CD11b (Fig. 2B). In addition, the numbers of $XCR1^-CD11b^+CD103^+$ cDC were reduced in *CD11c.Bcl6^{KO}* mice, while the numbers of $XCR1^-CD11b^+CD103^-$ cDC were less affected (Fig. 2B). Together, these results suggest that the decreass in migratory $XCR1^+$ and $XCR1^-CD11b^+CD103^+$ cDC seen in mLNs are caused by the absence of these populations, rather than a disability to migrate. Similar changes in cDC were seen in the lung and the blood in the absence of Bcl6, with reduced numbers and upregulation of CD11b in $XCR1^+$ cDC in both *XCR1.Bcl6^{KO}* and *CD11c.Bcl6^{KO}* mice, together with reduced numbers of $XCR1^-CD11b^+$ cDC in *CD11c.Bcl6^{KO}* mice (Suppl. Fig. 2). Interestingly, while $XCR1^+$ DCs upregulated CD11b in all organs, $XCR1^-CD11b^+$ DCs further upregulated CD11b particularly in systemic populations (spleen and resident DCs from the mLN and pLN), while peripheral $XCR1^-CD11b^+$ DC showed no further increase of their naturally high levels of CD11b (Suppl. Fig. 3). Thus, Bcl6 deficiency affects cDC in several locations.

cDC1 and cDC2 signatures are preserved in the absence of Bcl6 in DC

One of the most surprising findings from our studies was the expression of the cDC2 marker CD11b by the $XCR1^+$ cDC that were preserved in Bcl6-deficient mice. To determine whether this reflects the acquisition of CD11b by cDC1 or cDC2 with aberrant XCR1 expression, we sorted splenic $XCR1^+$ cDC (independent of CD11b expression) and $XCR1^-CD11b^+$ cDC from control, *XCR1.Bcl6^{KO}* and *CD11c.Bcl6^{KO}* mice for bulk RNA-sequencing (see Fig. 1A for gating). Principal component (PC) analysis showed that $XCR1^+$ cDC segregated from $XCR1^-CD11b^+$ cDC in all mouse models along PC axis 1, which accounted for 69% of the variance. This strongly supports the idea that Bcl6-deficient cDC1 and cDC2 maintained overall lineage identity (Fig. 3A). Nevertheless, PC2 separated the populations on the basis of Bcl6 presence or absence, accounting for 13% of the variance and suggesting that Bcl6 has a significant impact on the gene transcription profile of both cDC1 and cDC2. Interestingly, cDC1 from *XCR1.Bcl6^{KO}* and *CD11c.Bcl6^{KO}* mice clustered closely and were separated from control cDC1, while cDC2 in *CD11c.Bcl6^{KO}* mice were segregated from those in *XCR1.Bcl6^{KO}* and control mice, consistent with XCR1-cre being specific to cDC1 and indicating that Bcl6 regulates gene expression in both cDC subsets in a

https://doi.org/10.1038/s41467-024-46966-6

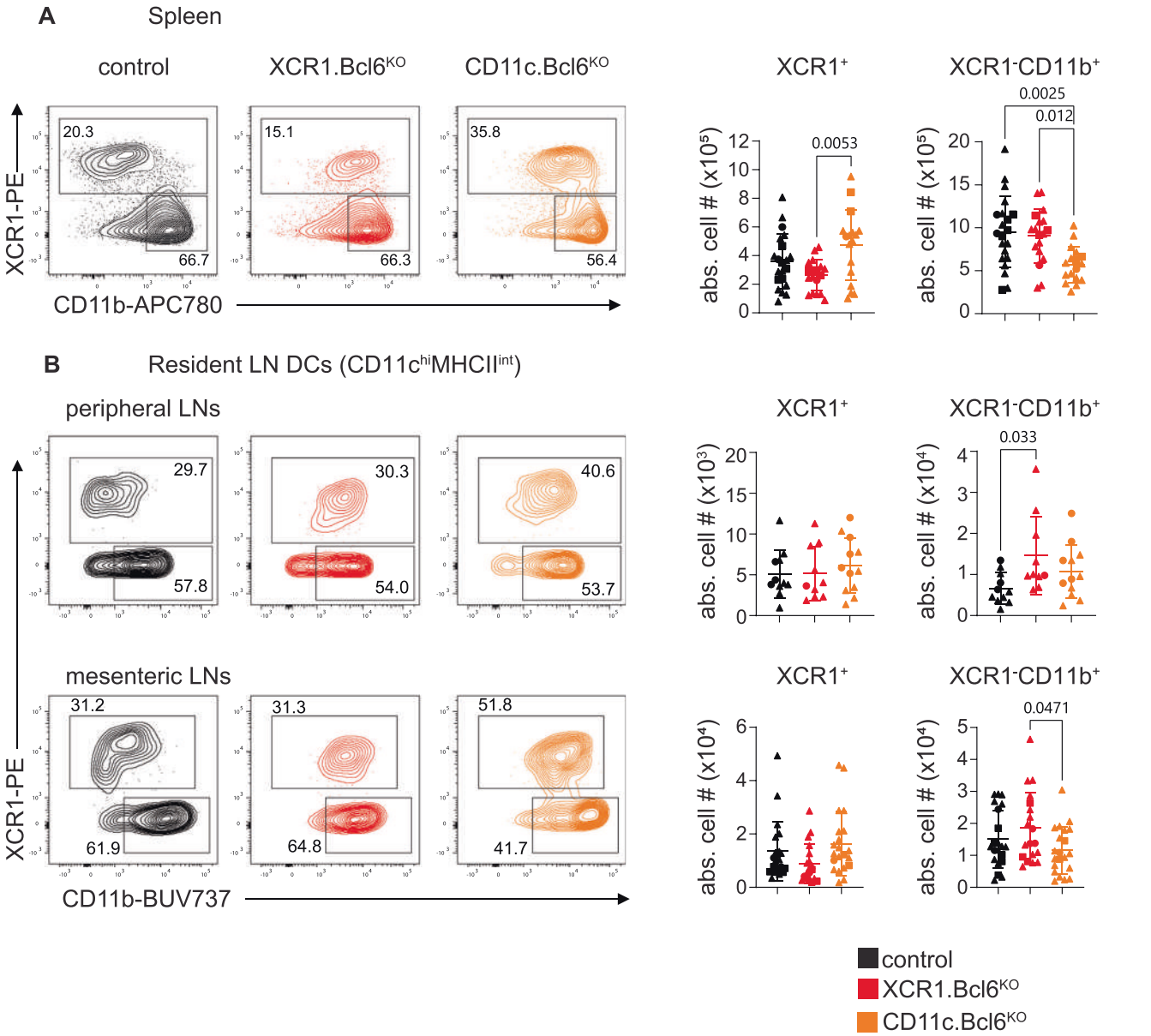

Fig. 1 | Phenotype and abundance of lymphoid tissue-resident cDC lacking Bcl6. A Left: Splenic XCR1$^+$ and XCR1$^-$CD11b$^+$ dendritic cell (DC) subsets in control (black), *XCR1.Bcl6^{KO}* (red), and *CD11c.Bcl6^{KO}* (orange) mice. Plots show representative staining profiles of gated live, single lineage$^-$ (CD3, CD19, CD64, B220, NK1.1), MHCII$^+$, and CD11c^{hi} splenocytes. Right: Absolute numbers of splenic XCR1$^+$ and XCR1$^-$CD11b$^+$ DC from control, *XCR1.Bcl6^{KO}*, and *CD11c.Bcl6^{KO}* mice. Statistical analysis by one-way ANOVA, exact *P* values are annotated. Data points represent values from individual mice pooled from 8 to 9 experiments with 1–5 mice per group, and lines represent means ± SD. **B** Left: Flow cytometry plots showing resident XCR1$^+$ and XCR1$^-$CD11b$^+$ DC subsets in the peripheral and mesenteric lymph nodes (pLN and mLN) of control, *XCR1.Bcl6^{KO}*, and *CD11c.Bcl6^{KO}* mice. Plots show representative staining profiles of gated single live, CD45$^+$, lineage$^-$ (CD3, CD19, CD64, B220, NK1.1), CD11c^{hi}MHCII^{int} resident DC. Right: Absolute numbers of resident cDC subsets in the pLN and mLN of control, *XCR1.Bcl6^{KO}*, and *CD11c.Bcl6^{KO}* mice. Statistical analysis by one-way ANOVA, exact *P* values are annotated. Data points represent values from individual mice pooled from 4 (pLN) and 8 (mLN) experiments with 2–3 (pLN) and 1–6 mice (mLN) per group, and lines represent means ± SD. Circles: females; triangles: males; squares: sex-information missing.

cell-intrinsic manner. PC3 accounted for 4% of the variance and showed opposite directional bias in Bcl6-deficient cDC1 and cDC2 (Fig. 3A). This suggests that Bcl6-mediated regulation of gene transcription may affect some targets in cDC1 and cDC2 differently.

To explore further how Bcl6 might regulate cDC lineage identity, we generated cDC1 and cDC2 signatures by identifying the top 50 genes that were differentially expressed between our control cDC1 and cDC2 and interrogated how these signatures were affected by a loss of Bcl6 expression (for gene lists and expression levels see Suppl. Data 1). Supporting their maintenance of lineage identity, XCR1$^+$ cDC from both *XCR1.Bcl6^{KO}* and *CD11c.Bcl6^{KO}* mice retained the expression of cDC1 markers, including *Irf8*, *Tlr3*, *Clec9a*, and *Cadm1* (Fig. 3B). However, *Cd8a* was downregulated in Bcl6-deficient XCR1$^+$ cDC and several genes associated with cDC2 identity were upregulated by XCR1$^+$ cDC in the absence of Bcl6, including *Sirpa*, *Zeb2*, *Csf1r*, and *Itgam* (encoding CD11b) (foldchange > 2, padjust <0.01). Although Bcl6-deficient CD11b$^+$ cDC2 did not express cDC1-specific markers, cDC2 from *CD11c.Bcl6^{KO}* mice showed altered expression of several classical cDC2 markers, of which some were further upregulated, such as *Csf1*, *Zeb2*, and *Itgam*, while others were downregulated, including *Clec4a4* and *CD4* (Fig. 3B). Despite maintenance of core lineage expression patterns, the overall transcriptional profiles of XCR1$^+$ and XCR1$^-$CD11b$^+$ cDC were

https://doi.org/10.1038/s41467-024-46966-6

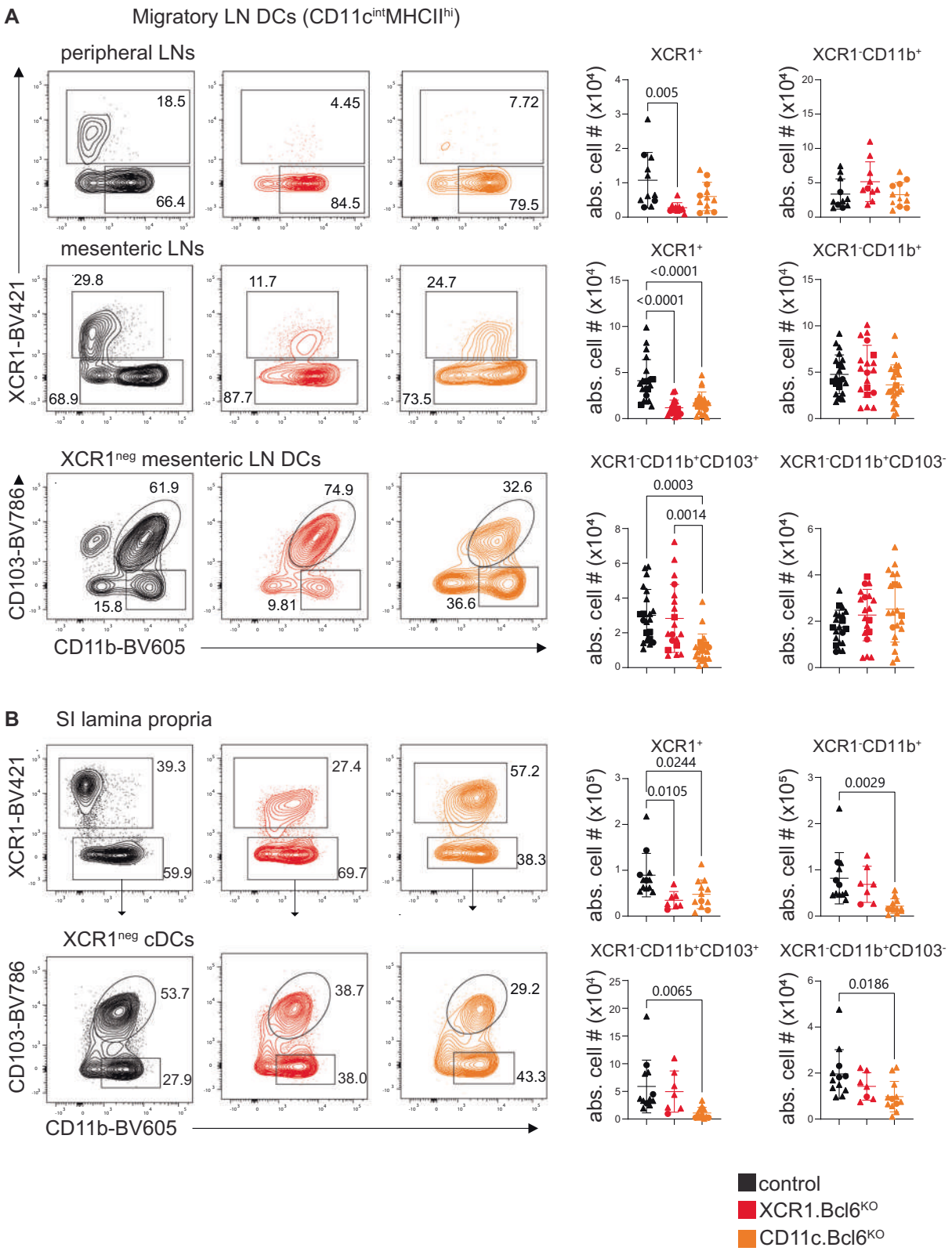

significantly altered in the absence of Bcl6 (Fig. 3A, C). In total, 607 genes were differentially regulated in XCR1$^+$ cDC from *XCR1.Bcl6^{KO}* mice compared with control cDC1, with 473 being upregulated and 134 downregulated. In contrast, of the 452 differentially regulated genes in cDC2 from *CD11c.Bcl6^{KO}* mice, only 206 were upregulated, compared with 246 downregulated genes (Fig. 3D, for a list of contributing genes, see Suppl. Data 2). Interestingly, only 79 genes were coordinately overexpressed in Bcl6-deficient cDC1 and cDC2, and 32 genes were coordinately downregulated in the absence of Bcl6 in both subsets. 12 genes were reciprocally regulated in the two subsets, of which 11 genes were upregulated in cDC1 and downregulated in cDC2 (including receptor-encoding genes *Ffar1* and *Lair1*, enzyme-encoding genes *Tgm2, Pigv*, and *Malt1* and genes encoding proteins implicated in cellular and intracellular adhesion and transport *Cdh17*, *Ctnnd2*, *Ston2*,

Fig. 2 | Phenotype and abundance of migratory cDC subsets lacking Bcl6. A Left: Flow cytometry plots showing migratory XCR1$^+$ and XCR1$^-$CD11b$^+$ dendritic cell (DC) subsets in the peripheral lymph nodes (LN) (pLN, top) and mediastinal LN (mLN, middle) of control (black), *XCR1.Bcl6^{KO}* (red), and *CD11c.Bcl6^{KO}* (orange) mice. mLN XCR1$^-$ DC are further sub-divided into CD103$^+$ and CD103$^-$ (bottom). Plots show representative staining profiles of live single, CD45$^+$, lineage$^-$ (CD3, CD19, CD64, B220, NK1.1), CD11c^{int}MHCII^{hi} migratory DC. Right: Absolute numbers of migratory cDC subsets from pLN and mLN of control, *XCR1.Bcl6^{KO}*, and *CD11c.Bcl6^{KO}* mice. Statistical analysis by one-way ANOVA, exact *P* values are annotated. Data points represent values from individual mice pooled from 4 (pLN) and 8 (mLN) experiments with 2–3 (pLN) and 1–6 mice (mLN) per group, and lines represent means ± SD. **B** Left: Flow cytometry plots showing SILP XCR1$^+$ and XCR1$^-$CD11b$^+$ DC subsets from control, *XCR1.Bcl6^{KO}*, and *CD11c.Bcl6^{KO}* mice. Plots show representative staining profiles of live, CD45$^+$, lineage$^-$ (CD3, CD19, CD64, B220, NK1.1), MHCII$^+$, CD11c^{hi} gated single cells. Right: Absolute numbers of XCR1$^+$ and XCR1$^-$CD11b$^+$ DC subsets from control, *XCR1.Bcl6^{KO}*, and *CD11c.Bcl6^{KO}* mice. Statistical analysis was performed by one-way ANOVA, exact *P* values are annotated. Data points represent values from individual mice pooled from 2 to 3 experiments with 2–3 mice per group, and lines represent means ± SD. Circles: females; triangles: males; squares: sex-information missing.

and *Rin2*). The gene for the actin-binding protein Plectin was the only gene upregulated in cDC2 and downregulated in cDC1. Taken together, although the lineage identity of splenic cDC1 and cDC2 is generally maintained in the absence of Bcl6, this does result in significant changes in subset-specific gene expression in both cDC subsets.

Bcl6-deficient cDC1 maintain the ability to cross-present antigen

To better characterize the impact of Bcl6-deficiency on cDC1, we next compared the expression of cDC1-related markers using flow cytometry. This confirmed the maintenance of Tlr3, Xcr1, Irf8, CD103, and Clec9a expression by XCR1$^+$ cDC from the spleen of *XCR1.Bcl6^{KO}* mice, as well as upregulation of CD11b and Sirpα and loss of CD8α (Fig. 4A). In addition, we detected higher expression of the costimulatory ligand CD24 on Bcl6-deficient cDC1.

The most characteristic property of cDC1 is to cross-present exogenous antigen to class I MHC-restricted CD8$^+$ T cells, a function that involves cell–surface receptors such as Clec9A (Dngr1) that mediate the uptake of dead cells[18,19]. Our gene expression analysis suggested that XCR1$^+$ cDC1 maintained the expression of *Clec9a* in the absence of Bcl6, and this was confirmed by flow cytometry (Fig. 4A). We therefore examined whether cross-presentation was intact in *XCR1.Bcl6^{KO}* animals by injecting heat-killed ovalbumin-expressing mouse embryonic fibroblasts (OVA-MEFs) into recipient mice adoptively transferred with OVA-specific TCR-transgenic CD8$^+$ T cells from OT-I mice. OT-I cell proliferation strictly depends on cDC1-mediated cross-presentation in this model[17]. OT-I cells proliferated to a similar extent in the spleens of OVA-MEF-injected *XCR1.Bcl6^{KO}* and control mice (Fig. 4B, C), suggesting that Bcl6-deficient cDC1 retain their ability to cross-present. OT-I cell proliferation was also observed in the mLN. In the mLN of *XCR1.Bcl6^{KO}* mice OT-I cells showed somewhat diminished proliferation compared to control mice. This most likely reflects the decreased number of migratory cDC1 in the mLN of *XCR1.Bcl6^{KO}* mice (Fig. 2A), as mLN cDC1 from *XCR1.Bcl6^{KO}* cross-presented antigen with comparable efficiency as control cDC1 in an in vitro cross-presentation assay upon cDC1-input normalization (Suppl. Fig. 4).

Bcl6-deficiency in cDC1 causes alterations in immunologically relevant pathways

For a broader assessment of whether the absence of Bcl6 influences the immunological functions of cDC1, we next performed gene set enrichment analysis of the RNA-Seq data from XCR1$^+$ cDC in *XCR1.Bcl6^{KO}* and control mice. This showed that several immunologically relevant gene ontology pathways were enriched within the differentially expressed gene sets, including *leukocyte adhesion*, *proliferation* and *activation*, as well as *production of IL-1* (Fig. 5A). In parallel, KEGG pathway analysis highlighted differences in *cytokine-cytokine receptor interactions, NOD-like receptor signaling pathway, MERK signaling pathway, hematopoiesis cell lineage, Tuberculosis* and *C-type lectin receptor signaling pathway* (Fig. 5B, C). Upregulated genes were generally enriched for pro-inflammatory signals, and among others, we found an over-representation of genes involved in the IL-6 pathway in cDC1 from *XCR1.Bcl6^{KO}* mice (Suppl. Fig. 5). Interestingly, we detected higher levels of serum IL-6 in *XCR1.Bcl6^{KO}* mice injected with the double-stranded RNA-mimic poly(I:C) when compared to treated controls (Fig. 5D). These data suggest that Bcl6-mediated transcriptional repression in cDC1 may tune the function of this subset[18,19,17].

Taken together, although cDC1-specific Bcl6 deficiency alters the phenotype and transcriptional profile of cDC1, the hallmark function of cDC1 to cross-present antigen is largely unaffected by the loss of Bcl6.

Bcl6-deficiency results in a selective loss of Notch2-dependent cDC2

In addition to its role in cDC1, our initial results also revealed a significant role for Bcl6 in the gene expression signature of cDC2. Furthermore, the numbers of cDC2 were reduced in the spleen of *CD11c.Bcl6^{KO}* mice, as were the numbers of cDC2 expressing CD103 in the intestinal LP and mLNs. Diminished cDC2 numbers in the blood of CD11c.Bcl6^{KO} mice suggest that this was not due to a release of cDC2 into the bloodstream (Suppl. Fig. 2B). The remaining cDC in the spleen of *CD11c.Bcl6^{KO}* mice also showed somewhat lower expression of MHCII and higher expression of CD11b than control cDC2 (Fig. 6A). Further phenotyping of spleen cDC2 in *CD11c.Bcl6^{KO}* mice revealed a striking loss of the ESAM^{hi} cDC2 subset (Fig. 6B and Suppl. Fig. 2). We verified our findings in an independent mouse model in which Bcl6 deletion was induced by cre recombinase under the control of the *Clec9a* promoter, which targets cDC precursors and their progeny and some pDCs but no other leukocytes[36]. These mice additionally carry a YFP reporter following a floxed stop cassette in the ubiquitous ROSA26 locus to monitor targeting efficiency. As in *CD11c.Bcl6^{KO}* mice, spleen cDC in *Clec9a.Bcl6^{KO}* mice showed altered CD11b expression and loss of ESAM^{hi} cDC2 (Fig. 6C, D and Suppl. Fig. 6). This was apparent in the analysis of bulk cDC2 in *Clec9a.Bcl6^{KO}* mice and was even more pronounced when pre-gating on YFP$^+$ instead of CD11c, which enriches cDC2 with a history of *Clec9a*-promoter activity (Fig. 6E). Importantly, this also shows that CD11c downregulation in the absence of Bcl6 does not account for the reported phenotype (for a side-by-side comparison of CD11c- and Clec9A-reporter-based gating strategies see Suppl. Fig. 7).

As expected[28], the ESAM^{lo} subset of cDC2 expressed slightly lower levels of CD11c compared to their ESAM^{hi} counterparts, and a significant proportion lacked expression of 33D1 and CD4, which were expressed uniformly by ESAM^{hi} cDC2 (Fig. 6F). The total population of cDC2 remaining in *CD11c.Bcl6^{KO}* mice resembled the ESAM^{lo} population in terms of these markers but expressed higher levels of CD11b and IRF4 than either ESAM^{hi} or ESAM^{lo} control cDC2 subset, suggesting these markers may be specific targets of Bcl6 repression.

To explore the nature of the cDC2 remaining in the spleen of *CD11c.Bcl6^{KO}* mice further, we performed gene set enrichment analysis (GSEA) of differentially expressed genes between *CD11c.Bcl6^{KO}* and control cDC2 in gene sets derived from publicly available bulk RNA-Seq data from ESAM^{hi} and ESAM^{lo} cDC2 from control spleen[37]. As expected from their usual predominance in the control spleen, control cDC2 gene signatures were highly enriched in ESAM^{hi} vs ESAM^{lo} gene sets, while *CD11c.Bcl6^{KO}* cDC2 gene signatures were highly enriched in ESAM^{lo} vs ESAM^{hi} gene sets (Fig. 7A). We next directly compared the set of genes that were differentially expressed in ESAM^{hi} vs ESAM^{lo} cDC2 with the gene set differentially expressed

https://doi.org/10.1038/s41467-024-46966-6

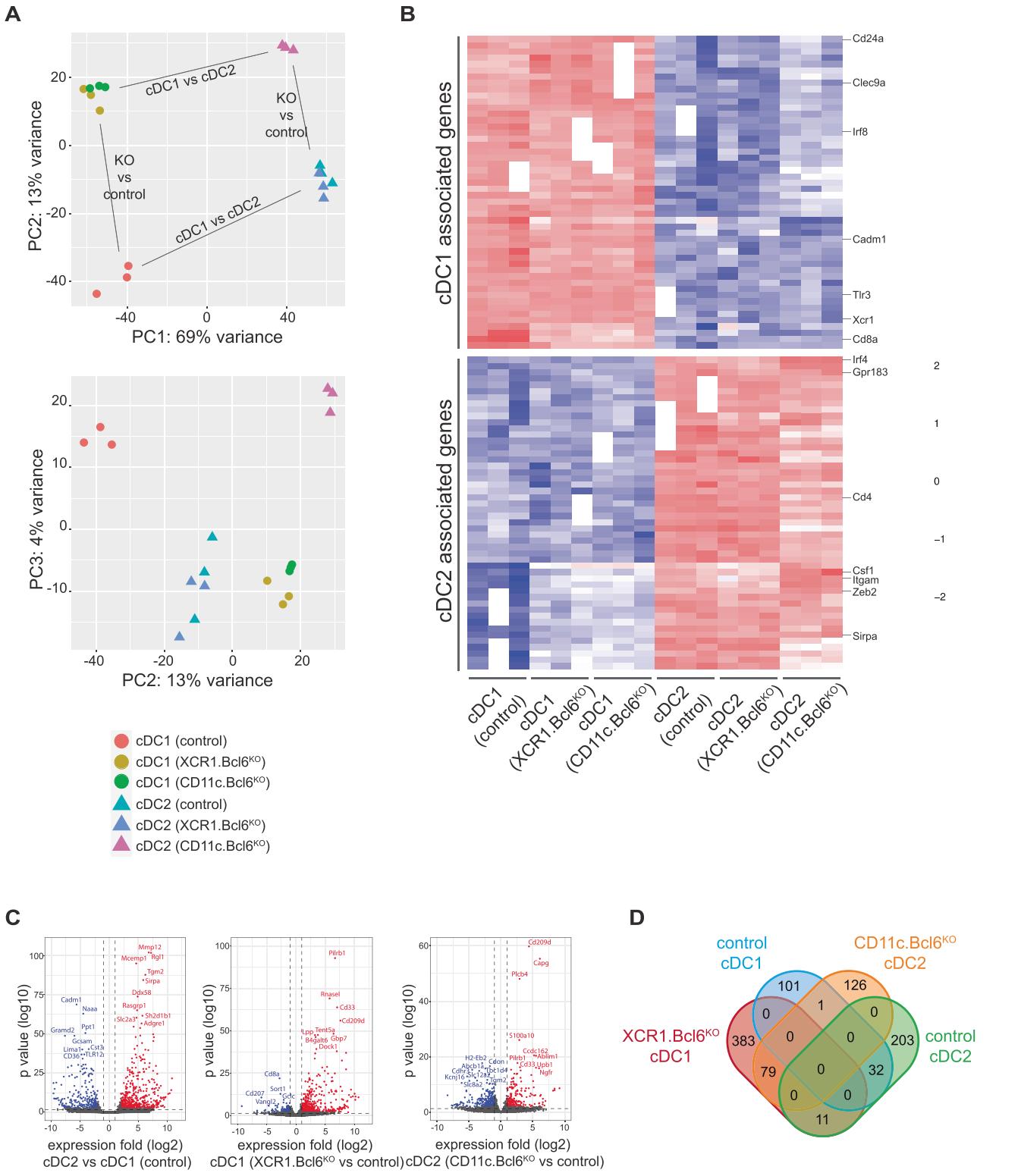

in *CD11c.Bcl6*^{KO} vs control cDC2. In accordance with the GSEA data, the majority of the top 50 genes expressed more prominently by ESAM^{hi} cDC2 were also significantly over-represented in the population of total control cDC2, which expressed much fewer of the top 50 genes from ESAM^{lo} cDC2 (Fig. 7B). Conversely, the genes overexpressed by total cDC2 from *CD11c.Bcl6*^{KO} spleen showed much more overlap with the top 50 genes expressed by ESAM^{lo} cDC2, while the genes overexpressed by ESAM^{hi} cDC2 were mostly downregulated in Bcl6-deficient cDC2 (Fig. 7B, for a complete gene list containing expression levels, see Suppl. Data 3). These data confirm that Bcl6 deficiency in DC causes the loss of the ESAM^{hi} lineage of splenic cDC2.

DC-specific loss of Bcl6 causes defects in Tfh and Tfr cell generation in the spleen

ESAM^{hi} spleen DC reside in the marginal zone bridging channels, where they play a prominent role in the induction of germinal centers (GC)[29].

Fig. 3 | Lineage identity of splenic Bcl6-deficient cDC subsets. A Principal component analysis (PCA) plot of gene expression data obtained from bulk RNA-seq using DESeq2 (PRJNA834905). Color-coded icons show classical dendritic cells (cDC)1 and cDC2 from the spleen of control, *XCR1.Bcl6*^{KO}, and *XCR1.Bcl6*^{KO} mice. Three replicates were included in each group. **B** Heatmap of selected highly expressed cDC1 or cDC2 associated genes in all RNA-Seq samples (50 most differentially expressed genes between cDC1 and cDC2 chosen from the 100 genes with highest expression level among total differentially expressed genes (fold change ≥ 2, padj: 0.01, calculated by DESeq2 using Benjamini–Hochberg corrections of two-sided Wald test *P* values) in control samples). The color scale represents the row *Z* score. **C** Volcano plots showing the global transcriptional differences between splenic cDC2 and cDC1 in control (left), *XCR1.Bcl6*^{KO} (middle) and *CD11c.Bcl6*^{KO} mice (right). Each circle represents one gene. The log2FoldChange (LFC) is represented on the *x*-axis. The *y*-axis shows the −(log10 of the *p* adjust value). A padj value of 0.01 (calculated by DEseq2 using Benjamini–Hochberg corrections of two-sided Wald test *P* values) and an absolute LFC of 1 is indicated by dashed lines. The upregulated or downregulated genes are shown in red or blue dots, respectively, and the top-ranked gene symbols with the lowest padj value were annotated in the plot. **D** VENN diagram showing significantly elevated differentially expressed genes (DEG) (|Log2foldchange | ≥1 and padj < 0.01) between *XCR1.Bcl6*^{KO} cDC1 (red) and control cDC1 (blue), and between *CD11c.Bcl6*^{KO} cDC2 (orange) and control cDC2 (green).

Confocal microscopy using CD11c as a pan-DC marker and TLR3 and Sirpα to define cDC1 and cDC2, respectively, confirmed a substantial loss of DC from this region in the *CD11c.Bcl6*^{KO} spleen (Fig. 8A). This was also evident in *Clec9a.Bcl6*^{KO} and *Clec9a.Bcl6*^{WT} control mice carrying a YFP reporter under the control of the *Clec9a* promoter, in which Bcl6-deficiency in DCs led to a similar decrease in marginal zone bridging channel DCs (Fig. 8B). To test the functional relevance of this defect, we adoptively transferred OVA-specific TCR-transgenic CD4$^+$ T cells (OT-II) into control and *CD11c.Bcl6*^{KO} mice immunized the mice with OVA + poly(I:C) intraperitoneally and assessed the generation of antigen-specific Tfh cells three days later (Suppl. Fig. 8A). We chose this timepoint because this early Tfh cell induction is independent of GC B cells[38,39], which are known to express CD11c and are required for the maintenance of Tfh cells at later times[40]. Although OT-II cells expanded normally in the *CD11c.Bcl6*^{KO} mice, in response to immunization, the early induction of antigen-specific CXCR5$^+$Bcl6$^+$ Tfh cells was markedly reduced in immunized *CD11c.Bcl6*^{KO} mice compared to control mice (Suppl. Fig. 8A), suggesting that Bcl6-dependent cDC indeed drive early Tfh cell induction in this model. To enable analysis of later time points of the Tfh cell response and to confirm our findings in mice in which Bcl6 deletion is confined to cDC, we next adoptively transferred naïve OT-II cells into *Clec9a.Bcl6*^{WT} control or *Clec9a.Bcl6*^{KO} mice, followed by i.p. immunization with NP-OVA in alum adjuvants and analysis of the spleen seven days later (Fig. 8C). The frequency of CXCR5$^+$PD-1$^+$ and CXCR5$^+$Bcl6$^+$ Tfh cells was significantly reduced in OT-II cells recovered from *Clec9a.Bcl6*^{KO} hosts as compared to control animals (Fig. 8D and Suppl. Fig. 8B). To better assess the long-term effects of DC-restricted Bcl6 deficiency on Tfh cell and humoral immune responses, we immunized *Clec9a.Bcl6*^{WT} and *Clec9a.Bcl6*^{KO} mice i.p. with NP-KLH/alum and analyzed the spleens two weeks later (Fig. 8E). Total spleen cellularity was not significantly increased in *Clec9a.Bcl6*^{KO} mice (Fig. 8F). As regulatory T (Treg) cells do not develop from naive OT-II precursor cells, such as in the previous adoptive transfer experimental setting, and Tfr cells share similarities with Treg cells and Tfh cells[41,42], such as expression of Foxp3 and Bcl6, respectively, we quantified all three subsets within the endogenous T cell compartment following NP-KLH/alum immunization. Total numbers of Foxp3$^-$ and Foxp3$^+$ CD4$^+$ T cells were not affected by DC-restricted Bcl6-deficiency (Fig. 8F and Suppl. Fig. 8C). While the frequencies of endogenous CXCR5^{int}PD-1^{int} and CXCR5^{int}Bcl6^{int} Tfh cells were reduced among conventional Foxp3$^-$ CD4$^+$ T cells of the conditional knockout mice, the frequencies of GC Tfh cells, gated as CXCR5^{hi}PD-1^{hi} or CXCR5^{hi}Bcl6^{hi}, were not altered in *Clec9a.Bcl6*^{KO} mice at day 14 after immunization (Fig. 8G, H, and Suppl. Fig. 8C). In contrast, we observed a strong reduction in CXCR5^{hi}PD-1^{hi} or CXCR5^{hi}Bcl6^{hi} Tfr cells among Foxp3$^+$ CD4$^+$ T cells (Fig. 8G, H, and Suppl. Fig. 8C), indicating that Bcl6 in DCs is particularly important for the generation of Tfr cells. To address the impact of DC-restricted Bcl6-deficiency on the antibody response, we assessed the NP-specific serum antibody levels at different time points following NP-KLH/alum immunization (Fig. 8 I), focusing on total IgG and the signature isotype induced by type-2 immunization with alum adjuvants, IgG1. Quantifying both the amounts of NP-specific antibodies against NP_{36}-coated BSA, a proxy for total NP-binding antibodies, as well as against NP_2-coated BSA, a proxy for high-affinity NP-binding antibodies, we found reduced NP-specific antibody responses in *Clec9a.Bcl6*^{KO} mice (Fig. 8J and Suppl. Fig. 8D). In conclusion, Bcl6 deficiency in cDC causes the loss of ESAM^{hi} cDC2 and impairs Tfh, Tfr, and antibody responses in the spleen.

DC-specific loss of Bcl6 causes defects in Th17 cell priming in the colon of mice infected with *C. rodentium*

In addition to their role in driving GC reactions in the spleen, Notch2-dependent cDC2 have been shown to support Th17-dependent immunity towards *C. rodentium* in the colon[22]. The colonic LP (cLP) of *CD11c.Bcl6*^{KO} mice contained significantly fewer cDC than control mice, with the most pronounced loss detected in the CD103$^+$ cDC2 population (Fig. 9A, B). To analyze whether Bcl6-deficiency recapitulated the functional consequences of Notch2-deficiency, we infected *CD11c.Bcl6*^{KO} and control littermates with *C. rodentium*. *CD11c.Bcl6*^{KO} mice lost comparable weight to control littermates early after infection, with delayed recovery as evidenced by significantly lower body weight from day 11 onwards (Fig. 9C). Consistent with a lack in weight difference between genotypes at day nine post-infection, colon length, and bacterial load were comparable at this time point, while there was a tendency towards shorter colons and elevated bacterial load in *CD11c.Bcl6*^{KO} mice compared to control littermates 21 days post-infection (Fig. 9C). At this late stage during infection, colons from *CD11c.Bcl6*^{KO} mice continued to show mild pathology, while control littermates appeared fully healed (Fig. 9D). In parallel, there were blunted Th17 responses in the cLP of *CD11c.Bcl6*^{KO} mice nine days after *C. rodentium* infection (Fig. 10A, gating strategies depicted in Suppl. Fig. 9), while Th1 and Treg numbers were not affected. This defect in Th17 priming was no longer evident 21 days after infection (Fig. 10B). To address whether our results were due to a lack of Bcl6 in bona fide DCs, we infected *Clec9a.Bcl6*^{KO} mice and controls with *C. rodentium* and analyzed their CD4 T cell compartment on day 9 post-infection. While we detected a trend towards lower RORγt$^+$ CD4 T cell numbers, Tbet$^+$ and Foxp3$^+$ CD4 T cells were more prominently affected (Suppl. Fig. 10A). Analysis of YFP expression as a surrogate of *Clec9a.cre* activity in intestinal DCs in *Clec9a.Bcl6*^{KO} mice, however, revealed only partial targeting of cDC2 in the gut, potentially explaining the moderate deficiency in Th17 priming (Suppl. Fig. 10B).

These data show that Bcl6-deficiency in CD11c$^+$ mononuclear phagocytes causes the loss of a prominent colonic cDC2 subset, with a consequent defect in Th17 priming in response to *C. rodentium* infection, leading to delayed healing and recovery.

Discussion

We show here that Bcl6-deficiency in the DC compartment causes major transcriptional alterations with subset-specific consequences. Specifically, Bcl6-deficient cDC1 acquire an XCR1/CD11b double-positive phenotype not seen in control mice, where XCR1 and CD11b are mutually exclusive markers of cDC1 and cDC2, respectively. However, Bcl6-deficient cDC1 retained a cDC1-like transcriptome, cDC1 lineage markers, and the ability to cross-present. The lack of Bcl6 in DC also revealed a critical role for Bcl6 in the development of the ESAM^{hi}

https://doi.org/10.1038/s41467-024-46966-6

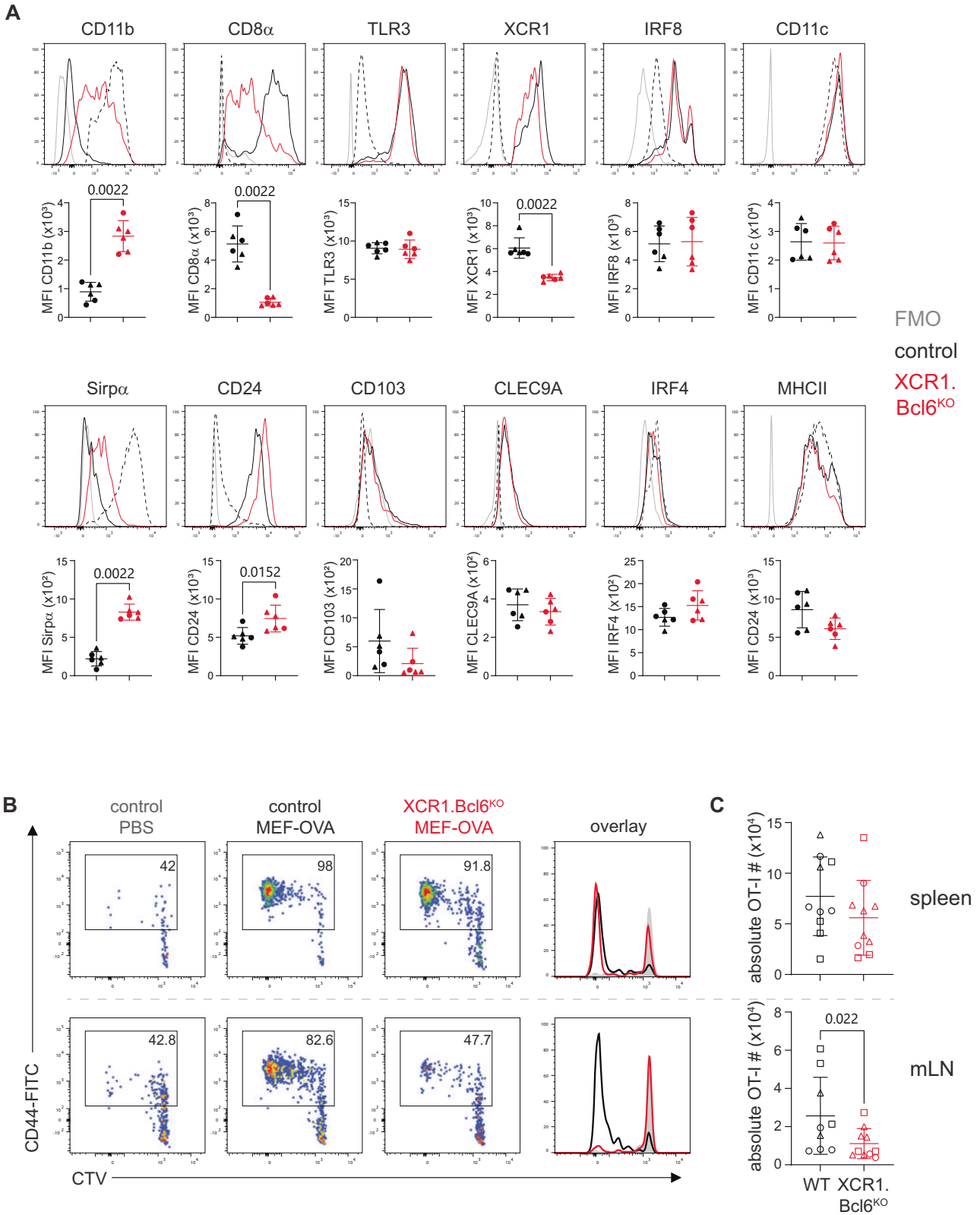

subset of cDC2 in the spleen and CD103$^+$CD11b$^+$ cDC2 in the intestines, and there was a parallel defect in splenic Tfh cell induction in response to protein antigen immunization and in intestinal Th17 induction in response to *C. rodentium* infection. Together these findings extend the role of Bcl6 to the regulation of cDC2 behavior in GC function and the periphery.

We previously described a selective loss of putative cDC1 in the spleen of Bcl6-deficient mice based on the absence of CD8α$^+$CD11b$^-$ cDC[20]. Here we refine this interpretation by showing that the numbers of resident cDC1 are, in fact normal when Bcl6 is lacking in CD11c$^+$ cells or cDC1, but they upregulate CD11b and down-regulate CD8α, causing them to merge into the classical cDC2 gate. In contrast, the numbers of

Fig. 4 | Phenotype and cross-presentation abilities by cDC1 deficient in Bcl6. **A** Flow cytometric analysis of classical dendritic cells (cDC)1 in the spleen of control and *XCR1.Bcl6*^{KO} mice. Representative histograms show indicated protein expression by control (black) and *XCR1.Bcl6*^{KO} (red) cDC1, with fluorescent minus one (FMO) staining shown in gray, and control cDC2 is shown as a dashed line. Dot plots show FMO-subtracted mean fluorescent intensity (MFI) values. Pre-gating on cDC1 and cDC2 was performed as in 1A. Histograms are representative of 3 independent experiments with 3 mice each MFI plots show 2 out of 3 experiments, and lines represent means ± SD. Statistical analysis using the Mann–Whitney test, exact *P* values are annotated. **B** Representative flow cytometry plots showing cell tracer violet (CTV) dilution and CD44 expression on OT-I cells (gated on live, CD3$^+$CD8$^+$CD45.1$^+$ single cells) in the spleen (top) and mesenteric lymph nodes (mLN, bottom) of control and *XCR1.Bcl6*^{KO} recipient mice 3 days after i.p. immunization with heat-shocked ovalbumin-expressing mouse embryonic fibroblasts (OVA-MEF). Data are representative of 3 independent experiments with 2–5 mice each. **C** Total number of OT-I cells in the spleen (right) and mLN (left) of immunized control and *XCR1.Bcl6*^{KO} mice. Data are pooled from 3 independent experiments with 1–4 mice each. Data points represent values from individual mice mouse, and lines represent means ± SD. Statistical analysis using the Mann–Whitney test, exact *P* values are annotated. Circles: females; triangles: males; squares: sex-information missing.

migratory CD11b$^-$ CD103$^+$ cDC1 are decreased in the mLN and intestinal mucosa of mice lacking Bcl6 within the DC compartment, a finding supported by defective cross-presentation activity in the mLNs. We currently cannot explain the differential effects of Bcl6 deficiency on resident versus migratory cDC1 populations. However, a similar dichotomy has been described recently for dependence on DC-SCRIPT, whose absence predominantly diminished resident cDC1[43]. As Bcl6 primarily acts as a transcriptional repressor, it is possible that DC-SCRIPT and Bcl6 integrate into a feedback loop to regulate cDC1 migration or survival upon maturation, and this idea requires further study.

As Bcl6 is not expressed by DC progenitors in the bone marrow and their frequency is not affected by the lack of Bcl6[35,44], Bcl6 seems to act downstream of other cDC1 lineage specifying TFs such as IRF8, Nfil3, BATF3, DC-SCRIPT, and Id2. In models deficient of those TFs, the cDC1 lineage is affected from the precursor level onwards, preventing their expression of all lineage markers, as well as their ability to cross-present antigen[10,12–14,43,45–48], hallmarks that were preserved in Bcl6-deficient cDC1. Rather, it appears that Bcl6 may fine-tune cDC1 identity by suppressing selected cDC2 genes at the mature state, and as a result, Bcl6-deficient cDC1 maintain key cDC1 genes such as XCR1, TLR3, and CLEC9A as well as cross-presentation function. However, they show a gene expression profile that suggests a cDC2-related "gain-of-function", with enhanced expression of genes of the cytokine-cytokine receptor pathway, cell adhesion and migration pathways, and pathways associated with inflammasome activity. Interestingly, cDC1 with upregulated CD11b and Sirpα have also been described when the TF ZEB2 is over-expressed from the pre-cDC stage onwards[25]. Exploring how Bcl6 interacts with this and other lineage-determining factors to regulate cDC1 gene expression and functions will be an important topic for future research.

CD11c.Bcl6^{KO} and *Clec9a.Bcl6*^{KO} mice lacked the dominant subset of ESAM^{hi} cDC2 in the spleen, and a comparison of gene expression profiles between ESAM^{hi} and ESAM^{lo} control cDC2 subsets and cDC2 from *CD11c.Bcl6*^{KO} mice showed that Bcl6-deficient cDC2 closely aligned with control ESAM^{lo} cDC2. However, this overlap was not absolute, suggesting that Bcl6-deficiency causes transcriptional changes in all cDC2. For example, the extent of dysregulation of IRF4 and CD11b expression in the absence of Bcl6 cannot solely be explained by the loss of ESAM^{hi} cDC2. In addition, both markers were also upregulated in Bcl6-deficient cDC1, again indicating a wider role for Bcl6 in control of mature cDC differentiation. Interestingly, the consequences of Bcl6-deficiency on cDC overlap with those previously shown for Notch2-deficiency[20,28,34]. Specifically, both strains show deficiencies in cDC1 and ESAM^{hi} cDC2, but it remains to be determined whether the apparent loss of cDC1 in Notch2-deficient animals reflects the genuine absence of these cells, or is because their phenotype has simply changed, as we show in Bcl6-deficient mice. Of note, the cDC1 marker CD24 is upregulated in both Bcl6- and Notch2-targeted mice (our study and[22,28]), arguing against a developmental defect within the cDC1 spleen compartment in Notch2-targeting models. It will be of interest to explore how the Notch2- and Bcl6-pathways interact in DC biology.

Consistent with the findings that cDC2 equivalent to the ESAM^{hi} population located preferentially in marginal zone bridging channels in the spleen[49], the dysregulation in splenic cDC populations in both Bcl6- and Notch2-deficient mice was associated with a loss of cDC from this region of the spleen ([29] and current results). Localization of cDC2 to the bridging channels is dependent on the homing receptor GPR183[50,51] and Bcl6 regulates GPR183 expression in B cells[52]. However, GPR183 expression levels were not altered in Bcl6-deficient cDC2, suggesting either that additional factors are required for the correct positioning of cDC2 in the spleen or that Bcl6-deficiency causes a development block or diminished survival within ESAM^{hi} cDC2 irrespective of their location. Along those lines, GPR183-deficiency in cDC2 specifically diminished antibody response generation to particulate antigen, while responses to soluble antigen were unaffected[51]. The defect in ESAM^{hi} cDC2 we found in *CD11c.Bcl6*^{KO} and *Clec9a.Bcl6*^{KO} mice were accompanied by reduced induction of Tfh cells in response to parenteral immunization with soluble OVA, suggesting a general deficiency in supporting GC reactions in these mice. While it has been suggested that Notch2 is needed to ensure correct positioning of cDC2 for access to antigen in the bloodstream[28], it has to our knowledge, not been addressed whether response deficits were limited to particulate antigen in these mice. Further investigation is needed to explore the importance of correct localization on development, survival, and antigen capture by cDC2 and how this might be controlled by a Bcl6–Notch2 axis.

DC-specific deletion of Bcl6 caused alterations in the generation of Tfh cells, Tfr cells, and corresponding antibody responses. As T and B cell-intrinsic expression of Bcl6 is known to be required for Tfh cell and GC B cell differentiation[33,53], our findings extend this concept to the DC stage. Our data indicate that Tfh and Tfr cell fates of activated conventional CD4$^+$ T cells and Treg cells, respectively, are predetermined or imprinted by Bcl6 expression patterns already in DCs. One interesting finding was the strong effect of DC-specific Bcl6 deficiency on Tfr cells, which are believed to mainly develop from thymic Tregs[41,42]. Given the stronger reduction in Tfh cells in *Clec9a.Bcl6*^{KO} mice at early stages following immunization (days three and seven), as compared to later stages (day 14), it is possible that a continued lack of Tfr-mediated suppression of Tfh cells may allow for a compensatory outgrowth of Tfh cells over time, thus mitigating the net effects of DC-specific Bcl6 deficiency. This would be in line with the multistep differentiation process of Tfh cells in which B cells become the sole antigen-presenting cell subset in GCs, with no classical DCs being present in GCs[54].

XCR1$^-$ CD11b$^+$CD103$^+$ intestinal LP DC were also reduced in the absence of Bcl6 in DC, again mirroring the phenotype observed in Notch2-deficient mice[22,28]. cDC2 are potent drivers of Th17 responses in the intestines[23,55], but recent findings suggest that DC-independent Th17 cell induction can also occur[56]. As *CD11c.Notch2*^{KO} mice succumb early to *C. rodentium* infection due to deficient IL-23-driven innate immunity, the adaptive immune response has not been investigated in this model[22]. In contrast, the early stages of infection were normal in *CD11c.Bcl6*^{KO} mice, but these mice showed a delay in recovery at later stages and altered kinetics of Th17 induction, with significantly lower

https://doi.org/10.1038/s41467-024-46966-6

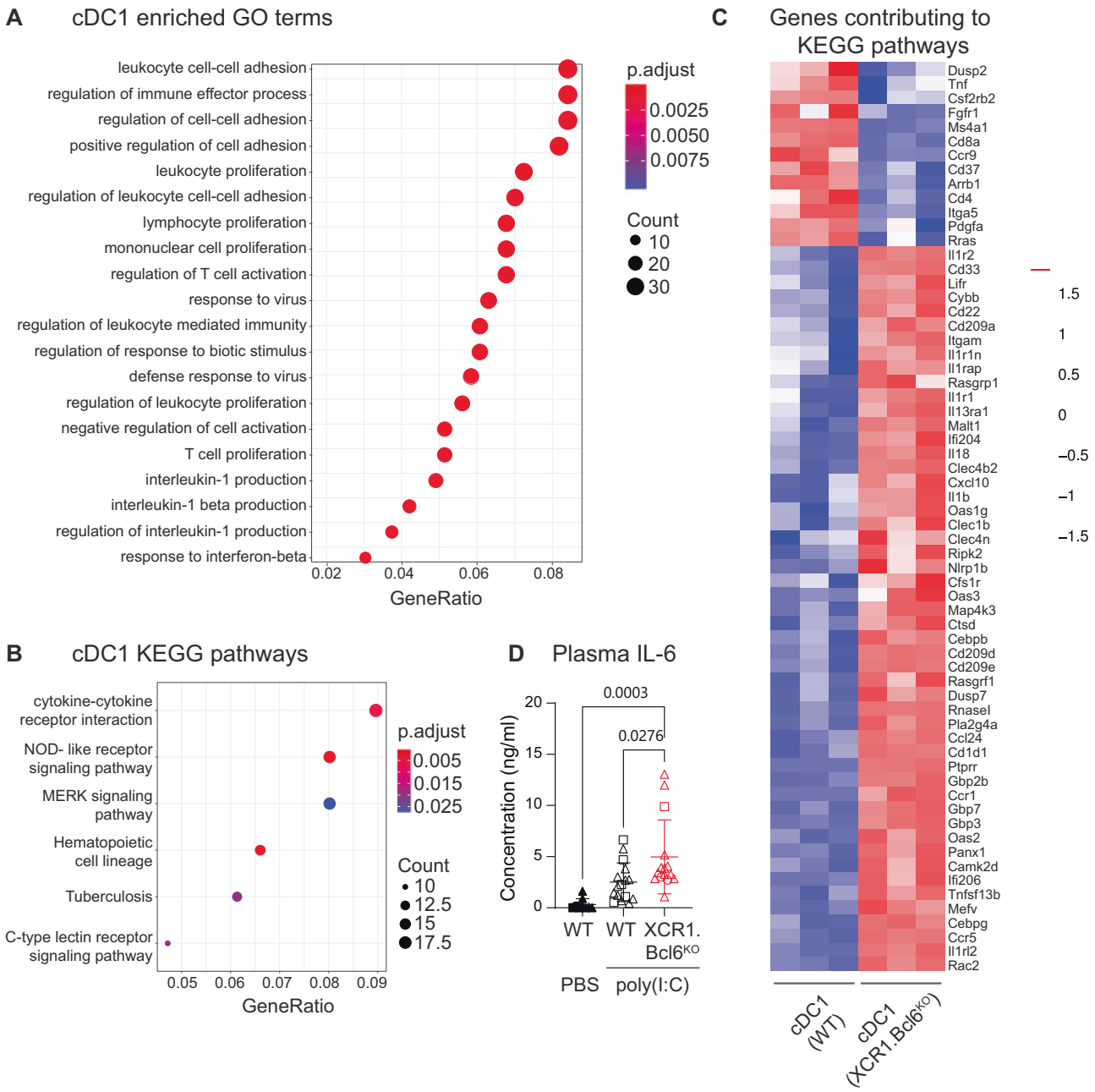

Fig. 5 | Differentially expressed genes in Bcl6-deficient splenic cDC1. A Gene ontology (GO) term enrichment analysis of differentially expressed genes (DEG) in *XCR1.Bcl6*^{KO} and control cDC1 (PRJNA834905). The *p* value calculated from GO term enrichment analysis is represented on the *x*-axis, and the y-axis shows the GO Biological Process (BP) terms. *P*-values were calculated by using enrichGO function from R package clusterProfiler with the one-sided hypergeometric test. **B** KEGG (Kyoto Encyclopedia of Genes and Genomes) term enrichment analysis of DEGs in *XCR1.Bcl6*^{KO} vs control cDC1. The GeneRatio value calculated from KEGG term enrichment analysis is represented on the *x*-axis, and the *y*-axis shows the KEGG enriched terms. **C** Heatmap of all genes contributing to the enriched KEGG pathways depicted in (**B**). The color scale represents the row *Z* score. **D** IL-6 levels in the serum of *XCR1.Bcl6*^{KO} vs control mice injected intraperitoneally with poly(I:C) 2 h before analysis. Data are pooled from 6 experiments with 1–6 mice each (2 experiments without untreated controls), and lines represent means ± SD. Statistical analysis was performed by one-way ANOVA (and Tukey's multiple comparison test), and exact *P* values were annotated. Circles: females; triangles: males; squares: sex-information missing.

Th17 numbers at day nine, which had normalized by day 21. We cannot currently explain the differences in the early innate immune response between *CD11c.Notch2*^{KO} and *CD11c.Bcl6*^{KO} mice, but our data are consistent with the idea that DCs play the dominant role in coordinating the adaptive immunity required to terminate the infection. However, while Bcl6-dependent cDC2 support optimal Th17 induction to *C. rodentium*, they are not essential for this response, as Th17 numbers normalized over time, possibly due to continuous proliferation in the presence of the pathogen.

Our results show that Bcl6 deficiency does not alter cDC1 and cDC2 lineage identity, but it alters their transcriptional profile and relative abundance of both lineages and their subsets in different tissues. Specifically, although cDC1 in all tissues examined acquired several cDC2 markers in the absence of Bcl6, they retained their transcriptional and functional identity as cDC1. In contrast, Bcl6 deficiency had differing effects on cDC2 subsets that depended on their location and phenotype, with selective depletion of ESAM^{hi} cDC2 in spleen and CD103^{+}CD11b^{+} cDC2 in the intestine. These effects were

https://doi.org/10.1038/s41467-024-46966-6

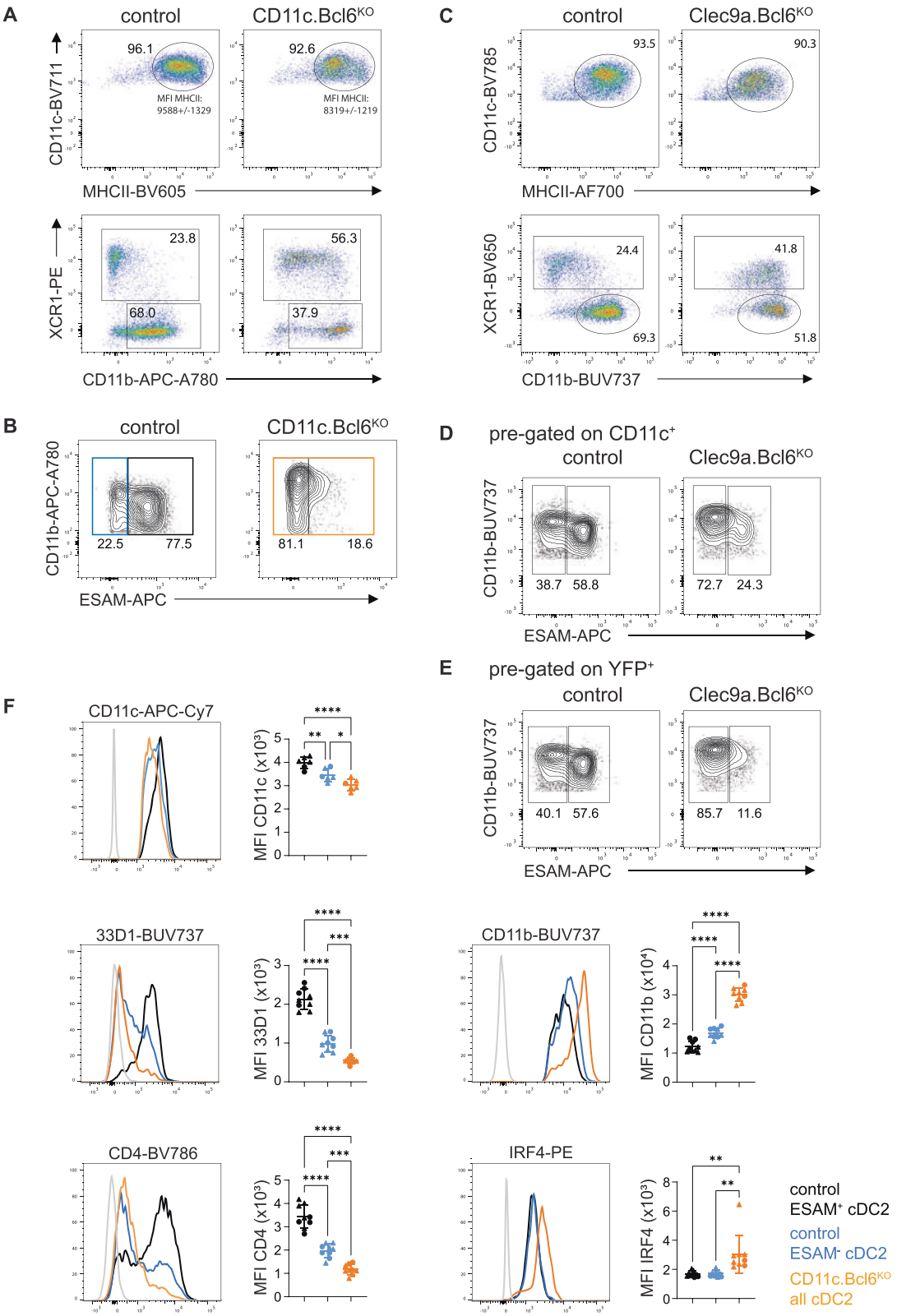

similar to those described for a deficiency in Notch2 and had significant functional consequences for adaptive immunity in the spleen and intestine. These data add to the emerging and poorly understood heterogeneity within the cDC2 compartment by establishing that certain cDC2 subsets require Bcl6 expression in the DC compartment in addition to Notch2- and lymphotoxin β-signaling. Finally, complementary to its established roles in controlling B and T cell-intrinsic cell fate decisions[53], our findings establish Bcl6 as a subset-specific regulator of DC development and function with critical consequences for the induction of adaptive immune responses.

Methods

All reagents, including manufacturer, catalog number, and dilutions, are listed in Suppl. Data 4.

https://doi.org/10.1038/s41467-024-46966-6

Fig. 6 | Phenotype and gene expression profiles of splenic Bcl6-deficient cDC2. **A** Representative flow cytometric analysis of classical dendritic cells (cDC)2 in the spleen of control and *CD11c.Bcl6*^{KO} mice, showing expression of CD11c vs MHCII (top panels) and XCR1 vs CD11b (lower panels) by live, lineage$^-$ (CD3, CD19, CD64, B220, NK1.1), CD11c$^+$ single cell-gated splenocytes. Data are representative of at least 8 independent experiments with 1–3 mice each. Reported mean fluorescent intensity (MFI) levels of MHCII are raw values and average deviation from 3 experiments with 3 mice each. **B** Representative flow cytometric analysis of ESAM^{hi} and ESAM^{lo} cDC2 in the spleen of control and *CD11c.Bcl6*^{KO} mice. Cells were pre-gated as XCR1$^-$CD11b$^+$ cDC2 from live, lineage$^-$ (CD3, CD19, CD64, B220, NK1.1), CD11c$^+$, MHCII$^+$ single cells. Data are representative of 3 independent experiments with 1–3 mice each. **C** Representative flow cytometric analysis of cDC2 in the spleen of control and *Clec9a.Bcl6*^{KO} mice, showing expression of CD11c vs MHCII (top panels) and XCR1 vs CD11b (lower panels, gated on CD11c$^+$, MHCII$^+$) by live, lineage$^-$ (CD3, CD19, CD64, B220, NK1.1) single cell-gated splenocytes. Data are representative of 2 independent experiments with 3 mice each. **D** Representative flow cytometric analysis of ESAM^{hi} and ESAM^{lo} cDC2 in the spleen of control and *Clec9a.Bcl6*^{KO} mice. Cells were pre-gated as XCR1$^-$CD11b$^+$ cDC2 from live, lineage$^-$ (CD3, CD19, CD64, B220, NK1.1), CD11c$^+$, MHCII$^+$ single cells (top). Data are representative of 2 independent experiments with 3 mice each, and lines represent means ± SD. **E** Same data as in **D**, but pre-gated on YFP$^+$ instead of CD11c$^+$ (see Suppl. Fig. 4 for full gating strategy). Data are representative of 2 independent experiments with 3 mice each, and lines represent means ± SD. **F** Representative flow cytometric analysis of expression of CD11c, 33D1, CD4, CD11b, and IRF4 by splenic XCR1$^-$CD11b$^+$ cDC2 from control (ESAM^{hi}: black, ESAM^{lo}: blue) or *CD11c.Bcl6*^{KO} mice (orange). FMO controls are depicted in gray. Gates correspond to those depicted in Fig. 6B. Results are representative of at least 2 (CD11c) or 3 (all others) independent experiments with 3 mice each, and lines represent means ± SD. Statistical analysis was performed by one-way ANOVA. *$P < 0.05$, **$P < 0.01$, ***$P < 0.001$ and ****$P < 0.0001$. Circles: females; triangles: males.

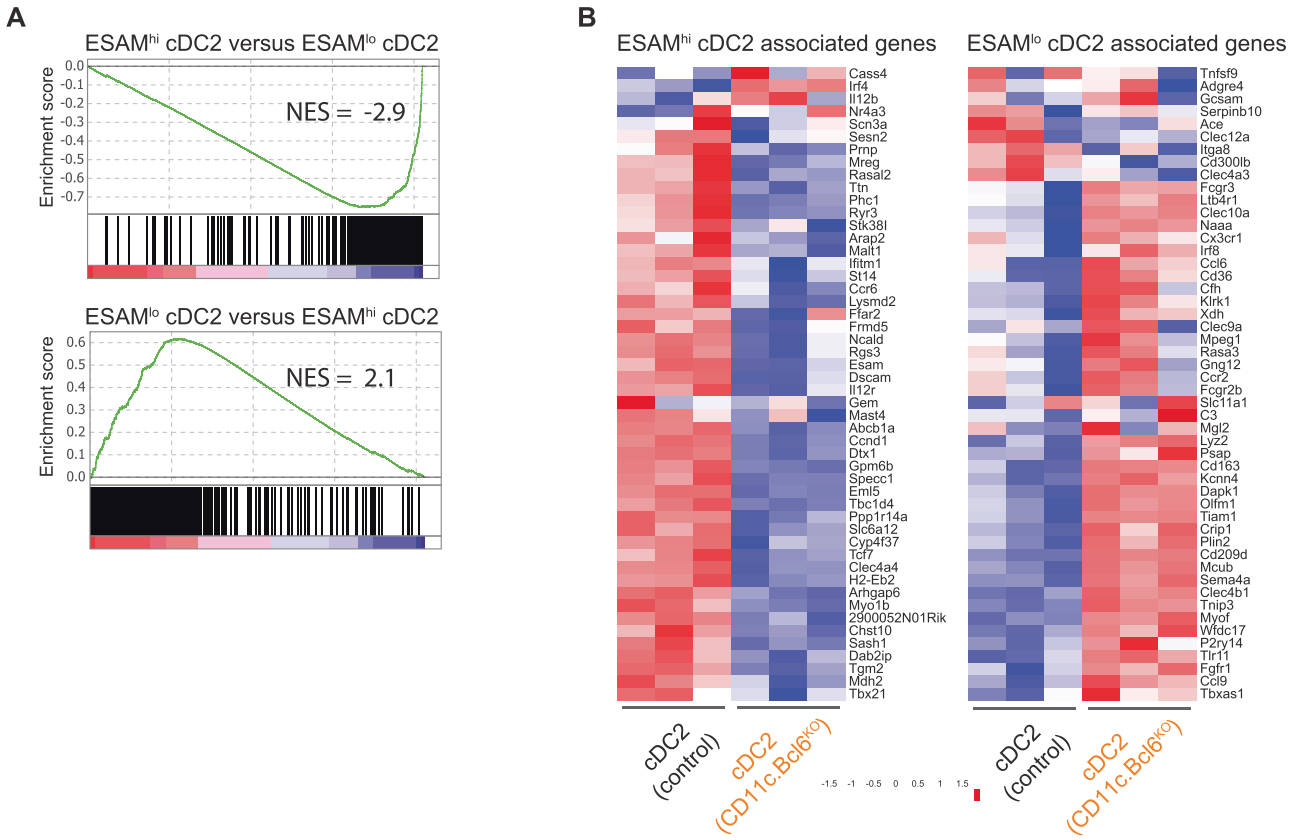

Fig. 7 | Gene signature comparisons between ESAM^{hi} and ESAM^{lo} cDC2 with Bcl6-deficient cDC2. **A** Gene set enrichment plots following *CD11c.Bcl6*^{KO} vs control classical dendritic cells (cDC)2 in an ESAM^{hi} cDC2 related gene set (top) vs an ESAM^{lo} cDC2 related gene set (bottom) (ESAM^{hi} and ESAM^{lo} gene set derived from GSE76132). NES normalized enrichment score. False discovery rate (FDR) *q*-value: 0.0. **B** The top 50 genes associated with spleen ESAM^{hi} cDC2 (left) or ESAM^{lo} cDC2 (right) were derived from GSE76132. Heatmaps show the expression of these genes in the RNA-Seq analysis of cDC2 from control and *CD11c.Bcl6*^{KO} spleen. The color scale represents the row *Z* score (Expression *Z*-scale).

Mice

Xcr1.cre (*B6-Xcr1*^{tm2Ciphe})[57], *CD11c.cre*[31], and *Clec9a.cre*[36] mice were crossed to *Bcl6*$^{fl/fl}$ mice[58] (from Alexander Dent or JAX.org stock number #023727) to obtain DC-specific Bcl6-knockout models. *Clec9a.Bcl6*^{KO} mice and *Clec9a.Bcl6*^{WT} control mice were both maintained homozygous for cre and additionally contained homozygous a *Rosa26*$^{fl\text{-}Stop\text{-}fl\text{-}YFP}$ allele (JAX.org stock number 006148). *CD11c.Bcl6* and *XCR1.Bcl6* models were maintained heterozygous for cre and negative littermates were used as control controls. Additional strains used in this study were B6.SJL-Ptprc^a Pepc^b/BoyJ (congenic C57BL/6.CD45.1 mice from the Jackson Laboratory), C57BL/6-Tg (TcraTcrb)1100Mjb/J and B6.Cg-Tg(TcraTcrb)425Cbn/J (OT-I and OT-II mice from Jackson Laboratory). Mice were group-housed in individually ventilated cages, maintained on a 12 h light and dark cycle at 22 °C and 55% humidity, and maintained under specific pathogen-free conditions. Euthanization was performed using cervical dislocation without anesthesia. Experimental groups were sex- and age-matched. Male and female littermates were used between 8 and 15 weeks of age, and RNA-Seq was performed on female mice only. All animal experiments were performed in accordance with European regulations and federal law of Denmark and Germany.

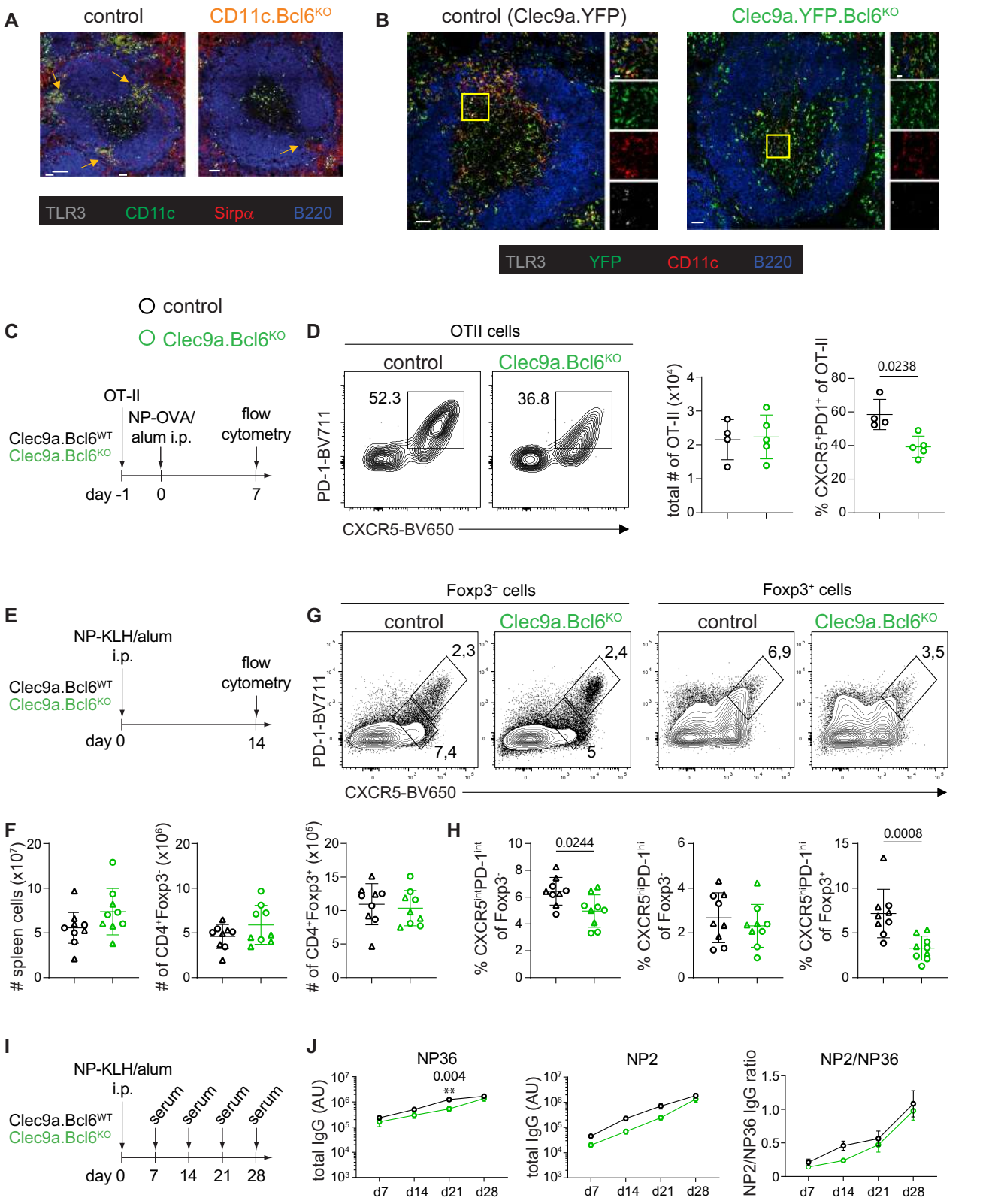

Permission was granted either by the Danish Animal Experiments Inspectorate, the Regierung von Oberbayern, or the Landesamt für Natur-, Umwelt und Verbraucherschutz NRW.

Cell preparation

Spleens, mLNs, and pLN (axillary, brachial, and inguinal) were digested in RPMI containing 5% FCS, 0.5 mg/ml Collagenase IV (USBiological), and 30 μg/ml DNase I grade II (Roche) for 45 min at room temperature. Red blood cells in the spleen and blood samples were subsequently lysed using red blood cell lysis buffer (ammonium chloride, potassium bicarbonate, EDTA, and MiliQ water) for 3 min at room temperature. For the OT-II adoptive transfer experiments, splenic single-cell suspensions were prepared and analyzed as previously described[59].

Fig. 8 | Impact of Bcl6 deficiency in splenic cDC on Tfh cell and antibody responses. A Confocal microscopy of spleens from *CD11c.Bcl6^{KO}* and control mice. TLR3 (gray), CD11c (green), Sirpα (red), B220 (blue). Scale bar = 50 μm. Arrows indicate marginal zone bridging channels. Images are representative of 4 (*CD11c.Bcl6^{KO}*), or 3 (control) replicates from individual mice. **B** Confocal microscopy of spleens from *Clec9a.Bcl6^{WT} and Clec9a.Bcl6^{KO}* mice, each carrying homozygous *Rosa26$^{fl\text{-}Stop\text{-}fl\text{-}YFP}$* alleles. TLR3 (gray), YFP (green), CD11c (red), B220 (blue). Scale bar = 50 μm. Single channel figures show areas in the yellow boxes. Images are representative of 4 replicates from individual mice. **C** Experimental design. **D** Representative flow cytometry of splenic OT-II (CD45.1/2) cells from *Clec9a.Bcl6^{WT}* and *Clec9a.Bcl6^{KO}* recipients 7 days after i.p. immunization with NP-OVA. Tfh cells were gated as CXCR5$^+$PD-1$^+$ live CD4$^+$CD19$^-$ lymphocytes. Statistical analysis was performed by two-way Mann–Whitney, exact *P* values are annotated. Each symbol represents one biological replicate ($n = 4–5$), and lines represent means ± SD. Data are representative of 2 independent experiments. **E** Experimental design. **F** Total cellularity and number of CD4$^+$Foxp3$^-$ and CD4$^+$Foxp3$^+$ cells in *Clec9a.Bcl6^{KO}* and control mice 14 days after i.p. injection with NP-KLH and alum. Data are pooled from 2 independent experiments with 4-5 mice per group, and lines represent means ± SD. **G** Representative flow cytometry of Foxp3$^-$ (left) and Foxp3$^+$ (right) CD4$^+$ T cell-gated splenocytes 14 days post-NP-KLH/alum i.p. immunization of *Clec9a.Bcl6^{KO}* and control mice. Foxp3$^-$: T follicular helper cells (Tfh) are gated as CXCR5^{int}PD-1^{int}, and germinal center Tfh are gated as CXCR5^{hi}PD-1^{hi}. Foxp3$^+$: T follicular regulatory cells are gated as CXCR5^{hi}PD-1^{hi}. **H** Quantification of data shown in (**G**). Statistical analysis was performed by the Mann–Whitney test and exact *P* values were annotated. Data are pooled from two independent experiments with 4–5 mice per group, and lines represent means ± SD. **I** Experimental design. **J** NP-specific total IgG in the serum from NP-KLH and alum immunized *Clec9a.Bcl6^{KO}* and control mice at indicated time-points as determined by ELISA for low (NP36)- and high (NP2)-affinity antibodies. Data are representative of two independent experiments with 4–5 mice, and lines represent means ± SED. Two-way ANOVA with Bonferroni post-hoc, exact *P* values are annotated. Circles: females; triangles: males.

Single-cell suspensions of the intestinal LP were prepared as described previously[60]. Briefly, the intestines were flushed with HBSS supplemented with FCS (10%), Peyer's patches were removed, and epithelial cells and mucus were removed by incubating tissue in HBSS supplemented with FCS (10%) and EDTA (2 mM) 3 times each for 15 min at 37 °C with continual shaking at 450 rpm. The remaining tissue pieces were digested in R10 media (RPMI 1640 supplemented with FCS (10%) containing DNase I grade II (30 μg/ml) and Liberase TM (58 μg/ml) for 20 min at 37 °C with a magnetic stirrer.

Lungs were perfused with PBS prior to resection. All lung lobes were cut into small pieces and digested in R5 media (RPMI 1640 supplemented with FCS (5%) containing DNase I grade II (30 μg/ml) and Liberase TM (50 μg/ml, Roche) for 45 min at 37 °C with a magnetic stirrer.

Intestinal LP and lung cell suspensions were filtered through 100 μm cell strainers (Fisher Scientific), and leukocytes were enriched by density gradient centrifugation with 40%/70% Percoll (GE Healthcare) prior to further analysis.

Flow cytometry

Single-cell suspensions were stained for multicolor analysis with the indicated fluorochrome- or biotin-conjugated antibodies after blocking with Fc block (purified anti-CD16/32). Antibodies were diluted in flow cytometry buffer (DPBS, 2% FCS), and staining was performed for 30 min on ice in the dark. LIVE/DEAD™ Fixable Near-IR Dead Cell Stain Kit (Invitrogen) or Fixable Viability Dye eFluor™-780 (Invitrogen) were used for determining the viability of cells.

Lymphocytes from *C. rodentium* infection experiments were treated with rmIL-23 (40 ng/ml, R&D) for 3 h at 37 °C with 5% CO_2, washed and further incubated with rmIL-23 (40 ng/ml), PMA (50 ng/ml, Sigma Aldrich), Ionomycin (750 ng/ml, Sigma Aldrich) and BD GolgiStop™ (containing monensin at 1:1000 dilution, BD) for an additional 3.5 h at 37 °C with 5% CO_2.

For intracellular staining, cells were fixed with the Foxp3 Fixation/Permeabilization kit from eBioscience. Samples were acquired on a Fortessa X20, an LSRFortessa, or a Symphony flow cytometer (BD Biosciences) using FACSDiva software (BD Biosciences) and analyzed with FlowJo software (Tree Star). All antibodies and working dilution are listed in Suppl. Data 4.

Splenic dendritic cell sorting and cDNA library preparation for RNA-seq

Splenic DC was enriched using the Dynabeads Mouse DC Enrichment kit (Invitrogen) and sorted on a BD FACS Melody to obtain cDC1 (B220$^-$CD64$^-$CD3$^-$CD19$^-$NK1.1$^-$CD11c^{hi}MHCII$^+$XCR1$^+$) and cDC2 (B220$^-$CD64$^-$CD3$^-$CD19$^-$NK1.1$^-$CD11c^{hi}MHCII$^+$CD11b$^+$XCR1$^-$). Sorted cells (2-4×10^4 per sample) were resuspended in 350 μl RNeasy Lysis Buffer (QIAGEN), and RNA was extracted using the QIAGEN RNeasy Mini kit (QIAGEN). RNA was washed, treated with DNase I (QIAGEN), and eluted per the manufacturer's instructions. RNA-seq libraries were prepared by combining the Nugen Ovation RNA-seq system V2 with NuGEN's Ultralow System V2 (NuGEN Technologies). The amplified libraries were purified using AMPure beads, quantified by qPCR, and visualized on an Agilent Bioanalyzer using BioA DNA High sensitivity (Agilent). The libraries were pooled equimolarly and run on a HiSeq 2500 as single-end reads of 50 nucleotide length.

RNA-sequencing data analysis

Sequencing reads were mapped to the mouse reference genome (GRCm38.85/mm10) using the STAR aligner (v2.7.6a)[61]. Alignments were guided by a Gene Transfer Format (Ensembl GTF GRCm38.101). Read count tables were normalized based on their library size factors using DESeq2 (v1.30.1)[62], and differential expression analysis was performed with a filter of log2foldChange > 1 and a *p*-adjust value < 0.01. For selected gene signatures (cDC1 and cDC2 or ESAM^{hi} and ESAM^{lo} DC2s), the 100 DEGs with the highest normalized count values were selected, out of which then the top 50 genes with the highest absolute log2FoldChange were depicted in heatmaps. RNA-seq reads aligned to genes from the GENCODE gene annotation were counted using Ensembl's BiomaRt-v2.46.3. Heatmap visualizations were done using pheatmap v1.0.12. Downstream statistical analyses and plot generation were performed in the R environment (v4.0.5)[63]. The online tool Venny 2.1 was used for the drawing of the Venn plots. Package PlotMA was used for visualizing gene expression changes from two different conditions (parameters: alpha = 0.01, type ="ashr")[64]. Principal Component Analysis (PCA) plots were drawn using PCAtools 2.2.0, with removeVar=0.01[65]. Volcano plots were drawn using the function of ggpubr 0.4.0[66]. Gene Set Enrichment Analysis was performed using Gene Ontology R package clusterProfiler 3.18.1 (category biological process) on DEGs obtained from DESeq2. The *p*-values were adjusted using "BH" (Benjamini–Hochberg) correction, and the cutoff was 0.01[67]. GO biological process terms were ranked by GeneRatio. The gene ratio is defined as the number of genes associated with the term in DEGs divided by the number of DEGs. For KEGG enrichment, DESeq2-derived DEGs were used[68]. Enrichments with a *p*-value from Fisher's exact test ≤ 0.05 were considered significant.

Confocal microscopy

Mice were sacrificed, spleens taken out, immediately washed with cold DPBS, and fixed with either 4% PFA in PBS for 12 h or 1% PFA in PBS for 24 h, followed by an overnight wash with washing buffer PBS-XG (PBS + 5% FCS + 0.2% Triton X-100). Samples were embedded in warm 4% low melting agarose for sectioning. 60-100 μm sections were cut using a Vibratome 1200 S (Leica) and stored until use. For staining, sections were incubated with primary antibodies in 500 μl washing buffer in a 24-well plate overnight at 4 °C under constant agitation

https://doi.org/10.1038/s41467-024-46966-6

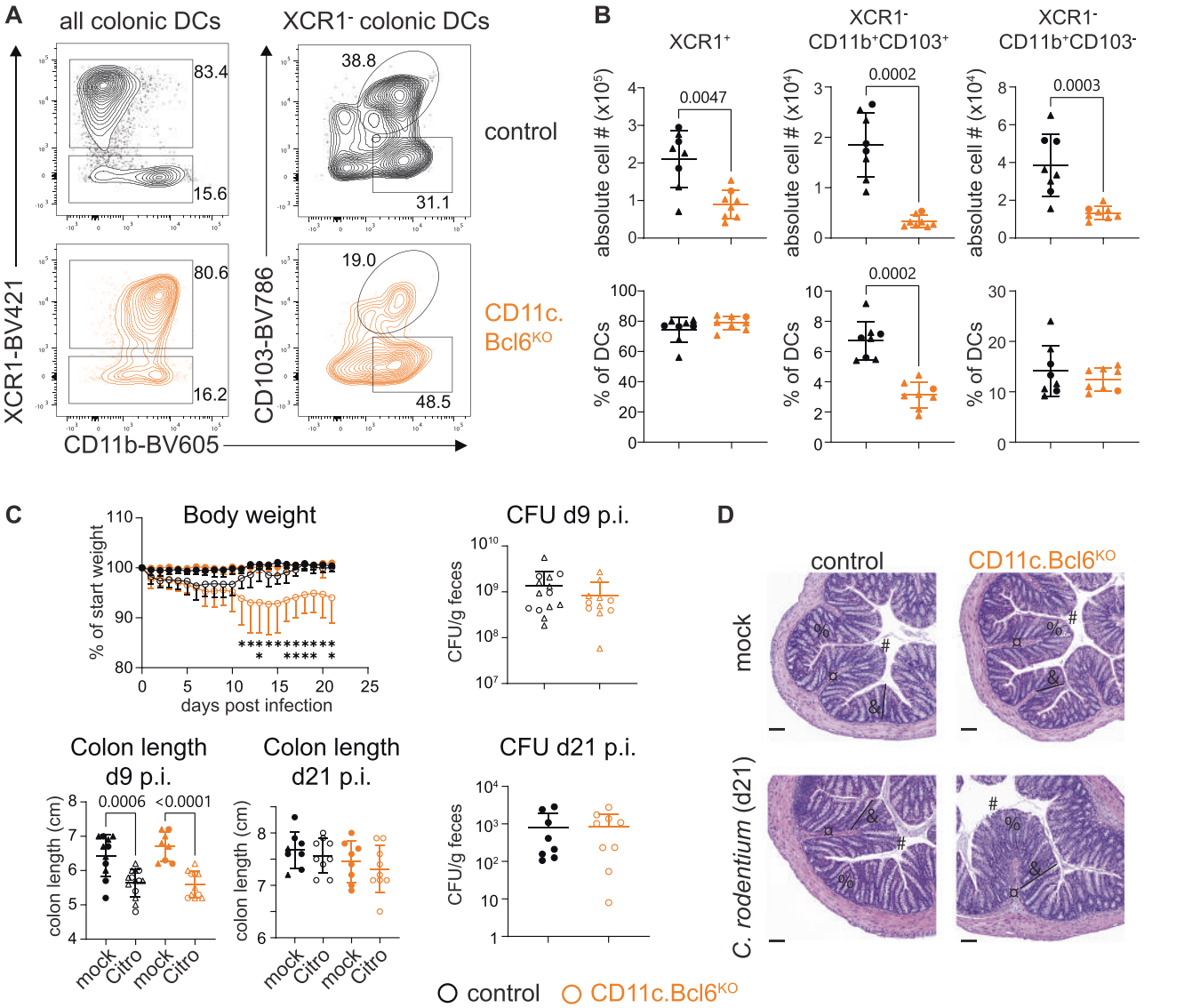

Fig. 9 | *Citrobacter rodentium* infection in mice with Bcl6 deletion in cDC. A Left: Flow cytometry plots showing cLP XCR1$^+$ and XCR1$^-$CD11b$^+$ DC subsets gated on all dendritic cells (DC) (live, CD45$^+$, lineage$^-$ (CD3, CD19, CD64, B220, NK1.1), MHCII$^+$, CD11c^{hi} single cells. Right: XCR1$^-$ DC is further subdivided into CD103$^+$ and CD103$^-$ classical DC2 (cDC2) from control and *CD11c.Bcl6^{KO}* mice. **B** Absolute numbers (top) and proportions (bottom) of colon lamina propria XCR1$^+$, XCR1$^-$CD103$^+$CD11b$^+$, and XCR1$^-$CD103$^-$CD11b$^+$ DC subsets from control and *CD11c.Bcl6^{KO}* mice. Data points represent values from individual mice pooled from 3 experiments with 2–3 mice each, and lines represent means ± SD. Statistical analysis using the Mann–Whitney test, exact *P* values are annotated. **C** Percentage of weight loss of mock and *C. rodentium* infected control and *CD11c.Bcl6^{KO}* mice. Each symbol represents the mean weight loss of all mice within the group at the indicated time point post-infection versus their starting weight, and error bars represent SD; statistical analysis using two-way ANOVA (and Tukey's multiple comparison test) with Geisser–Greenhouse correction, $*P < 0.05$ and $**P < 0.01$ (top left). Colon lengths in mock and infected mice at 9 or 21 days post inoculation; statistical analysis by one-way ANOVA (and Tukey's multiple comparison test), exact *P* values are annotated (bottom left). *C. rodentium* titers in feces were measured as colony-forming units (CFU) of infected control and *CD11c.Bcl6^{KO}* mice at indicated days post-infection; statistical analysis using Mann–Whitney test, not significant (ns, right). All data points represent values from individual mice, lines represent means ± SD, and data is pooled from 2 to 3 experiments with 3–5 mice per mock/*C. rodentium*-infected group. **D** H&E-stained sections of the distal colon of mock and *C. rodentium* infected control and *CD11c.Bcl6^{KO}* mice 21 days post-inoculation. Scale bar, 100 μm. Symbols: # epithelial lining; ¤ leukocyte infiltration; % goblet cell destruction; & villus length. Representative of 4–5 mice per group from one experiment.

(120 rpm), followed by at least 6 h of washing in 5 ml washing buffer. To enhance the YFP signal, a primary unlabeled anti-GFP antibody was used in the experiments based on *Clec9a.Bcl6^{WT}* and *Clec9a.Bcl6^{KO}* mice, each carrying homozygous Rosa26fl-Stop-fl-YFP alleles. This antibody was detected in a secondary antibody incubation step overnight in 500 μl PBS-XG in a 24-well plate, followed by an additional washing step in 5 ml washing buffer for 6 h. All antibodies and working dilution are listed in Suppl. Data 4. Sections were mounted using ProLong Gold Glass and images were acquired on a Zeiss LSM710 or a Zeiss LSM900 confocal laser microscope. Digital pictures were acquired with Zen software (Zeiss) and processed using Imaris Viewer (Oxford Instruments).

Cross-presentation assays

In vivo: Naïve CD8$^+$ T cells from OT-I donors were enriched using the Dynabeads® Untouched™ Mouse T Cells kit (Invitrogen) and stained in 1 ml DPBS with CellTrace Violet dye (Invitrogen) for 10 min at 37 °C. 1×10^6 OT-I cells were transferred into recipients one day before i.p. injection of 5×10^6 cells/mouse of H-2$^{\beta m1}$ MEFs expressing truncated non-secreted OVA (OVA-MEF)[17]. One day after immunization,

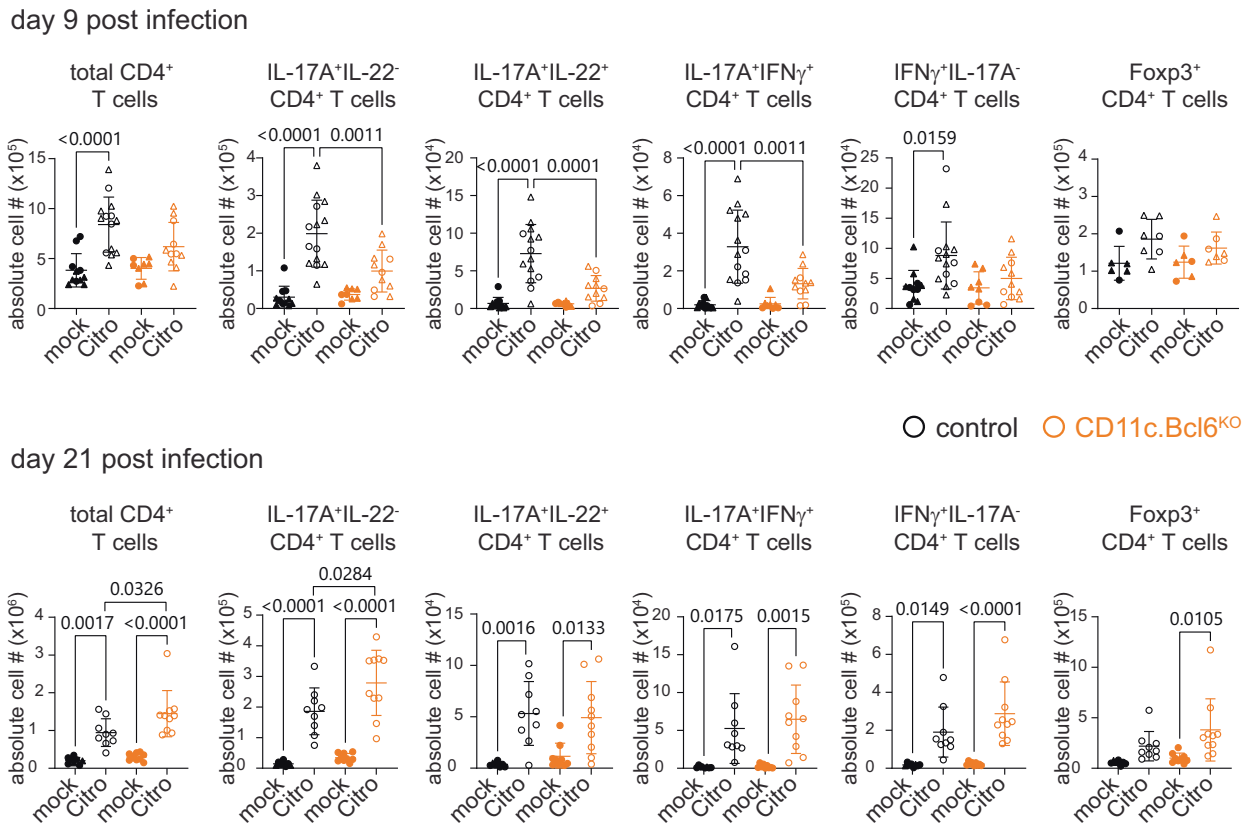

Fig. 10 | T cell responses to *Citrobacter rodentium* infection in mice with Bcl6 deletion in cDC. A Numbers of total CD4$^+$ T cells, IL-17A$^+$IL-22$^-$, IL-17A$^+$IL-22$^+$, IL-17A$^+$IFNγ$^+$, IFNγ$^+$IL-17$^-$ and Foxp3$^+$ CD4$^+$ T cells in the cLP of mock and *C. rodentium* infected control and *CD11c.Bcl6^{KO}* mice at day 9 post-inoculation. Data points represent values from individual mice pooled from 2 to 4 experiments with 2–4 mice per group, and lines represent means ± SD. Statistical analysis is performed by one-way ANOVA, and exact *P* values are annotated. **B** Numbers of total CD4$^+$ T cells, IL-17A$^+$IL-22$^-$, IL-17A$^+$IL-22$^+$, IL-17A$^+$IFNγ$^-$, IFNγ$^+$IL-17$^-$ and Foxp3$^+$ T cells in the cLP of mock and *C. rodentium* infected control and *CD11c.Bcl6^{KO}* mice at day 21 post-inoculation. Data points represent values from individual mice pooled from 2 experiments with 4–5 mice per group, and lines represent means ± SD. Statistical analysis is performed by one-way ANOVA, and exact *P* values are annotated. Circles: females; triangles: males.

recipients were injected with FTY720 (20 μg/mouse, Cayman) in saline i.p. Mice were sacrificed three days after immunization.

In vitro: DCs were enriched from spleen and mLN using the Dynabeads Mouse DC Enrichment kit (Invitrogen), and naïve CD8 T cells from OT-I donors were isolated using the Dynabeads Untouched Mouse T Cells kit (Invitrogen), both according to manufactures protocol. OT-I cells were stained with CellTrace Violet dye (1:1000, Invitrogen) for 10 min at 37 °C. Enriched DCs from both mLN and spleen were incubated with OVA (EndoFit, InvivoGen) at a concentration of 250 μg/ml in culture media (RPMI 1640 supplemented with 10% FCS, 55 μM β-mercaptoethanol and Penicillin-Streptomycin-Glutamin 100× (Gibco)) for 2 h at 37 °C and washed twice. DCs for negative control were not incubated with OVA. The frequency of cDC1s in each sample was determined using flow cytometry, and 670 cDC1s were plated in a cell culture treated 96-well U bottom plate with 0.2×10^6 OT-I cells in culture media supplemented with 1 μg/ml LPS. For the positive control, 0.2×10^6 OT-I cells were stimulated with 10 μg/ml aCD3 (eBioscience, clone 17A2) (plate bound) and 1 μg/ml aCD28 (eBioscience, clone 37.51). Flow cytometry-based analysis was carried out after incubation for 65 h at 37 °C with 5% CO_2.

Induction of Tfh cells and antibody responses in vivo

For adoptive transfer experiments into *CD11c.Bcl6^{KO}* or control hosts, naïve CD4$^+$ T cells were enriched from homozygous TCR-transgenic OT-II (CD45.1/.2) donors using the Dynabeads Untouched™ Mouse CD4 Cells kit (Invitrogen). 1×10^5 OT-II cells were transferred intravenously (i.v.), and one day later, recipients were immunized i.p. with ovalbumin grade V (OVA, 0.5 mg, Sigma Aldrich) together with poly(I:C) (100 μg, Sigma-Aldrich). Controls received PBS alone, and mice were sacrificed three days after immunization. For adoptive transfer experiments into *Clec9a.Bcl6^{WT}* or *Clec9a.Bcl6^{KO}* hosts, naïve CD8$^-$CD19$^-$CD44$^{int/low}$CD62L^{hi}CD25$^-$ CD4$^+$ T cells were sorted from heterozygous OT-II (CD45.1/2) donors on BD FACSAria III or Fusion cell sorters. 5×10^{54} OT-II cells were injected i.v., and one day later, recipient mice were immunized i.p. with a 1:1 mixture of 50 μg NP_{17}-OVA (Biosearch Technologies/BioCat) in PBS and Imject Alum (Thermo Fisher). Spleens were dissected and analyzed by flow cytometry on day 7. For assessment of endogenous Tfh and Tfr cell responses, *Clec9a.Bcl6^{WT}* or *Clec9a.Bcl6^{KO}* mice were immunized i.p. with 50 μg NP_{32}-KLH (Biosearch Technologies/BioCat) in PBS and Imject Alum (Thermo Fisher). Spleens were dissected and analyzed by flow cytometry on day 14. In independent NP_{32}-KLH/alum-immunized cohorts, blood samples were collected on days 7, 14, 21, and 28 using Microvette 200 Serum Gel CAT tubes (Sarstedt), and NP-specific serum antibody levels were determined by ELISA.

ELISA

IL-6 levels in the serum of mice injected intraperitoneally with PBS or 100 μg poly(I:C) 2 h before analysis were determined using BD OptEIA™ Mouse IL-6 ELISA Set.

To measure NP-specific serum IgG1 and total IgG, half-area radioimmunoassay plates (#3690, Corning) were coated with 25 μl of 10 μg/ml NP-BSA in PBS (N-5050XL-10-BS with loading ratio of 2 or N-5050H-10-BS with loading ratio of 36, both Biosearch Technologies/BioCat)

overnight at 4 °C. The next day, plates were washed four times with PBS + 0,005% Tween20 and then blocked with 70 µl PBS + 2% BSA for 2 h at RT. After four washing steps, serial dilutions of serum from immunized mice were added to the plate and incubated on a plate shaker for 2 h at RT. Pooled sera from day 28-immunized mice were used as standard. Next, plates were washed four times, and 25 µl of a 1:500 dilution of the respective detection antibody (goat anti-mouse IgG(H + L)-alkaline phosphatase (AP) conjugate (Southern Biotech/Biozol) or goat anti-mouse IgG1-AP (Southern Biotech/Biozol) was added to each well and incubated for 45 min while shaking. Plates were washed four times and then incubated with 70 µl of Alkaline Phosphatase Solution (Sigma Aldrich) for 20 min. Plates were read for absorbance at 405 nm (TriStar plate reader). Resulting data were plotted as concentration (*x*-axis) versus OD (OD, *y*-axis) in Excel, then fit to a sigmoidal 4-parameter logistic (4PL) model by utilizing the four parameter logistic (4PL) curve calculator (AAT Bioquest Inc.). The sigmoidal 4PL equations were then used to calculate the concentration of individual samples. Values are expressed as arbitrary units (AU).

Citrobacter rodentium infection

The *C. rodentium* strain DBS100 (ATCC 51459; American Type Culture Collection) was used as described[69] with some amendments. Briefly, *C. rodentium* cultures were grown in Luria-Bertani (LB) medium to an OD_{600} of 1–1.5. Mice were orally inoculated with LB broth or 2×10^9 CFU *C. rodentium*, and their weight was monitored daily. Fecal samples were collected on indicated days post-infection, serially diluted in PBS and plated on Brilliance™ *E. coli*/coliform Agar (Thermo Fisher). *C. rodentium* colonies, from at least three dilutions per sample, were enumerated and normalized to the weight of feces.

For histopathology, 0.5 cm of the distal colon was immediately placed in 10% formalin and processed by the DTU Histology Core for hematoxylin and eosin (H&E) staining. Images were acquired on a Pannoramic MIDI II scanner (3DHISTECH) and visualized with CaseViewer software 2.4 (3DHISTECH). The severity of the infection was assessed in a blinded manner.

Statistical analysis

Statistical analyses were performed with Graphpad Prism 9.0 (Graphpad Software). While symbols in data graphs give information on the sex of the individual mice in the experiments, we did not perform sex-stratified statistics due to variable group size.

Reporting summary

Further information on research design is available in the Nature Portfolio Reporting Summary linked to this article.

Data availability

The RNA-sequencing data generated in this study have been deposited in the NCBI SRA database under accession code PRJNA834905. Flow cytometry data is available upon request. Source data are provided in this paper.

References

1. Guilliams, M. et al. Dendritic cells, monocytes and macrophages: a unified nomenclature based on ontogeny. *Nat. Rev. Immunol.* **14**, 571–578 (2014).
2. Steinman, R. M. The dendritic cell system. *Annu. Rev. Immunol.* **9**, 271–296 (1991).
3. Durai, V. & Murphy, K. M. Functions of murine dendritic cells. *Immunity* **45**, 719–736 (2016).
4. Allenspach, E. J., Lemos, M. P., Porrett, P. M., Turka, L. A. & Laufer, T. M. Migratory and lymphoid-resident dendritic cells cooperate to efficiently prime naive CD4 T cells. *Immunity* **29**, 795–806 (2008).
5. Lewis, S. M., Williams, A. & Eisenbarth, S. C. Structure and function of the immune system in the spleen. *Sci. Immunol.* **4**, eaau6085 (2019).
6. Eisenbarth, S. C. Dendritic cell subsets in T cell programming: location dictates function. *Nat. Rev. Immunol.* **19**, 89–103 (2018).
7. Calabro, S. et al. Differential intrasplenic migration of dendritic cell subsets tailors adaptive immunity. *Cell Rep.* **16**, 2472–2485 (2016).
8. Idoyaga, J., Suda, N., Suda, K., Park, C. G. & Steinman, R. M. Antibody to Langerin/CD207 localizes large numbers of CD8α + dendritic cells to the marginal zone of mouse spleen. *Proc. Natl Acad. Sci. USA* **106**, 1524–1529 (2009).
9. Sichien, D. et al. IRF8 transcription factor controls survival and function of terminally differentiated conventional and plasmacytoid dendritic cells, respectively. *Immunity* **45**, 626–640 (2016).
10. Schiavoni, G. et al. ICSBP is essential for the development of mouse type I interferon-producing cells and for the generation and activation of CD8α+ dendritic cells. *J. Exp. Med.* **196**, 1415–1425 (2002).
11. Hildner, K. et al. Batf3 deficiency reveals a critical role for CD8alpha + dendritic cells in cytotoxic T cell immunity. *Science* **322**, 1097–1100 (2008).
12. Kashiwada, M., Pham, N. L. L., Pewe, L. L., Harty, J. T. & Rothman, P. B. NFIL3/E4BP4 is a key transcription factor for CD8α+ dendritic cell development. *Blood* **117**, 6193–6197 (2011).
13. Bagadia, P. et al. An Nfil3–Zeb2–Id2 pathway imposes Irf8 enhancer switching during cDC1 development. *Nat. Immunol.* **20**, 1174–1185 (2019).
14. Hacker, C. et al. Transcriptional profiling identifies Id2 function in dendritic cell development. *Nat. Immunol.* **4**, 380–386 (2003).
15. Cerovic, V. et al. Lymph-borne CD8α+ dendritic cells are uniquely able to cross-prime CD8+ T cells with antigen acquired from intestinal epithelial cells. *Mucosal Immunol.* **8**, 38–48 (2015).
16. Joeris, T. et al. Intestinal cDC1 drive cross-tolerance to epithelial-derived antigen via induction of FoxP3+CD8+ Tregs. *Sci. Immunol.* **6**, eabd3774 (2021).
17. Sancho, D. et al. Identification of a dendritic cell receptor that couples sensing of necrosis to immunity. *Nature* **458**, 899–903 (2009).
18. Ahrens, S. et al. F-actin is an evolutionarily conserved damage-associated molecular pattern recognized by DNGR-1, a receptor for dead cells. *Immunity* **36**, 635–645 (2012).
19. Zhang, J.-G. et al. The dendritic cell receptor Clec9A binds damaged cells via exposed actin filaments. *Immunity* **36**, 646–657 (2012).
20. Watchmaker, P. B. et al. Comparative transcriptional and functional profiling defines conserved programs of intestinal DC differentiation in humans and mice. *Nat. Immunol.* **15**, 98–108 (2014).
21. Tussiwand, R. et al. Klf4 expression in conventional dendritic cells is required for T helper 2 cell responses. *Immunity* **42**, 916–928 (2015).
22. Satpathy, A. T. et al. Notch2-dependent classical dendritic cells orchestrate intestinal immunity to attaching-and-effacing bacterial pathogens. *Nat. Immunol.* **14**, 937–948 (2013).
23. Persson, E. K. et al. IRF4 transcription-factor-dependent CD103(+) CD11b(+) dendritic cells drive mucosal T helper 17 cell differentiation. *Immunity* **38**, 958–969 (2013).
24. Williams, J. W. et al. Transcription factor IRF4 drives dendritic cells to promote Th2 differentiation. *Nat. Commun.* **4**, 2990 (2013).
25. Scott, C. L. et al. The transcription factor Zeb2 regulates development of conventional and plasmacytoid DCs by repressing Id2. *J. Exp. Med.* https://doi.org/10.1084/jem.20151715 (2016).
26. Ichikawa, E. et al. Defective development of splenic and epidermal CD4+ dendritic cells in mice deficient for IFN regulatory factor-2. *Proc. Natl Acad. Sci. USA* **101**, 3909–3914 (2004).
27. Wu, L. et al. RelB is essential for the development of myeloid-related CD8alpha- dendritic cells but not of lymphoid-related CD8alpha+ dendritic cells. *Immunity* **9**, 839–847 (1998).
28. Lewis, K. L. et al. Notch2 receptor signaling controls functional differentiation of dendritic cells in the spleen and intestine. *Immunity* **35**, 780–791 (2011).

29. Briseño, C. G. et al. Notch2-dependent DC2s mediate splenic germinal center responses. *Proc. Natl Acad. Sci. USA* **115**, 10726–10731 (2018).
30. Fasnacht, N. et al. Specific fibroblastic niches in secondary lymphoid organs orchestrate distinct Notch-regulated immune responses. *J. Exp. Med.* **211**, 2265–2279 (2014).
31. Caton, M. L., Smith-Raska, M. R. & Reizis, B. Notch–RBP-J signaling controls the homeostasis of CD8 − dendritic cells in the spleen. *J. Exp. Med.* **204**, 1653–1664 (2007).
32. Lu, E., Dang, E. V., McDonald, J. G. & Cyster, J. G. Distinct oxysterol requirements for positioning naïve and activated dendritic cells in the spleen. *Sci. Immunol.* **2**, eaal5237 (2017).
33. Choi, J. & Crotty, S. Bcl6-mediated transcriptional regulation of follicular helper T cells (TFH). *Trends Immunol.* **42**, 336–349 (2021).
34. Ohtsuka, H. et al. Bcl6 is required for the development of mouse CD4+ and CD8 + dendritic cells. *J. Immunol.* **186**, 255–263 (2011).
35. Bagadia, P. et al. Bcl6-independent in vivo development of functional type 1 classical dendritic cells supporting tumor rejection. *J. Immunol.* https://doi.org/10.4049/jimmunol.1901010 (2021).
36. Schraml, B. U. et al. Genetic tracing via DNGR-1 expression history defines dendritic cells as a hematopoietic lineage. *Cell* **154**, 843–858 (2013).
37. Lau, C. M. et al. Leukemia-associated activating mutation of Flt3 expands dendritic cells and alters T cell responses. *J. Exp. Med.* **213**, 415–431 (2016).
38. Baumjohann, D., Okada, T. & Ansel, K. M. Cutting /s of BCL6 Expression during T Follicular Helper Cell Development. *J. Immunol.* **187**, 2089–2092 (2011).
39. Goenka, R. et al. Cutting edge: dendritic cell-restricted antigen presentation initiates the follicular helper T cell program but cannot complete ultimate effector differentiation. *J. Immunol.* **187**, 1091–1095 (2011).
40. Baumjohann, D. et al. Persistent antigen and germinal center B cells sustain T follicular helper cell responses and phenotype. *Immunity* **38**, 596–605 (2013).
41. Ribeiro, F., Perucha, E. & Graca, L. T follicular cells: the regulators of germinal center homeostasis. *Immunol. Lett.* **244**, 1–11 (2022).
42. Wing, J. B., Lim, E. L. & Sakaguchi, S. Control of foreign Ag-specific Ab responses by Treg and Tfr. *Immunol. Rev.* **296**, 104–119 (2020).
43. Zhang, S. et al. Type 1 conventional dendritic cell fate and function are controlled by DC-SCRIPT. *Sci. Immunol.* **6**, eabf4432 (2021).
44. Zhang, T. T. et al. Dynamic expression of BCl6 in murine conventional dendritic cells during in vivo development and activation. *PLoS ONE* **9**, 1–12 (2014).
45. Durai, V. et al. Cryptic activation of an Irf8 enhancer governs cDC1 fate specification. *Nat. Immunol.* **20**, 1161–1173 (2019).
46. Grajales-Reyes, G. E. et al. Batf3 maintains autoactivation of Irf8 for commitment of a CD8α+ conventional DC clonogenic progenitor. *Nat. Immunol.* **16**, 708–717 (2015).
47. Seillet, C. et al. Nfil3 is required for the development of all innate lymphoid cell subsets. *J. Exp. Med.* **211**, 1733–1740 (2014).
48. Kusunoki, T. et al. TH2 dominance and defective development of a CD8+ dendritic cell subset in Id2-deficient mice. *J. Allergy Clin. Immunol.* **111**, 136–142 (2003).
49. Dudziak, D. et al. Differential antigen processing by dendritic cell subsets in vivo. *Science* **315**, 107–111 (2007).
50. Gatto, D. et al. The chemotactic receptor EBI2 regulates the homeostasis, localization and immunological function of splenic dendritic cells. *Nat. Immunol.* **14**, 446–453 (2013).
51. Yi, T. & Cyster, J. G. EBI2-mediated bridging channel positioning supports splenic dendritic cell homeostasis and particulate antigen capture. *eLife* **2**, e00757 (2013).
52. Huang, C. et al. The BCL6 RD2 domain governs commitment of activated B cells to form germinal centers. *Cell Rep.* **8**, 1497–1508 (2014).
53. Crotty, S., Johnston, R. J. & Schoenberger, S. P. Effectors and memories: Bcl-6 and Blimp-1 in T and B lymphocyte differentiation. *Nat. Immunol.* **11**, 114–120 (2010).
54. Baumjohann, D. & Fazilleau, N. Antigen-dependent multistep differentiation of T follicular helper cells and its role in SARS-CoV-2 infection and vaccination. *Eur. J. Immunol.* **51**, 1325–1333 (2021).
55. Schlitzer, A. et al. IRF4 transcription factor-dependent CD11b+ dendritic cells in human and mouse control mucosal IL-17 cytokine responses. *Immunity* **38**, 970–983 (2013).
56. Kedmi, R. et al. A RORγt+ cell instructs gut microbiota-specific Treg cell differentiation. *Nature* https://doi.org/10.1038/s41586-022-05089-y (2022).
57. Wohn, C. et al. Absence of MHC class II on cDC1 dendritic cells triggers fatal autoimmunity to a cross-presented self-antigen. *Sci. Immunol.* **5**, eaba1896 (2020).
58. Hollister, K. et al. Insights into the Role of Bcl6 in follicular Th cells using a new conditional mutant mouse model. *J. Immunol.* **191**, 3705–3711 (2013).
59. Baumjohann, D. & Ansel, K. M. Tracking early T follicular helper cell differentiation in vivo. *Methods Mol. Biol.* **1291**, 27–38 (2015).
60. Johansson-Lindbom, B. et al. Functional specialization of gut CD103 + dendritic cells in the regulation of tissue-selective T cell homing. *J. Exp. Med.* **202**, 1063–1073 (2005).
61. Dobin, A. et al. STAR: ultrafast universal RNA-seq aligner. *Bioinformatics* **29**, 15–21 (2013).
62. Love, M. I., Huber, W. & Anders, S. Moderated estimation of fold change and dispersion for RNA-seq data with DESeq2. *Genome Biol.* **15**, 550 (2014).
63. R Core Team (2020). *R: A Language and Environment for Statistical Computing*. (R Foundation for Statistical Computing, Vienna, Austria, 2020).
64. Stephens, M. False discovery rates: a new deal. *Biostatistics* **18**, 275–294 (2017).
65. Blighe, K. and A. L. *PCAtools: everything Principal Components Analysis*. https://github.com/kevinblighe/PCAtools (2019).
66. Alboukadel Kassambara. *ggpubr:'ggplot2' Based Publication Ready Plots* (2020).
67. Yu, G., Wang, L.-G., Han, Y. & He, Q.-Y. clusterProfiler: an R Package for Comparing Biological Themes Among Gene Clusters. *OMICS* **16**, 284–287 (2012).
68. Qiu, Y.-Q. KEGG Pathway Database. in *Encyclopedia of Systems Biology*, Vol. 1 (eds. Dubitzky, W., Wolkenhauer, O., Cho, K.-H. & Yokota, H.) 1068–1069 (Springer New York, 2013). https://doi.org/10.1007/978-1-4419-9863-7_472.
69. Rizk, J. et al. The cIAP ubiquitin ligases sustain type 3 γδ T cells and ILC during aging to promote barrier immunity. *J. Exp. Med.* **220**, e20221534 (2023).

Acknowledgements

We thank Katrine Fog Starup, Julien Vandamme, Frank Dahlström, and Jennifer-Christin Becker for excellent technical support, the Lahl, Agace, Bekiaris, and Baumjohann laboratories for fruitful discussions, and Prof Allan Mowat for intellectual input and manuscript editing. *Bcl6*$^{fl/fl}$ mice were kindly gifted by Alexander Dent, and the OVA-MEF line was from Caetano Reis e Sousa. H&E sections were processed by Susanne Primdahl, and histology data was generated using research infrastructure at DTU National Food Institute, including FOODHAY (Food and Health Open Innovation Laboratory, Danish Roadmap for Research Infrastructure). We acknowledge the BMC Core Facility Flow Cytometry of LMU Munich for providing equipment and the Core Facility of the Medical Faculty at the University of Bonn for providing support and instrumentation funded by the Deutsche Forschungsgemeinschaft (DFG, German Research Foundation) (387333827, 216372545, 216372401, 387335189).

Funding for this project was provided by the China Scholarship Council fellowship (HX), the Lundbeck Foundation Fellowship R215-2015-4100 and R396-2022-373 (K.L.), the Ragnar Söderberg Foundation Fellowship in Medicine (K.L.), Vetenskapsrådet 2014-3595 (K.L.), Cancerfonden 21 1826 Pj (K.L.), the Novo Nordisk Foundation 18038 (K.L.), the Crafoord Foundation (K.L.), the European Research Council ERC-2016-STG-715182 (B.S.), Deutsche Forschungsgemeinschaft (DFG, German Research Foundation) Emmy Noether grant Schr 1444/1-1, Project-ID 360372040—SFB 1335 (project 8) and 322359157-FOR2599-A03 (B.S.), Deutsche Forschungsgemeinschaft (DFG, German Research Foundation) Emmy Noether Program BA 5132/1-1 and BA 5132/1-2 (252623821), SFB 1054 Project B12 (210592381) and Germany's Excellence Strategy EXC2151 (390873048) (D.B.).

Author contributions

Conceptualization: D.B. and K.L. Methodology: H.X., I.U., J.H., H.N., L.B., I.K., Y.C., S.H., U.M., L.Z., A.S., C.-F.P., B.S., D.B. and K.L. Investigation: H.X., I.U., J.H., H.N., L.B., I.K., S.H., U.M., L.Z., B.S., D.B. and K.L. Visualization: H.X., I.U., U.M., D.B. and K.L. Funding acquisition: H.X., D.B., B.S. and K.L. Project administration: K.L. Supervision: C.-F.P., A.S., B.S., D.B. and K.L. Writing—original draft: K.L. Writing—review & editing: I.U., B.S., D.B. and K.L.

Competing interests

The authors declare no competing interests.

Additional information

Supplementary information The online version contains supplementary material available at https://doi.org/10.1038/s41467-024-46966-6.

Correspondence and requests for materials should be addressed to Dirk Baumjohann or Katharina Lahl.

Peer review information *Nature Communications* thanks Lei Jin and the other, anonymous, reviewer(s) for their contribution to the peer review of this work. A peer review file is available.

Supplementary Figure file

Genomic deletion of Bcl6 differentially affects conventional dendritic cell subsets and compromises Tfh/Tfr/Th17 cell responses

Hongkui Xiao[1,*], Isabel Ulmert[1,*], Luisa Bach[2], Johanna Huber[3], Hamsa Narasimhan[4,5], Ilia Kurochkin[6,7], Yinshui Chang[2,3], Signe Holst[1,8,9], Urs Mörbe[1], Lili Zhang[10], Andreas Schlitzer[10], Carlos-Filipe Pereira[6,7,11], Barbara U. Schraml[4,5], Dirk Baumjohann[2,3], Katharina Lahl[1,8, 9, 12]

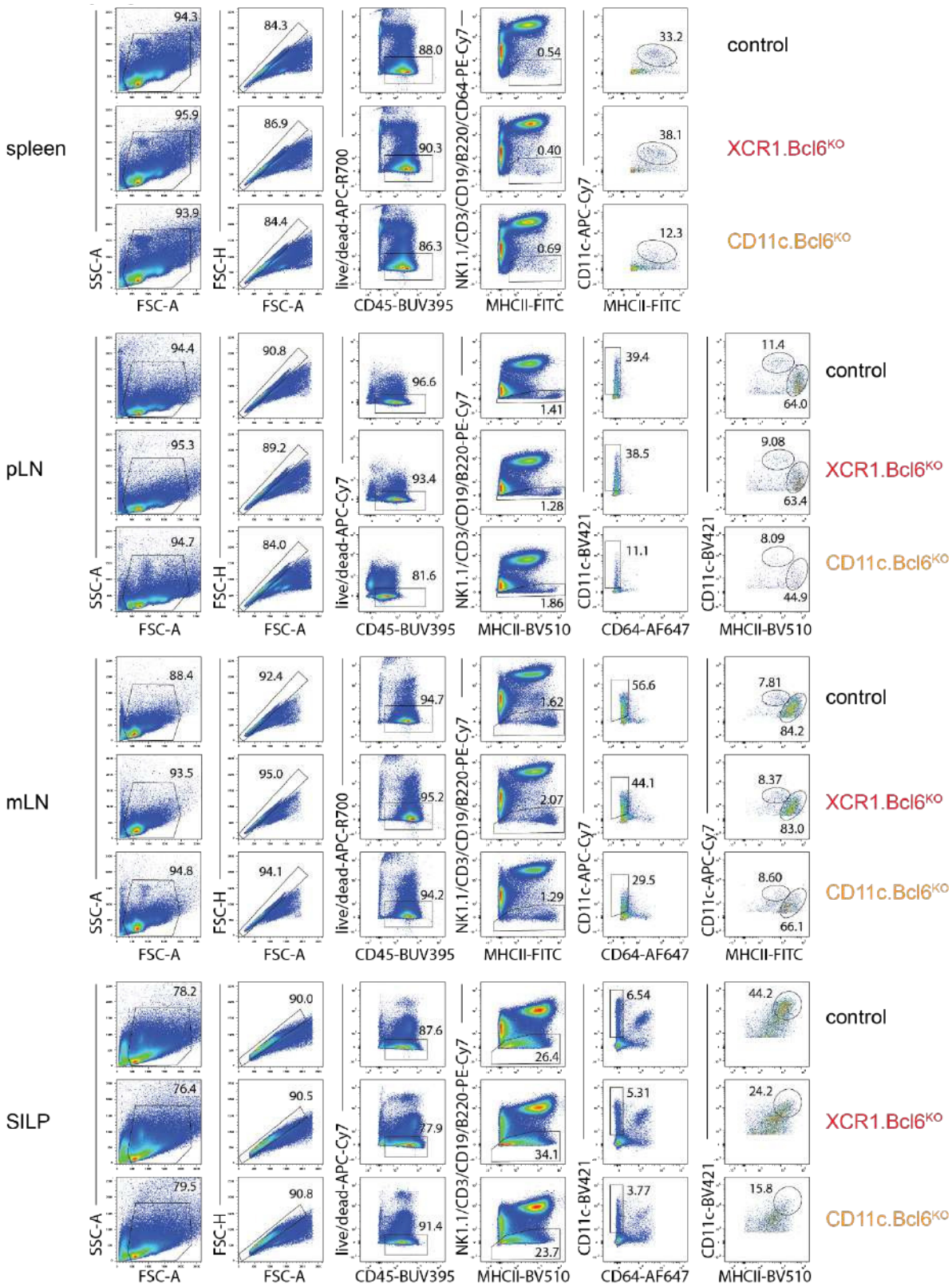

Supplementary Figure 1: Full gating strategy for spleen, pLN, mLN and SILP cDC from control, *XCR1.Bcl6*^{KO}, and *CD11c.Bcl6*^{KO} mice (used for main article Figures 1 and 2).

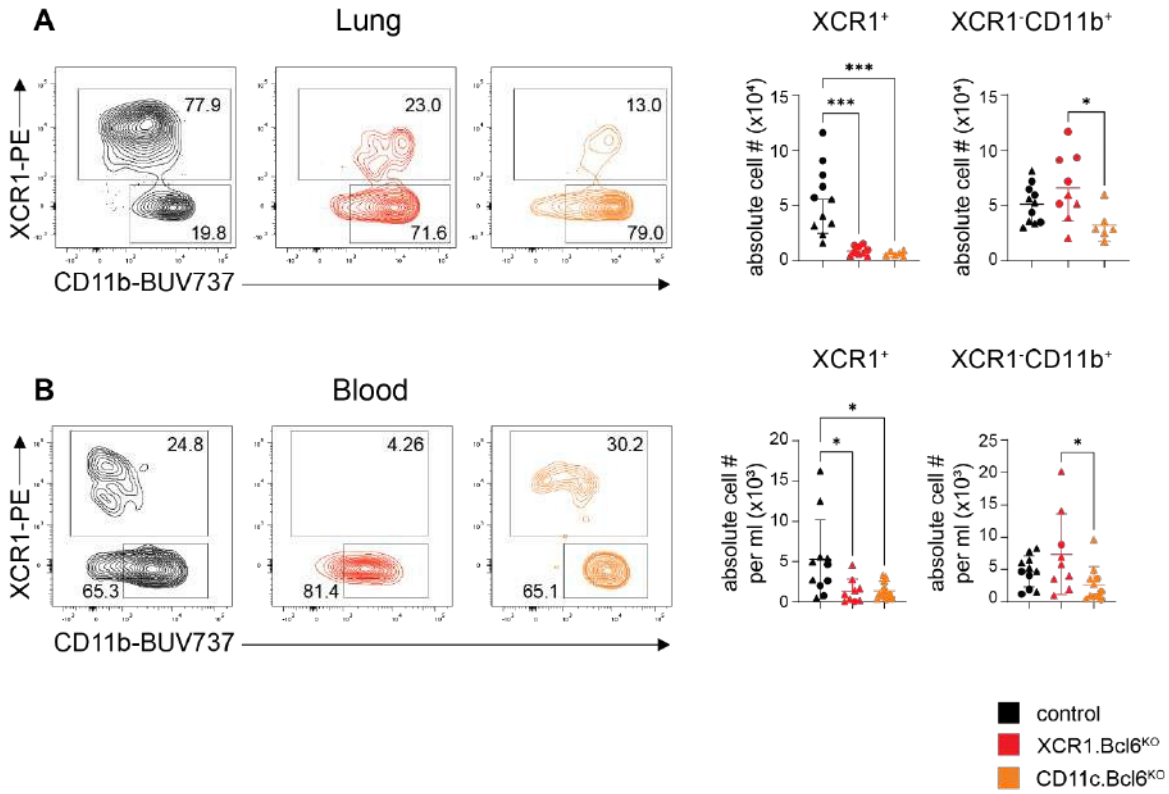

Supplementary Figure 2

A. Left: Flow cytometry plots show XCR1⁺ and XCR1⁻CD11b⁺ DC subsets in the lungs of control, *XCR1.Bcl6^{KO}* and *CD11c.Bcl6^{KO}* mice. The plots show representative staining profiles of live, CD45⁺, lineage⁻ (CD3, CD19, CD64, B220, NK1.1), MHCII⁺, CD11c^{hi} gated single cells. Right: Absolute numbers of cDC subsets in the lungs of control, *XCR1.Bcl6^{KO}*, and *CD11c.Bcl6^{KO}* mice. Statistical analysis by one-way ANOVA.** P<0.01, **** P<0.0001. Data points represent values from individual mice pooled from 2-3 experiments and lines represent means +/- SD.

B. Left: Representative flow cytometry plots of blood XCR1⁺ and XCR1⁻CD11b⁺ DC subsets from control, XCR1.Bcl6^{KO} and CD11c.Bcl6^{KO}. Shown are representative staining profiles of live, CD45⁺, lineage⁻ (CD3, CD19, CD64, B220, NK1.1), MHCII⁺, CD11c^{hi} gated single cells. Right: Absolute numbers of cDC1 and cDC2 in blood of control, XCR1.Bcl6^{KO}, and CD11c.Bcl6^{KO} mice. Statistical analysis by one-way ANOVA, significance at * P<0.05. Data points are normalized to volume of blood drawn and represent values from individual mice pooled from 4 experiments; lines represent means +/- SD from each genotype.

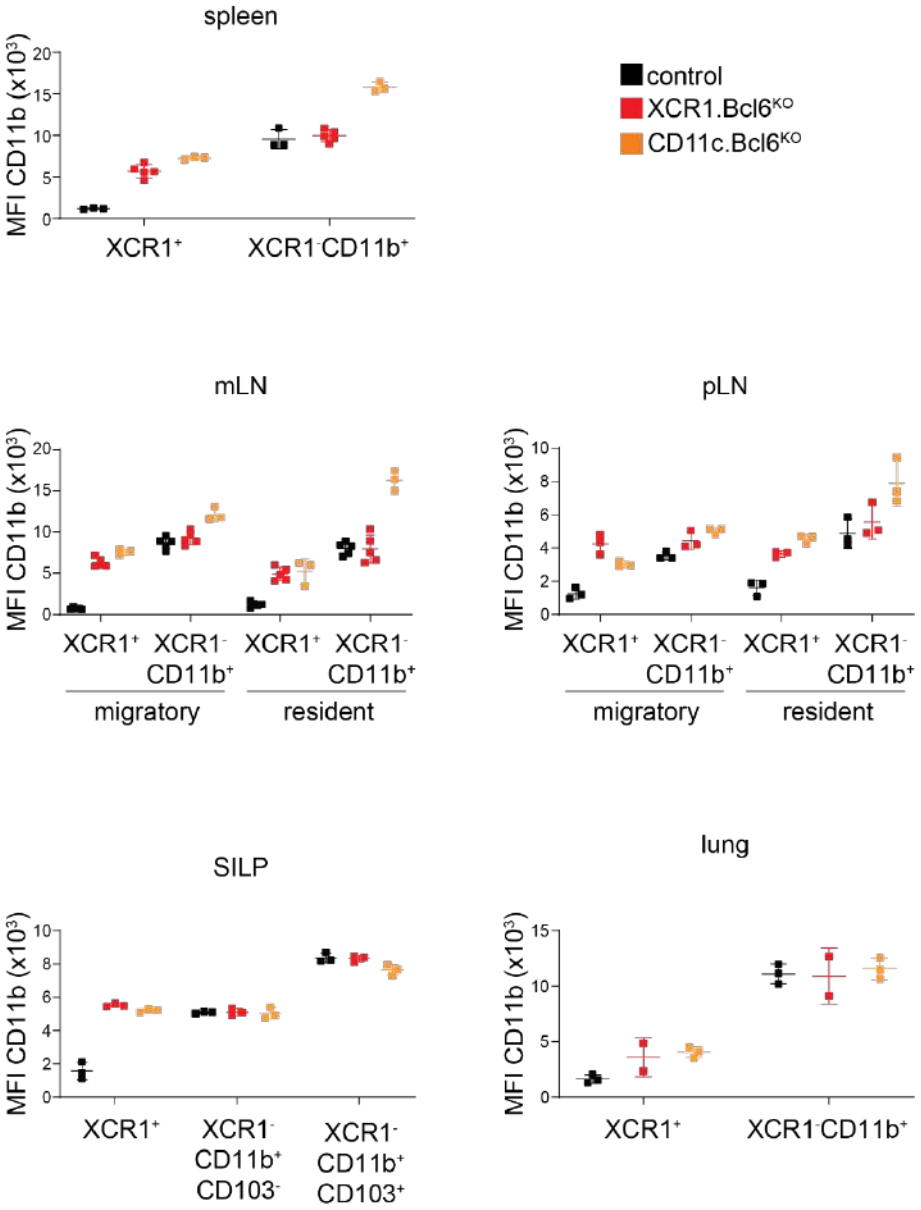

Supplementary Figure 3

Raw values of CD11b MFI in XCR1⁺ and XCR1⁻CD11b⁺ (spleen, mLN, pLN and lung) or XCR1⁺ and XCR1⁻CD11b⁺CD103⁻ and CD11b⁺CD103⁺ (SILP) cDC from control, *XCR1.Bcl6^{KO}*, and *CD11c.Bcl6^{KO}* mice. Note that different organs were stained using different panels and CD11b MFI values are therefore not comparable across organs. Data depicts one representative experiment of at least 3 per organ with 2-3 mice each.

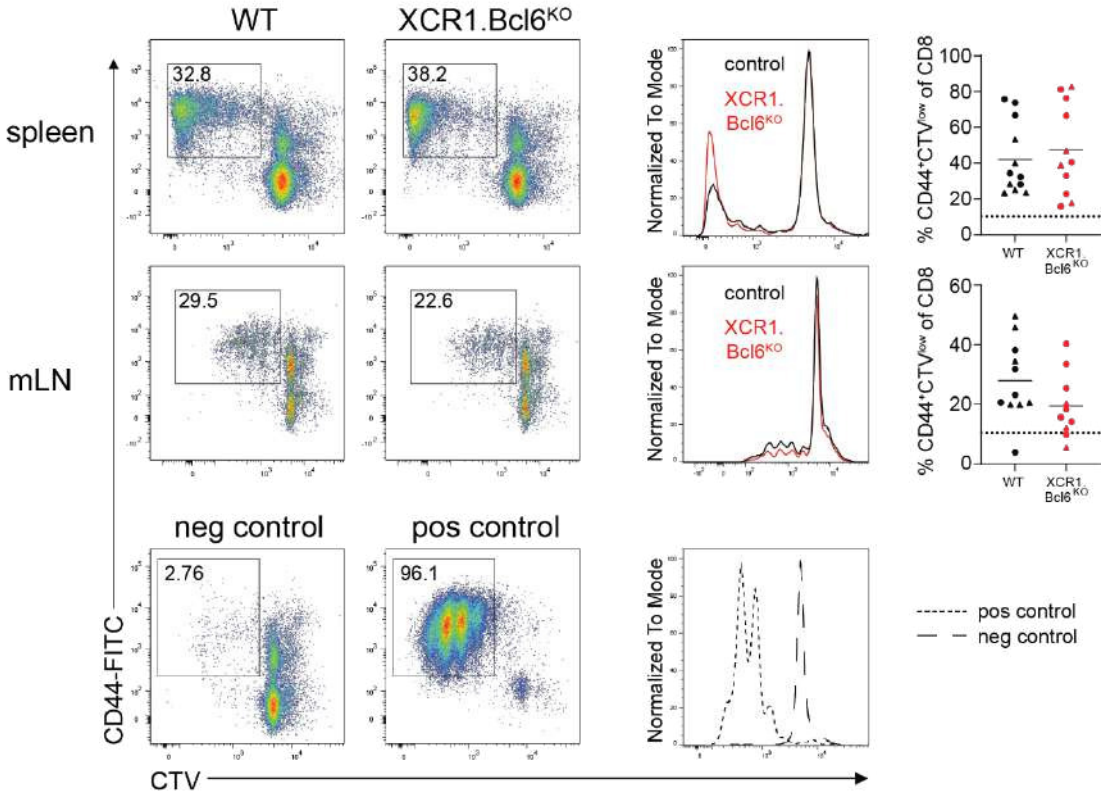

Supplementary Figure 4

Representative flow cytometry plots showing CTV dilution and CD44 expression on OT-I cells (gated on live, CD11c$^-$, CD8α$^+$ single cells) following 65h incubation with OVA pulsed and LPS stimulated cDC1 isolated from spleen (top) and mLN (bottom) of control and *XCR1.Bcl6^{KO}* mice. Data are representative of four independent experiments with 2-3 mice each.

Histograms show CTV dilution in OT-I cells after incubation with OVA pulsed cDC1 isolated from spleen and mLN of control and *XCR1.Bcl6^{KO}* mice. Bottom histogram shows CTV dilution in OT-I cells after incubation with anti-CD3 and anti-CD28 (positive control) and non-pulsed cDC1 (negative control).

Percentage of CD44$^+$ CTV^{low} OT-I cells after incubation with cDC1s isolated from spleen and mLN of control and *XCR1.Bcl6^{KO}* mice. Data is pooled from four independent experiments. Each dot represents one mouse, solid lines represent means +/- SD and dotted lines represent the average percentage of CD44$^+$ CTV^{low} OT-I cells from negative controls across all independent experiments.

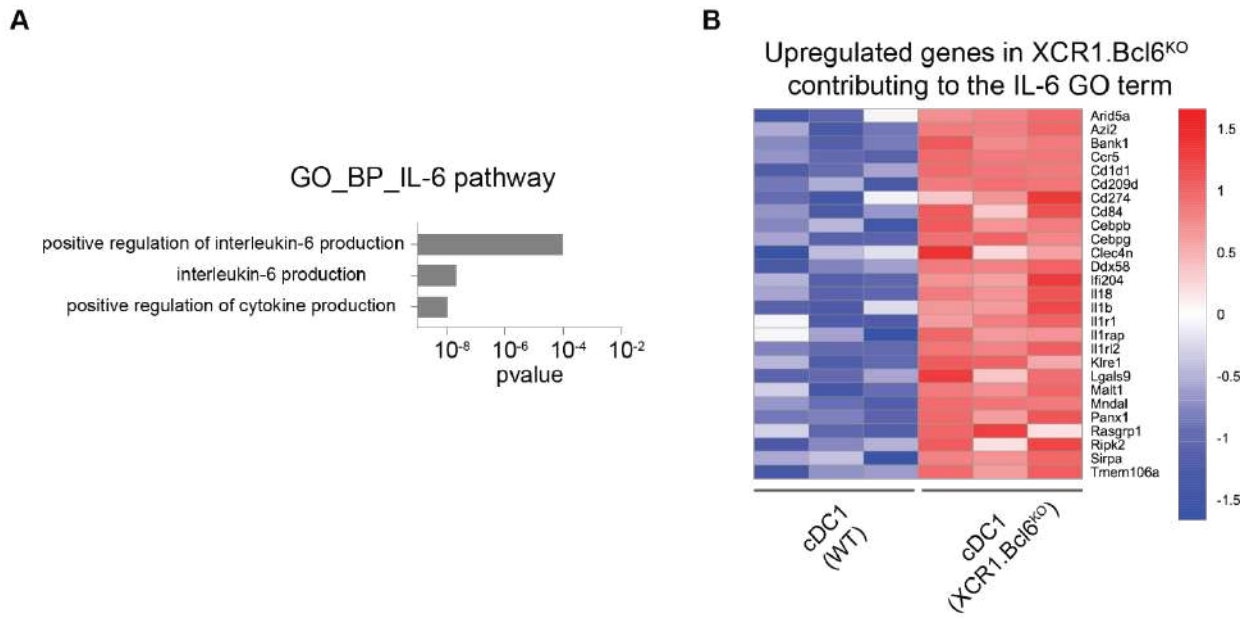

Supplementary Figure 5

A. IL-6 pathway gene ontology (GO) term enrichment analysis of differentially expressed genes (DEGs) in *XCR1.Bcl6*^{KO} and control cDC1. The p value calculated from GO term enrichment analysis is represented on the x-axis and the y-axis shows the GO Biological Process (BP) terms. Only terms related to positive regulation of IL-6 production are depicted.

B. Heatmap of all upregulated genes in *XCR1.Bcl6*^{KO} cDC1 contributing to the enriched IL-6 pathways depicted in A. The color scale represents the row Z score.

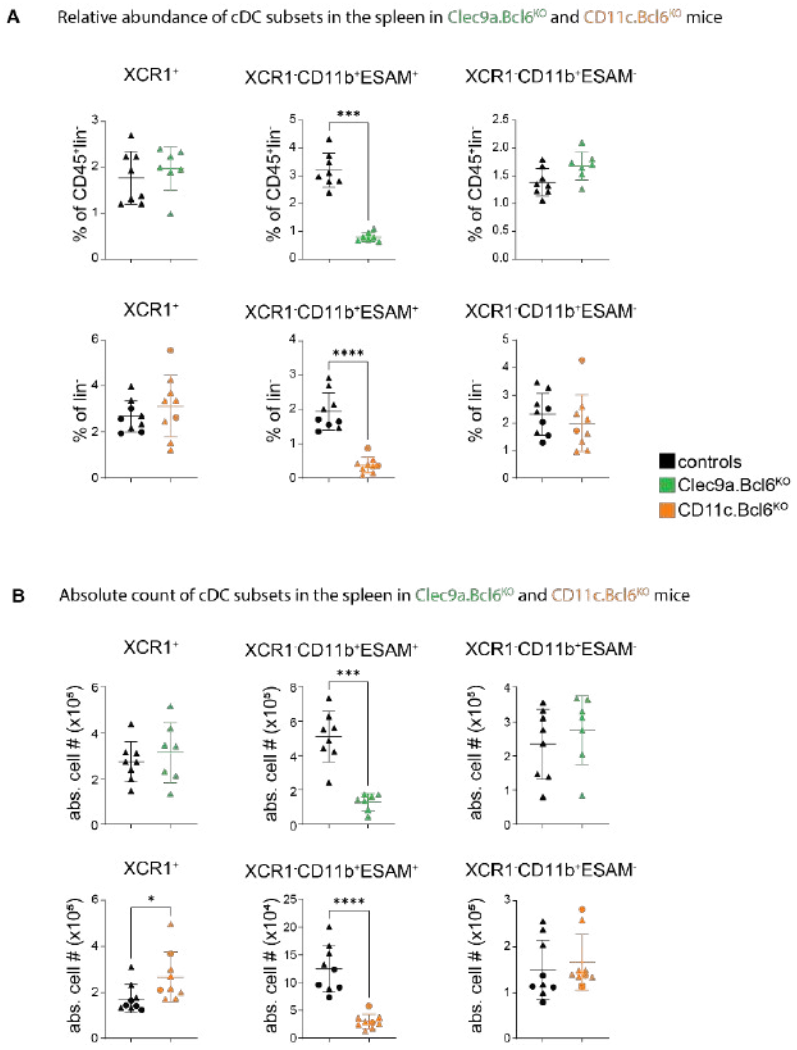

Supplementary Figure 6

A. Relative proportions of XCR1$^+$, XCR1$^-$CD11b$^+$ESAM^{hi} and XCR1$^-$CD11b$^+$ESAM^{lo} subsets in the spleen of Clec9a.*Bcl6*^{KO} (top) and CD11c.*Bcl6*^{KO} (bottom) mice. Cells were pre-gated on single live, CD45$^+$, lineage$^-$ (CD3, CD19, TER119, B220, NK1.1), MHCII$^+$, CD11c^{hi}. Data points represent values from individual mice pooled from 2-3 experiments and lines represent means +/- SD. Statistical analysis using Mann-Whitney test, *** P<0.001 and **** P<0.0001.

B. Numbers of XCR1$^+$, XCR1$^-$CD11b$^+$ESAM^{hi} and XCR1$^-$CD11b$^+$ESAM^{lo} subsets in the spleen of control, Clec9a.*Bcl6*^{KO} normalized to volume of suspension (top) and CD11c.*Bcl6*^{KO} shown as absolute numbers (bottom). Data points represent values from individual mice pooled from 2-3 experiments and lines represent means +/- SD. * P<0.05, *** P<0.001 and **** P<0.0001, by Mann-Whitney test.

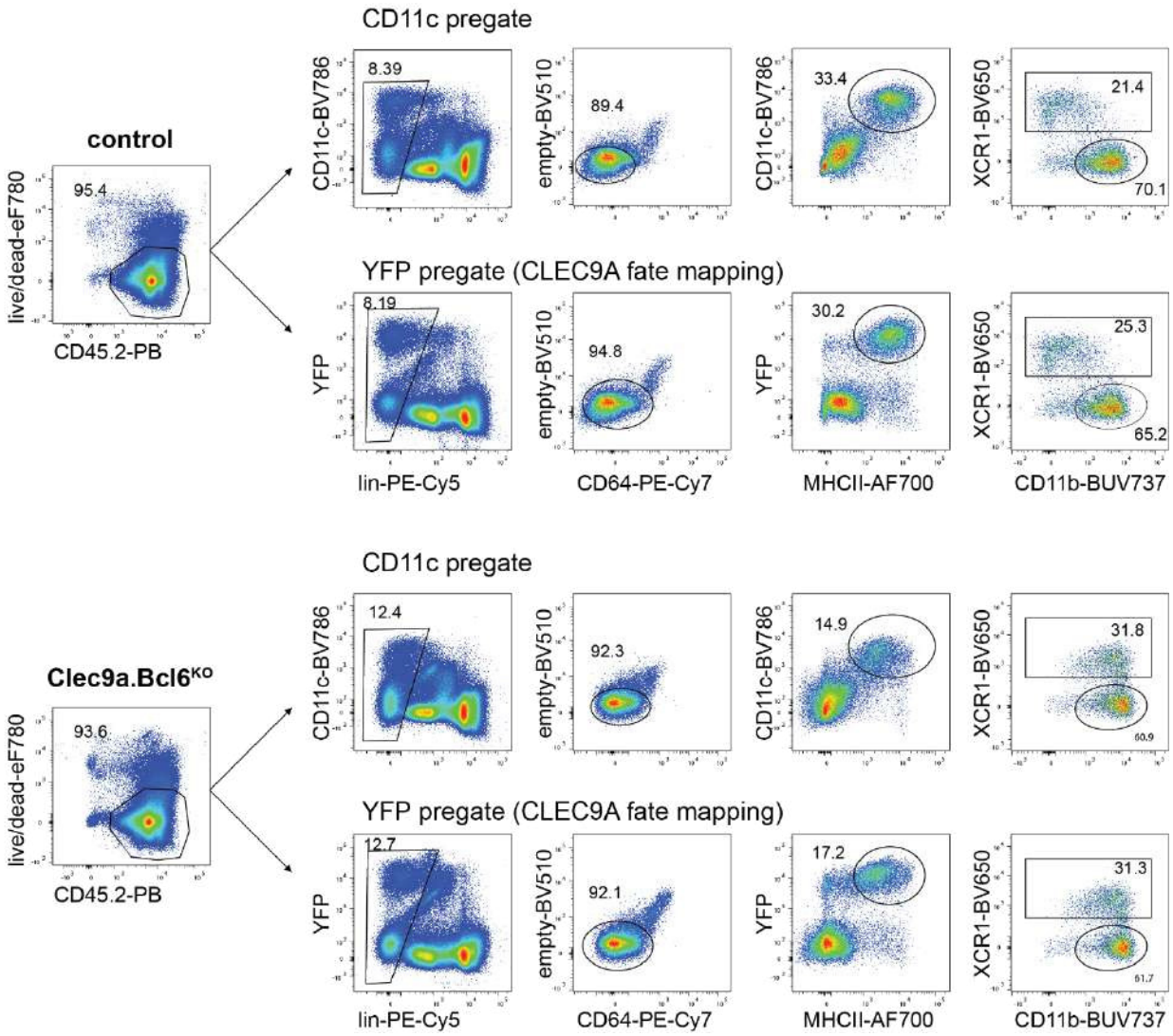

Supplementary Figure 7

FACS plots showing alternative gating strategies for cDCs in Clec9a.*Bcl6*^{KO} and control mice. CD11c pre-gate: classical CD11c-based gating; YFP pre-gate: Gating based on *Clec9a* fate mapping (Clec9a.*Bcl6*^{KO} mice contain the *R26-ROSA*^{YFP} locus). Data is representative for 3 experiments with 2-3 mice each.

Supplementary Figure 8

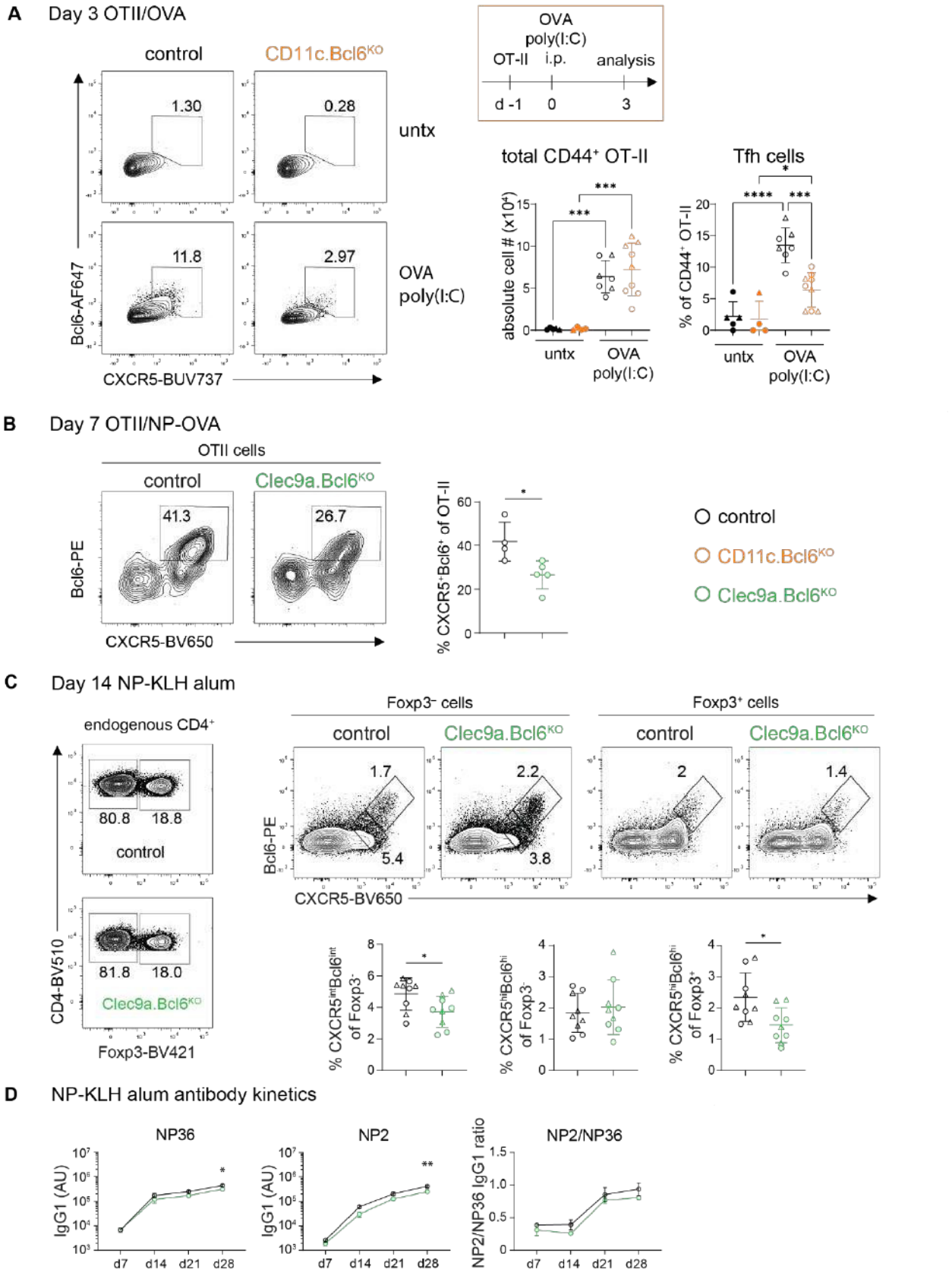

Supplementary Figure 8

A. Representative flow cytometric analysis of early Tfh cell induction amongst OT-II cells in the spleen of control and *CD11c.Bcl6*^{KO} mice 3 days after i.p. immunization with OVA and poly(I:C) or with PBS as a control. Tfh were gated as live CD4$^+$Vβ5.2$^+$CD45.1$^+$CD45.2$^+$CD44$^+$Bcl6$^+$CXCR5$^+$ and the results are representative of three experiments with 3-5 mice each. Right: Numbers of total CD44$^+$ OT-II T cells (left panel), left: proportions (right panel) of OVA-specific Tfh cells in the spleens of control and *CD11c.Bcl6*^{KO} mice 3 days after i.p. immunization with OVA and poly(I:C) or with PBS as a control. Statistical analysis was performed by one-way ANOVA. * P<0.05, ** P<0.01, *** P<0.001 and **** P<0.0001. Data points represent values from individual mice pooled from three experiments with 3-5 mice each in OVA/poly(I:C) immunized groups. Each experiment contained at least one untreated control per genotype; lines represent means +/- SD.
B. Bcl6-staining and Bcl6-based quantification of OT-II (CD45.1/2) Tfh cells of data presented in Figure 8C, D.
C. Foxp3-staining of endogenous CD4$^+$ T cells and Bcl6-staining and Bcl6-based quantification of Tfh cells, GC Tfh cells, and Tfr cells complementary to data presented in Figure 8E to H.
D. NP-specific IgG1 antibody titers accompanying total IgG data presented in Figure 8I, J.

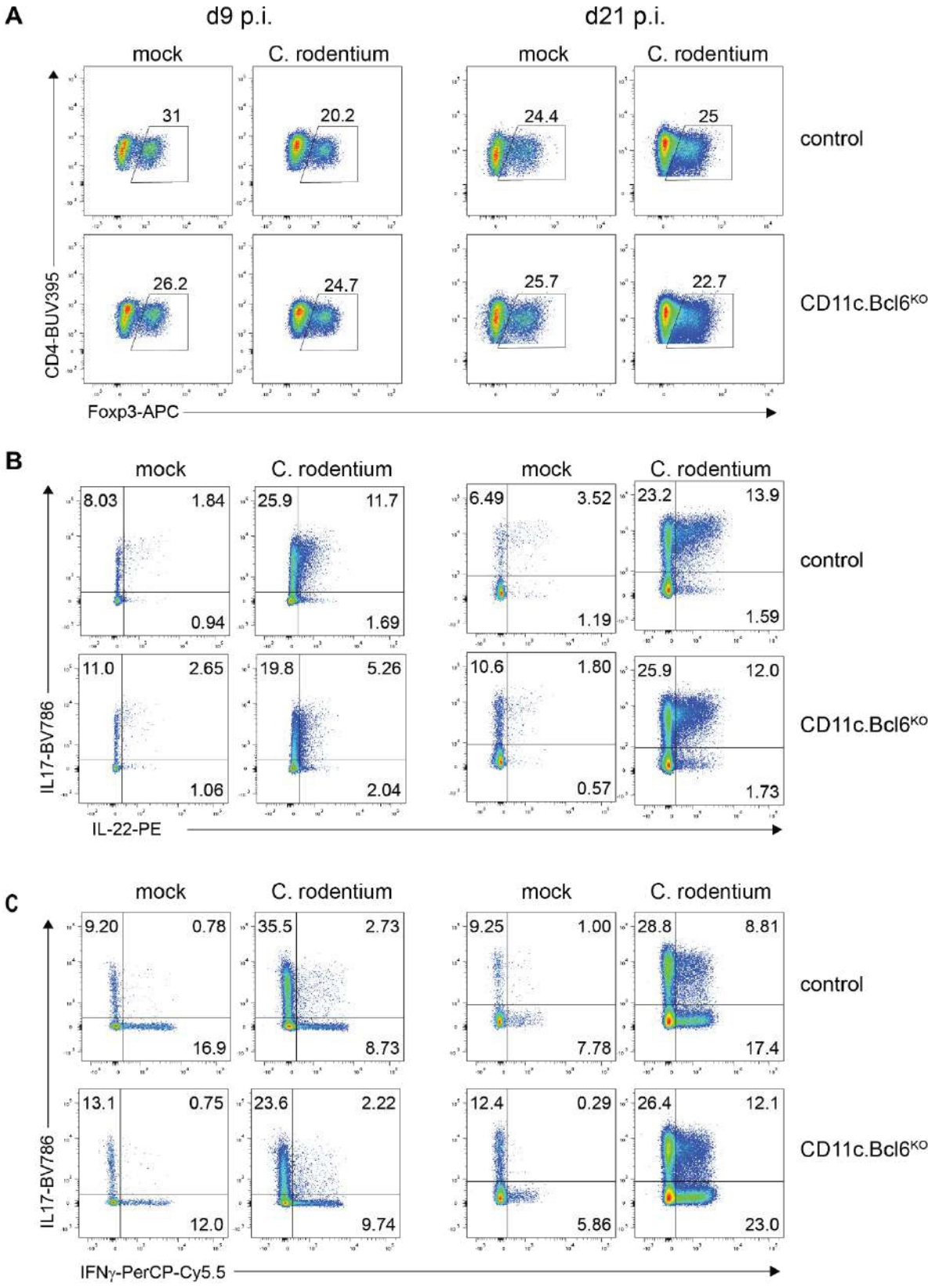
A
d9 p.i.
d21 p.i.
mock
C. rodentium
mock
C. rodentium
31
20.2
24.4
25
control
26.2
24.7
25.7
22.7
CD11c.Bcl6KO
CD4-BUV395
Foxp3-APC
B
mock
C. rodentium
mock
C. rodentium
8.03
1.84
0.94
25.9
11.7
1.69
6.49
3.52
1.19
23.2
13.9
1.59
control
11.0
2.65
1.06
19.8
5.26
2.04
10.6
1.80
0.57
25.9
12.0
1.73
CD11c.Bcl6KO
IL17-BV786
IL-22-PE
C
mock
C. rodentium
mock
C. rodentium
9.20
0.78
16.9
35.5
2.73
8.73
9.25
1.00
7.78
28.8
8.81
17.4
control
13.1
0.75
12.0
23.6
2.22
9.74
12.4
0.29
5.86
26.4
12.1
23.0
CD11c.Bcl6KO
IL17-BV786
IFNγ-PerCP-Cy5.5

Supplementary Figure 9

A. Representative flow cytometry plots showing Foxp3^{+} CD4^{+} T cells (gated on live, CD45^{+}, CD3^{+}TCRb^{+} singlets) in the cLP of mock and C. rodentium infected control and CD11c.Bcl6^{KO} mice at day 9 (left) or day 21 (right) post inoculation (used for main article Figure 10).
B. Representative flow cytometry analysis showing IL-17A^{+}IL-22^{+} CD4^{+} T cells (gated on live, CD45^{+}, CD3^{+}TCRb^{+} singlets) in the cLP of mock and C. rodentium infected control and CD11c.Bcl6^{KO} mice at day 9 (left) or day 21 (right) post inoculation (used for main article Figure 10).
C. Representative flow cytometry plots showing IL-17A^{+}IFNg^{+} CD4^{+} T cells (gated on live, CD45+, CD3^{+}TCRb^{+} singlets) in the cLP of mock and C. rodentium infected control and CD11c.Bcl6^{KO} mice at day 9 (left) or day 21 (right) post inoculation (used for main article Figure 10).

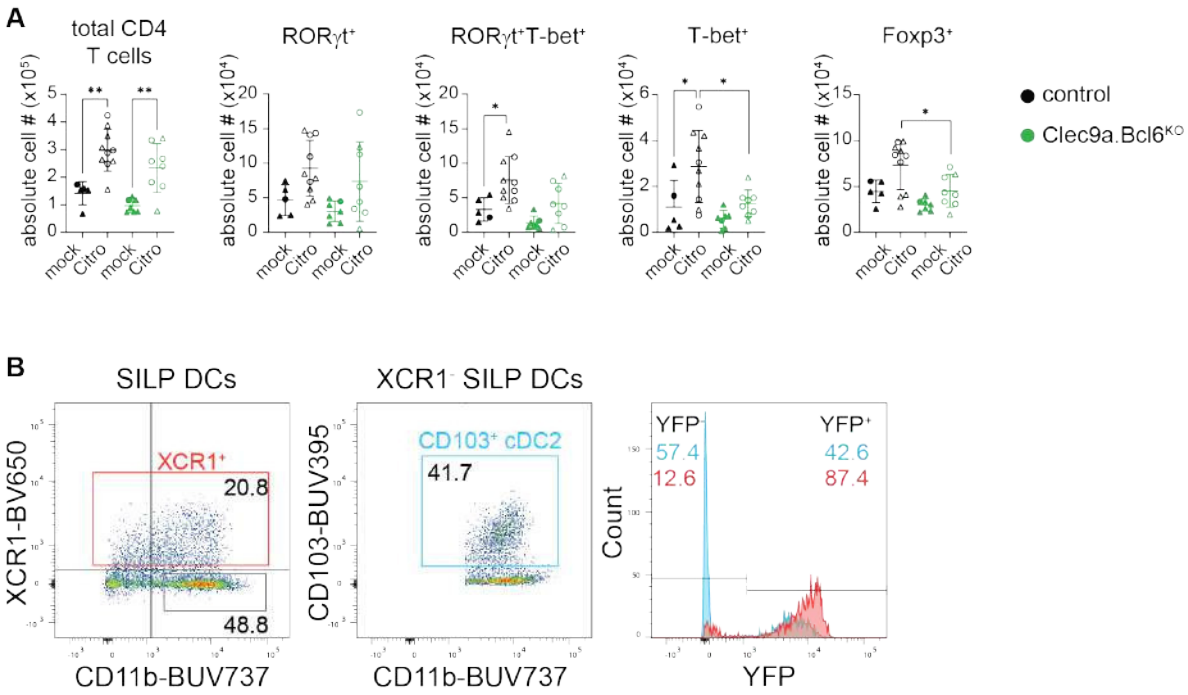

Supplementary Figure 10

A. Numbers of total CD4⁺ T cells, RORgt⁺, RORgt⁺T-bet⁺, T-bet⁺, and Foxp3⁺ CD4⁺ T cells in the cLP of mock and *C. rodentium* infected control and *Clec9a.Bcl6*^{KO} mice at day 9 post inoculation. Statistical analysis performed by one-way ANOVA, * P<0.05, ** P<0.01, *** P<0.001 and **** P<0.0001. Data representative of 3 independent experiments with 1-3 mice each.

B. Left: Flow cytometry plot showing XCR1⁺ and XCR1⁻CD11b⁺ gating on SILP DCs, pre-gated on live, lineage⁻ (CD3, CD19, CD64, B220, NK1.1), CD11c⁺, MHCII⁺ single cells; right: Sub-gate on XCR1⁻CD11b⁺ cells. Histogram shows YFP-expression in XCR1+ cDC1 (red) and XCR1⁻CD11b⁺CD103⁺ cDC2 (blue). Data representative of 2 experiments with 3 mice each.

5. References

1. Vyas JM, Van der Veen AG, Ploegh HL. The known unknowns of antigen processing and presentation. Nat Rev Immunol. 2008;8(8):607-18.

2. Guermonprez P, Valladeau J, Zitvogel L, Thery C, Amigorena S. Antigen presentation and T cell stimulation by dendritic cells. Annu Rev Immunol. 2002;20:621-67.

3. Kambayashi T, Laufer TM. Atypical MHC class II-expressing antigen-presenting cells: can anything replace a dendritic cell? Nat Rev Immunol. 2014;14(11):719-30.

4. Miranda de Carvalho C, Bonnefont-Rebeix C, Rigal D, Chabanne L. "Dendritic cells in different animal species: an overview". Pathol Biol (Paris). 2006;54(2):85-93.

5. Villadangos JA, Schnorrer P. Intrinsic and cooperative antigen-presenting functions of dendritic-cell subsets in vivo. Nat Rev Immunol. 2007;7(7):543-55.

6. Bosteels V, Janssens S. Striking a balance: new perspectives on homeostatic dendritic cell maturation. Nat Rev Immunol. 2024.

7. Macri C, Dumont C, Johnston AP, Mintern JD. Targeting dendritic cells: a promising strategy to improve vaccine effectiveness. Clin Transl Immunology. 2016;5(3):e66.

8. Palucka K, Banchereau J. Dendritic-cell-based therapeutic cancer vaccines. Immunity. 2013;39(1):38-48.

9. Karsunky H, Merad M, Cozzio A, Weissman IL, Manz MG. Flt3 Ligand Regulates Dendritic Cell Development from Flt3+ Lymphoid and Myeloid-committed Progenitors to Flt3+ Dendritic Cells In Vivo. The Journal of Experimental Medicine. 2003;198(2):305-13.

10. Rodrigues PF, Alberti-Servera L, Eremin A, Grajales-Reyes GE, Ivanek R, Tussiwand R. Distinct progenitor lineages contribute to the heterogeneity of plasmacytoid dendritic cells. Nat Immunol. 2018;19(7):711-22.

11. Dress RJ, Dutertre CA, Giladi A, Schlitzer A, Low I, Shadan NB, et al. Plasmacytoid dendritic cells develop from Ly6D(+) lymphoid progenitors distinct from the myeloid lineage. Nat Immunol. 2019;20(7):852-64.

12. Cabeza-Cabrerizo M, Cardoso A, Minutti CM, Pereira da Costa M, Reis e Sousa C. Dendritic Cells Revisited. Annu Rev Immunol. 2021;39:131-66.

13. Ziegler-Heitbrock L, Ohteki T, Ginhoux F, Shortman K, Spits H. Reclassifying plasmacytoid dendritic cells as innate lymphocytes. Nat Rev Immunol. 2023;23(1):1-2.

14. Schraml BU, van Blijswijk J, Zelenay S, Whitney PG, Filby A, Acton SE, et al. Genetic tracing via DNGR-1 expression history defines dendritic cells as a hematopoietic lineage. Cell. 2013;154(4):843-58.

15. Cabeza-Cabrerizo M, van Blijswijk J, Wienert S, Heim D, Jenkins RP, Chakravarty P, et al. Tissue clonality of dendritic cell subsets and emergency DCpoiesis revealed by multicolor fate mapping of DC progenitors. Sci Immunol. 2019;4(33).

16. Salvermoser J, van Blijswijk J, Papaioannou NE, Rambichler S, Pasztoi M, Pakalniskyte D, et al. Clec9a-Mediated Ablation of Conventional Dendritic Cells Suggests a Lymphoid Path to Generating Dendritic Cells In Vivo. Front Immunol. 2018;9:699.

17. Schraml BU, Reis e Sousa C. Defining dendritic cells. Curr Opin Immunol. 2015;32:13-20.

18. Guilliams M, Ginhoux F, Jakubzick C, Naik SH, Onai N, Schraml BU, et al. Dendritic cells, monocytes and macrophages: a unified nomenclature based on ontogeny. Nat Rev Immunol. 2014;14(8):571-8.

19. Papaioannou NE, Salei N, Rambichler S, Ravi K, Popovic J, Kuntzel V, et al. Environmental signals rather than layered ontogeny imprint the function of type 2 conventional dendritic cells in young and adult mice. Nat Commun. 2021;12(1):464.

20. Sulczewski FB, Maqueda-Alfaro RA, Alcantara-Hernandez M, Perez OA, Saravanan S, Yun TJ, et al. Transitional dendritic cells are distinct from conventional DC2 precursors and mediate proinflammatory antiviral responses. Nat Immunol. 2023;24(8):1265-80.

21. Leylek R, Alcantara-Hernandez M, Lanzar Z, Ludtke A, Perez OA, Reizis B, et al. Integrated Cross-Species Analysis Identifies a Conserved Transitional Dendritic Cell Population. Cell Rep. 2019;29(11):3736-50 e8.

22. Villani AC, Satija R, Reynolds G, Sarkizova S, Shekhar K, Fletcher J, et al. Single-cell RNA-seq reveals new types of human blood dendritic cells, monocytes, and progenitors. Science. 2017;356(6335).

23. Dutertre CA, Becht E, Irac SE, Khalilnezhad A, Narang V, Khalilnezhad S, et al. Single-Cell Analysis of Human Mononuclear Phagocytes Reveals Subset-Defining Markers and Identifies Circulating Inflammatory Dendritic Cells. Immunity. 2019;51(3):573-89 e8.

24. Liu Z, Wang H, Li Z, Dress RJ, Zhu Y, Zhang S, et al. Dendritic cell type 3 arises from Ly6C(+) monocyte-dendritic cell progenitors. Immunity. 2023;56(8):1761-77 e6.

25. Villar J, Segura E. Decoding the Heterogeneity of Human Dendritic Cell Subsets. Trends in Immunology. 2020;41(12):1062-71.

26. Pakalniskyte D, Schraml BU. Tissue-Specific Diversity and Functions of Conventional Dendritic Cells. Adv Immunol. 2017;134:89-135.

27. Durai V, Bagadia P, Granja JM, Satpathy AT, Kulkarni DH, Davidson JTt, et al. Cryptic activation of an Irf8 enhancer governs cDC1 fate specification. Nat Immunol. 2019;20(9):1161-73.

28. Grajales-Reyes GE, Iwata A, Albring J, Wu X, Tussiwand R, Kc W, et al. Batf3 maintains autoactivation of Irf8 for commitment of a CD8alpha(+) conventional DC clonogenic progenitor. Nat Immunol. 2015;16(7):708-17.

29. Hildner K, Edelson BT, Purtha WE, Diamond M, Matsushita H, Kohyama M, et al. Batf3 deficiency reveals a critical role for CD8alpha+ dendritic cells in cytotoxic T cell immunity. Science. 2008;322(5904):1097-100.

30. Anderson DA, 3rd, Dutertre CA, Ginhoux F, Murphy KM. Genetic models of human and mouse dendritic cell development and function. Nat Rev Immunol. 2021;21(2):101-15.

31. Murphy TL, Murphy KM. Dendritic cells in cancer immunology. Cell Mol Immunol. 2022;19(1):3-13.

32. Tussiwand R, Everts B, Grajales-Reyes GE, Kretzer NM, Iwata A, Bagaitkar J, et al. Klf4 expression in conventional dendritic cells is required for T helper 2 cell responses. Immunity. 2015;42(5):916-28.

33. Briseno CG, Satpathy AT, Davidson JTt, Ferris ST, Durai V, Bagadia P, et al. Notch2-dependent DC2s mediate splenic germinal center responses. Proc Natl Acad Sci U S A. 2018;115(42):10726-31.

34. Lewis KL, Caton ML, Bogunovic M, Greter M, Grajkowska LT, Ng D, et al. Notch2 receptor signaling controls functional differentiation of dendritic cells in the spleen and intestine. Immunity. 2011;35(5):780-91.

35. Brown CC, Gudjonson H, Pritykin Y, Deep D, Lavallee VP, Mendoza A, et al. Transcriptional Basis of Mouse and Human Dendritic Cell Heterogeneity. Cell. 2019;179(4):846-63 e24.

36. Nutt SL, Chopin M. Transcriptional Networks Driving Dendritic Cell Differentiation and Function. Immunity. 2020;52(6):942-56.

37. Lukowski SW, Rodahl I, Kelly S, Yu M, Gotley J, Zhou C, et al. Absence of Batf3 reveals a new dimension of cell state heterogeneity within conventional dendritic cells. iScience. 2021;24(5):102402.

38. Walsh SM, Sheridan RM, Lucas ED, Doan TA, Ware BC, Schafer J, et al. Molecular tracking devices quantify antigen distribution and archiving in the murine lymph node. Elife. 2021;10.

39. Abramson J, Dobes J, Lyu M, Sonnenberg GF. The emerging family of RORgammat(+) antigen-presenting cells. Nat Rev Immunol. 2024;24(1):64-77.

40. Durai V, Bagadia P, Briseno CG, Theisen DJ, Iwata A, Davidson JTt, et al. Altered compensatory cytokine signaling underlies the discrepancy between Flt3(-/-) and Flt3l(-/-) mice. J Exp Med. 2018;215(5):1417-35.

41. Maraskovsky E, Daro E, Roux E, Teepe M, Maliszewski CR, Hoek J, et al. In vivo generation of human dendritic cell subsets by Flt3 ligand. Blood. 2000;96(3):878-84.

42. Naik SH, Proietto AI, Wilson NS, Dakic A, Schnorrer P, Fuchsberger M, et al. Cutting edge: generation of splenic CD8+ and CD8- dendritic cell equivalents in Fms-like tyrosine kinase 3 ligand bone marrow cultures. J Immunol. 2005;174(11):6592-7.

43. Meredith MM, Liu K, Darrasse-Jeze G, Kamphorst AO, Schreiber HA, Guermonprez P, et al. Expression of the zinc finger transcription factor zDC (Zbtb46, Btbd4) defines the classical dendritic cell lineage. J Exp Med. 2012;209(6):1153-65.

44. Satpathy AT, Kc W, Albring JC, Edelson BT, Kretzer NM, Bhattacharya D, et al. Zbtb46 expression distinguishes classical dendritic cells and their committed progenitors from other immune lineages. J Exp Med. 2012;209(6):1135-52.

45. Meredith MM, Liu K, Kamphorst AO, Idoyaga J, Yamane A, Guermonprez P, et al. Zinc finger transcription factor zDC is a negative regulator required to prevent activation of classical dendritic cells in the steady state. J Exp Med. 2012;209(9):1583-93.

46. Merad M, Sathe P, Helft J, Miller J, Mortha A. The dendritic cell lineage: ontogeny and function of dendritic cells and their subsets in the steady state and the inflamed setting. Annu Rev Immunol. 2013;31:563-604.

47. Zhou W, Zhou L, Zhou J, Bank JRILC, Chu C, Zhang C, et al. ZBTB46 defines and regulates ILC3s that protect the intestine. Nature. 2022;609(7925):159-65.

48. Kabir AU, Zeng C, Subramanian M, Wu J, Kim M, Krchma K, et al. ZBTB46 coordinates angiogenesis and immunity to control tumor outcome. Nat Immunol. 2024;25(9):1546-54.

49. Basso K, Dalla-Favera R. Roles of BCL6 in normal and transformed germinal center B cells. Immunol Rev. 2012;247(1):172-83.

50. Choi J, Crotty S. Bcl6-Mediated Transcriptional Regulation of Follicular Helper T cells (T(FH)). Trends Immunol. 2021;42(4):336-49.

51. Watchmaker PB, Lahl K, Lee M, Baumjohann D, Morton J, Kim SJ, et al. Comparative transcriptional and functional profiling defines conserved programs of intestinal DC differentiation in humans and mice. Nat Immunol. 2014;15(1):98-108.

52. Ohtsuka H, Sakamoto A, Pan J, Inage S, Horigome S, Ichii H, et al. Bcl6 is required for the development of mouse CD4+ and CD8alpha+ dendritic cells. J Immunol. 2011;186(1):255-63.

53. Bagadia P, O'Connor KW, Wu R, Ferris ST, Ward JP, Schreiber RD, et al. Bcl6-Independent In Vivo Development of Functional Type 1 Classical Dendritic Cells Supporting Tumor Rejection. J Immunol. 2021;207(1):125-32.

54. Zhang S, Coughlan HD, Ashayeripanah M, Seizova S, Kueh AJ, Brown DV, et al. Type 1 conventional dendritic cell fate and function are controlled by DC-SCRIPT. Sci Immunol. 2021;6(58).

55. Zimmermannova O, Ferreira AG, Ascic E, Velasco Santiago M, Kurochkin I, Hansen M, et al. Restoring tumor immunogenicity with dendritic cell reprogramming. Sci Immunol. 2023;8(85):eadd4817.

56. Suzuki S, Honma K, Matsuyama T, Suzuki K, Toriyama K, Akitoyo I, et al. Critical roles of interferon regulatory factor 4 in CD11bhighCD8alpha- dendritic cell development. Proc Natl Acad Sci U S A. 2004;101(24):8981-6.

57. Bajana S, Roach K, Turner S, Paul J, Kovats S. IRF4 promotes cutaneous dendritic cell migration to lymph nodes during homeostasis and inflammation. J Immunol. 2012;189(7):3368-77.

58. Bajana S, Turner S, Paul J, Ainsua-Enrich E, Kovats S. IRF4 and IRF8 Act in CD11c+ Cells To Regulate Terminal Differentiation of Lung Tissue Dendritic Cells. J Immunol. 2016;196(4):1666-77.

59. Minutti CM, Piot C, Pereira da Costa M, Chakravarty P, Rogers N, Huerga Encabo H, et al. Distinct ontogenetic lineages dictate cDC2 heterogeneity. Nat Immunol. 2024;25(3):448-61.

60. Huang X, Ferris ST, Kim S, Choudhary MNK, Belk JA, Fan C, et al. Differential usage of transcriptional repressor Zeb2 enhancers distinguishes adult and embryonic hematopoiesis. Immunity. 2021;54(7):1417-32 e7.

61. Liu TT, Kim S, Desai P, Kim DH, Huang X, Ferris ST, et al. Ablation of cDC2 development by triple mutations within the Zeb2 enhancer. Nature. 2022;607(7917):142-8.

62. Eberl G. RORgammat, a multitask nuclear receptor at mucosal surfaces. Mucosal Immunol. 2017;10(1):27-34.

63. Eberl G, Marmon S, Sunshine MJ, Rennert PD, Choi Y, Littman DR. An essential function for the nuclear receptor RORgamma(t) in the generation of fetal lymphoid tissue inducer cells. Nat Immunol. 2004;5(1):64-73.

64. Hepworth MR, Monticelli LA, Fung TC, Ziegler CG, Grunberg S, Sinha R, et al. Innate lymphoid cells regulate CD4+ T-cell responses to intestinal commensal bacteria. Nature. 2013;498(7452):113-7.

65. Hepworth MR, Fung TC, Masur SH, Kelsen JR, McConnell FM, Dubrot J, et al. Immune tolerance. Group 3 innate lymphoid cells mediate intestinal selection of commensal bacteria-specific CD4(+) T cells. Science. 2015;348(6238):1031-5.

66. von Burg N, Chappaz S, Baerenwaldt A, Horvath E, Bose Dasgupta S, Ashok D, et al. Activated group 3 innate lymphoid cells promote T-cell-mediated immune responses. Proc Natl Acad Sci U S A. 2014;111(35):12835-40.

67. Miller CN, Waterfield MR, Gardner JM, Anderson MS. Aire in Autoimmunity. Annu Rev Immunol. 2024;42(1):427-53.

68. Klein L, Petrozziello E. Antigen presentation for central tolerance induction. Nat Rev Immunol. 2025;25(1):57-72.

69. Gardner JM, Metzger TC, McMahon EJ, Au-Yeung BB, Krawisz AK, Lu W, et al. Extrathymic Aire-expressing cells are a distinct bone marrow-derived population that induce functional inactivation of CD4(+) T cells. Immunity. 2013;39(3):560-72.

70. Yamano T, Dobes J, Voboril M, Steinert M, Brabec T, Zietara N, et al. Aire-expressing ILC3-like cells in the lymph node display potent APC features. J Exp Med. 2019;216(5):1027-37.

71. Wang J, Lareau CA, Bautista JL, Gupta AR, Sandor K, Germino J, et al. Single-cell multiomics defines tolerogenic extrathymic Aire-expressing populations with unique homology to thymic epithelium. Sci Immunol. 2021;6(65):eabl5053.

72. Lyu M, Suzuki H, Kang L, Gaspal F, Zhou W, Goc J, et al. ILC3s select microbiota-specific regulatory T cells to establish tolerance in the gut. Nature. 2022;610(7933):744-51.

73. Akagbosu B, Tayyebi Z, Shibu G, Paucar Iza YA, Deep D, Parisotto YF, et al. Novel antigen-presenting cell imparts T(reg)-dependent tolerance to gut microbiota. Nature. 2022;610(7933):752-60.

74. Kedmi R, Najar TA, Mesa KR, Grayson A, Kroehling L, Hao Y, et al. A RORgammat(+) cell instructs gut microbiota-specific T(reg) cell differentiation. Nature. 2022;610(7933):737-43.

75. Dobes J, Ben-Nun O, Binyamin A, Stoler-Barak L, Oftedal BE, Goldfarb Y, et al. Extrathymic expression of Aire controls the induction of effective T(H)17 cell-mediated immune response to Candida albicans. Nat Immunol. 2022;23(7):1098-108.

Acknowledgements

First and foremost, Prof. Barbara Schraml I thank you for giving me the opportunity to work in your group. Through this PhD you have provided me with innumerable and diverse learning opportunities regarding different aspects of being a scientist for which I'm truly grateful. I believe I would not have learned and grown half as much without your guidance and supervision, or in any other lab.

Thank you to all past and current members of the Schraml Lab for your support over the last few years. I cannot name all, but I must mention a few. Dr.Nikos Papaioannou discovered RORγt$^+$DCs and kindly worked me into the Schraml Lab and this project. My fellow lab rats Kaushikk, Dogus and Ramin - lab life wouldn't have been the same without you guys, and Kaushikk- no, a monkey could not have done it! Starting a PhD in a new country in the middle of a pandemic would not have been the same without having you guys beside me. You have been constant and supportive companions during this PhD, for which I'm truly grateful. Thank you for teaching me science and more in the lab and during our breaks.

I'm grateful to all the great collaborators I got to work with during my PhD. Thank you especially for your support in getting the RORγt$^+$DC story out to the scientific community. Dr. Maria Richter, thank you for your friendship beyond our collaboration

Thank you to the IMPRS-LS and MMRS PhD programs (especially Dr. Verena Kochan) for your support and organizing great lectures and workshops. Thank you to my TAC members Prof. Dr. Christina Schulz and Prof. Dr. Marc Schmidt-Supprian for your scientific inputs and support during this PhD.

I acknowledge and thank all the funding sources which allow for the research in our lab. And I would also like to take this opportunity to acknowledge and thank all the mice sacrificed for my research.

This chapter of my life has been one of the most challenging but also one of the most rewarding yet. It would not have been the same without support from my friends and family. Mariia, Yusuf, Benji and Jacob, thank you for all the talks, nature walks, boardgames, dinners and for exploring Munich with me. Tanvi, Dhanesh, and Panchu - you didn't always understand what I was doing or why I was doing it, but you always listened and supported me in different ways for which I'm grateful.

Thank you to the Shakibas - Tanja, Bamdad and Navid for being my family away from family. Ramin, you know I couldn't have done this without you.

Vaideghi Paati, I love and appreciate your enthusiasm for hearing what I'm up to, and for your constant support and well wishes for all my experiments and endeavors. And last but not least, nothing would be possible without my parents Nachu and Radhika. Pa, thank you for sparking my interest in science and for helping me grow into a scientist. Ma, thank you for supporting me in a way no one else can. I dedicate this thesis to you both.